System-Level Analysis and Design for Reliability and Security in Wireless Networks

Jinchuan Tang

Kellogg College

Department of Engineering Science, University of Oxford

Supervised by Prof. Justin P. Coon

A thesis submitted to the University of Oxford for the degree of

Doctor of Philosophy in Engineering Science

Hilary 2019

Abstract

Thesis Title: System-Level Analysis and Design for Reliability and Security in Wireless Networks
Name: Jinchuan Tang
College: Kellogg
Degree: Doctor of Philosophy
Term and Year of Submission: Hilary 2019

The performance of four wireless network scenarios, focusing on reliable device-to-device (D2D) communications and secure physical layer communications, is analyzed based on stochastic geometry in this thesis. The analyses and methodologies in this thesis constitute a comprehensive framework for system-level analysis and design of reliability and security in future wireless networks.

Since reliability is the cornerstone of security in wireless communications, the first scenario focuses on enhancing the reliability of concurrent D2D transmissions in a Poisson clustered out-band D2D network. Two convex optimization schemes are proposed to maximize the joint coverage probability and minimize the power consumption for reliable concurrent transmissions. Meanwhile, the second scenario focuses on route selection for end-to-end reliability, which is jointly characterized by coverage, delay and trust criteria, in the multi-hop D2D based mission-critical communication systems. The proposed algorithm ensures that the candidate links meet the given requirements of the criteria while selecting the best path based on end-to-end coverage, timeliness or trust probabilities.

Apart from the reliability issues discussed above, wireless communication networks including D2D networks are vulnerable to eavesdropping attacks. Thus, the third scenario moves on to study the meta distribution of the secrecy rate for a legitimate link in the presence of randomly located eavesdroppers (EDs) modeled by a Poisson point process. The meta distribution characterizes the fraction of the realizations of EDs that yield a target secrecy rate. Finally, the fourth scenario studies secure wireless communications in the presence of unmanned aerial vehicle (UAV) jamming and randomly located UAV EDs modeled by a uniform binomial point process. A fitting function on the line-of-sight probability is proposed so that a tractable expression is derived for the secure connection probability (SCP). The trends of the SCP on the transmit signal to jamming power ratio, UAV jammer location and UAV height are analyzed.

Acknowledgements

First and foremost, I express my sincere gratitude to my supervisor Prof. Justin P. Coon for his patience, motivation and endless support of my research in Oxford. His guidance helps me to carry out my whole research and writing of this thesis.

Also, I especially thank my regular collaborators Dr. Gaojie Chen and Dr. David E. Simmons, who gave a tremendous number of comments and suggestions on our publications and pointed out the right directions for my technical works.

Meanwhile, my sincere thanks also go to Dr. Hachem Yassine, Mr. Dene A. Hedges, Dr. Mihai-Alin Badiu, Dr. Ye Liu, Dr. Shahriar E. Tajbakhsh and Dr. Shuping Dang as well as other colleagues, who provided me an opportunity to learn from them and widen my horizon.

Besides, I would like to thank the reviewers of my publications, and my D. Phil. status assessors Prof. Dominic O'Brien and Prof. Ekaterina Shamonina, who provided very useful comments and encouragement to improve the quality of my research. I would also like to thank my examiners Prof. Dominic O'Brien at the University of Oxford and Prof. Kai-Kit Wong at the University College London, who provided indispensable comments to improve the quality of my research.

Furthermore, I would like to thank the Department of Engineering Science and Kellogg College, University of Oxford to fund my travel to 2017 IEEE International Conference on Communications (ICC) in Paris, France.

Also, I would like to thank Prof. Timothy O'Farrell and Miss Gemma Stephens at the University of Sheffield, and the Engineering and Physical Sciences Research Council (EPSRC) to organize and fund my attendance to the CommNet2 PhD summer schools focusing on security and energy efficiency.

Most importantly, to my beloved parents and younger sister, I thank you all for your unconditional support and encouragement throughout my study period in Oxford.

List of Publications

1) **J. Tang**, G. Chen, and J. P. Coon, "Secrecy Performance Analysis of Wireless Communications in the Presence of UAV Jammer and Randomly Located UAV Eavesdroppers," in *IEEE Transactions on Information Forensics and Security*, vol. 14, no. 11, pp. 3026 – 3041, Nov. 2019.

2) **J. Tang**, G. Chen, and J. P. Coon, "Route selection based on connectivity-delay-trust in public safety networks," in *IEEE Systems Journal*, vol. 13, no. 2, pp. 1558–1567, June 2019.

3) **J. Tang**, G. Chen, and J. P. Coon, "Joint coverage enhancement by power allocation in Poisson clustered out-of-band D2D networks," in *IEEE Transactions on Vehicular Technology*, vol. 67, no. 12, pp. 11537 – 11548, Dec. 2018.

4) **J. Tang**, G. Chen, and J. P. Coon, "Meta distribution of the secrecy rate in the presence of randomly located eavesdroppers," in *IEEE Wireless Communications Letters*, vol. 7, no. 4, pp. 630 – 633, Feb. 2018.

5) **J. Tang**, G. Chen, J. P. Coon, and D. E. Simmons, "Distance distributions for Matérn cluster processes with application to network performance analysis," in *Proc. IEEE International Conference on Communications (ICC).* Paris, France: IEEE, 2017.

6) **J. Tang**, J. P. Coon, and G. Chen, "Optimal cross-tier power allocation for D2D multi-cell networks," in *Proc. IEEE Global Communications Conference (GLOBECOM).* Washington, D.C., USA: IEEE, 2016.

Acronyms

1G	First generation
2G	Second generation
3D	Three-dimensional
3G	Third generation
3GPP	Third Generation Partnership Project
4G	Fourth generation
5G	Fifth generation
AMPS	Advanced Mobile Phone System
ATG	Air-to-ground
AWGN	Additive white Gaussian noise
BPP	Binomial point process
CCDF	Complementary cumulative distribution function
CDF	Cumulative distribution function
CRCPR	Constructive-Relay-based CooPerative Routing
CSCP	Conditional secure connection probability
CSI	Channel state information
CUE	Cellular user equipment
D2D	Device-to-device
DUE	Device-to-device user equipment
EDs	Eavesdroppers
eNB	Evolved Node B
EPS	Evolved packet system
FDMA	Frequency division multiple access
FSPL	Free space path loss
GSM	Groupe Spécial Mobile
HARQ	Hybrid automatic repeat request
HetNets	Heterogeneous networks
i.i.d.	Independent and identically distributed
IEEE	Institute of Electrical and Electronics Engineers
IMT	International mobile telecommunications
IoT	Internet-of-things
ISM	Industrial, scientific and medical
JPAMS	Joint power allocation and mode selection
LCD	Lost call delayed

LDPCs	Low-density parity-check codes
LoS	Line-of-sight
LTE	Long-term evolution
MAC	Medium access control
Mbps	Megabits per second
MCC	Mission-critical communications
MCData	Mission-critical data
MCPTT	Mission-critical push-to-talk
MRC	Maximal ratio combining
NLoS	Non-line-of-sight
OFDM	Orthogonal frequency-division multiplexing
OFDMA	Orthogonal frequency-division multiple access
OMA	Orthogonal multiple access
PCP	Poisson cluster process
PDF	Probability density function
PGFL	Probability generating functional
PHCP	Poisson hard-core process
PLS	Physical layer security
PPP	Poisson point process
ProSe	Proximity services
PSA	Public service agency
PUSCH	Physical uplink shared channel
QoS	Quality of service
RAT	Radio access technology
RB	Resource block
SC-FDMA	Single-carrier frequency division multiple access
SCP	Secure connection probability
SINR	Signal-to-interference-plus-noise ratio
SIR	Signal-to-interference ratio
SNR	Signal-to-noise ratio
SSL	Secure sockets layer
TDMA	Time division multiple access
UAVs	Unmanned aerial vehicles
UE	User equipment
UEDs	Unmanned aerial vehicle eavesdroppers
WCDMA	Wideband code division multiple access
WLANs	Wireless local area networks

Contents

List of Figures

List of Tables

List of Mathematical Notations

A_i	Traffic intensity
α, η	Path loss exponent
$\alpha_{ij} - 1$	Number of successful interactions from heads i to j
$\mathrm{Beta}(a, b)$	Beta function with shape parameters $a, b > 0$
β	Predetermined SINR threshold of a link in the first research chapter
$\beta_{ij} - 1$	Number of failed interactions from heads i to j
C	Indices of all clusters
$\mathbb{C}$	Complex numbers
c	Confidence interval of θ_{ij}
D_j, D_{ij}	Timeliness probability from cluster heads i to j
$d_{kj}, l_{k,j}$	Distance between nodes k and j
E_k	Event: the head transmits in active cluster k
$\overline{\mathrm{E}}_k$	Event: a member transmits in active cluster k
$\mathbb{E}[X]$	Expectation of the random variable X
η_{L}	Mean of excess path loss for LoS channel
η_{N}	Mean of excess path loss for NLoS channel
$\overline{F}(R_t, \cdot)$	Meta distribution of the secrecy rate R_t
G_e	Gain due to coding and antennas
$G_{p,q}^{m,n}(\cdot)$	Meijer G-function
$\Gamma(\cdot)$	Gamma function
$\mathbf{H}/\mathbf{D}/\mathbf{T}$	Probability matrices of coverage/timeliness/trust
H_{ij}	Coverage probability from cluster heads i to j
$H_t/D_t/T_t$	Threshold of coverage/timeliness/trust probability
$\lvert h_{xy}\rvert^2, F_{xy}$	Instantaneous power of Rayleigh fading while transmitting from node x to y
I_{ij}	Interference experienced at node j while transmitting signal from i
I_j	Interference measured at UE j
$I_{p_t}(a, b)$	Regularized incomplete beta function, $a, b > 0$
J	End-to-end path
$\mathcal{L}_I^h(s \mid a_{kj})$	Laplace transform of the interference from heads k to j
$\mathcal{L}_I(s)$	Laplace transform of the inter-cluster interference
L_n	Set of indices belonging to the transmitting DUEs inside cluster $n \in (1, ..., N_c)$
$L_T \backslash \{i\}$	Set of all the simultaneously transmitting DUEs from all of the clusters

L_T	Indices of all simultaneously transmitting DUEs
l_i	Index of forwarding cluster head i
λ	Carrier wavelength
λ_e	Intensity of eavesdroppers
λ_o	Intensity of parent points
λ_{u_i}	Mean call rate per user in cluster i, in call/min
M_b	bth moment of the CSCP for the colluding scenario
μ	Mean service rate
$[x]^+, \max(0, x)$	Maximal number amongst 0 and x
$\max_{e \in \Phi}(\cdot)$	Maximal SNR amongst all eavesdroppers
N	Number of servers
$\mathbb{N}$	Natural numbers
N_0	AWGN power at each node, in watt
N_c	Number of clusters
$\mathcal{N}(\mathbf{x}_o, \sigma^2\mathbf{I})$	Isotropic Gaussian distribution centred at point $\mathbf{x}_o$ with standard deviation σ along each coordinate axis and $\mathbf{I}$ is a 2×2 identity matrix
ν	Carrier frequency
$\mathcal{O}$	Observed interactions between heads i and j
P_i, P_s	Transmit power of nodes i and s
$\mathbb{P}\{\cdot\}$	Probability of an event enclosed
$\mathbb{P}\{Q_k\}$	Probability of queuing in cluster k
$\mathbb{P}_{\mathrm{L}}^{s,e}$	Probability of a link (s, e) to be LoS
$\mathbb{P}_{\mathrm{N}}^{s,e}$	Probability of a link (s, e) to be NLoS
Φ_o	Poisson point process
Ψ_E	Set of eavesdroppers
$p_{H_J}/p_{D_J}/p_{T_J}$	End-to-end coverage/timeliness/trust probability of path J
p_{ij}^c	Coherent coverage probability from node i to j within a cluster
p_{ij}^{nc}	Non-coherent coverage probability from node i to j within a cluster
p_{ij}^{sc}	Single-cluster approximation coverage probability from node i to j within a cluster
P_{kj}	Received power at UE j from UE k
P_d	Transmit power of each UE
$\mathbb{Q}$	Rational numbers
Q_i	Event: a call is delayed in cluster i
R	Radius of a cluster
$\mathbf{R}$	Link cost matrix
$\mathbb{R}$	Real numbers
$\mathcal{R}_t$	Target secrecy rate, in bit/s/Hz
SINR_{ij}	SINR at node j while transmitting from node i

$\text{SNR}_{s,y}$	Instantaneous SNR of the received signal from node s to node y
$\sum_{e\in\Phi}(\text{SNR}_e)$	Summation of the SNRs at all the eavesdroppers $e \in \Phi$
T_{ij}^{mean}	Mean trust probability from cluster heads i to j
T_{ij}^{robust}	Robust trust probability from cluster heads i to j
t	Link spectrum efficiency, in bit/s/Hz
τ	Delay threshold per hop, in seconds
τ_{hold}	Average call holding time of a user, in seconds
θ_{ij}	Probability of successful interactions
$\theta_{s,e}$	Elevation angle from s to e in radians
$\text{Var}[Y]$	Variance of the random variable Y
W_i	Random variable for the delay of a user in cluster i
$\mathbb{Z}$	Integers
$\mathbb{Z}^+$	Positive integers
ζ	Signal-to-interference-plus-noise ratio threshold

Chapter 1

Introduction

This chapter provides an overview of the research projects focusing on the analysis and design for reliable and secure communications of wireless networks. Initially, an overview on the reliability and security of wireless communications is given. Then, the motivation behind the research disclosed in this thesis is discussed. Finally, the contributions and organization are provided.

1.1 Overview

In 1948, a major breakthrough from the Shannon-Hartley theorem [1] established the capacity of a finite-bandwidth continuous-time Gaussian noise channel. It revealed that the reliable communications at a given rate over a noisy channel could be achieved through error-correction coding with arbitrarily small error probability. In the 1970s, Bell Labs along with academic institutions and companies around the world developed the theory and techniques of cellular radio-telephony to provide wireless communications. Since then, wireless communications have experienced an exponential growth and a fast progress over the past few decades, which has transformed the way people live and work. It is expected that there will be 7 trillion wireless devices serving over 7 billion people by 2020 [2].

In wireless communications, reliability and security of the links are challenging due to the inherent broadcast nature of the wireless medium, which causes the transmitted signals to arrive at all receivers in the coverage area. The undesired transmitted signals at the intended receivers cause interference, and signals intercepted by the unauthorized receiver lead to eavesdropping. To deal with the exponential growth of normal and sensitive data flow over wireless networks, the information reliability and security have been considered as the two important design goals in modern communication systems [3–5]. Since the performance of wireless communications is closely related to network geometry, and the wireless channels are inherently governed by a series of stochastic processes including the nodes' spatial distribution, shadowing and fading, it has become increasingly important to account for the randomness of network geometric topology while performing reliability and security analysis and design for future wireless networks.

1.1.1 Reliable Communications

The main task of the wireless physical layer is to transmit a signal reliably in the presence of varying channels, thermal noise and interference [6]. To achieve reliable communications, the signal-to-interference-plus-noise ratio (SINR) of each communication link must meet a target threshold [7]. To reduce interference and increase the spectrum efficiency for reliable communications, the limited spectrum is reused when there are sufficient distances between the transceivers [8]. The intelligent allocation and reuse of channels through a coverage region gives rise to the cellular architecture, which became the turning point in wireless communications.

Following the continued theoretical development and hardware advancement in wireless technologies dating primarily from 1980 to the present, mobile cellular networks have evolved through the first generation (1G) to the fourth generation (4G) with the design objective to handle as many connections as possible in a given bandwidth in the most efficient way with reliability. Orthogonal multiple access (OMA) techniques, such as frequency division multiple access (FDMA) for Advanced Mobile Phone System (AMPS) in the 1G standard and time division multiple access (TDMA) for Groupe Spécial Mobile (GSM) in the 2G standard, serve a single user in each orthogonal resource block for intra-cell bandwidth allocation, while the resource blocks were only shared among the non-neighboring cells [9]. Meanwhile, convolutional codes, which were invented by Peter Elias [10] back in 1955, were the *de facto* codes for reliable 2G mobile communications. In addition, a closed loop power control with long update interval (480 ms) was adopted in order to retain the target SINR threshold [11]. Although these systems mitigated the intra-cell interference and the inter-cell interference from immediate neighbors, they offered a very low level of spectrum efficiency. In the early 2000s, 3G standards started to adopt universal frequency reuse across the cells by using code division multiple access (CDMA), where multiple users can communicate simultaneously on one frequency at the cost of multiple access interference (MAI). The Shannon-capacity approaching turbo codes which were invented by Claude Berrou et al. [12] in 1993, were used to enhance link reliability. In order to reach a target SINR, a combination of open loop and closed loop power controls with a frequent update in the latter were implemented to compensate for channel gain including fast fading [13].

To avoid the MAI problem, 4G shifted to orthogonal frequency-division multiple access (OFDMA). By assigning subsets of subcarriers to individual users while targeting full spectrum reuse throughout cells, each cell has nearly full system capacity for reliable transmission [14, 15]. Additionally, turbo codes, fractional power control and hybrid automatic repeat request (HARQ) were adopted to enhance the reliability of 4G cellular systems [16, 17]. Apart from cellular systems, the Wi-Fi family of the Institute of Electrical and Electronics Engineers (IEEE) 802.11 standards have been used for wireless local area networks (WLANs) since 1997. In 1999, the 802.11a standard started to adopt orthogonal frequency-division multiplexing (OFDM) as the air interface. In IEEE 802.11-2012, convolutional codes are the minimum requirement for forward error correction while low-density parity-check codes (LDPCs) are defined in IEEE 802.11n-2009/ IEEE 802.11-2012 as an option [18, 19]. In addition, different transmit power control schemes have been proposed for Wi-Fi [20].

To further increase the spectrum efficiency of the 4G system, device-to-device (D2D) communication was proposed in long-term evolution (LTE) *Release 12* by the 3rd generation partnership project (3GPP). It enables D2D user equipment (DUEs) in proximity to communicate directly without going through an evolved Node B (eNB). Early studies have shown that D2D communication can improve data rate, increase spectral efficiency, reduce power consumption, and further offload the traffic in dense mobile communication networks [21]. Currently, D2D communication is considered as an essential component of a fifth generation (5G) system, which seamlessly incorporates multiple radio access technologies (RATs), such as cellular, Wi-Fi and Bluetooth, to provide a so-called "network of networks" service [22]. Due to the spectrum shortage confronting the massive growth of wireless devices and the fact that letting transmitted signals interfere with each other in a controlled way increases capacity [23], frequency and time resources are intensively reused [24]. However, improving network capacity and spectrum efficiency by activating more D2D pairs in the networks is a big challenge in wireless communications, since reliable communications are challenged by the interference due to concurrent D2D transmissions. To manage interference levels and protect the cellular user equipment (CUE), many methods such as power control and channel allocations have been proposed in the literature [25]. In particular, the cellular based power control schemes were adapted to D2D communications while the optimization based power control schemes were also introduced to achieve higher spectrum efficiency or lower power consumption [26]. Meanwhile, channel allocations help the active D2D devices to either share the same resources with CUEs or use spectrum dedicated to D2D communications to decrease the interference generated by the D2D devices. To completely avoid interference with the cellular users, it is beneficial to implement D2D communications outside the cellular spectrum for the time being [27]. Recently, stochastic geometry has been used to analyze the reliability based on the coverage probability and the average rate of a typical link in a network. The use of these tools reveal the optimum network parameters for designing more reliable communication networks [28–30].

1.1.2 Secure Communications

The security of wireless communications has conventionally relied on key-based cryptographic algorithms at the network layer or above. Before cryptography, encryption was undergoing development for centuries. It was only realized by Auguste Kerckhoff in 1883 that keeping a key secret would be sufficient for a cypher to maintain confidentiality even if the attacker fully understands the algorithm. This was later restated by Claude Shannon as a maxim – "the enemy knows the system". In 1949, one year after the groundbreaking work on information theory, Shannon published another landmark work [31] which laid the information-theoretic foundations of modern cryptography. In his work, Shannon proved that if the key is at least the same length as the ciphertext, i.e., a one-time pad key, then perfect security is achievable. Due to the strict requirement on key length, it is difficult to transmit very long messages or guarantee key freshness since the safe exchange of keys is not guaranteed. Currently, both symmetric- and nonsymmetric- key cryptosystems are based on computational security. The strength of the key is based upon its resistance to brute-force attacks. Although the probability of cracking such a key using current computational techniques and algorithms is extremely small, cyphers based on computational security are not future proof due to the relentless growth of computational power and the possibility of discovering new cracking algorithms. Besides, in the internet-of-things

(IoT) applications with 5G, devices range from well-resourced smartphones to devices with limited capabilities, and the implementation of computationally expensive cryptographic techniques can be challenging among these lightweight devices [32–35]. Therefore, the potential growth in computational power and the need to support IoT applications motivate the study of security solutions that are provably unbreakable [36].

Physical layer security (PLS) avoids computationally expensive cryptography and can achieve provable security at the physical layer. In 1978, Wyner [37] and subsequently Csiszár and J. Körner [38] revealed that, at the level of the physical layer, it is theoretically possible to have reliable transmission at a positive rate in perfect secrecy via a noisy wire-tap channel. These pioneering works relaxed the secrecy criterion by requiring asymptotically statistical independence as the block length increases in a noisy system rather than strict statistical independence as in Shannon's criterion of perfect secrecy in a noiseless system [39]. Later, the result from [40] confirmed that the secrecy capacity of a legitimate link is the capacity difference between the legitimate link and the eavesdropping link for Gaussian noisy channels. In the meantime, cryptography developed rapidly for its computational security, and PLS did not receive much attention. In 1995, with the goal to achieve perfect security rather than computational security, [41] proved that even if the channel of the legitimate link was worse than the eavesdropping channel, it could generate a secret key at the physical layer. This reignited the confidence in PLS, and more theoretical contributions on coding and modulation schemes for reliable and secure communication over Gaussian and fading wiretap channels have been proposed in the following years [42, 43]. Notably, the work in [44] has shown that fading has a positive impact on secrecy capacity and rate adaptation based on channel state information. To enhance PLS, two secrecy enhancing techniques are widely studied in the literature [45]: one is to create so-called guard zones by stopping the transmissions whenever eavesdroppers

(EDs) are discovered within them; another way is to transmit artificial noise, i.e., jamming, to make the confidential messages hard to decode at the EDs. Recently, the unpredictability of EDs has also been taken into consideration. In particular, randomly located EDs are normally modeled as a point process, and the performance of PLS over fading channels has been broadly investigated under a stochastic geometry framework.

1.2 Motivation

This section gives the motivation to study reliable D2D communications and PLS based on stochastic geometry.

In wireless communications, reliable transmission is the cornerstone of achieving secure transmission at the physical layer [37,40]. Although D2D communications have been proposed and used for both commercial applications [46] and mission-critical applications [21], there are still several challenges associated with the reliability of D2D networks. Due to spectrum sharing, the interference among mobile users is a significant problem in D2D communications [47]. The intended transmitter and interferers are mutually affected by each other, because the increase of the transmit power of a link will increase its reliability while degrading the performance of others. Besides, due to path loss, multipath fading and the randomness of the spatial locations of mobile users, it becomes difficult to predict the exact interference of the concurrent transmissions for proper interference management. Furthermore, the reliability of D2D communications over an end-to-end path is also challenged by the activities and behaviors of forwarding nodes. In addition, the studies in [27,48–50] have shown that direct communication within a group of DUEs can improve the performance of a cellular system in terms of signaling overhead, spectral efficiency, and energy efficiency. And, clustered D2D networks exist in real or standardized scenarios, such as hotspots for content distribution in heterogeneous cellular networks [51] and mission-critical group communications for public safety networks [52]. Thus, it becomes necessary to find new and sophisticated methods that are suitable for use in networks of positional randomness.

Due to the broadcast nature of wireless signals, wireless communication networks including D2D networks are also vulnerable to attacks. In an open access environment, the surrounding terminals including other receivers could act as potential EDs [53]. Since the secrecy performance of PLS is related to the capacity at the legitimate receiver and EDs, the physical properties of terminals, including the path loss, shadowing, fading and the ambiguous locations of EDs, must be considered. And, the transmit power of the transmitter will also affect the signal-to-noise ratios (SNRs) of both legitimate and eavesdropping links, thus affecting the secrecy performance. Meanwhile, with the advantages of low cost, high flexibility and coverage capability, unmanned aerial vehicles (UAVs) have also posed a significant risk to ground wireless communications when acting as EDs. In that case, the line-of-sight (LoS) link conditions from the ground transmitter to the UAV will also affect the secrecy performance. Finally, when considering anti-eavesdropping techniques such as jamming, ubiquitous artificial interference could degrade the legitimate link rate as well as the eavesdropping links. Therefore, the community is in great need of developing tractable tools to model and analyze the secrecy performance for EDs with positional randomness.

Since the performance of wireless transmissions depends heavily on the spatial locations of the mobile devices, both the reliable D2D communications and secure physical layer communications are mainly affected by the network geometry and the spatial distribution of interferers and eavesdroppers. Stochastic geometry has been proposed to model random network topologies with high accuracy. Compared with traditional models through Monte-Carlo trials, these methods offer analytic tractability to study the average behavior of a wireless network over many spatial realizations of wireless nodes modeled by point processes. Stochastic geometry has been used in the past few years for the system-level analysis of D2D networks as well as PLS [29,54]. Specifically, reliability enhancing techniques such as power control and channel allocations [26, 55] and PLS enhancing techniques such as guard zone and jamming [56] have been analyzed and designed based on stochastic geometry.

The thesis hereby focuses on the system-level analysis and design for reliability and security for next-generation networks based on stochastic geometry.

1.3 Thesis Contribution and Organization

Following the previous sections on the overview and motivation for reliable and secure communication, we present the contributions and organization of the thesis in this section. The thesis mainly studies four different, but important, wireless systems based on D2D technology and PLS, which have different system models and are suitable for different scenarios. All the analysis methods and performance improvement techniques used in those systems are newly proposed. The organization of the remaining parts of this thesis as well as the contributions are given as follows. All nomenclatures, abbreviations and mathematical notations are independently defined for the system in each chapter to achieve clarity. Meanwhile, most of the analytical results given throughout this thesis are derived by Mathematica or manually, and the numerical results are generated by Monte Carlo simulations via MATLAB.

Chapter 2 begins with reviewing the technical aspects of D2D communications. A retrospective of the preliminaries relevant to D2D communications is provided, in which a series of key concepts are introduced. In particular, the interference management related to the reliable communication has been addressed. Following this, PLS is addressed for a general wire-tapping channel model. Finally, the fundamentals of stochastic geometry for wireless modeling are provided. This lays the foundation for designing a reliable and secure wireless network.

Chapter 3 is the first of four research chapters. This work proposes two new power allocation frameworks for performance optimization in both centralized and distributed clustered out-band D2D networks. In particular, it studies the joint coverage probability of D2D links in a fading environment. Two types of Poisson cluster processes, namely Matérn and modified Thomas cluster processes, are used to model the gathering behavior of the DUEs. Unlike traditional analysis based on coverage probability, the joint coverage probability helps to capture the mutual interference from concurrent transmission links under the same channel resources. A novel distance distribution for the Matérn cluster processes has been derived to aid the formulation of the typical coverage probability. As a result, the power allocation framework that focuses on joint coverage maximization, and another framework that focuses on power minimization under the joint coverage constraint, have been formulated. The convex counterparts of the original non-convex problems have been obtained. In addition, to reduce the information reported to the centralized or localized controllers, different approximations on the joint coverage probabilities are investigated. The simulations have demonstrated that the performance of the target cluster and the whole network will be optimum over the fixed power and open loop schemes when using the proposed optimization frameworks. This chapter is joint work with Prof. Justin P. Coon, Dr. Gaojie Chen and Dr. David E. Simmons. The research has been published in one journal, *Transactions on Vehicular Technology* [57] © 2018 IEEE, in *the Proceedings of International Conference on Communications (ICC)* [58] © 2017 IEEE, and in *the Proceedings of Global Communications Conference (GLOBECOM)* [59] © 2016 IEEE.

Chapter 4 proposes a novel route selection method to find a reliable end-to-end link constrained by *coverage, timeliness*, and *trust* probabilities for mission-critical data (MCData) public safety networks. Along with interference, it also considers the delay of the transmission requests and the behaviors of neighboring groups. This contrasts with previous results on route selection [60–62] where noise and interference are considered for reliable transmissions. As a result, queuing theory and trust are introduced to model the delay of the transmission requests and the uncooperative behaviors of forwarding DUEs. The interference coming from neighboring clusters is discovered to be related to the queuing system which has not been seen in previous literature. Besides, robust trust based on a confidence interval is first introduced to describe the uncooperative behavior of users. Simulations show that, by designing such a route selection, the end-to-end reliability is enhanced when compared to the route selection only considering interference. This chapter is joint work with Prof. Justin P. Coon and Dr. Gaojie Chen. The main content of the research has been published in one journal, *System Journal* [63] © 2019 IEEE.

Chapter 5 is the first chapter focusing on PLS. It firstly presents the meta distribution of the secrecy rate, which can provide the fraction of the realizations of EDs fulfilling a target secrecy rate in a wireless network. Focusing on both the noise-limited regime and the high SNR regime, the meta distribution is studied based on a system model, where a primary link coexists with a secondary network of potential EDs modeled as a Poisson point process (PPP). The meta distribution can either be formulated using the Gil-Pelaez theorem with the imaginary moments of the conditional secure connection probability (CCSP) given the realization of EDs or approximated by the beta distribution with the first two moments only. The distribution of EDs is assumed to obey the PPP in a plane. The EDs can work in either colluding or non-colluding modes. This thesis is the first work to investigate the secure and reliable transmission of a ground link with the help of the meta distribution. This chapter is joint work with Prof. Justin P. Coon and Dr. Gaojie Chen. The main content of the research has been published in one journal, *Wireless Communications Letters* [64] ©

2018 IEEE.

Chapter 6 describes a new system model to analyze the secure connection probability (SCP) of a wireless link in the presence of the UAV EDs (UEDs) within a finite area of space. A friendly UAV jammer has been introduced to increase the secrecy performance of the legitimate link. The spatial distribution of UEDs obeying a uniform binomial point process (BPP) is used to characterize the randomness of the UEDs. The BPP itself is known to be a challenge in performance analysis due to its boundary effects. Moreover, a piecewise function is proposed to approximate the line-of-sight probability for the air-to-ground links, which not only provides a better approximation than using the existing sigmoid-based fitting but allows one to derive the analytic expression for the secure connection probability of the legitimate ground link in the presence of non-colluding UEDs. The performance of the SCP with respect to the transmitting-to-jamming power ratio, the height of the UAVs, and the UAV jammer location has been investigated. This chapter is joint work with Prof. Justin P. Coon and Dr. Gaojie Chen. The research has been published in one journal, *Transactions on Information Forensics and Security* [65] © 2019 IEEE.

Chapter 7 summarizes the thesis and presents its conclusions. Suggestions and ideas are proposed and discussed for future research in the field of reliability and security for wireless networks.

Chapter 2

Research Overview

This chapter focuses on the theories and models that have been used in the literature, which will support the studies in the following chapters to analysis and design for reliable and secure wireless transmissions. The main underlying principles of these theories and models are explained, followed by the review of their state of art applications in the literature.

2.1 D2D Communications

D2D communication is a paradigm in 4G and future 5G cellular networks, which allows user equipments (UEs), namely mobile devices, in close proximity[1] to communicate directly without the radio signal travelling through the base station, e.g., the evolved Node B (eNB) in 4G, or the core network. The mobile devices which work for D2D communications are called D2D UEs (DUEs), and the mobile devices which connect to eNBs for cellular communications are called cellular UEs (CUEs).

[1]The proximity is in a broader sense rather than just physical distance, which may also be found based on channel conditions, signal-to-interference-plus-noise ratio (SINR), throughput, or delay [66].

2.1.1 Classification

Based on spectrum usage, D2D communications can be primarily classified into in-band D2D communication and out-band D2D communication. Each category can have two exclusive working modes as shown in Figure 2.1.

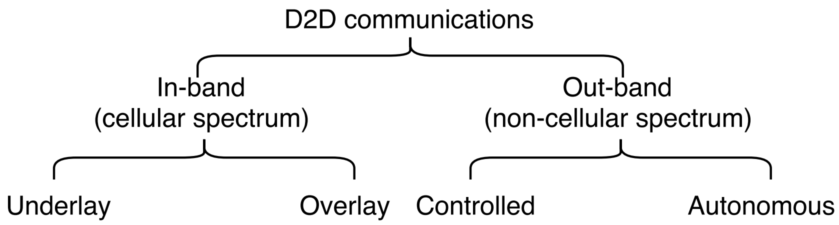

Figure 2.1: D2D classification.

2.1.1.1 In-band D2D communication

Depending on whether CUEs and DUEs use the same cellular resource for concurrent transmissions, in-band D2D communication can correspondingly operate in underlay or overlay modes. In the underlay mode, cellular uplink resource sharing for D2D communications is favoured over downlink for it is easier to handle the co-channel interference at the eNBs than the CUEs [66], and the downlink has a heavy traffic in the network [67]. In the overlay mode, a proportion of the cellular spectrum is reserved for D2D communications only.

The advantages of in-band D2D communication include accessing control by network operators and spectrum efficiency improvement by exploiting spatial diversity. The disadvantages are mainly complicated interference management in underlay mode and inefficient cellular resource utilization in overlay mode.

2.1.1.2 Out-band D2D communication

The out-band D2D communication often operates in the unlicensed spectrum such as the industrial, scientific and medical (ISM) radio bands. Radio access technologies like WiFi-Direct, ZigBee, and Bluetooth are the ideal candidates for out-band D2D communication. Depending on whether a cellular network manages its D2D communications or not, out-band D2D can be further divided into the controlled mode and autonomous mode. In the controlled mode, the management of the D2D communications is assisted by the cellular network [21]. In the autonomous mode, the management of D2D communication is left to DUEs.

One significant benefit of out-band D2D communication is the interference avoidance between the D2D and cellular links. Another benefit is to deliver more capacity without increasing the operational and capital expenditure [68]. Besides, it is possible to establish cellular and D2D links simultaneously since only cellular devices with two radio access technologies (e.g., long-term evolution (LTE) and Wi-Fi) can use out-band D2D communications [25]. Furthermore, LTE-Unlicensed has been proposed to enable LTE in the unlicensed spectrum [69, 70]. However, out-band D2D communications may suffer from a loss of synchronization, low data rate, and high latency due to the interference and collisions caused by ISM devices [71], [67].

2.1.2 Proximity-Based Services

Since *Release 12* of the 3rd generation partnership project (3GPP), proximity services (ProSe) have been developed to support D2D communications. The goal is to reduce the network load, increase capacity in a given bandwidth and extend network coverage. It is applicable to both commercial and public safety applications. In general, the ProSe have three core functions: device discovery, direct communication, and relay [72].

2.1.2.1 Device discovery

Device discovery involves detecting and identifying nearby D2D terminals. It allows for advertising and detecting useful information provided by the UEs in proximity without the need for establishing a communication link. During peer discovery, one party sends a beacon signal for synchronization proposes, and the other party scans and captures the beacon so that two devices can meet and communicate with each other using the same resource. In network-assisted D2D communications, the network infrastructure such as the eNB can coordinate the channel resource for sending and scanning beacons [73]. In the uncontrolled D2D network, the discovery process requires that the peers scan for beacons at different times and frequencies according to some randomized procedure so that the devices can discover each other [25].

2.1.2.2 Direct communication

Direct communication includes *one-to-one* communication and *one-to-many* communication to support direct data and group communications. Without adding more complications, DUEs uses the same uplink transmission scheme as the LTE CUEs, i.e., single-carrier frequency division multiple access (SC-FDMA), for transmission and reception. In order to have a large coverage, the direct data communication channel is expected to have a narrowband format with relatively low spectral efficiency [25]. Meanwhile, group communication with broadcast support requires the serving operator's authorization prior to communications.

2.1.2.3 Relay

Relay exists mainly in three different technologies in D2D communications [74–76].

1. Layer 1 relay, namely repeater or amplify-and-forward relay, relays the radio signals at the physical layer by amplifying and forwarding the signal. Since no data decoder exists at the repeater, the signal, noise, and interference are amplified altogether.

2. Layer 2 relay, namely decode-and-forward relay, is implemented to reduce the noise and interference by decoding and encoding the messages in layer 2 of the

relay. It spends more time than the repeater due to data processing.

3. A layer 3 relay works in a similar way to a layer 2 relay in terms of coding and decoding. Apart from this, a layer 3 relay offers other useful features such as ciphering for security, and it allows the relay UE to be treated as an eNB by another UE to reuse LTE functions instead of adding new functions [77].

2.1.3 Interference in D2D Communications

Addressing the interference among eNB, CUEs, and DUEs due to resource sharing plays a key role in achieving optimized reliability. By enabling D2D communications in a cellular network, the cellular architecture has been transformed into two-tier heterogeneous networks (HetNets). The first tier is the layer for conventional cellular communication, namely macrocell tier, while the second tier is the DUEs for D2D communication, namely device tier [78]. As a result of co-channel deployment of DUEs, there are two types of interference: co-tier and cross-tier interference.

Co-tier interference refers to the interference between the nodes within the same tier. In the LTE system, the co-tier interference is due to multiple DUEs sharing similar resource blocks. As a result, intra-cell interference, which was previously negligible in the conventional cellular case because of orthogonality between the cellular users [79,80], is no longer negligible. Besides, new types of inter-cell interference caused by DUEs from a cell to the DUEs and CUEs in other cells have to be dealt with.

Cross-tier interference refers to the interference between the D2D link and the cellular link as a result of reusing the cellular resources. Depending on whether uplink or downlink resources have been used for D2D links, two types of interference, i.e., uplink interference and downlink interference, are created. When the uplink is used for D2D transmission, the signal from the CUE transmitter will interfere with the D2D receiver and vice versa. When the downlink is used for D2D transmission, the signal from eNB will interfere with the D2D receiver and the signal from the D2D transmitter will interfere with the CUE receiver.

2.1.4 Performance Metrics for Interference Channels

Cumulative interference characterizes the aggregated instantaneous interference from all undesired transmitters. Abstracting all the eNBs and the UEs as the nodes, the cumulated interference at node j is

$$I_j = \sum_{k \in \Psi_I} P_{r_{kj}} = \sum_{k \in \Psi_I} P_k g_{kj} \ell(d_{kj}) |h_{kj}|^2 \tag{2.1}$$

where Ψ_I denotes the interfering nodes, $P_{r_{kj}}$ is the received power at node j while transmitting from node k, g_{kj} is the total antenna gain, P_k is the transmit power of node k, $\ell(d_{kj})$ is the path loss, which is a function of distance between nodes k and j denoted by d_{kj}, and $|h_{ij}|^2$ is the channel fading coefficient.

The **signal-to-interference-plus-noise ratio (SINR)** of the received signal at node j while transmitting from the intended node i is

$$\mathrm{SINR}_{ij} = \frac{P_{r_{ij}}}{N_0 + I_j} \tag{2.2}$$

where the noise power at each receiver node is given by $N_0 = 10^{\mathrm{NF}/10} k T_0 B$, where $k = 1.38 \times 10^{-23}$ J/K is Boltzmann's constant, $T_0 = 290$ K is the room temperature, B is the transmission bandwidth, and NF is the noise figure of the receiver in dB [81].

Channel capacity is the maximum rate for reliable transmission over a communication channel. When the interferers employ Gaussian codebooks for transmission, which is equivalent to the use of Gaussian signaling in [82], or when the interferers employ a spreading code [28], the resulting interference is additive white Gaussian noise (AWGN). Then, the channel capacity of link i, j in bit/s under the instantaneous channel and interference assumptions can be written as

$$C_{ij} = B \log_2(1 + \mathrm{SINR}_{ij}) \tag{2.3}$$

where B is the bandwidth of the channel in hertz. Furthermore, a metric called *ergodic capacity* can be used to measure the long-term achievable rate by averaging over all network realization states including channel and interference [83].

Coverage probability is the probability that a given information rate is supported by a communication channel. The complement of coverage probability is called outage probability. Due to small-scale fading [84], a mobile radio channel has a varying channel characteristic h_{ij}, and the received signal will experience periods of fades. The coverage probability of a link is the likelihood that the actual SINR of the link is higher than a predetermined threshold $S = 2^t - 1$, where $t = R_b/B$ is the predefined link spectrum efficiency and R_b is the target rate of the link in bit/s. A higher spectral efficiency enables nodes to transfer more data per Hz on the same spectrum, resulting in a lower cost-per-bit [85]. The coverage probability from node i to j is given by

$$p_{ij} = \mathbb{P}\{\mathrm{SINR}_{ij} > S\} = \mathbb{P}\left\{|h_{ij}|^2 > \frac{S(N_0 + I_{ij})}{g_{ij}\ell(d_{ij})P_i}\right\} \tag{2.4}$$

Depending on the statistics of h_{ij} measured in different environments, the expressions for the coverage probability can be formulated for Rayleigh fading [86, Eq.15-16], Racian fading [87], and Nakagami fading [88]. The probability distributions in [28,89] are also applicable to some specific scenarios.

2.1.5 Interference Control Schemes

Interference control schemes focus on who is responsible for interference management. Interference management algorithms are normally based on the performance metrics like the ones in the previous section. The algorithms often need to make a trade-off between scalability and performance.

In a **centralized** scheme, the eNB manages the interference for both CUEs and DUEs. This type of scheme requires that all users within the network report their information such as the channel state information (CSI) or the interference to the eNB [90]. Based on the obtained information, the eNB decides the resources and transmit power level allocated to CUEs, DUEs, or both. Due to the potential signalling overhead for exchanging information, this scheme could be used for small-scale D2D networks.

Compared to the centralized scheme, a **distributed** scheme allows the DUEs themselves to carry out the interference management autonomously without the support of the eNB. The control and computational overhead are heavily reduced due to limited information and feedback from others. But the interference management among the devices becomes difficult due to the lack of neighbour information. Thus, this method is more suitable for large-scale D2D networks.

A **semi-distributed** scheme, or a hybrid scheme, tries to combine the centralized and distributed schemes so that a moderate amount of information and feedback is required. Its performance often lies between these two schemes. This scheme is suitable for moderately large networks [91].

2.1.6 Interference Management

Interference management plays a major role in achieving reliable D2D communications. In general, interference management algorithms for D2D communications often rely on the availability of large-scale channel state information [92]. After the successful peer discovery, D2D candidates find each other for potential communication. To initialize the communication link, interference management via *mode selection* will determine the type of D2D or cellular operations. Afterwards, the fundamental research challenges are *resource allocation* for dedicated or reuse cellular spectrum and efficient *power control* if the reuse happens [93]. The following discussion gives both the basic and state-of-the-art D2D interference management.

Mode selection helps to find the optimum strategy for the coexistence of DUEs and CUEs under given network conditions to improve performance metrics such as overall network throughput, transmit power, and energy consumption. The strategy relies on knowing a certain amount of channel information to make a correct decision on the working mode. Fundamentally, different channel conditions in the direct link and the cellular link via eNB enable a device with one air interface to select a link with better performance [94].

Based on the availability of channel estimation in each transmission slot, mode selection can be further categorized into slow and fast mode selections. Slow mode selection usually is based on the large-scale channel information such as received signal strength, the distance or interference level between the terminals. For example, the authors of [95] considered the large-scale path loss experienced on the D2D link and cellular link. A weighted path loss of the D2D link was compared against the path loss on the cellular link for mode selection. The weight was used to tune the importance towards one working mode. In contrast to slow mode selection, fast mode selection uses full channel information via channel estimation in each scheduling slot to further capture the effect due to fast fading. The operating modes of the UEs depend on the estimated SINRs of the potential cellular link that connects the DUE to the eNB and the potential direct D2D link in the slot. Under coordinated radio resource management across cells, simulation results have shown a reduction of 95% of packet delay for D2D transmissions without sacrificing the performance of cellular transmissions [96].

Compared to fast mode selection, slow mode selection helps to reduce the number of unnecessary communication mode switches due to a temporary change of the channel condition and to reduce the frequency on link configuration and signaling overhead. In the case where fast channel estimation is not valid due to high dynamics of UEs and low complexity requirements on the transceivers, the statistics of the devices can be used to increase the robustness of the system. For example, the work of [97] considered mode switching based on average threshold D2D distance rather than an instantaneous value by exploiting the statistics of the locations of DUEs to reduce the signaling overhead but still keep some useful information for slow mode selection.

Radio resource allocation is an important step, which allocates certain spectrum for D2D communications. The previous discussion has demonstrated that D2D links could generate co-tier interference and cross-tier interference.

To alleviate the cross-tier interference, DUEs and CUEs could be arranged to work in separate spectrum. This could be the case of the overlay mode in in-band D2D communication, autonomous and controlled modes in out-band D2D communication. In [98], the authors investigated the optimization of the rate when given a carrier sensing threshold for mode selection, and a fraction of the cellular spectrum is exclusively assigned for overlay in-band D2D. In [99], a resource allocation framework was proposed where the uplink spectrum is divided into two orthogonal portions by assigning one portion to D2D communication and another portion to cellular communication in an in-band overlay multi-cell network. Out-band D2D for content storage was studied in [100]. Furthermore, by creating an interference graph that models the interference of the network, the authors of [101] proposed graph-based scheduling, where D2D transmissions can be scheduled in a way that nearby D2D and cellular transmissions will not happen on the same channel resources.

To handle the co-tier interference for a D2D communication underlay cellular network, the work of [102] allows multiple D2D pairs to share one channel. The packages of D2D pairs can form combinatorial bidders while the eNB is the seller in the channel allocation process. The seller sells channel resources to maximize their combinatorial utilities. The results show that D2D-enabled underlay cellular networks can increase the system energy efficiency compared to the conventional cellular system. In [103], unlike previous works requiring full CSI, the statistical CSI is needed. To solve the resulting high-complexity problem, candidate DUE sets are first narrowed down according to required outage probability constraints, which are used to construct a simplified bipartite graph. In addition, fairness is also an important factor in resource allocation. A fair resource allocation method in scenarios wherein multiple DUEs coexist with multiple CUEs has been studied in [104].

Depending on the complexity of the compensation at the transmitter, **power control** schemes can be divided into static and dynamic schemes. In a 3G network based on wideband code division multiple access (WCDMA), all links in a cell share the same spectrum and create intra-cell interference. A fast closed loop power control scheme is used for both uplink and downlink [105]. Especially on the uplink, the base station frequently estimates the received SINR and commands the mobile devices to adjust the transmit power to meet the target SINR. The rate of this measure-command-react cycle is 1.5 kHz, which is even faster than the speed of fast Rayleigh fading for low to moderate mobile speeds [106]. In addition, channel equalization can also be used to compensate the influence of random fluctuations appearing in the radio channel [107]. As a result, the variations of the path loss, shadowing and fading are captured, and the near-far problem due to imbalance among all the uplink signals is solved. In the LTE cellular network, the resources allocated to different CUEs of a cell are orthogonal to each other, and a slow power control scheme is used to compensate the variations of the path loss and shadowing, i.e., large-scale fading [108]. Since inter-symbol interference can be perfectly mitigated given that the maximum time delay of the channel is smaller than the guard interval duration, the sub-channels experience a flat fading channel. Thus, a one-tap equalizer is used at the LTE receiver.

For D2D-enabled LTE cellular networks, it is natural to base the strategy on LTE uplink power control to reduce design complexity [109]. Firstly, devices can transmit with *a fixed-level preconfigured transmit power* regardless of the channel variation. The benefit of the scheme is that the feedback of channel information is not required, because all D2D transmitters use a fixed transmit power and every D2D transmitter determines when to transmit data on its own without centralized control [110]. This is particularly helpful to the scenario where eNB assisted power control for D2D communications is not feasible for DUEs which are outside of coverage areas [72] or the scenario where feedback congestion happens in a large-scale network. Secondly, the transmitter can adopt conventional *open loop* scheme, which fully utilizes the LTE path loss compensation capability so that a full path loss inversion can be performed. Thirdly, *fractional power control*, or open loop with fractional path loss compensation, can partially compensate the path loss, which allows the received SINR and the corresponding transmission rate to decrease as the path loss increases. This was originally used to reduce inter-cell interference when the CUE at the edge needs to transmit to the eNB. For both conventional and D2D-enabled LTE cellular networks, system-level performance analysis and optimization must be carried out to find the fraction parameter for this type of power control scheme in order to achieve the optimum result [108].

In the literature, the work of [111] ensures that the CUEs have sufficient coverage probability by limiting the interference created by underlaid DUEs while attempting to support as many D2D links as possible. For the distributed power control method, expressions for the coverage probabilities of cellular and D2D links were derived, and a lower bound on the sum rate of the D2D links was provided. In [26], the authors proposed a channel allocation scheme together with a set of three power control schemes to mitigate interference in a D2D underlaid cellular system modeled as a random network using the mathematical tool of stochastic geometry. The first two power control schemes compensate for large-scale path loss effects and maximize the D2D sum rate by employing distance-dependent path loss parameters of the D2D link and the base station, including an error estimation margin. The third scheme is an adaptive power control scheme based on a variable target SINR, which limits the interference caused by D2D users and provides sufficient coverage probability for cellular users.

In many cases, to fulfil certain design goals, one may need to combine different interference management approaches. The **joint design** in [112] aims at maximizing the overall system throughput while guaranteeing the SINR of both D2D and cellular links. The optimization problem could be decomposed into power control, joint mode selection, and channel assignment. To address the joint optimization of power and mode selection under imperfect CSI, the authors of [113] proposed an optimal energy-aware joint power allocation and mode selection (JPAMS) scheme. The solution for the power minimization for both D2D and cellular links constrained by the quality of service (QoS) was provided. Based on the proposed power allocation, the mode selection problem in the presence of imperfect CSI was addressed.

The research of [93] proposed a centralized decision-making framework at the macro base station for D2D communication underlaying a two-tier cellular network. The framework prefers a D2D overlay mode to underlay mode if the D2D devices are close to each other and orthogonal resources are available. Otherwise, D2D underlay mode is enabled when both the maximum distance and the interference threshold are satisfied. A geometric vertex search approach was adopted to solve the power allocation problem.

The authors of [114] considered joint mode selection and radio resource allocation to improve overall system throughput. The maximization of the sum of users' data rates constrained by interference and power were formulated for both D2D and CUE links. A coalition formation game with transferable utility was used to solve the optimization problem. A coalition between the D2D and CUE links who share the same resource blocks was formed in the game, and the best response strategy was used in coalition formation.

In [115], a resource allocation scheme was studied for a multi-D2D communications underlay cellular network, where each D2D pair can share subcarrier resources with multiple CUEs. An optimization problem was formulated to maximize the sum spectrum efficiency of the HetNet while guaranteeing a positive system gain and the rate requirement of CUEs. A heuristic greedy algorithm was designed to make the subcarrier matching between CUEs and DUEs based on maximum sum spectrum efficiency, and then an efficient power allocation algorithm per D2D pair was developed based on the Lagrangian dual method.

2.2 Physical Layer Security

As with reliable communications, wireless communication security is another driving factor for the evolution of wireless communication systems. Incorporating security capabilities at the physical layer can complement cryptography-based high-level security so that more secure links can be established [116]. This section will introduce a series of basic concepts in modeling and designing a reliable and secure communication system with physical layer security.

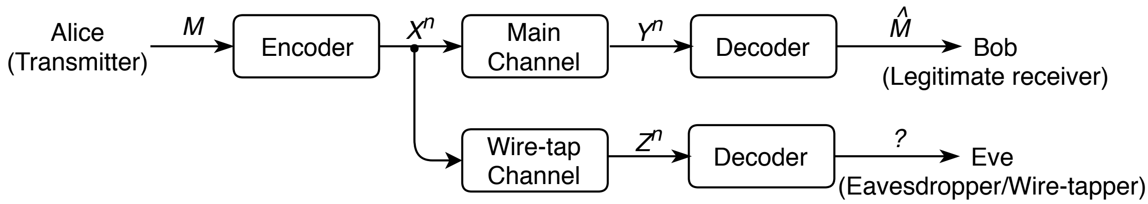

Figure 2.2: Wire-tap channel mode.

2.2.1 Wire-Tap Channel

As seen in Figure 2.2, the transmitter is assumed to work as a stationary ergodic finite alphabet source. A binary message word M consisting of k bits is encoded into an n-vector X^n code word, which then works as the input to the main channel. For Wyner's classic wire-tap channel model, during the message transmission, only the wire-tap channel is corrupted by Gaussian noise. Since practical wireless channels are always noise corrupted, the Gaussian wire-tap channel model is considered instead. In this model, both the main and wire-tap channels are assumed to be corrupted by independent and identically distributed (i.i.d.) Gaussian noise. The legitimate receiver makes an estimate $\hat{M}$ of M based on the output Y^n of the main channel, incurring a block (i.e., message word) error rate

$$P_e = \mathbb{P}\left\{M \neq \hat{M}\right\}. \tag{2.5}$$

Meanwhile, the fractional equivocation of the eavesdropper (ED) can be defined as [40]

$$\Delta = \frac{H(M \mid Z^n)}{H(M)} \tag{2.6}$$

where $H(M) = -\sum_i p_i \log_2 p_i$ is the Shannon entropy, p_i is the probability of character number i appearing in the set of characters of the message M, $H(M \mid Z^n)$ is the conditional entropy, and the rate of transmission for the main channel is defined as

$$R = \frac{H(M)}{n}. \tag{2.7}$$

A pair (R^*, d^*) is achievable, if for all $\epsilon > 0$, there exists an encoder-decoder pair so that

$$R \geq R^* - \epsilon, \quad \Delta \geq d^* - \epsilon, \quad \text{and } P_e \leq \epsilon. \tag{2.8}$$

For the Gaussian wire-tap channel model, denoting the capacity difference between the main and wire-tap channels as C_s, the authors of [40] proved that $(R^*, d^*) = (C_s, 1)$ is achievable. This means that, by transmitting below the rate C_s, it is feasible to completely confuse the ED even though it has received Z^n via the wire-tap channel. The proof of achievable secrecy capacity in the Gaussian wire-tap channel satisfies the *weak secrecy* condition, which is defined as

$$\lim_{n\to\infty} \frac{I(M; Z^n)}{n} = 0 \tag{2.9}$$

where the mutual information $I(M; Z^n) = H(M) - H(M \mid Z^n)$. In addition, to strengthen the definition for secrecy, the *strong secrecy* condition is defined as

$$\lim_{n\to\infty} I(M; Z^n) = 0 \tag{2.10}$$

while perfect secrecy condition is defined as

$$I(M; Z^n) = 0. \tag{2.11}$$

According to [117, 118], any coding scheme that satisfies the weak secrecy condition can be converted into a coding scheme that satisfies the strong secrecy condition.

2.2.2 Performance Metrics for Wire-Tap Channels

2.2.2.1 Secrecy Capacity

The secrecy capacity of a Gaussian wire-tap channel is the highest coding rate at which both the reliability and security constraints in (2.8) are satisfied.

The instantaneous SNR at a receiver y from a transmitter x is

$$\mathrm{SNR}_{x,y} = \frac{P_x |h_{x,y}|^2 \ell(d_{xy})}{N_y} \tag{2.12}$$

where N_y is the noise power at the receiver y. Denoting Alice, Bob, and a set of EDs as s, d, and Ψ_E, respectively, the secrecy capacity for multiple wire-tap channels under instantaneous fading is given by [119]

$$\begin{aligned} C_s &= C_M - C_W \\ &= \left[\log_2\left(1 + \mathrm{SNR}_{s,d}\right) - \log_2\left(1 + \mathscr{F}_{e\in\Psi_E}\left(\mathrm{SNR}_{s,e}\right)\right)\right]^+ \end{aligned} \tag{2.13}$$

where C_M is the capacity of main channel, and C_W is the channel capacity achieved by wire-tap channels. $[x]^+$ denotes $\max(0, x)$, operator $\mathscr{F}_{e\in\Psi_E}(\cdot)$ is a function related to different eavesdropping diversity schemes. Typically, as it will be shown in Section 2.2.3, $\mathscr{F}(\cdot)$ can be either $\sum_{e\in\Psi_E}(\cdot)$ for the *colluding* scenario or $\max_{e\in\Psi_E}(\cdot)$ for the *non-colluding* scenario. If $C_s > 0$, the secrecy capacity C_s can be achieved while transmitting the message from s to d regardless of the presence of the EDs. The secrecy capacity is accomplished by assigning multiple codewords for each possible message and sending one at random in a manner that receiver d can reliably decode while the best guess for the EDs remains uniformly random [38].

It is clear that instantaneous CSI knowledge from Alice to any ED is assumed to be known for the above metric. This could be the case when the ED may be another legitimate user who transmits signals but is not allowed to receive the confidential message from the source [42].

2.2.2.2 Secure Connection Probability

When the instantaneous CSI is not available, the statistics of the spatial locations and fading of the unknown EDs are assumed to obey certain distributions that can reflect the nature of wireless systems. Then, the average secrecy performance over all potential eavesdropping realizations of the channel states can be captured. This gives rise to a study of the secure connection probability. The secure connection probability measures the probability of successfully achieving an instantaneous secrecy capacity C_s larger than a target secrecy rate $R_s > 0$. R_s is the minimum requirement for successful reception of information at the receiver. The complement of secure connection probability is called secrecy outage probability. The secure connection probability can be written as [120]

$$p_s(R_s) = \mathbb{P}\left\{C_s > R_s\right\}. \tag{2.14}$$

This implies that the instantaneous secrecy capacity is greater than a target secrecy rate $R_s > 0$. The operational significance of this definition is that [42], when setting the secrecy rate R_s, Alice is assuming that the capacity of the wire-tap channel is given by $C'_W = C_M - R_s$. As long as $R_s < C_s$, Eve's channel will be worse than Alice's estimation, i.e., $C_W < C'_W$, then the wire-tap codes used by Alice will ensure perfect secrecy. Otherwise, if $R_s > C_s$ then $C'_W > C_W$ and secrecy is compromised.

2.2.3 Eavesdropping Diversity Schemes

Due to the broadcast nature of the wireless medium, wireless transmission is exposed to an adversarial network of multiple EDs. The two most important adversarial models are named non-colluding and colluding eavesdropping, which exploit different degrees of spatial diversity to decode the transmitted signals. These are considered in the literature for secrecy performance analysis based on physical layer security [116, 121].

2.2.3.1 Non-colluding Eavesdropping

Non-colluding eavesdropping describes the scenario where the eavesdropping behaviour is carried out by independent attackers. During the transmission at any time, regardless of whoever has successfully eavesdropped the full or part of the message, the confidentiality of the message is compromised. In the fading environment, an ED may not always have the strongest instantaneous SNR among the others, and the one with the highest instantaneous SNR has the best opportunity to compromise the transmission secrecy. Therefore, the theory behind non-colluding eavesdropping is very similar to selection combining in a diversity system, where the message from multiple EDs with the largest instantaneous SNR is chosen.

As a consequence, at time t, the baseband signal of the diversity branch at ED i can be written as

$$r_i(t) = g_i x(t) + n_i(t) \tag{2.15}$$

where $x(t)$ is the transmit signal, g_i is the complex channel gain, $n_i(t)$ for all $i \in \Psi_E$ are independent complex white Gaussian noise process with equal variance, $r_i(t)$ is the received signal at ED i, and the corresponding instantaneous SNR of node i is given by

$$\mathrm{SNR}_i = \frac{\mathbb{E}\left[|x(t)|^2\right]}{\sigma_n^2}|g_i|^2 \tag{2.16}$$

where $\mathbb{E}[\cdot]$ is the expectation, and σ_n^2 is the noise power, which is assumed to be the same in all the branches. Therefore, the instantaneous SNR of non-colluding eavesdropping, $\mathrm{SNR}_{\mathrm{nc}}$, is given by

$$\mathrm{SNR}_{\mathrm{nc}} = \max_i \left(\mathrm{SNR}_i\right). \tag{2.17}$$

2.2.3.2 Colluding Eavesdropping

Colluding eavesdropping is the case where the EDs exchange and combine the information received by all the EDs to decode the secret message. It is a centralized eavesdropping scenario, which is theoretically similar to the maximal ratio combining (MRC) technique carried out by optimum branch weighting to maximize aggregated SNR. In detail, the signals from the receive antenna of different EDs are weighted according to individual noise powers and instantaneous channel powers, then the results are coherently combined in a centralized controller [122]. The linear combiner output of the baseband signals from different EDs is given by

$$y(t) = \sum_{i\in\Psi_E} w_i \left(g_i x(t) + n_i(t)\right) = x(t) \sum_{i\in\Psi_E} w_i g_i + \sum_{i\in\Psi_E} w_i n_i(t). \tag{2.18}$$

The instantaneous signal and noise powers at the combiner output can be written as

$$\sigma_y^2 = \mathbb{E}\left[|x(t)|^2\right] \left|\sum_{i\in\Psi_E} w_i g_i\right|^2, \text{ and } \sigma_{\text{nc}}^2 = \sigma_n^2 \sum_{i\in\Psi_E} |w_i|^2 \tag{2.19}$$

while the instantaneous SNR at the combiner output can be expressed as

$$\text{SNR}_c = \text{SNR}_{\text{av}} \frac{\left|\sum_{i\in\Psi_E} w_i g_i\right|^2}{\sum_{i\in\Psi_E} |w_i|^2} \tag{2.20}$$

and

$$\text{SNR}_{\text{av}} = \frac{\mathbb{E}\left[|x(t)|^2\right]}{\sigma_n^2} \tag{2.21}$$

which is the average SNR, and it is assumed to be the same for all branches. According to the Cauchy-Schwarz inequality for complex parameters, we have

$$\left|\sum_{i\in\Psi_E} w_i g_i\right|^2 \leq \sum_{i\in\Psi_E} |w_i|^2 \sum_{i\in\Psi_E} |g_i|^2 \tag{2.22}$$

which holds with equality for $w_i = cg_i^*$, and c is an arbitrary complex constant. Since the exact value of the constant does not matter due to cancellation on both sides in (2.22), one could always scale w_i during the weighting procedure such that $\sum_{i\in\Psi_E} |w_i|^2 = 1$ [123]. Then, the right-hand side of (2.22) becomes $\sum_{i\in\Psi_E} |g_i|^2$. As a result, the maximum aggregated SNR exists for the aggregated instantaneous SNR when $w_i = cg_i^*$, which is given by

$$\mathrm{SNR}_{\mathrm{MRC}} = \mathrm{SNR}_{\mathrm{av}} \sum_{i\in\Psi_E} |g_i|^2 = \sum_{i\in\Psi_E} \mathrm{SNR}_i. \tag{2.23}$$

Therefore, the output SNR of MRC is equal to the sum of the SNRs of all individual receive antennas.

2.3 Stochastic Geometry for Network Modeling

As shown in previous sections, many performance metrics are functions of the *network geometry* on which the path loss and the fading characteristics are dependent. Stochastic geometry allows one to study the average behavior over many spatial realizations of a network whose nodes are placed according to some random point patterns. These patterns statistically describe the irregular nature of the wireless nodes such as interferers [124] and EDs [116, 121], and analytically quantify the performance metrics on interference and eavesdropping when the exact locations and channels of nodes are impossible to know or predict. Since the patterns play a role in the modeling, point process theory is often considered to be the main subfield of stochastic geometry.

The following parts of this section introduce typical point processes including uniform binomial point process (BPP), Poisson point processes (PPP), and Poisson cluster processes (PCPs), and their applications in modeling the nodes' positions in wireless networks.

2.3.1 Binomial Point Process (BPP)

Given a space $S \subset \mathbb{R}^n$, a point process X consisting of m i.i.d. points with common density f is called a uniform BPP of m points in a bounded set $B \subset S$, and it is denoted as

$$X \sim binomial(B, m, f) \tag{2.24}$$

where f is a density function on a set B, and $m \in \mathbb{N}$. The uniform BPP on B is the superposition of m independent and uniformly distributed points on B, and

$$f(x) = \begin{cases} 1/|B|, & x \in B \\ 0, & \text{otherwise} \end{cases} \tag{2.25}$$

where $|B|$ is the length, area, volume or more generally, the Lebesgue measure, of B. A realization of a uniform BPP is given in Figure 2.3.

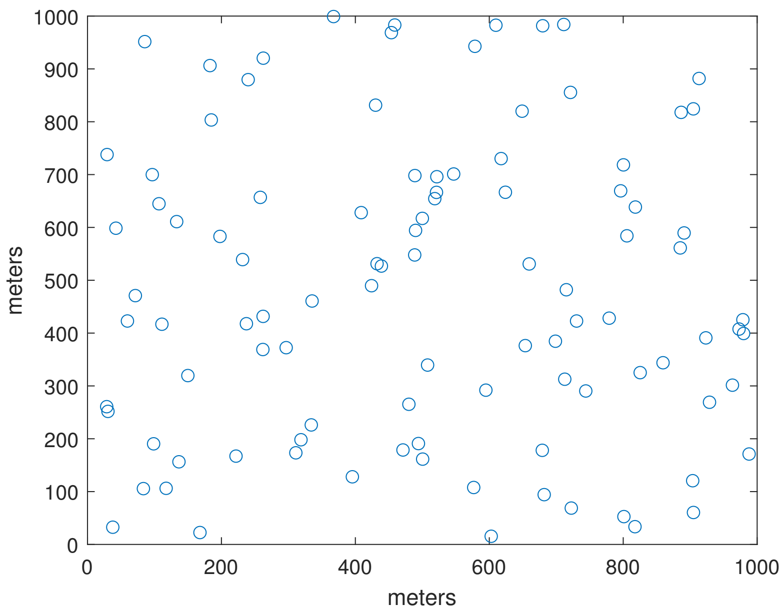

Figure 2.3: Points generated from a BPP with $m = 100$.

2.3.1.1 BPP-based Network Modeling: Applications and Limitations

The uniform BPP is used to model the pattern of a *known* number of nodes in a *finite* wireless network. Since the interference and the SINR seen at the center of the network are different from that of the network boundary, the main use of this model is to study the performance of a user at all locations. For example, the authors of [125] modeled the locations of nodes as a uniform BPP to study the performance of an arbitrarily located reference receiver in a circular region under uniform transmitter selection and k-closest transmitter selection policies. In [126], a finite network of unmanned aerial vehicles (UAVs) serving a given region was studied by modeling this network as a BPP. The downlink coverage probability of a reference receiver located at an arbitrary position on the ground assuming Nakagami-m fading for all wireless links was also derived.

In general, the limitation of the BPP can be seen in two aspects. Firstly, the BPP requires a known number of nodes. In a D2D-enabled cellular network, links may be established randomly, and only the average number of users may be known. Secondly, the analytic complexity related to the performance metrics is very complicated due to boundary effects. To solve the above problems, PPPs and PCPs are often used.

2.3.2 Poisson Point Process (PPP)

A PPP is a type of random object abstracted as points randomly positioned in a mathematical space [127], and it has been used to model the pattern of nodes in a *large-scale* wireless network [128]. In a two-dimensional continuous space $S \subset \mathbb{R}^2$, the number of the objects N generated in the space is Poisson distributed, thus it has probability

$$\mathbb{P}\{N = n\} = \frac{\Lambda^n}{n!} e^{-\Lambda} \tag{2.26}$$

where $\Lambda = \int_B \lambda(\mathbf{x})\,\mathrm{d}\mathbf{x}$, $\Lambda \in [0,\infty)$, $\lambda(\mathbf{x})$ is the intensity function for any bounded set $B \subset S$. If $\lambda(\mathbf{x})$ is a non-negative constant, the PPP is said to be homogeneous, otherwise, it is inhomogeneous. For easy notation, the intensity of a homogeneous PPP is denoted as λ.

2.3.2.1 Expectation of Random Sums over PPP

Let $u(\mathbf{x})$ be a real-valued function of the event's location $\mathbf{x}$, then the random sum over a PPP Φ is given by $\sum_{\mathbf{x}\in\Phi} u(\mathbf{x})$. For a two-dimensional homogeneous PPP Φ, its expectation follows Campbell's Theorem [129], which can be written as

$$\mathbb{E}\left[\sum_{\mathbf{x}\in\Phi} u(\mathbf{x})\right] = \lambda \int_B u(\mathbf{x})\,\mathrm{d}\mathbf{x}. \tag{2.27}$$

2.3.2.2 Expectation of Random Products over PPP

Let $v(\mathbf{x})$ be a real-valued function, the expectation of the random product $\prod_{\mathbf{x}\in\Phi} v(\mathbf{x})$ over Φ is defined by the probability generating functional (PGFL) of a PPP, which can be written as

$$\mathbb{E}\left[\prod_{\mathbf{x}\in\Phi} v(\mathbf{x})\right] = \exp\left\{-\lambda \int_B [1 - v(\mathbf{x})]\,\mathrm{d}\mathbf{x}\right\} \tag{2.28}$$

where $0 < v(\mathbf{x}) \leq 1$ for all $\mathbf{x} \in B$, while $v(\mathbf{x}) = 1$ for $\mathbf{x} \notin B$ so that there are only a finite number of non-unit terms in the aforementioned product, which converges [130].

2.3.2.3 PPP-based Network Modeling: Applications and Limitations

PPPs are used to model various components of a telecommunications network, including UEs and base station locations, with meaningful results. Unlike the analysis based on the classic hexagonal model, the PPP models provide tractable analytic expressions for specific performance metrics such as coverage probability thanks to the independence between different points and the simple form of the PGFL. Early results in [131] also showed that the Voronoi tessellation cellular system with a PPP modeling base stations is a lower bound to a hexagonal cellular system in performance metrics like connection probability in normal shadow fading conditions and a good approximation in the presence of high shadow fading standard deviation. Further results in [132] showed that a PPP closely approximates the power control result in a hexagonal grid model. Since PPPs can capture the nature of mobile devices with tractability in performance metrics, and the same devices can act as EDs if they are compromised, PPPs have also been used to model the spatial distribution of EDs [53, 116, 133].

The PPP model may be inadequate when the node locations exhibit correlations. Firstly, it is difficult to use a PPP to model the nodes that cluster together because they work in the same area or due to the impact of medium access control (MAC) protocols [134]. Secondly, in HetNets such as D2D-enabled two-tier cellular networks, PPPs can not capture spatial coupling between UEs and eNBs that exists in real-world HetNet deployments [135]. Areas close to an eNB are expected to achieve higher performance when comparing to the edge, and the edge user performance is the bottleneck of the cellular system [136]. To model the non-uniform behavior of wireless nodes, the PCP has been adopted.

2.3.3 Poisson Cluster Processes (PCPs)

PCPs are a specific type of cluster process generated from the realizations of a homogeneous PPP for the parent process and a finite point process for the offspring processes. When generating a PCP, the parent process is drawn from a PPP to get the sample parent points first, then each sample parent point is replaced by a realization of the offspring process to form clusters.

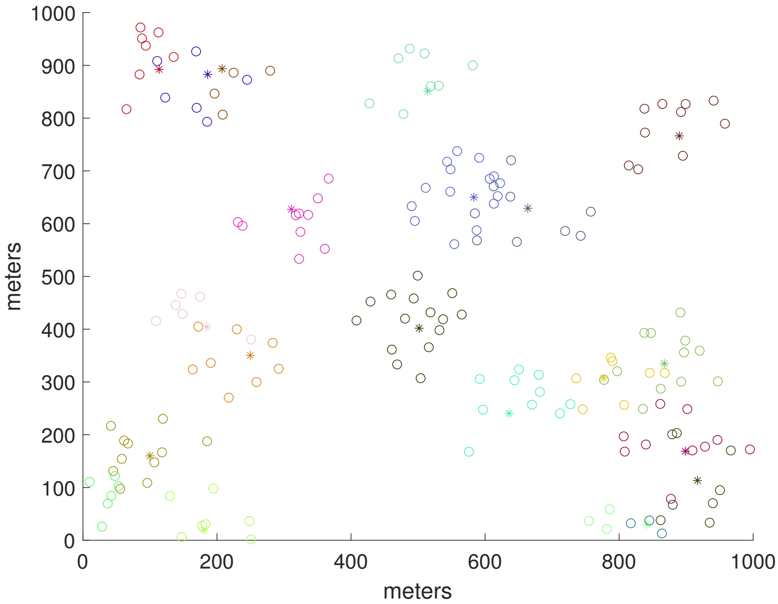

Figure 2.4: Matérn clusters where $*$ denotes a parent point, and $\circ$ denotes an offspring point. The parent density is 12.5 points per km^2. $R = 100$ m; each cluster has an average of 9 offspring points.

2.3.3.1 Neyman-Scott Process

The Neyman-Scott process is a PCP in which the number of offspring points belonging to all clusters are generated from i.i.d. discrete random variables on the nonnegative integers with specific probabilities [129]. The offspring points of the representative cluster are i.i.d. around the parent point with intensity measure $F(B) = \int_B f(x)\,\mathrm{d}x$, where $f(x)$ is the scattering density of the offspring process. If $f(x)$ is isotropic, then the corresponding Neyman-Scott process is isotropic [134]. The realization of the process does not include the parent points but only their offspring points.

The following parts focus on two important cases of Neyman-Scott process named Matérn cluster processes and modified Thomas cluster processes.

2.3.3.2 Matérn Cluster Process

For a Matérn cluster process in $\mathbb{R}^2$, every parent point, e.g., $\mathbf{x}_o$, is replaced by a Poisson number of offspring points located uniformly within disc $b(\mathbf{x}_o, R)$, where R

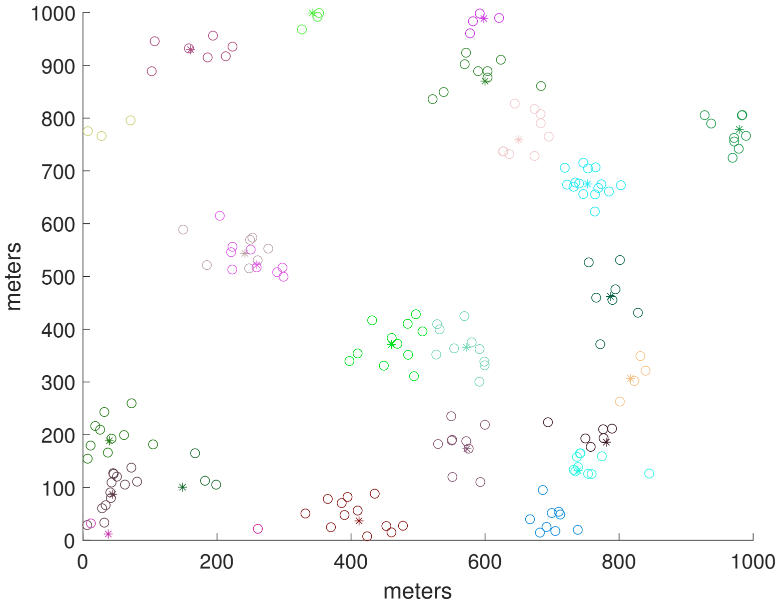

Figure 2.5: Modified Thomas clusters where $*$ denotes a parent point, and $\circ$ denotes an offspring point. The parent density is 12.5 points per km^2; $\sigma = 33.3$ m; an average of 9 offspring points exist within a cluster.

is the radius. An example of the Matérn clusters is shown in Figure 2.4. Given a parent point $\mathbf{x}_o$, the probability density function (PDF) of any of its offspring points is given by

$$f(\mathbf{u} - \mathbf{x}_o \mid R) = \frac{1}{\pi R^2}, \text{ for } \|\mathbf{u} - \mathbf{x}_o\| \leq R. \tag{2.29}$$

The PDF of the distance between two offspring points of a cluster is given by [137]

$$f_{R_m}(r_m) = \frac{4r_m}{\pi R^2}\left(\cos^{-1}\left(\frac{r_m}{2R}\right) - \frac{r_m}{2R}\sqrt{1 - \left(\frac{r_m}{2R}\right)^2}\right). \tag{2.30}$$

2.3.3.3 Modified Thomas Cluster Process

The modified Thomas cluster process is another cluster process, where the displacement of offspring points from a parent point in each axis is Gaussian $\mathcal{N}(0, \sigma^2)$; σ^2 is the variance. An example of the modified Thomas cluster process is shown in Figure 2.5. It is suitable for the scenario where most of the wireless nodes are concentrated while some comparably distant nodes also want to connect. Conditioning on a parent point $\mathbf{x}_o$, the PDF of any of its offspring points is given by

$$f(\mathbf{u}-\mathbf{x}_o \mid \sigma^2) = (2\pi\sigma^2)^{-1} \exp\left(-\frac{\|\mathbf{u}-\mathbf{x}_o\|^2}{2\sigma^2}\right). \tag{2.31}$$

Based on the derivation of the Euclidean distance between two normally distributed points in an N-dimensional space [138], [139], the PDF of the distance between two points within a cluster is given by

$$f_{R_t}(r_t \mid \sigma) = \frac{r_t}{\sigma^2} e^{-r_t^2/(2\sigma^2)}. \tag{2.32}$$

Let R_d be a random variable representing the distance between an offspring point and a non-offspring point of a modified Thomas cluster process with variance σ^2, and denoting the given distance from the cluster origin to the non-offspring point as R_y, the conditional PDF of R_d is written as

$$f_{R_d}(r_d \mid R_y) = \frac{r_d}{\sigma^2} \exp\left(-\frac{r_d^2 + R_y^2}{2\sigma^2}\right) I_0\left(\frac{r_d R_y}{\sigma^2}\right) \tag{2.33}$$

where $I_0(z)$ is the zeroth order modified Bessel function of the first kind, and

$$I_0(x) = \frac{1}{\pi} \int_0^{\pi} \exp\left(x \cos(\theta)\right) \, \mathrm{d}\theta. \tag{2.34}$$

2.3.3.4 Expectation of Random Products over PCP

For a given function $g : \mathbb{R}^2 \to [0, 1]$ and $\int_{\mathbb{R}^2} |1 - g(\mathbf{x})| \, \mathrm{d}\mathbf{x} < \infty$, where $\mathbf{x} = (x_1, x_2)$ denotes the Cartesian coordinate of a point in the two-dimensional plane, the PGFL of a Neyman-Scott process Φ is given by [134]

$$\begin{aligned}\mathbb{G}_\Phi(g) &= \mathbb{E}_\Phi\left[\prod_{\mathbf{x}\in\Phi} g(\mathbf{x})\right] \\ &= \exp\left\{\lambda_o \int_0^{2\pi}\int_0^{\infty}\left[\eta\left(\int_{\mathbb{R}^2} g(\mathbf{x}+\mathbf{s_1})f(\mathbf{x})\,\mathrm{d}\mathbf{x}\right)-1\right] r\,\mathrm{d}r\,\mathrm{d}\theta\right\},\end{aligned} \tag{2.35}$$

where λ_o denotes the intensity of the parent process, $\mathbf{s_1} = (r\cos(\theta), r\sin(\theta))$, $\eta(z) = e^{\overline{m}(z-1)}$ is the moment-generating function of a Poisson random variable which describes the distribution of the number of offspring points with mean $\overline{m}$ in a cluster, and $f(\mathbf{x})$ is the PDF of the points in a cluster centered at $(0,0)$, which equals (2.29) for a Matérn cluster process with radius R and (2.31) for a modified Thomas cluster process with variance σ^2.

Having the conditional distance PDF given by (2.33) for the modified Thomas processes[2] and noticing that $R_y = r$, we see that if $g(\mathbf{x})$ is equal to a distance function $g_1(||\mathbf{x}||)$, the PGFL is given by

$$\mathbb{G}_\Phi(g_1) = \exp\left\{2\pi\lambda_o \int_0^{\infty}\left[\eta\left(\int_0^{\infty} g_1(x) f_{R_d}(x \mid r)\,\mathrm{d}x\right)-1\right] r\,\mathrm{d}r\right\}. \tag{2.36}$$

Notably, the number of integrals is reduced from 4 integrals in (2.35) to 2 integrals in (2.36). This is very important because: Firstly, (2.36) eliminates the unnecessary numerical integral errors introduced by the two extra integrals; Secondly, since both $g(\cdot)$ and $g_1(\cdot)$ are related to the distance between the non-offspring and offspring points in practice, the distance based function $g_1(\cdot)$ shows this distance relation clearly, while the point based function $g(\cdot)$ requires that the same distance relation must be established via the parent point.

[2]Meanwhile, the first research chapter will give proof of the equation for the conditional distance PDF of Matérn cluster processes as a novel contribution to the field of point process theory.

2.3.3.5 PCP-based Network Modeling: Applications and Limitations

The authors of [140] considered the aggregate interference of a downlink K-tier HetNet, where the transmitting base stations are clustered following a PCP, but their transmit power, node densities, and link reliabilities are different in each tier. The outage probability, the coverage probability, and the average achievable rate were studied for such networks. They concluded that the fundamental difference between a PPP and a PCP is that, for a PPP, the number of simultaneously covered mobiles and the network capacity linearly increase with K, while they decrease for a PCP until the curves saturate at some point. The authors of [141] developed a new spatial model for D2D networks in which the device locations are modeled as a PCP. The uniform content availability and k-closest content availability policies were used to select the content provider within a cluster. The exact expressions and approximations for the coverage probability and area spectral efficiency were derived. Recently, the authors of [142] characterized and modeled large-scale UAV-enabled post-disaster recovery cellular networks. The drone small cells are clustered around the site of a destroyed base station, where the coverage probability, area spectral efficiency, and the energy efficiency for the downlink mobile user were quantified.

In the above works based on PCPs, the system performance metrics, such as coverage probability and mean achievable rate, are usually in complex form involving multiple integrals. To reduce the complexity, a PPP model can be used to approximate the analysis, and bounds on these example metrics can be achieved in closed form [134]. Moreover, when there are either one or two pairs of nodes in a cluster, a cluster process named a Gauss-Poisson process can be used to obtain a good trade-off between modeling accuracy and tractability [143]. Furthermore, a PCP model is not suitable for repulsive behavior among the nodes. To address this limitation, a Poisson hard-core process (PHCP) in which no two nodes can be closer than a repulsion radius from one another was proposed in [144] for two-tier HetNets, where the spatial distributions of transmitters in the first-tier and the second-tier networks followed a PHCP and a PPP, respectively.

2.4 Summary

In this chapter, a number of important aspects of D2D technology, physical layer security, and stochastic geometry have been reviewed. Firstly, the interference management for D2D communications, such as power control, which acts as the most important method to combat interference is discussed. Performance metrics, such coverage probability, that help to guide the design of schemes to combat interference were covered. Secondly, it has been shown that it is theoretically possible to build a secure communication system with physical layer security. By considering two extremes of eavesdropping diversity schemes, i.e., non-colluding and colluding eavesdropping, performance metrics, such as secure connection probability, can help one to study the secrecy performance of a wireless link in the presence of multiple EDs. Finally, to model the random behavior of nodes, stochastic geometry has been discussed. Spatial point processes including BPPs, PPPs, and PCPs will facilitate the modeling of wireless nodes in different network scenarios in later chapters.

Chapter 3

Joint Coverage Enhancement by Power Allocation in Poisson Clustered Out-Band D2D Networks

This chapter focuses on power allocation in a Poisson clustered out-band device-to-device (D2D) network. Two optimization schemes based on the joint coverage probability of concurrent D2D transmission links are proposed for both the target cluster and the whole network. The joint coverage probability can capture the correlation of the interference in space and time. With a differing amount of location information of D2D user equipments (DUEs) being available in centralized and localized communication solutions, the joint coverage probability is formulated based on coherent, non-coherent lower bound, and single-cluster approximation pairwise coverage probabilities. By maximizing the joint coverage probability formulated in this way, the reliability of the network can be enhanced. Moreover, by minimizing the power consumption of a set of DUEs for a given joint coverage probability requirement, the green aspect of 5G and future communication networks is fulfilled. The above optimization problems are not convex, and their convex counterparts are formulated. The simulation results show that, compared with the conventional long-term evolution (LTE) open loop and fixed power schemes, the joint coverage probability and power consumption are respectively optimized by applying the proposed schemes.

3.1 Introduction

According to international mobile communications (IMT)-2020, the capability to support a maximum connection density of $10^6/\text{km}^2$ is to be expected in future communication networks [4]. However, the limited number of resource blocks (RBs) and scheduling policies in current LTE systems may not fulfil such a requirement. In the networks where the density is high, and energy or spectrum efficiency is of the utmost importance, the clustering of the DUEs is a good option since it can bring lower signaling overhead, higher spectral efficiency, and better energy efficiency compared with legacy cellular systems [50]. Furthermore, due to the fact that the locations of DUEs are constrained by factors such as geographical differences, urban planning, and land availability, D2D communications could also inevitably be clustered and mutually interfere in existing networks [30, 50, 134, 145]. The clustered network models which proceed within such a paradigm for D2D content distribution can be found in [146–149].

To model and analyze the performance of the clustered networks, a class of Poisson cluster processes (PCPs) has been used [51, 135, 140, 150–152]. The performance analyses of a random network are given mainly by the fact that the connection reliability for a DUE pair could be severely affected by the interference due to the concurrent transmitting user equipments (UEs) on the same channel [134]. The authors of [85] analyzed the outage probability of the modified Thomas cluster based LTE two-tier femtocell networks, where all UEs transmit with a fixed power. The authors of [141] studied the area spectral efficiency of the modified Thomas clusters for the clustered D2D networks. However, interference observed at a given location is temporally and/or spatially correlated; ignoring this correlation by only considering the coverage probability of a typical link may lead to the incorrect characterization of network performance [153]. To identify such correlation, the joint coverage probability, namely joint complementary cumulative distribution function (CCDF) of the signal-to-interference-plus-noise ratio (SINR), has been used to study the joint statistics across space or time [154–156]. These analyses are normally built on the assumption that all UEs have either the fixed power or path loss inversion power strategy, which does not guarantee the optimum or desired joint coverage performance.

Power allocation is an effective interference management mechanism to reduce interference and enhance the performance of a wireless network. Traditional power control schemes for LTE focus on reducing the interference between D2D and cellular users in the in-band D2D communications [90], and stochastic geometry has been adopted to analyze the performance of those schemes. For example, in [95] and [157], Poisson based analytical modeling and optimization for spectrum underlay D2D communications were respectively studied. A strategy to use the harvested radio frequency energy from interferers to perform path loss inversion power control for D2D communications was considered in [158]. Centralized and localized power allocation methods for Poisson based D2D underlaid cellular networks were investigated in [111]. Regardless of these achievements for in-band D2D communications, due to the absence of a central controller, performing power control on a link-by-link basis is a complicated task for the autonomous out-band solution especially in a clustered large-scale wireless network. A bottleneck can be created in the network when the localized controller in each cluster exchanges the location information of the D2D transmitters with other clusters to obtain the accurate interference levels for power control. Since the tools from stochastic geometry can characterize the interference statistically by exploiting the spatial distribution of the clustered D2D transmitters [148], it would be desirable to incorporate them into power control so that the joint coverage probability is enhanced without the need for frequent feedback from the clusters. Meanwhile, interference management techniques are lacking for the controlled D2D out-band solution, and traditional interference management such as the case in [90] focuses on reducing the interference between D2D and cellular users in the in-band D2D communications based on techniques such as power allocation. Consequently, the preconfigured transmit power level has been used as a viable method for the out-band D2D networks [81, 134, 141, 159, 160], which does not necessarily achieve the optimum joint coverage performance. Furthermore, the idea of green radio communications requires the action to further reduce power consumption in order to limit the subsequent impact on the environment in the form of CO_2 emissions [161], and traditional link-based schemes are not capable of providing such reduction while maintaining a given joint coverage performance.

This chapter, therefore, proposes two power allocation frameworks for performance optimizations on joint coverage and power consumption in the target cluster and the whole network in Poisson clustered out-band D2D networks. The simulations have shown that the performance of the target cluster and the whole network given by the proposed schemes will be optimum over the fixed power and open loop schemes.

The contributions of the chapter are:

1. Two optimization frameworks are proposed to enhance coverage performance in the target cluster and the whole network. They are suitable for both commercial content distribution and the public safety applications where high joint coverage probability and lower power consumption are desired.

2. The joint coverage probability has been formulated based on the coherent, non-coherent lower bound, and single-cluster approximation coverage probabilities,

which depend on a differing amount of location information pertaining to the clustered DUEs. As a result, the proposed schemes can be applied to both centralized and localized D2D networks.

3. A lower bound on the inter-cluster interference from Matérn clusters has been discovered, which is derived based on a newly proposed conditional distance probability density function (PDF).

4. The original formulated problems are not convex but are proved to be have convex counterparts after the transformation of optimization variables and problems.

The rest of the chapter is structured as follows. Section 3.2 begins with the system model and addresses three different formulations for the pairwise coverage probability. Section 3.3 focuses on the formulation and optimizations on the joint coverage probability. Section 3.4 gives the simulation results and discussion, and Section 3.5 concludes the chapter.

3.2 System Model

In this chapter, a stochastic model for clustered out-band D2D networks is considered, where the gathering behavior of DUEs is modeled by the PCPs. For a given channel resource, each cluster is assumed to contain an average of $\overline{m}$ D2D pairs. For each pair, there is one content requester (receiving DUE) and one content provider (transmitting DUE). Two types of PCPs, i.e., Matérn and modified Thomas cluster processes (see Figure 3.1) are investigated. The origins of the clusters are distributed in the plane according to a Poisson point process Φ_o with intensity λ_o. For an origin at $\mathbf{x}_o$, the Matérn clustered DUEs are independently, identically, and uniformly distributed in the disc of radius R. For the same origin, the modified Thomas clustered DUEs obey the isotropic Gaussian distribution $\mathcal{N}(\mathbf{x}_o,\, \sigma^2\mathbf{I})$ with standard deviation σ along each coordinate axis, and $\mathbf{I}$ is a 2×2 identity matrix [162]. The DUEs are assumed to share the same channel resources throughout the clusters. As shown in last chapter and the references within, the reuse of channel resources to achieve high spectrum efficiency is the trend in 4G and future communication networks. Besides, as long as the system performance is acceptable, this also allows the network to avoid the enormous signaling overhead caused by accommodating the feedback from the receivers [163, 164]. The conditional density functions of DUEs are given by the following expressions [134]:

Matérn

$$f(\mathbf{u} \mid \mathbf{x}_o, R) = \frac{1}{\pi R^2},\ \text{for}\ \|\mathbf{u}-\mathbf{x}_o\| \leq R \tag{3.1}$$

Modified Thomas

$$f(\mathbf{u} \mid \mathbf{x}_o, \sigma^2) = -\frac{1}{2\pi\sigma^2} \exp\left(-\frac{\|\mathbf{u}-\mathbf{x}_o\|^2}{2\sigma^2}\right) \tag{3.2}$$

Since the probability that a Gaussian random variable $X \sim \mathcal{N}(0,\, \sigma^2)$ lies in the interval $[-3\sigma, 3\sigma]$ is equal to 0.997 [165], by letting $\sigma = R/3$, then the average numbers of the Matérn and the modified Thomas clustered DUEs within radius R are approximately the same. Under this condition, the performance differences between the uniformly distributed and the normally concentrated DUEs become comparable. Without loss of generality, the channels are assumed to be static over a block time and independently and identically Rayleigh distributed from one block to the next [166].

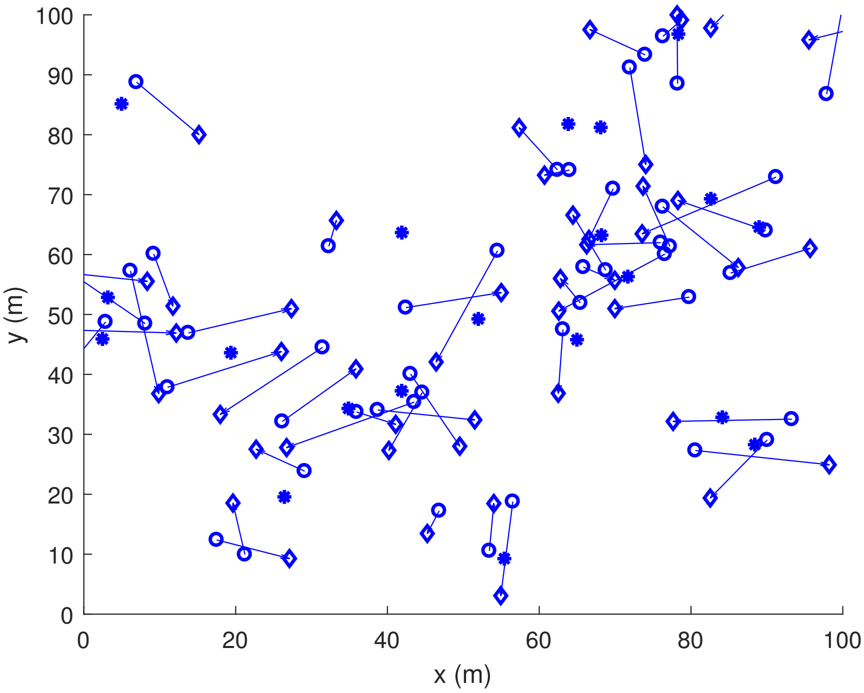

(a) Matérn clusters, $R = 12.5$ m.

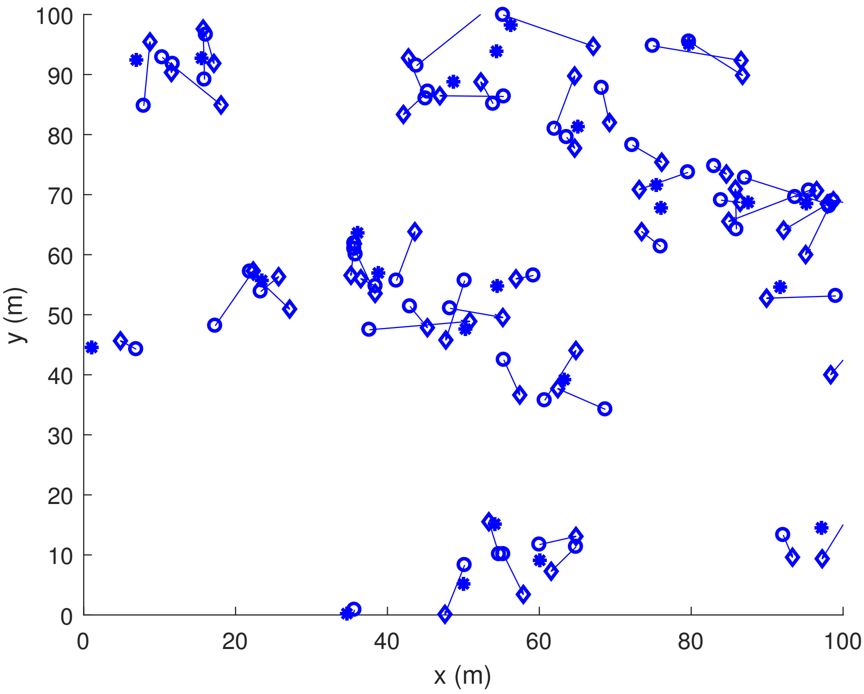

(b) Modified Thomas clusters, $\sigma \approx 4.2$ m.

Figure 3.1: Illustration of clustered transmitting and receiving DUEs. $*$: cluster origin, $\circ$: transmitting DUE, $\diamond$: receiving DUE, $\rightarrow$: transmission link, $\lambda_o = 2000$ cluster/km^2, $\overline{m} = 2$, and the connection density is 4×10^3/km^2. © 2018 IEEE.

3.2.1 Received Signal

For simplicity of notation, unique node indices $\{i\}$ are given to all DUEs. The received signal power at node j while transmitting from node i is [167]

$$P_{ij} = G_e \ell(d_{ij}) F_{ij} P_i \tag{3.3}$$

where P_i is the transmit power of node i, $\ell(d_{ij}) = (\lambda/4\pi)^2 d_{ij}^{-\alpha}$; λ represents the carrier wavelength; d_{ij} is the pair distance between node i and j; α is the path loss exponent. Although this model has a singularity as $d_{ij} \to 0$, such a singularity has a negligible effect on the results from a coverage perspective [151, 168]. The gain due to coding, transmitting antenna and receiving antenna at any receiving DUE is G_e. F_{ij} models the power of Rayleigh fading which obeys exponential distribution with unit mean [169]. The transmit power P_j for any DUE without applying any power allocation scheme is denoted by the preconfigured transmit power P_d.

3.2.2 Signal-to-Interference-plus-Noise Ratio

For a given realization of the cluster process, let N_c denote the number of clusters and L_n represent the set of indices belonging to the transmitting DUEs inside cluster $n \in (1, ..., N_c)$, the union of all simultaneously transmitting DUE sets is denoted by $L_T = \bigcup_n L_n$. In the presence of both intra-cluster and inter-cluster interference, the SINR at node j while transmitting from node i is given by [170]

$$\mathrm{SINR}_{ij} = \frac{P_{ij}}{N_0 + I_{ij}} \tag{3.4}$$

where N_0 is the additive white Gaussian noise (AWGN) power at each node. The corresponding interference at node j is written as

$$I_{ij} = \sum_{k \in L_T \setminus \{i\}} P_{kj} \tag{3.5}$$

where $L_T \setminus \{i\}$ denotes the set of all the interfering DUEs from all of the clusters.

3.2.3 Coverage Probability

In this section, *coherent*, *non-coherent lower bound*, and *single-cluster approximation* coverage probabilities are formulated. The major difference between the coherent and non-coherent coverage probabilities[1] is that the former requires all location information of the DUEs to be reported back to a central controller such as the base station, while the latter requires the DUEs within the target cluster to report their location information to either the centralized controller or a DUE member working as the localized controller. Besides, the non-coherent coverage probability also requires the statistical information on the distribution of the interference of neighboring clusters. This statistical information can be obtained at the centralized controller by analyzing the received location information of inter-cluster DUEs in the long term. It will be further sent to the localized controller if the controller is in charge of performing the optimization. The single-cluster approximation considers only the intra-cluster interference, which requires the location information of the DUEs within the same cluster to be sent to either the centralized or the localized controller.

[1]The use of the terms "coherent" and "non-coherent" is inspired by 1) joint coherent and non-coherent transmission where spatial channel state information feedback is only needed for the former; 2) coherent and non-coherent detection where the knowledge of the phase of the carrier frequency is needed for the former.

3.2.3.1 Coherent Coverage Probability

The coverage probability of a link is the probability that the SINR of the link is higher than a predetermined threshold $\beta = 2^t - 1$ with link spectrum efficiency t bit/s/Hz.

Lemma 1. Given the distances and transmit powers from all transmitting nodes to a receiving node j, the coherent coverage probability from nodes i to j in a cluster is written as

$$\begin{aligned} p_{ij}^{\mathrm{c}} &= \mathbb{P}\{\mathrm{SINR}_{ij} > \beta\} \\ &= \mathbb{P}\left\{F_{ij} > \frac{\beta(N_0 + I_{ij})}{G_e \ell(d_{ij}) P_i}\right\} \\ &= \exp\left(-\frac{\beta N_0}{G_e \ell(d_{ij}) P_i}\right) \prod_{k \in L_T \setminus \{i\}} \left(1 + \frac{\beta \ell(d_{kj}) P_k}{\ell(d_{ij}) P_i}\right)^{-1} \end{aligned} \tag{3.6}$$

where $\mathbb{P}\{\cdot\}$ denotes the probability of an event.

Proof. See Appendix 3.A.1. □

The analysis above needs to have the knowledge of distances (via the device location information) and transmit powers of all the concurrent transmitting nodes, which could result in heavy traffic on the network back-haul [171].

3.2.3.2 Non-Coherent Coverage Probability

In some scenarios, where only the knowledge of the location information of the DUEs within the target cluster is known, and the transmit power of other clusters is fixed to be the same preconfigured value due to a lack of interference management, the statistical properties of the clusters based on stochastic geometry can be exploited to formulate a non-coherent coverage probability. Given the distances and transmit powers from all the transmitting nodes to a receiving node inside the same cluster and the cluster statistics, the non-coherent coverage probability between the transmitting node i and receiving node j in cluster n is written as

$$p_{ij}^{\mathrm{nc}} = \exp\left(-\frac{\beta N_0}{G_e \ell(d_{ij}) P_i}\right) \prod_{k \in L_n \setminus \{i\}} \left(1 + \frac{\beta \ell(d_{kj}) P_k}{\ell(d_{ij}) P_i}\right)^{-1} \mathcal{L}_I\left(\frac{\beta}{G_e \ell(d_{ij}) P_i}\right) \tag{3.7}$$

where $\mathcal{L}_I(s)$ is the Laplace transform of the inter-cluster interference given by the probability generating functional of the Neyman-Scott cluster process [134]. Hence,

$$\mathcal{L}_I(s) = \exp\left(-2\pi\lambda_o \int_0^\infty \left[1 - \xi(s, R_y)\right] R_y \, \mathrm{d}R_y\right) \tag{3.8}$$

where

$$\xi(s, R_y) = \exp\left\{-\overline{m} \int_0^\infty \frac{g(x)}{s^{-1} + g(x)} f_{R_d}(x \mid R_y) \, \mathrm{d}x\right\} \tag{3.9}$$

and $g(x) = G_e P_d \ell(x)$. Equation (3.8) is the result of the moment-generating function of the Poisson process Φ_o for parent points. Equation (3.9) is the Laplace transform of the interference from one cluster, given the distance R_y between the origin of the interference cluster and the receiving node in cluster n. $f_{R_d}(r_d \mid R_y)$ is the conditional distance PDF of DUEs. For Matérn and modified Thomas cluster processes, their conditional distance PDFs are respectively given by

Matérn

$$f_{R_d}(r_d \mid R_y) = \frac{c(r_d)}{\pi R^2} \tag{3.10}$$

$$c(r_d) = \begin{cases} 2\pi r_d, & r_d \leq R - R_y \\ 2\pi r_d - c_1(r_d), & R - R_y < r_d \text{ and } r_d^2 \leq R^2 - R_y^2 \\ c_1(r_d), & R^2 - R_y^2 < r_d^2 \\ 0, & \text{otherwise} \end{cases} \tag{3.11}$$

where $c_1(r_d)$ is defined by

$$c_1(r_d) = \begin{cases} 2r_d \arcsin \frac{\sqrt{4R_y^2 r_d^2 - (R_y^2 - R^2 + r_d^2)^2}}{2R_y r_d}, & (R_y + R - r_d)(R_y - R - r_d) \leq 0 \\ 0, & \text{otherwise.} \end{cases} \tag{3.12}$$

Proof. See Appendix 3.A.2. □

Modified Thomas

$$f_{R_d}(r_d \mid R_y) = \frac{r_d}{\sigma^2} \exp\left(-\frac{r_d^2 + R_y^2}{2\sigma^2}\right) I_0\left(\frac{r_d R_y}{\sigma^2}\right) \tag{3.13}$$

where $I_0(z)$ is the zeroth order modified Bessel function of the first kind.

Proof. See [164]. □

Numerically evaluating the integral form of (3.8) is time-consuming and does not lead to much insight. Thus, a closed-form lower bound on the Laplace transform of the inter-cluster interference is captured by the following Lemma.

Lemma 2. The Laplace transforms of the inter-cluster interference of both the Matérn and modified Thomas cluster processes are lower bounded by

$$\mathcal{L}_I(s) \geq \exp\left(-\pi\lambda_o\overline{m}\frac{(sG_e(\frac{\lambda}{4\pi})^2 P_d)^{2/\alpha}}{\mathrm{sinc}(2/\alpha)}\right). \tag{3.14}$$

Proof. For a proof of this lemma for the Matérn cluster process based on the conditional distance PDF (3.10), please see Appendix 3.A.3. For a proof of this lemma for the modified Thomas cluster process, please see [141]. □

As a result of Lemma 2, a lower bound on the non-coherent coverage probability is written as

$$p_{ij}^{\mathrm{nc}} \geq \exp\left(-\frac{\beta N_0}{G_e \ell(d_{ij}) P_i}\right) \prod_{k \in L_n \setminus \{i\}} \left(1 + \frac{\beta \ell(d_{kj}) P_k}{\ell(d_{ij}) P_i}\right)^{-1} \exp\left(-\pi \lambda_o \overline{m} \frac{\left(\beta P_d / (d_{ij}^{-\alpha} P_i)\right)^{2/\alpha}}{\mathrm{sinc}(2/\alpha)}\right). \tag{3.15}$$

3.2.3.3 Single-Cluster Approximation Coverage Probability

In the cases where only the intra-cluster interference is taken into consideration, the single-cluster approximation coverage probability between the transmitting node i and receiving node j in cluster n is given by

$$p_{ij}^{\mathrm{sc}} = \exp\left(-\frac{\beta N_0}{G_e \ell(d_{ij}) P_i}\right) \prod_{k \in L_n \setminus \{i\}} \left(1 + \frac{\beta \ell(d_{kj}) P_k}{\ell(d_{ij}) P_i}\right)^{-1} \tag{3.16}$$

where the only difference between (3.6) and (3.16) is that L_n is used instead of L_T. The relationship between the non-coherent and single-cluster approximation coverage probabilities is given by

$$p_{ij}^{\mathrm{nc}} = p_{ij}^{\mathrm{sc}} \mathcal{L}_I \left(\frac{\beta}{G_e \ell(d_{ij}) P_i}\right). \tag{3.17}$$

3.3 Joint Coverage Probability and Convex Optimization

In this section, convex optimization problems to maximize joint coverage probability and minimize power consumption are formulated for the target cluster and the whole network.

3.3.1 Joint Coverage Probability

Let κ denote either the target cluster or all clusters in the network depending on the objects of interest in optimization. The joint coverage probability of κ is determined by the coverage probability of each DUE pair within κ, which can be formulated as

$$p_s = \prod_{i \in L_\kappa} p_{ik_i} \tag{3.18}$$

where k_i is the index of the corresponding receiving DUE that DUE i connects to, and p_{ik_i} is the coverage probability from i to k_i.

Specifically, the joint coverage probability of the target cluster can be formulated based on the coherent formulation in (3.6) accurately, or approximated by either the non-coherent lower bound in (3.15) or the single-cluster approximation in (3.16). Since the location information of all the nodes must be known in (3.6), the joint coverage probability based on the coherent formulation is only suitable for centralized communication networks. Meanwhile, the joint coverage probability based on the non-coherent lower bound requires the knowledge of the location information of the DUEs within the target cluster and the statistical information on the distribution of inter-cluster interference. Thus, it is suitable for both the centralized and partially localized communication networks, where the latter allows the optimizations to run locally with the statistical information distributed by the centralized controller. Furthermore, the joint coverage probability based on the single-cluster approximation requires the location information of the DUEs, which is suitable for both centralized and localized communication networks.

Meanwhile, the joint coverage probability of the whole network can be formulated based on the coherent formulation, non-coherent lower bound, and single-cluster approximation. Like the target cluster case, the coherent formulation can be applied to the centralized communication networks, while the non-coherent lower bound formulation can be applied to both the centralized and partially localized networks. Since the coverage probabilities of the DUE pairs in one cluster are independent of another in the single-cluster approximation, both the centralized and localized communication networks can be applied to the optimization based on those schemes.

3.3.2 Problem Formulation and Convex Optimization

3.3.2.1 Maximizing Joint Coverage Probability

For many applications including content distribution and mission-critical communications, it is desirable that the joint coverage of the target cluster or the whole network is maximized. This is because the D2D communications within the cluster or the network could have the best joint coverage performance. Meanwhile, it is even better if a similar or lower amount of average power per DUE is consumed compared with other power allocation schemes such as the fixed power scheme. To achieve such a goal, the optimization problem to maximize the joint coverage probability of κ is formulated.

$$\text{maximize} \qquad p_s(\mathbf{P}_\kappa) \tag{3.19}$$

$$\text{subject to} \qquad \mathrm{P_L} \leq P_i \leq \mathrm{P_U}, \quad i \in L_\kappa \tag{3.20}$$

with variables $\mathbf{P}_\kappa$, where $\mathbf{P}_\kappa = (P_i)$ is a vector that represents the transmit power levels for all the transmitting DUEs within κ, and the function $p_s(\mathbf{P}_\kappa)$ explicitly denotes (3.18) as a function of $\mathbf{P}_\kappa$; $\mathrm{P_L}$ and $\mathrm{P_U}$ are respectively the lower and upper bounds of the transmit power for DUEs which take part in the optimization; $\mathrm{P_L}$ is given by the minimum transmit power[2] of the DUE; $\mathrm{P_U}$ is set as P_d, so that, when optimizing the target cluster, the performance boost after optimization will not rise at the cost

[2]It is a design challenge to make a transmitter with a tunable transmit power range under certain low power level [172]. Therefore, the minimum transmit power for a UE is given by P_L instead of 0 Watt. Please see [173, Ch. 6] for minimum UE transmit power in LTE networks.

of other interfering clusters with the preconfigured transmit power P_d. Meanwhile, when optimizing the whole network based on the non-coherent lower bound, although DUEs within each cluster could have different transmit powers during optimization, the non-coherent lower bound formulation focuses on the worst case where all DUEs in other clusters are considered as transmitting with the maximum allowed power $\mathrm{P_U}$ regardless of their actual optimized power. This reduces the information shared from neighboring clusters at the cost of overestimating the averaged inter-cluster interference, which contrasts with the single-cluster approximation that does not consider the inter-cluster interference. Since the non-coherent lower bound and single-cluster approximation coverage probabilities of a D2D link in a cluster do not rely on the exact transmit power of neighboring clusters during optimization, the above optimization problem on maximizing the joint coverage probability of a whole network is equal to individually maximizing the joint coverage probability of each cluster. As a result, the optimization framework can be applied to both centralized and localized controllers. The optimization problem formulated above is not convex. To further analyze the optimization problem, the following theorem is required:

Theorem 1. The joint coverage probability in (3.19) is log-concave in $\tilde{\mathbf{P}}_\kappa$ when formulated based on the coherent formulation, non-coherent lower bound, and single-cluster approximation, where the ith element of $\tilde{\mathbf{P}}_\kappa$ is $\tilde{P}_i = \ln P_i$.

Proof. See Appendix 3.A.4. □

As a result of Theorem 1, the optimization problem is transformed into

$$\begin{aligned} &\text{maximize} && \ln p_s(\tilde{\mathbf{P}}_\kappa) && (3.21)\\ &\text{subject to} && \ln \mathrm{P_L} \le \tilde{P}_i \le \ln \mathrm{P_U}, \quad i \in L_\kappa && (3.22) \end{aligned}$$

with variable $\tilde{\mathbf{P}}_\kappa$. The surge of computational power, algorithms, and new coding approaches makes it possible to solve modest-size convex optimization problems in

Algorithm 1: Maximizing joint coverage probability.

Given: Strictly feasible $\tilde{\mathbf{P}}_\kappa$, counter $t = 0$, $\tilde{\mathbf{P}}_\kappa^t$ denotes the value of $\tilde{\mathbf{P}}_\kappa$ at t, $\tilde{\mathbf{P}}_\kappa^t = (\tilde{P}_i^{\,t})$, $\mu_0 > 0$, tolerance $\epsilon > 0$, and m is the total number of inequalities in (3.22).

Repeat:

1 Finding central path: Compute $\tilde{\mathbf{P}}_\kappa^t$ by minimizing $\Psi(\tilde{\mathbf{P}}_\kappa^t, \mu_t) = -\ln p_s(\tilde{\mathbf{P}}_\kappa^t) - \mu_t \left(\sum_{i \in L_\kappa} \ln\left(\tilde{P}_i^{\,t} - \ln \mathrm{P_L}\right)\right) - \mu_t \left(\sum_{i \in L_\kappa} \ln\left(\ln \mathrm{P_U} - \tilde{P}_i^{\,t}\right)\right)$ via the Newton-based method with the line search or trust region step control [174],

2 Update: $\tilde{\mathbf{P}}_\kappa := \tilde{\mathbf{P}}_\kappa^t$, and $\mu_{t+1} \in (0, \mu_t)$, where $\mu_t/\mu_{t+1} \in [10, 20]$ works well in practice [176],

3 Stop if $mu_t < \epsilon$ is achieved.

4 Increase t by 1.

microsecond or millisecond scales [174, 175]. Hence, the computational complexity of the power allocation solution given in (3.21) would not pose a difficulty in practice. A preliminary algorithm based on interior-point methods [176, 177] is summarized in Algorithm 1, and an interior-point solver to (3.21) - (3.22), which combines line search and trust region steps [178], is available from Matlab optimization toolbox.

3.3.2.2 Minimizing Power Consumption

In the green communications paradigm, reducing device transmit power consumption is beneficial to save the battery life of the DUEs and the subsequent impact on the environment in the form of CO_2 emissions. If an acceptable joint coverage probability is provided, how to minimize transmit power consumption while achieving such a joint coverage probability has been raised. To tackle it, the following formulas are provided to minimize the total transmit power consumption:

$$\text{minimize} \quad \sum_{i \in L_\kappa} P_i \tag{3.23}$$

$$\text{subject to} \quad \mathrm{P_L} \le P_i \le \mathrm{P_U}, \quad i \in L_\kappa, \tag{3.24}$$

$$\bar{p}_s < p_s(\mathbf{P}_\kappa) \tag{3.25}$$

with variables $\mathbf{P}_\kappa$, where $\bar{p}_s$ is a specified threshold corresponding to the minimum joint coverage probability for the DUE pairs within κ. $\mathrm{P_U}$ is set as P_d. Like the optimization on maximizing the joint coverage probability, when optimizing the whole network based on the non-coherent lower bound, the formulation focuses on the worst case where all DUEs in other clusters are considered as transmitting at the maximum allowed power $\mathrm{P_U}$ regardless of their actual optimized power. Since (3.25) is not convex, we need the following theorem to transform the original optimization problem into a convex optimization problem.

Theorem 2. Let $\tilde{P}_i = \ln P_i$, (3.23) - (3.25) can be transformed into a convex optimization problem, which is given by

$$\text{minimize} \quad \ln \sum_{i \in L_\kappa} \exp(\tilde{P}_i) \tag{3.26}$$

$$\text{subject to} \quad \ln \mathrm{P_L} \leq \tilde{P}_i \leq \ln \mathrm{P_U}, \quad i \in L_\kappa, \tag{3.27}$$

$$\ln \bar{p}_s - \ln p_s(\tilde{\mathbf{P}}_\kappa) < 0 \tag{3.28}$$

with variable $\tilde{\mathbf{P}}_\kappa$.

Proof. See Appendix 3.A.5. □

The corresponding preliminary algorithm based on interior-point methods is summarized in Algorithm 2, and (3.26) - (3.28) can also be implemented by using Matlab's interior-point solver.

3.4 Simulation Results and Discussion

In order to test the proposed algorithms against relevant benchmarks, simulations based on LTE parameters were developed.

Algorithm 2: Minimizing power consumption.

Given: Strictly feasible $\tilde{\mathbf{P}}_\kappa$, counter $t = 0$, $\tilde{\mathbf{P}}_\kappa^t$ denotes the value of $\tilde{\mathbf{P}}_\kappa$ at t, $\tilde{\mathbf{P}}_\kappa^t = (\tilde{P}_i^t)$, $\mu_0 > 0$, tolerance $\epsilon > 0$, and m is the total number of inequalities in (3.27) and (3.28).

Repeat:

1 Finding central path: Compute $\tilde{\mathbf{P}}_\kappa^t$ by minimizing $\Psi(\tilde{\mathbf{P}}_\kappa^t, \mu_t) = \ln \sum_{i\in L_\kappa} \exp(\tilde{P}_i^t) - \mu_t \left(\sum_{i\in L_\kappa} \ln\left(\tilde{P}_i^t - \ln \mathrm{P_L}\right)\right) - \mu_t \left(\sum_{i\in L_\kappa} \ln\left(\ln \mathrm{P_U} - \tilde{P}_i^t\right) + \ln\left(\ln p_s(\tilde{\mathbf{P}}_\kappa^t) - \ln \bar{p}_s\right)\right)$ via the Newton-based method with the line search or trust region step control,

2 Update: $\tilde{\mathbf{P}}_\kappa := \tilde{\mathbf{P}}_\kappa^t$, and $\mu_{t+1} \in (0, \mu_t)$, where $\mu_t/\mu_{t+1} \in [10, 20]$,

3 Stop if $m\mu_t < \epsilon$ is achieved.

4 Increase t by 1.

3.4.1 Simulation Configuration

In the simulation, DUEs are randomly deployed on a plane with area A according to Matérn and modified Thomas cluster processes. The parameters used in the simulation are given in Table 3.1 unless otherwise specified. The Matlab 'fmincon' interior-point algorithm is used in the simulations. During each iteration, one cluster closest to the plane center is selected as the target cluster. The benchmarks in the simulations are conventional open loop and fixed power schemes [173,179]. The DUE transmit power for the physical uplink shared channel (PUSCH) transmission is given by [179]

$$P_{PUSCH}^{ij} = \min\{P_{\max}, 10\log_{10} M + P_0 + al_{ij}\} \text{ [dBm]} \tag{3.29}$$

where M is the number of assigned resource blocks (RBs); an RB is the smallest unit of resources that can be allocated to a user, which is 180 kHz wide in frequency and 1 slot long in time; $P_0 = \{\beta + P_N\}$ [dBm/RB], β is the open loop target signal-to-noise ratio (SNR), P_N is the noise power per RB, and $l_{ij} = -10\log_{10}(G_e\ell(d_{ij}))$; a is the cell-specific path loss compensation factor. All RBs are assumed to be allocated to each DUE and all DUEs adopt an open loop scheme with $a = 1$ (i.e., full path loss inversion). For the optimization of the target cluster, the transmit power of all DUE

Table 3.1: System Parameters © 2018 IEEE

Parameter	Value
Layout	Random clusters
Plane area A	4×4 km^2
Spectrum allocation (Uplink)	20 MHz
Duplex mode	Half duplex
Thermal noise power density	-174 dBm/Hz
Matérn cluster radius R	12.5 m
Modified Thomas cluster standard variance σ	$R/3$
Average Number of DUE pairs per cluster $\overline{m}$	3
Maximum DUE transmit power $P_{\max}$	23 dBm
Minimum DUE transmit power $P_{\min}$	-40 dBm
Coding gain	0 dB
DUE antenna gain	0 dBi
DUE noise figure	9 dB
DUE link spectrum efficiency	0.05 bit/s/Hz
Carrier frequency	2.4 GHz
Path loss exponent	2.7
Preconfigured transmit power of DUE P_d	-15 dBm
Simulation iterations	5×10^4

transmitters in interfering clusters before the optimization is assumed to be given by the preconfigured transmit power P_d.

When maximizing the joint coverage probability for the target cluster/whole network, the optimization was performed first in the target/all cluster(s), and the corresponding averaged transmit power was achieved for the target/all cluster(s). Then, the fixed power scheme was performed in the target/all cluster(s) using the average of previously optimized power levels in the target/all cluster(s). Finally, the open loop is performed in the target/all cluster(s). For the target cluster optimization, since the transmit power of all clusters before optimization is P_d and the optimized power within the target cluster is upper bounded by P_d, the optimization can increase the joint coverage probability of the target cluster without degrading the coverage probabilities of neighboring clusters.

When minimizing power consumption for the target cluster/whole network, the fixed power scheme with power level P_d was performed first in the target/all cluster(s), and the corresponding joint coverage probability of the target/all cluster(s) was achieved. Then, the optimization scheme was performed in the target/all cluster(s) with the threshold $\bar{p}_s$ given by the joint coverage probability of the target/all cluster(s) from the fixed power scheme. For the optimizations based on the non-coherent lower bound and single-cluster approximation, if there is no feasible solution found, the transmit power of the DUEs will be given by P_d. The simulation results are obtained by averaging over 50,000 independent Monte Carlo trials.

3.4.2 Simulation Results

3.4.2.1 Maximizing Joint Coverage Probability of the Target Cluster

Figure 3.2 gives the joint coverage probabilities of the DUEs in the target cluster after applying different power allocation schemes. The plots of all the simulation results on joint coverage probabilities are based on the coherent coverage probability formulation for accuracy. One can easily see that all performance curves drop heavily as the cluster intensity λ_o increases. In practice, the typical connection density supported by an LTE system is 2,000 active devices in a square kilometer [180], which corresponds to $\lambda_0 = \frac{2000}{2\times\overline{m}} \times 10^{-6} \approx 3.33 \times 10^{-4}$ cluster/m^2. The distribution of the locations of the DUEs has a noticeable effect on the performance under the same $\overline{m}$. Among the optimizations, the performance of the optimization based on the coherent formulation is the best. The optimization based on the non-coherent lower bound has slightly worse performance than the coherent formulation, while the single-cluster approximation based optimization performs the worst. Compared with other schemes, the open loop scheme performs the worst. This is because it only compensates for the path loss from the transmitter to the intended receiver without considering the fading and interference. Thus, as the cluster intensity increases, the open loop scheme would not be suitable for out-band D2D networks. Meanwhile, all the optimization schemes perform better than their fixed power counterparts, which use the averaged power of the target cluster after the optimization over each realization. In detail, when the cluster intensity is below 10^{-4} cluster/m^2, the proposed

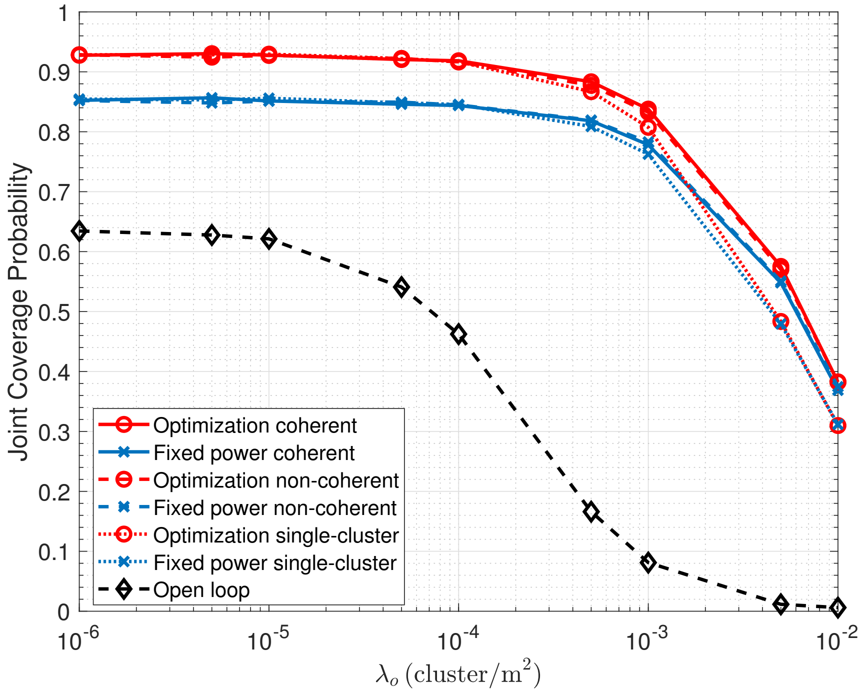

(a) Matérn.

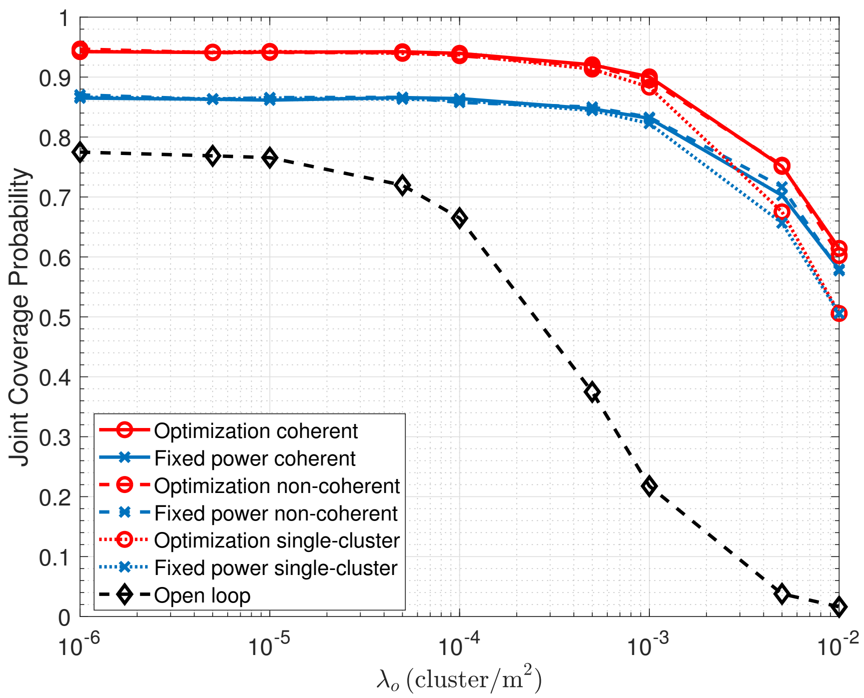

(b) Modified Thomas.

Figure 3.2: Joint coverage probability of the target cluster *vs.* λ_o for the joint coverage probability maximization, open loop and fixed power schemes. © 2018 IEEE.

optimizations exhibit 8% better joint coverage probabilities than their fixed power counterparts. Besides, all the optimizations have the same performance in the low intensity regime. This is because the inter-cluster interference is negligible at lower intensities. Hence, the joint coverage probability based on the coherent formulation, non-coherent lower bound, and single-cluster approximation are approximately the same. Furthermore, compared with other proposed schemes at higher cluster intensities, the optimization based on the single-cluster approximation performs the worst since it ignores the inter-cluster interference from neighboring clusters.

Figure 3.3 compares the average power consumption of the DUE in the target cluster with different power allocation schemes. Both the Matérn cluster and modified Thomas cluster processes have similar trends in the average power consumption for different cluster intensities. In the proposed scheme, the optimizations based on the coherent formulation and single-cluster approximation consume the least amount of power. The average transmit power levels from the optimization based on the single-cluster approximation are the same for different cluster intensities, since the single-cluster approximation only considers the DUEs within the target cluster and $\overline{m}$ is fixed. Meanwhile, the open loop scheme achieves the lowest power consumption at -40 dB since it only compensates for the path loss among the DUEs. According to (3.29), when the distance is too short, the minimum transmit power is used. Compared with the upper limit of the transmit power at -15 dBm, the optimizations based on the coherent and non-coherent lower bound formulations decrease the average transmit power by at most 2 dB at $\lambda_o = 10^{-6}$ cluster/m^2 and 0.45 dB at $\lambda_o = 10^{-2}$ cluster/m^2. The reason why there is almost no power saving for the latter intensity can be explained as follows. As λ_o increases, the inter-cluster interference becomes dominant, and the proposed optimizations based on both coherent and non-coherent lower bound formulations must boost the transmit power of the DUEs within the target cluster to increase the SINR, until it reaches the upper bound of transmit

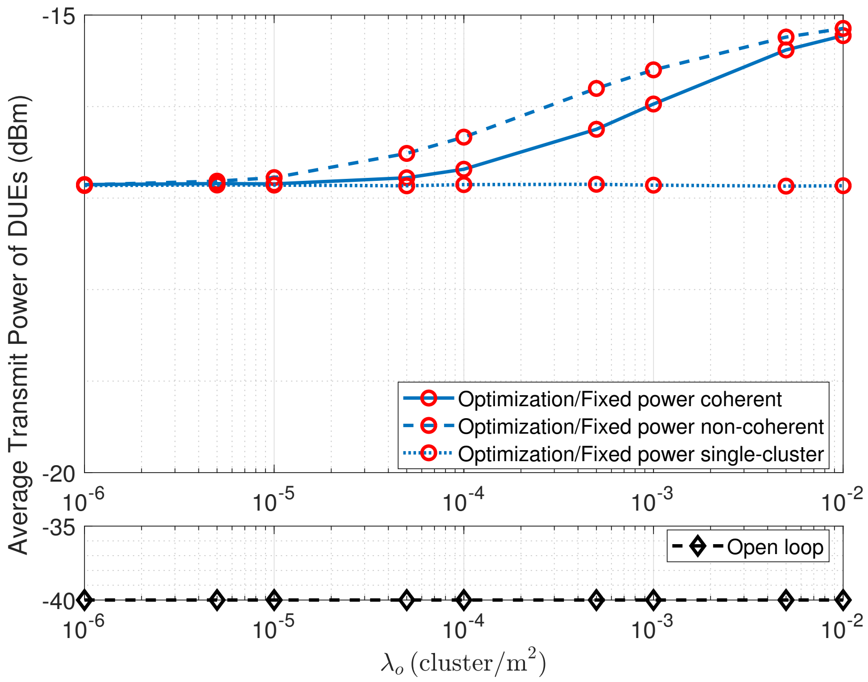

(a) Matérn.

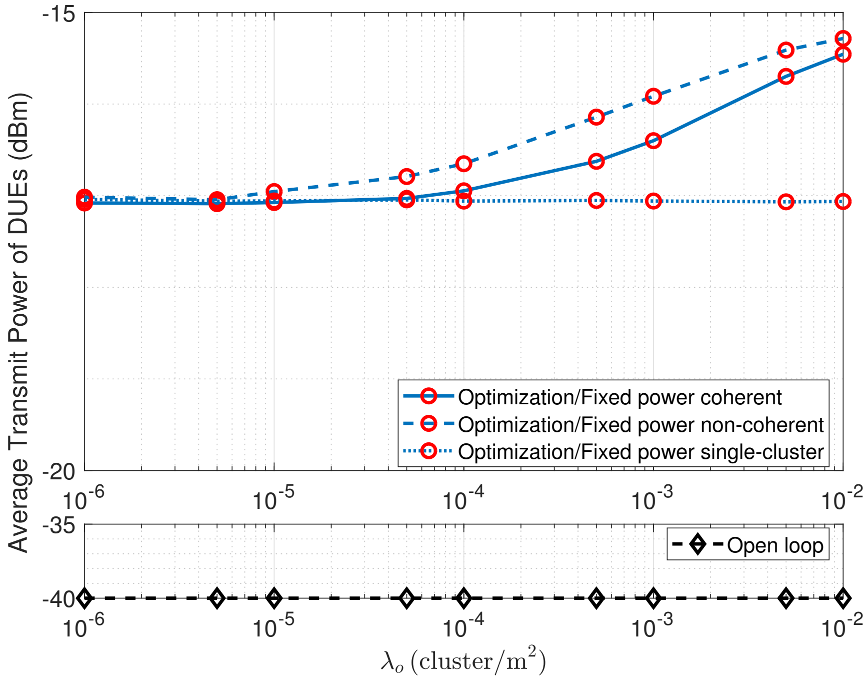

(b) Modified Thomas.

Figure 3.3: Average transmit power of the DUEs in the target cluster *vs.* λ_o for the joint coverage probability maximization, open loop and fixed power schemes. © 2018 IEEE.

power.

3.4.2.2 Minimizing Power Consumption of the Target Cluster

Figure 3.4 depicts the achieved joint coverage probabilities of the target cluster for power minimization using the fixed power scheme as the benchmark. In the fixed power scheme, the transmitter power for all clusters is given by P_d. During each trial, the threshold $\bar{p}_s$ is given by the joint coverage probability based on coherent formulation over the realization of the clusters and P_d. The open loop scheme is omitted in the simulation since there are no adjustable parameters which allow the scheme to reach a predefined threshold for the joint coverage probability. It is evident that the optimization based on the coherent formulation matches $\bar{p}_s$. This can be explained by the fact that when minimizing power consumption, the coherent formulation has full knowledge of all the DUEs' locations and transmit powers. Hence, it guarantees that $\bar{p}_s$ can be achieved. The optimization based on the non-coherent lower bound formulation performs better than $\bar{p}_s$ when λ_o is less than 10^{-3} cluster/m^2, while it achieves the worse performance when λ_o is greater than 10^{-3} cluster/m^2. The optimization based on the non-coherent lower bound formulation does not always match $\bar{p}_s$ for it is an approximation to the actual joint coverage probability which considers the statistics of the inter-cluster interference rather than the exact value. The optimization based on the single-cluster approximation is far from achieving $\bar{p}_s$ as λ_o is increasing because it ignores the inter-cluster interference whose impact on the joint coverage performance increases as λ_o increases.

Figure 3.5 shows the corresponding average transmit power of the DUEs as discussed in Figure 3.4. Among all optimization formulations, the joint coverage probability based on the single-cluster approximation consume the least power, but the corresponding joint coverage probabilities are far away from achieving the required $\bar{p}_s$. Compared with the fixed power scheme, the optimization based on the coherent for-

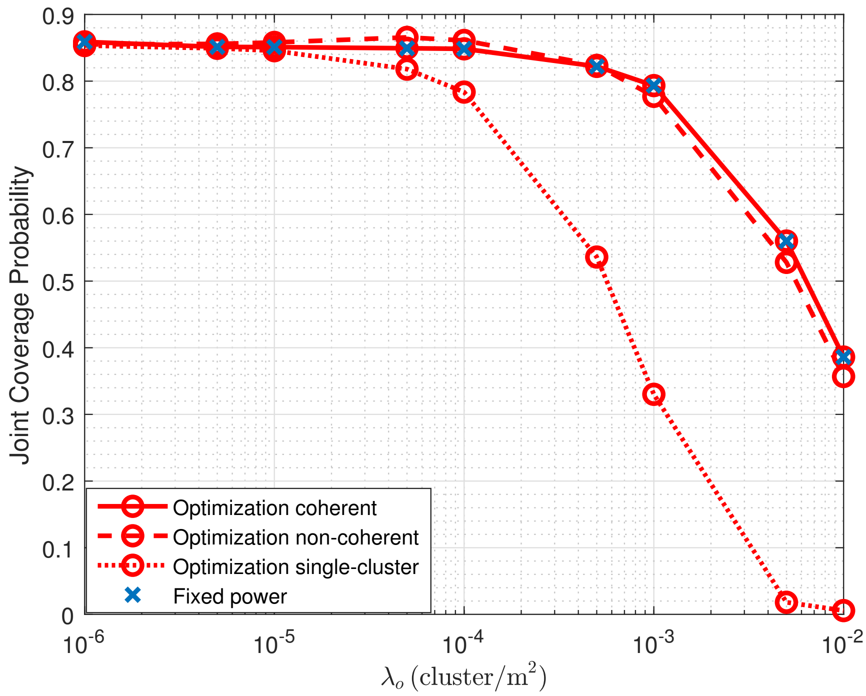

(a) Matérn.

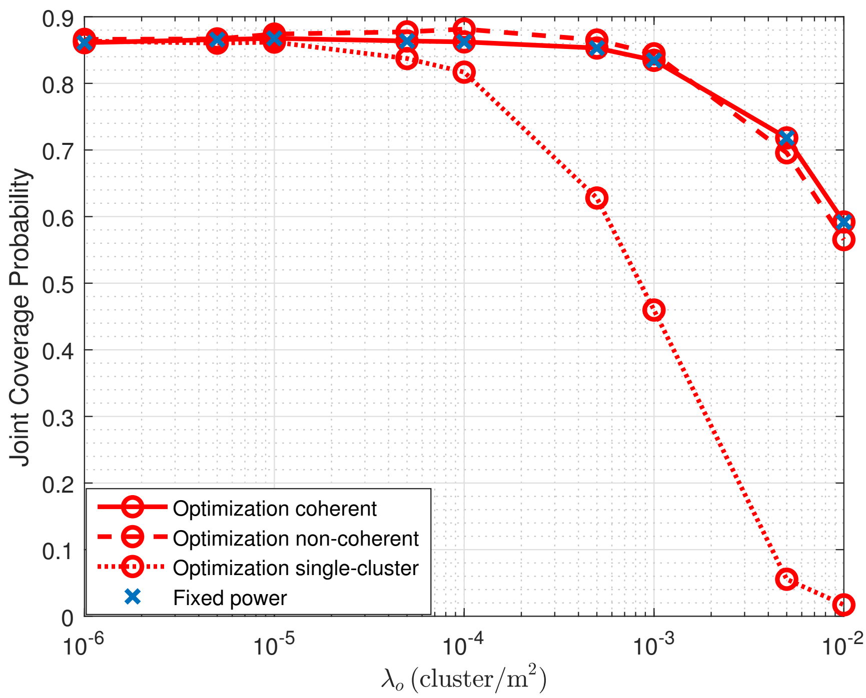

(b) Modified Thomas.

Figure 3.4: Joint coverage probability of the target cluster *vs.* λ_o, given by benchmarking the power consumption minimization against the fixed power scheme.

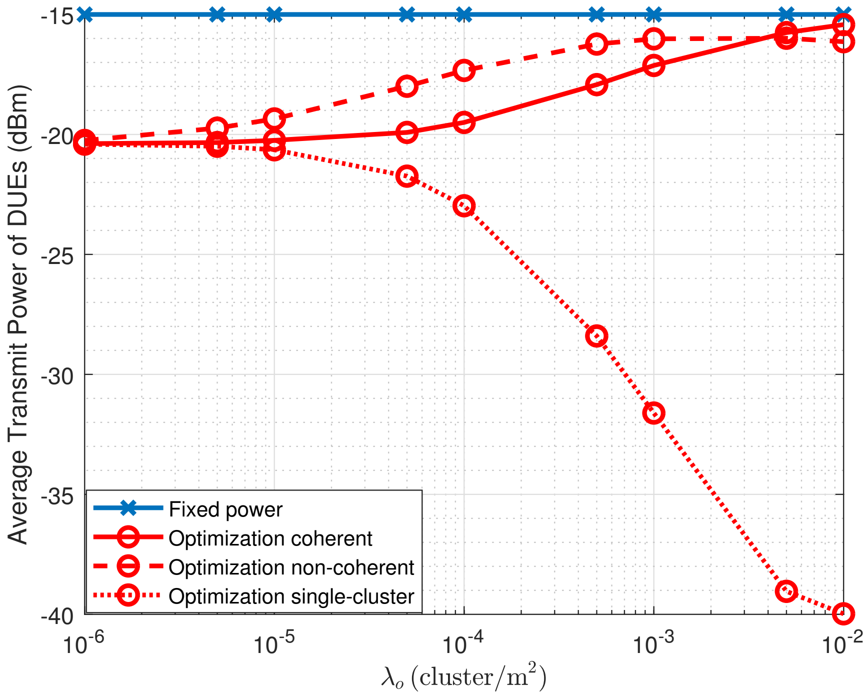

(a) Matérn.

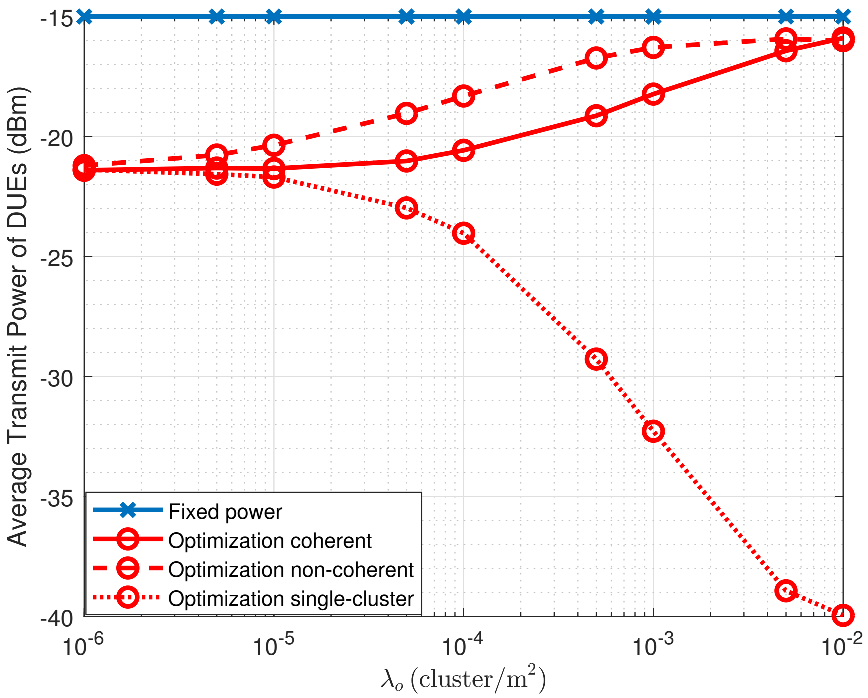

(b) Modified Thomas.

Figure 3.5: Transmit power of the typical DUE in the target cluster *vs.* λ_o, given by benchmarking the power consumption minimization against the fixed power scheme.

mulation saves power by at most 1 dB to 6 dB from $\lambda_o = 10^{-6}$ cluster/m^2 to $\lambda_o = 10^{-2}$ cluster/m^2, while there is a maximum gap of 2 dB between it and the non-coherent formulation at some intensities such as $\lambda_o = 10^{-4}$ cluster/m^2. The performance drop slows down from $\lambda_o = 5 \times 10^{-3}$ cluster/m^2 to $\lambda_o = 10^{-2}$ cluster/m^2 is because that the optimization has reach the lower bound of the transmit power at $\lambda_o = 10^{-2}$ cluster/m^2. As a result of these observations, the coherent and non-coherent formulations are more suitable for fulfilling the requirement of green communications, while giving similar performance to that of the fixed power scheme.

3.4.2.3 Maximizing Joint Coverage Probability of the Whole Network

As shown in Figure 3.6(a), the joint coverage probability of the whole network increases as A decreases, where an average of 16 Matérn clusters are within the network[3]. Compared with the full power and open loop schemes, the optimization based on coherent formulation performs best while the one based on non-coherent lower bound formulation also gives similar results to the coherent counterparts in most of the cases. The fixed power schemes have a similar joint coverage probability to their optimization counterparts when A is below 10^2 m^2 and around 10% smaller when A is above 10^4 m^2. Meanwhile, Figure 3.6(b) shows that the proposed optimization based on the coherent formulation consumes around 2 dB less power than the upper transmit power limit $\mathrm{P_U} = -15$ dBm when A is above 10^4 m^2. When A is below 10^4 m^2, there is still power saving, but the saving drops as A decreases. The non-coherent optimization consumes the most in power as result of increasing the transmit power of each DUE to combat the overestimated inter-cluster interference in average. Further-

[3]Due to the similar trends appearing in the joint coverage probability and average power consumption for both the Matérn cluster and modified Thomas cluster processes, only the discussion on the Matérn cluster processes is presented in this subsection. Meanwhile, different from previous settings for the target cluster optimizations which are based on a fixed A and different λ_o, the simulations for all cluster optimizations are based on an average of 16 Matérn clusters and different A. This is because as the number of clusters increases, the simulations take a very long time to complete 5×10^4 trials.

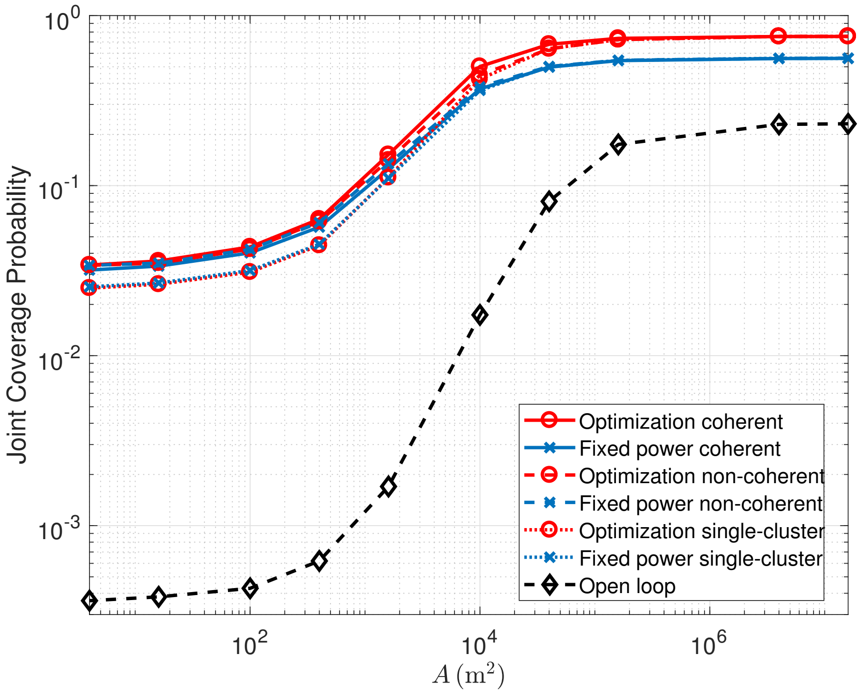

(a)

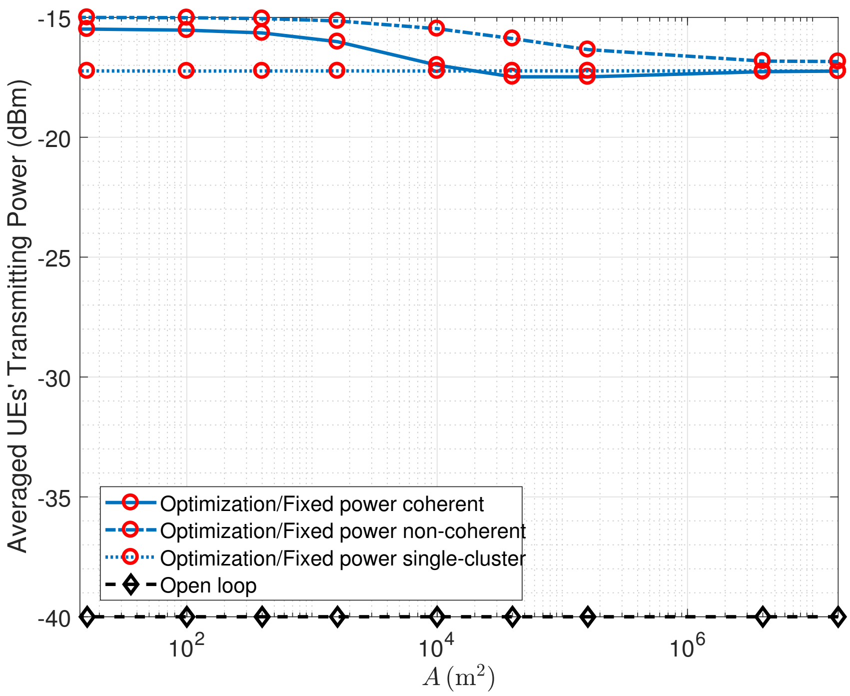

(b)

Figure 3.6: The joint coverage probability (a) and average transmit power (b) of all clusters *vs.* A for the joint coverage probability maximization, open loop and fixed power schemes.

more, the optimizations based on both the coherent formulation and single-cluster approximation spend the same average transmit power and achieve the same joint coverage probability when A is large. This is because only the intra-cluster interference is taking effect at a large A, and both the coherent formulation and single-cluster approximation have captured this interference in their formulations. When A is small, the inter-cluster interference becomes non-negligible, and the optimization based on the coherent formulation could boost the performance further at the cost of increasing the average transmit power of the DUEs within the network.

3.4.2.4 Minimizing Power Consumption of the Whole Network

Figure 3.7 gives the joint coverage probability of the whole network and the average transmit power after power consumption minimization given the fixed power scheme as the benchmark. As shown in Figure 3.7(a), the coherent optimization achieves similar performance to the fixed power scheme when the threshold $\bar{p}_s$ during each simulation trial is obtained by the joint coverage probability of the fixed power scheme. Although, the optimization based on non-coherent lower bound formulation consumes the most power as a result of overestimating the average inter-cluster interference, it overachieves the required threshold in the given settings. Meanwhile, the optimization based on the single-cluster approximation fails to achieve the required $\bar{p}_s$ when A is small. That is because the inter-cluster interference increases as A decreases for a given average number of clusters in A, and the single-cluster approximation does not consider the inter-cluster interference. The average transmit power in Figure 3.7(b) shows that the optimization based on the coherent formulation saves around 1 dB to 11 dB for the given range of A. Hence, the optimization based on the coherent formulation could be applied to power saving for green communications while maintaining the same performance as the fixed power scheme. Meanwhile, the optimization based on the single-cluster approximation has a similar performance to

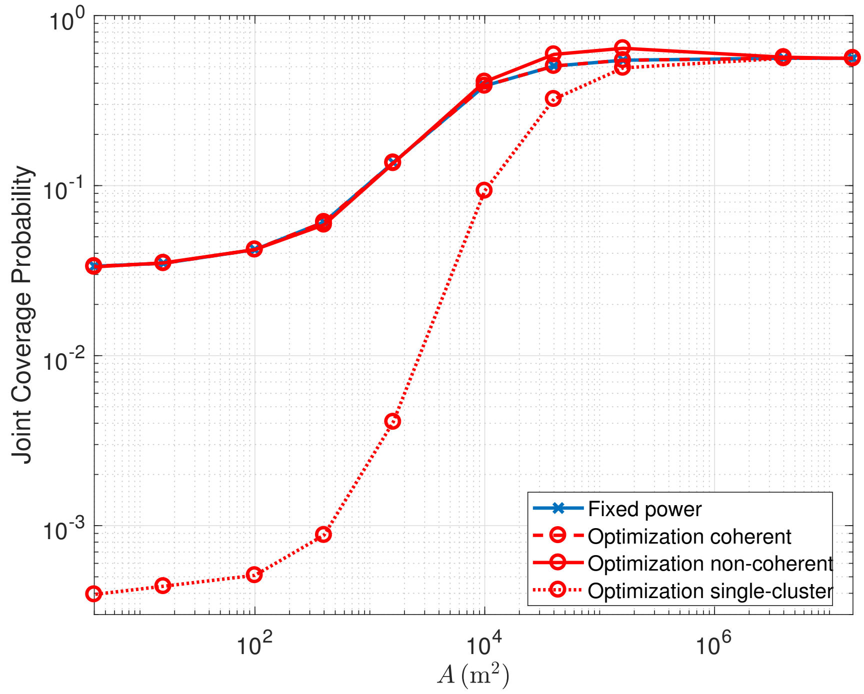

(a)

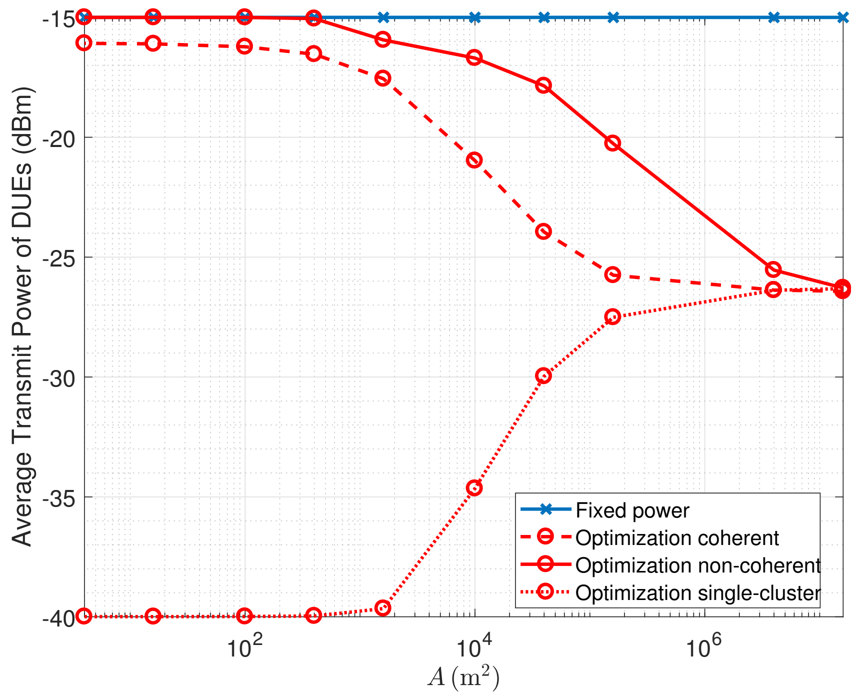

(b)

Figure 3.7: The joint coverage probability (a) and average transmit power (b) of all clusters *vs.* A, given by benchmarking the power consumption minimization against the fixed power scheme.

the optimization based on the coherent formulation when A is very large. That is because when A is very large, only the intra-cluster interference matters, and both formulations have taken the intra-cluster interference into account.

3.5 Summary

In this chapter, the performance of an out-band D2D network characterized by joint coverage probability maximization and power minimization is enhanced. The joint coverage probabilities are formulated based on the coherent, non-coherent lower bound and single-cluster approximation coverage probabilities. Compared with conventional open loop and fixed power allocation schemes, the joint coverage probability of the target cluster is maximized. The power minimization enables DUEs to have the least power consumption while maintains the same performance compared with the fixed power scheme. Apart from this, a discussion on the feasibility of the optimizations to a bounded path loss model can be found in Appendix 3.A.6. Therefore, these optimization frameworks will facilitate the applications of commercial and public safety and fulfil the idea of green D2D communications in 5G communication networks and beyond.

3.A Appendices

3.A.1 Proof of Lemma 1

Proof. Assuming the number of elements in L_T is m, let $a_1 = F_{ij}$, $\{a_2, ..., a_m\}$ be an ordered set of $\left\{\frac{\beta \ell(d_{kj}) F_{kj} P_k}{\ell(d_{ij}) P_i} \mid k \in L_T \backslash \{i\}\right\}$, and $b = \frac{\beta N_0}{G_e \ell(d_{ij}) P_i}$, then

$$\begin{aligned}
\mathbb{P}\{\text{SINR}_{ij} > \beta\} &= \mathbb{P}\left\{F_{ij} > \frac{\beta(N_0 + I_{ij})}{G_e \ell(d_{ij}) P_i}\right\} \\
&= \mathbb{P}\left\{F_{ij} > \sum_{k \in L_T \backslash \{i\}} \frac{\beta \ell(d_{kj}) F_{kj} P_k}{\ell(d_{ij}) P_i} + \frac{\beta N_0}{G_e \ell(d_{ij}) P_i}\right\} \\
&= \mathbb{P}\left(a_1 > \sum_{i=2}^{m} a_i + b\right).
\end{aligned} \tag{3.30}$$

Since each element of $\{a_1, ..., a_m\}$ is proportional to the element of an ordered set of exponential variables $\{F_{l,j} \mid l \in L_T\}$, $a_1, ..., a_m$ are independent exponentially distributed random variables. Denoting the mean of a_i by $1/\gamma_i$, then

$$\begin{aligned}
\mathbb{P}\left(a_1 > \sum_{i=2}^{m} a_i + b\right) &= \int_{c_m=0}^{\infty} ... \int_{c_2=0}^{\infty} \mathbb{P}\left(a_1 > \sum_{i=2}^{m} c_i + b\right) \prod_{i=2}^{m} \gamma_i \exp(-\gamma_i c_i)\, \mathrm{d}c_2 ... \mathrm{d}c_m \\
&= \int_{c_m=0}^{\infty} ... \int_{c_2=0}^{\infty} \exp\left(-\gamma_1 \sum_{i=2}^{m} c_i - \gamma_1 b\right) \prod_{i=2}^{m} \gamma_i \exp(-\gamma_i c_i)\, \mathrm{d}c_2 ... \mathrm{d}c_m \\
&= \exp\left(-\gamma_1 b\right) \prod_{i=2}^{m} \int_{c_i=0}^{\infty} \gamma_i \exp\left(-(\gamma_1 + \gamma_i) c_i\right)\, \mathrm{d}c_i \\
&= \exp\left(-\gamma_1 b\right) \prod_{i=2}^{m} \frac{\gamma_i}{\gamma_1 + \gamma_i}.
\end{aligned} \tag{3.31}$$

After calculating γ_i by inverting the expectation values of $a_1, ..., a_m$, (3.6) is obtained. This concludes the proof. □

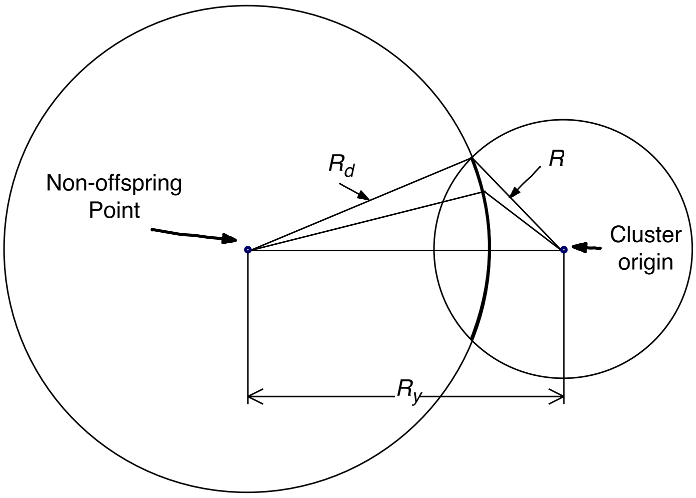

Figure 3.8: The non-offspring point is outside the cluster, and a cluster encloses the arc of a circle. © IEEE 2017.

3.A.2 Proof of the Conditional Distance PDF of Matérn Cluster Process

Proof. When $R_y > R$, the non-offspring point is outside the Matérn cluster. The possible locations of the offspring point that have the same distance to the non-offspring point are on the arc of a circle that is enclosed by the cluster as shown in Figure 3.8. When R_d is increasing from $R_y - R$ to $R_y + R$, the cluster can be filled with an infinite number of non-overlapping arcs, and each arc represents a class of points that have the same distance to the non-offspring point. The arc length is given by

$$c(r_d) = \begin{cases} c_1(r_d), & r_d \in [R_y - R, R_y + R], \\ 0, & \text{otherwise}; \end{cases} \tag{3.32}$$

where

$$c_1(r_d) = 2r_d \arcsin \frac{\sqrt{4R_y^2 r_d^2 - (R_y^2 - R^2 + r_d^2)^2}}{2R_y r_d} \tag{3.33}$$

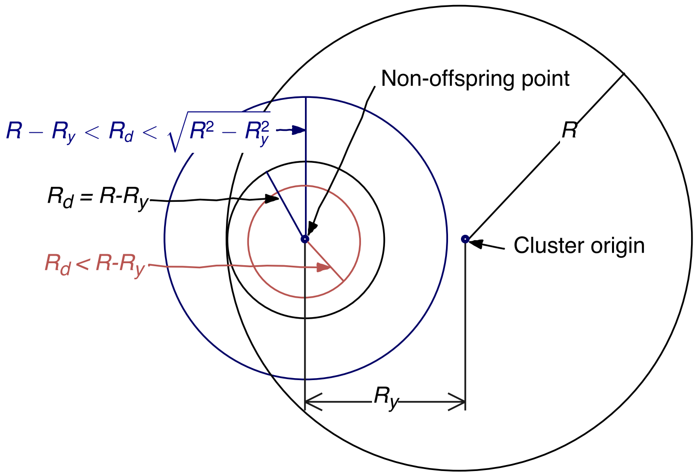

Figure 3.9: The non-offspring point is inside the cluster, and a cluster encloses an arc or a circle where $R_d < \sqrt{R^2 - R_y^2}$. © IEEE 2017.

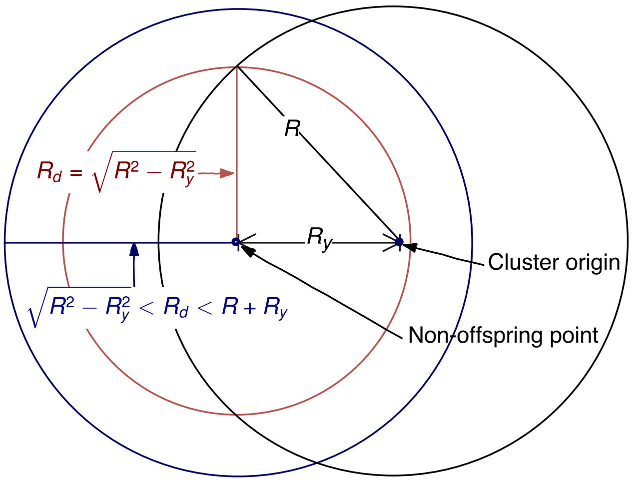

Figure 3.10: The non-offspring point is inside the cluster, and a cluster encloses an arc or a circle where $R_d > \sqrt{R^2 - R_y^2}$. © IEEE 2017.

while the corresponding density for R_d is achieved in (3.10).

When $0 < R_y \leq R$, the non-offspring point is inside the Matérn cluster. The possible locations of the offspring point that have the same distance to a non-offspring point could be on: (i) the circle centered at the non-offspring point when $R_d \leq R - R_y$ as depicted in Figure 3.9; (ii) the arc of a circle with radius R_d that is enclosed by the cluster with radius R as seen in Figures 3.9 and 3.10.

The former is the perimeter of a circle with radius R_d, which is the first case of

(3.34), where

$$c(r_d) = \begin{cases} 2\pi r_d, & r_d \le R - R_y, \\ 2\pi r_d - c_1(r_d), & R - R_y < r_d \le \sqrt{R^2 - R_y^2}, \\ c_1(r_d), & \sqrt{R^2 - R_y^2} < r_d \le R + R_y, \\ 0, & \text{otherwise.} \end{cases} \tag{3.34}$$

The latter belongs to the second and third cases of (3.34). $\sqrt{R^2 - R_y^2}$ is the boundary to decide if the circular arc enclosed by the cluster is the major or minor arc of a circle with radius R_d.

When $R_y = 0$, the non-offspring point is overlapping with the cluster origin. The possible locations of the offspring point that have the same distance to the non-offspring point form a circle with radius R_d centered at the cluster origin. It belongs to the first case in (3.34). By simplified the combined result of (3.32) with (3.34), (3.10) is achieved, this concluding the proof. □

3.A.3 Proof of Lemma 2

For the Matérn cluster process,

$$\begin{aligned} \mathcal{L}_I(s) &= \exp\left(-2\pi\lambda_o \int_0^\infty [1 - \xi(s, R_y)]\, R_y \,\mathrm{d}R_y\right) \\ &\overset{(a)}{\ge} \exp\left(-2\pi\lambda_o \int_0^\infty \int_0^\infty \frac{\overline{m} g(x)}{s^{-1} + g(x)} f_{R_d}(x \mid R_y)\,\mathrm{d}x R_y\,\mathrm{d}R_y\right) \\ &\overset{(b)}{=} \exp\left(-2\pi\lambda_o \overline{m} \int_0^\infty \frac{g(x)}{s^{-1} + g(x)} x\,\mathrm{d}x\right) \\ &= \exp\left(-\pi\lambda_o \overline{m} \frac{\left(sG_e(\frac{\lambda}{4\pi})^2 P_d\right)^{2/\alpha}}{\mathrm{sinc}(2/\alpha)}\right) \end{aligned} \tag{3.35}$$

where (a) is the result of $\exp(-ax) \ge 1 - ax$ for $a \ge 0$; (b) is because $\int_0^\infty f_{R_d}(x \mid R_y) R_y \,\mathrm{d}R_y = \int_0^\infty x f_{R_d}(R_y \mid x)\,\mathrm{d}R_y = x$, which is given by Lemma 3. This concludes the proof.

Lemma 3. $\int_0^\infty f_{R_d}(x \mid R_y) R_y \, \mathrm{d}R_y = \int_0^\infty x f_{R_d}(R_y \mid x) \, \mathrm{d}R_y = x$, where $f_{R_d}(x \mid R_y)$ is given by (3.10).

Proof. For a given $x \geq 0$, equation (3.10) guarantees that x and R_y are interchangeable in terms of both equations and domains in $f_{R_d}(x \mid R_y) R_y$. Thus,

$$\int_0^\infty f_{R_d}(x \mid R_y) R_y \, \mathrm{d}R_y = \int_0^\infty x f_{R_d}(R_y \mid x) \, \mathrm{d}R_y. \tag{3.36}$$

Meanwhile, for a given x, $f_{R_d}(R_y \mid x)$ is a conditional PDF. Therefore, $\int_0^\infty x f_{R_d}(R_y \mid x) \, \mathrm{d}R_y = x \int_0^\infty f_{R_d}(R_y \mid x) \, \mathrm{d}R_y = x$. This concludes the proof. □

3.A.4 Proof of Theorem 1

3.A.4.1 Proof of Coherent and Single-Cluster Approximation Coverage Probability Formulations

The formulations of coherent and single-cluster approximation coverage probabilities have similar mathematical structures because the number of the interferers in a single-cluster case is just a subset of the interferers of the coherent case. Thus, the proof for the corresponding joint coverage probability based on coherent and single-cluster approximation coverage probabilities is given as follows.

Proof. Considering that a node i transmits signals to node j, let $\mathbf{W}_{-j}$ denote all the interfering channel gains at node j, $\mathbf{W}_j = [W_{ij}, \mathbf{W}_{-j}]$ represents all the channel gains, the tilde symbol over a scalar or a vector denotes the element-wise natural logarithm operation on the original variables [181]. For a realization $\tilde{\mathbf{w}}_j$ of $\tilde{\mathbf{W}}_j$, the marginal PDF of $\tilde{\mathbf{W}}_{-j}$ is given by integrating out $\tilde{w}_{ij}$

$$f_{\tilde{\mathbf{W}}_{-j}}(\tilde{\mathbf{w}}_{-j}) = \int f_{\tilde{\mathbf{W}}_j}(\tilde{\mathbf{w}}_j) \, \mathrm{d}\tilde{w}_{ij}. \tag{3.37}$$

Meanwhile, under Rayleigh fading, the PDF of channel power gain is an exponential function, which can be written as

$$f_{W_{ij}}(w_{ij}) = \begin{cases} \lambda_{ij} e^{-\lambda_{ij} w_{ij}} & w_{ij} \geq 0 \\ 0 & w_{ij} < 0 \end{cases} \tag{3.38}$$

where $1/\lambda_{ij} = G_e \ell(d_{ij})$ is the averaged channel power gain. Then, the corresponding PDF of $\tilde{W}_{ij}$ is given by transformation of random variable W_{ij}. Taking the logarithmic of the PDF of $\tilde{W}_{ij}$ yields

$$\ln f_{\tilde{W}_{ij}}(\tilde{w}_{ij}) = \ln \lambda_{ij} + \tilde{w}_{ij} - \lambda_{ij} \exp(\tilde{w}). \tag{3.39}$$

Since $-\lambda_{ij} \exp(\tilde{w}_{ij})$ is concave, $f_{\tilde{W}_{ij}}(\tilde{w}_{ij})$ is log-concave in $\tilde{w}_{ij}$, and the log-concavity is preserved in the joint PDF $f_{\tilde{\mathbf{W}}_j}(\tilde{\mathbf{w}}_j)$. This is because $f_{\tilde{\mathbf{W}}_j}(\tilde{\mathbf{w}}_j)$ is given by the product of the PDFs of independent and identically distributed (i.i.d.) random variables $\tilde{\mathbf{W}}_j$. Furthermore, $f_{\tilde{\mathbf{W}}_{-j}}(\tilde{\mathbf{w}}_{-j})$ is log-concave function since: if $g_1 : \mathbb{R}^n \times \mathbb{R}^m \to \mathbb{R}$ is log-concave, then, $g_2(x) = \int_{y \in \mathbb{R}^m} g_1(x, y)\, \mathrm{d}y$ is a log-concave function of x on $\mathbb{R}^n$.

Given that $\tilde{\mathbf{W}}_{-j} = \tilde{\mathbf{w}}_{-j}$ has occurred, the formulation of the coverage probability is similar to Appendix 3.A.1, which can be written as

$$p_{ij}(\tilde{\mathbf{P}}_\kappa) = \int \bar{F}_{\tilde{W}_{ij}}(g_{ij}(\tilde{\mathbf{P}}_\kappa, \tilde{\mathbf{w}}_{-j})) f_{\tilde{\mathbf{W}}_{-j}}(\tilde{\mathbf{w}}_{-j})\, \mathrm{d}\tilde{\mathbf{w}}_{-j} \tag{3.40}$$

where

$$\begin{aligned} \bar{F}_{\tilde{W}_{ij}}(\tilde{w}_{ij}) =& 1 - F_{\tilde{W}_{ij}}(\tilde{w}_{ij}), \\ g_{ij}(\tilde{\mathbf{P}}_\kappa, \tilde{\mathbf{w}}_{-j}) =& \ln \left\{ N_0 \exp(\tilde{\beta} - \tilde{P}_i) + \sum_{\{k | \tilde{w}_{kj} \in \tilde{\mathbf{w}}_{-j}\}} \exp(\tilde{\beta} + \tilde{w}_{kj} + \tilde{P}_k - \tilde{P}_i) \right\} \end{aligned} \tag{3.41}$$

$F_{\tilde{W}_{ij}}(\tilde{w}_{ij})$ and $\bar{F}_{\tilde{W}_{ij}}(\tilde{w}_{ij})$ are the cumulative distribution function (CDF) and the complementary CDF (CCDF) of $\tilde{W}_{ij}$, respectively. Since $\bar{F}_{\tilde{W}_{ij}}(\tilde{w}_{ij})$ is nonincreasing in $\tilde{w}_{ij}$, and $\ln(x)$ is increasing in x, $\ln \bar{F}_{\tilde{W}_{ij}}(\tilde{w}_{ij})$ is nonincreasing function. This can be easily explained as follows: For a nonincreasing function $f_1(x)$, if $x_1 < x_2$, then $f_1(x_1) \geq f_1(x_2)$. For an increasing function $f_2(x)$, $f_2(f_1(x_1)) \geq f_2(f_1(x_2))$. Thus, $f_2(f_1(x))$ is a nonincreasing function. Meanwhile, since $f_{\tilde{W}_{ij}}(\tilde{w}_{ij})$ is log-concave in $\tilde{w}_{ij}$, the CCDF $\bar{F}_{\tilde{W}_{ij}}(\tilde{w}_{ij})$ is log-concave in $\tilde{w}_{ij}$ [182]. Since $g_{ij}(\tilde{\mathbf{P}}_\kappa, \tilde{\mathbf{w}}_{-j})$ is a convex function and $\ln \bar{F}_{\tilde{W}_{ij}}(\tilde{w}_{ij})$ is nonincreasing and concave, $\ln \bar{F}_{\tilde{W}_{ij}}(g_{ij}(\tilde{\mathbf{P}}_\kappa, \tilde{\mathbf{w}}_{-j}))$ is concave [174]. Therefore, $\bar{F}_{\tilde{W}_{ij}}(g_{ij}(\tilde{\mathbf{P}}_\kappa, \tilde{\mathbf{w}}_{-j}))$ is log-concave. The integration in (3.37) and (3.40), and multiplication between CCDF and PDF in (3.40) preserve log-concavity. Thus, the product of either coherent and single-cluster approximation coverage probabilities yields p_s, which is also log-concave in $\tilde{\mathbf{P}}_\kappa$. This concludes the proof. □

3.A.4.2 Proof of Non-Coherent Lower Bound Coverage Probability Formulation

Proof. Applying variable transformations $\tilde{P}_i = \ln P_i$ and taking the natural logarithm on both sides of (3.17) yield

$$\ln p_{ij}^{\mathrm{nc}} = \ln p_{ij}^{\mathrm{sc}} + \ln \mathcal{L}_I \left(\frac{\beta}{G_e \ell(d_{ij}) \exp(\tilde{P}_i)} \right) \tag{3.42}$$

$\ln p_{ij}^{\mathrm{sc}}$ is concave in $\tilde{\mathbf{P}}_\kappa$ as given by the first proof in Appendix 3.A.4 and

$$\ln \mathcal{L}_I \left(\frac{\beta}{G_e \ell(d_{ij}) \exp(\tilde{P}_i)} \right) \geq -\pi \lambda_o \overline{m} \frac{\left(\beta d_{ij}^\alpha \exp(-\tilde{P}_i) P_d\right)^{2/\alpha}}{\operatorname{sinc}(2/\alpha)} \tag{3.43}$$

where the right side is also concave in $\tilde{P}_i \in \tilde{\mathbf{P}}_\kappa$. This is because its second order derivative with respect to $\tilde{P}_i$ is $-A \left(\frac{2}{\alpha}\right)^2 \exp\left(-\frac{2}{\alpha}\tilde{P}_i\right) < 0$, where $A = \pi \lambda_o \overline{m} \frac{\left(\beta d_{ij}^\alpha P_d\right)^{2/\alpha}}{\operatorname{sinc}(2/\alpha)}$. Therefore, the lower bound on p_{ij}^{nc} given by (3.15) is log-concave in $\tilde{\mathbf{P}}_\kappa$. The objective in (3.19) is also log-concave, because the product of lower bounded non-coherent coverage probabilities is still log-concave. This concludes the proof. □

3.A.5 Proof of Theorem 2

Let $\tilde{P}_i = \ln P_i$ and taking the natural logarithm on (3.23) - (3.25), a transformed optimization problem is obtained in (3.26) - (3.28). A function with a log-sum-exponent form given by (3.26) is convex in $\tilde{\mathbf{P}}_\kappa$ [174, pp. 72 and 74]. In (3.28), the function $\ln \bar{p}_s - \ln p_s(\tilde{\mathbf{P}}_\kappa)$ is convex in $\tilde{\mathbf{P}}_\kappa$, because: 1) according to Theorem 1, $-\ln p_s(\tilde{\mathbf{P}}_\kappa)$ is convex for the coherent, non-coherent lower bound and single-cluster approximation coverage probability formulations; 2) the affine operation that adding $\ln \bar{p}_s$ to $-\ln p_s(\tilde{\mathbf{P}}_\kappa)$ keeps the convexity in the result [174]. Therefore, the optimization problem given by (3.26) - (3.28) is convex in $\tilde{\mathbf{P}}_\kappa$. This concludes the proof.

3.A.6 Further Discussion on Path Loss Model

Although the path loss model has a singularity as the distance between nodes i and j goes to zero, i.e., $d_{ij} \to 0$. However, according to [151, 168], such a singularity has a negligible effect on the results from a coverage perspective. As an example illustrated in [168], if an interferer and a receiver are very close to each other, the adopted unbounded path loss model would lead to an artificially small SINR, and the receiver would very likely be in outage even if the singularity was removed. In this case, the unbounded path loss model could simplify the analysis without substantially affecting the numerical and simulation results [168]. Based on this, the unbounded path loss model, which is directly proportional to $d_{ij}^{-\alpha}$, is adopted throughout the thesis. Furthermore, for achieving a wider physical applicability for $d_{ij} < 1$, a bounded path loss model $\min(1, d_{ij}^{-\alpha})$ from (5) of [183] can also be applied to the optimizations in this chapter. One simple way to implement this path loss model is to let any $d_{ij} < 1$ to be one in the different formulations for coverage probability. Besides, (3.15) could still serve as a valid lower bound for non-coherent coverage probability even after changing the path loss model from $d_{ij}^{-\alpha}$ to $\min(1, d_{ij}^{-\alpha})$, which can be explained as follows:

Compared to the unbounded path loss model $d_{ij}^{-\alpha}$, the gain for $d_{ij} < 1$ is the only difference in the bounded path loss model $\min(1, d_{ij}^{-\alpha})$. The gain for $d_{ij} < 1$ is larger than 1 in the unbounded path loss model, while the gain for $d_{ij} < 1$ is equal to one in the bounded path loss model. Thus, less interference from clusters of interferers to receiver j is obtained when using bounded path loss model rather than the unbounded one. As a result, the Laplace transform of the inter-cluster interference based on the bounded path loss model would be larger than the unbounded one, where the latter is lower bounded by (3.15).

Chapter 4

Route Selection Based on Coverage-Delay-Trust in Public Safety Networks

Following the last chapter on the performance improvement over a single-hop device-to-device (D2D) communications paradigm, this chapter moves onto a paradigm based on mission-critical communications (MCC) systems which require multi-hop D2D communications to enhance the ever-growing demand for network coverage further. MCC systems have emerged as one of the key elements of the new 5G build-out for public safety networks. Focusing on the end-to-end reliable transmission in MCC systems, this chapter proposes a route selection method based on coverage, delay, and trust probabilistic models. To begin with, the coverage probability between a pair of user equipments (UEs) in the presence of interference from other MCC groups has been analyzed. Then, the timeliness probability studies the level of confidence for the delay requirement. In addition, the trust probability is formulated based on a beta distribution function to prevent potential attacks from malicious nodes and ensure secure interactions among the forwarding UEs. By combining the three probabilistic models in a way to meet the given requirements of the MCC system, the optimal route selection method based on Dijkstra's algorithm is investigated. Simulation results validate the proposed models and theoretical analysis. The methods presented herein provide useful insight into designing MCC systems for 5G public safety and disaster relief networks.

4.1 Introduction

4.1.1 Background

As introduced in the 3rd Generation Partnership Project (3GPP) *Release 13*, mission-critical push-to-talk (MCPTT) provides an enhanced arbitrated method by which two or more users can engage in mission-critical group communications based upon 3GPP evolved packet system (EPS) services [184]. Floor control allows mission-critical group communications to regulate the access to shared channels and arbitrate transmission request contentions. When multiple requests occur, one UE is guaranteed to talk (i.e., take the floor) while others are either rejected or queued based on the priorities of the users in contention. Overriding the current talker by a higher priority user and imposing a limitation of talk time promote the chances for other users to use the service. Further development of MCC in mission-critical video and mission-critical data creates an opportunity to reuse base functionality documented in the stage one requirements for MCPTT [185] and enables the first responders to go far beyond basic push-to-talk with new features such as group chat, file sharing, location sharing and much more. Although the mission-critical service in the long-term evolution (LTE) or future 5G standards will be primarily targeting public service agencies (PSAs), i.e., police, fire brigade, and ambulance, it is still capable of general commercial applications for other industries and service departments such as utility companies and railway stations.

In general, users from different mission-critical organizations communicate in separate groups for different tasks by using their MCC UEs. In many practical off-network scenarios, responders are dispatched to investigate an area that is far away from their affiliated group. To report the situations back to this group in the formats of text messages, recorded voice, video clips or other types of data, the leading UEs from nearby groups can cooperate to forward the messages in an ad hoc fashion [81, 186, 187]. To yield a reliable and secure path, the models related to coverage, delay, and trust need to be addressed for route selection.

4.1.2 Related Work

Network coverage is an essential requirement to guarantee reliable communications among UEs. The coverage probability or the outage probability has been used to characterize the point-to-point link quality under the fading channel statistically. The outage probability for a cooperative relay network in the presence of inter-cell interference was analyzed in [170]. The probability of full connectivity of high density random networks in confined geometries was developed in [188]. The use of D2D relays as a disaster relief solution and the network performance were studied in [30]. In [189], a systematic cooperative routing scheme named Constructive-Relay-based CooPerative Routing (CRCPR) was proposed to provide greater robustness against node mobility-induced link breaks. In the meantime, geographical constraints [134] and some task properties such as rescue missions inside houses on fire could make the group communications exhibit clustering behavior. The interference and outage in clustered wireless ad hoc networks modeled by Matérn cluster and modified Thomas cluster processes were studied in [134]. The performance of modified Thomas clusters in D2D networks based on the distance probability density function (PDF) was analyzed in [141]. The joint coverage enhancement based on Matérn clusters and modified Thomas clusters was addressed in last chapter. In [62], a communication-aware route selection strategy was proposed to yield high throughput for ongoing data transmissions. However, it did not consider the clustering behavior of group communications. Furthermore, the quality of inter-cluster communications in MCC networks depends on the call activities of UEs within each cluster, and the call activities through limited channel resources could cause delays. Therefore, the coverage analysis should be linked to the delay modeling to obtain more accurate results.

During route selection, the forwarding UEs with lowest delays in meeting transmission requests are desired. The queuing mechanism for utilizing the shared resource blocks in the mission-critical group communications decides that the service for forwarding the messages is not always immediately available. Consequently, the guaranteed deadline requirement from classic real-time systems is infeasible and a timeliness probabilistic model is proposed to capture the level of confidence for the delay requirement [190]. The *timeliness probability* is defined to be the probability that a transmission request needs to wait for at most a given time threshold τ until the resource blocks become available. To study the transmission request delay in each cluster head for message forwarding, trunking theory is used. Two major classes of trunking radio systems named lost call cleared (LCC) and lost call delayed (LCD) systems were studied in [191]. The former does not provide a queue for requests. The latter allows a transmission request to the queue, in a buffer, and waits until a server is available, which fits the flow control for MCPPT services. Meanwhile, a probabilistic metric was proposed in [190], where Gaussian distribution was used to approximate the distribution of end-to-end delay. The interflow and intraflow interferences have been considered in [192] to reduce packet losses and retransmissions for shorter delay.

Secure message delivery is very crucial to the mission-critical service since nodes may not cooperate or may act maliciously towards the message forwarding, which can cause the message to be lost or corrupted. Secure sockets layer (SSL) and some other traditional cryptographic tools attach a message authentication code to the transmitted data so that the UE at the destination can detect the malicious behaviors of forwarding UEs such as data tampering [193]. However, by using SSL alone, it is still very challenging for the UE at the destination to locate the malicious forwarding UEs along a multi-hop path and report them back to the source via a different path where the behaviors of the UEs along this new path also need to be confirmed. Hence, to determine whether a neighboring node will assist to forward the messages in a timely manner, trust establishment schemes have been proposed [193, 194]. Trust exploits the fact that a source UE can monitor the forwarding operation of the neighboring UEs due to the broadcast nature of radio. Based on an accumulated number of observations on whether each time the forwarding is successful, the source UE can choose to trust one neighboring UE in the future forwarding operations. Given the number of observations on the forwarding operations over a link, the trust probability of a link can be formulated based on a beta distribution function, which has been actively used in Bayesian inference [195]. For example, an early study on trust establishment in a mobile ad hoc network was conducted in [196], where the forwarded packet was buffered and checked with the original message for a match. Besides, a passive monitoring of forwarded data traffic to estimate the behavior of a node without buffer was proposed in [194]. Furthermore, proximity-based trust and experience-based trust modeling in random wireless networks were proposed in [197]. In addition, the selective packet drop behavior in the selfish relay has been studied in [198] for route selection where the effects of coverage and delay are ignored.

4.1.3 Contributions

To the best of the author's knowledge, the work discussed herein is the first to study the route selection method based on *coverage, timeliness*, and *trust* probabilities for mission-critical group communications. The contributions of the chapter are:

1. The coverage probability among the UEs in an MCC system in the presence of the interference coming from other MCC clusters is characterized. The interference is explicitly characterized based on the delay modeling. Therefore, the interplay between stochastic geometry and queuing theory is addressed.

2. The robust trust probability, which considers the confidence of the trust as a result of the number of iterations in a beta reputation system, is proposed.

3. A route selection method that considers the coverage, timeliness, and trust probabilities simultaneously is proposed for an MCC public safety network.

The proposed route selection method could provide a useful guideline to design the MCC system for 5G public safety and disaster relief networks.

The rest of the chapter is structured as follows: Table 4.1 gives the notation and symbols which are used throughout the chapter. Section 4.2 begins with a description of the system model and addresses the probabilistic models for coverage, delay, and trust of a given link. Section 4.3 focuses on the route selection based on the three probabilistic models mentioned above. Section 4.4 gives the simulation results and discussion, and Section 4.5 concludes the chapter.

4.2 System Model

4.2.1 Network Layout

As shown in Figure 4.1, K MCC groups are randomly distributed on the plane. This research focuses on choosing a path to forward messages from one MCC group to another in a mission-critical public safety network working in the off-network mode. Each group is assumed to form a cluster with radius R, and there are m_i members and one group leader within cluster i. The group leader is fixed at the cluster center, and the group members are uniformly distributed within the cluster. The group leaders'

Table 4.1: Notation and Symbols © 2019 IEEE

Symbol	Description
R	Radius of a cluster
λ_{u_i}	Mean call rate per user in cluster i
τ_{hold}	Average call holding time of a user
P_d	Transmit power of each UE
G_e	Gain due to coding and antennas
I_j	Interference measured at UE j
P_{kj}	Received power at UE j from UE k
d_{kj}	Pairwise distance between UEs k and j
η	Path loss exponent
$\|h_{kj}\|^2$	Instant power of Rayleigh fading
E_k	Event: the head transmits in active cluster k
$\overline{\mathrm{E}}_k$	Event: a member transmits in active cluster k
$\mathcal{L}_I^h(s \mid a_{kj})$	Laplace transform of the interference from heads k to j given E_k
$\mathbb{P}\{\cdot\}$	Probability of an event
Q_i	Event: a call is delayed in cluster i
$\mathbb{P}\{Q_k\}$	Probability of queuing in cluster k
ζ	Signal-to-interference-plus-noise ratio (SINR) threshold
H_{ij}	Coverage probability from cluster heads i to j
C	Indices of all clusters
A_i	Traffic intensity
μ	Mean service rate
N	Number of servers
W_i	Delay of a user in cluster i
τ	Delay threshold in a cluster
D_j, D_{ij}	Timeliness probability from cluster heads i to j
$\alpha_{ij} - 1$	Number of successful interactions from heads i to j
$\beta_{ij} - 1$	Number of failed interactions from heads i to j
θ_{ij}	Probability of successful interactions
T_{ij}^{mean}	Mean trust probability from cluster heads i to j
$\mathcal{O}$	Observed interactions between heads i and j
c	Confidence interval of θ_{ij}
T_{ij}^{robust}	Robust trust probability from cluster heads i to j
$\mathbf{H}/\mathbf{D}/\mathbf{T}$	Probability matrices of coverage/timeliness/trust
$H_t/D_t/T_t$	Thresholds of coverage/timeliness/trust
$\mathbf{R}$	Link cost matrix
J	End-to-end path
$p_{H_J}/p_{D_J}/p_{T_J}$	End-to-end coverage/timeliness/trust probability of J
l_i	Index of forwarding cluster head i

UEs work as cluster heads, and they are capable of forwarding messages from one group to another. The spatial distribution of UEs during each hop is assumed to be mutually independent. As discussed in the previous chapter and other works, this work assumes the channel reuse throughout the clusters is unity due to the aggressive reuse of frequency channels for high spectrum utilization in different wireless systems, and multi-hop wireless networks are no exception [199]. The transmit power of each UE is P_d. The gain due to coding, the transmitting antenna, and the receiving antenna is G_e. All channels are assumed to experience block Rayleigh fading and the channels remain constant over one block but vary independently from one block to another. The corresponding channel gains are independently exponentially distributed with unit mean.

According to the standard in [200], the talker is in charge of the flow arbitration, and the floor request queue will be transferred from the former talking UE to the new talking UE in the off-network mode. The flow control module for each cluster is assumed to use an $M/M/1$ queuing system, where two Ms, in turn, denote the memoryless Poisson distribution of the call requests process and an exponential distribution for the call holding time [191, 201], and the number 1 indicates that a single server exists for the queue because at most one UE within a group is allowed to transmit at a time. The $M/M/1$ queue is one of the canonical queuing models in communication [202]. It assumes that the arrival process and service time distribution are Markovian. This is particularly suitable to model the scenario where all users transmit messages with the highest priority for the best service. As a result, the highest-priority jobs in each cluster naturally form a simple $M/M/1$ system. During the busy time, the call requests from a user in cluster i are assumed to be Poisson distributed with an average rate of λ_{u_i} calls per minute, and a user in any cluster holds a call for τ_{hold} seconds in average. The holding time is assumed to be exponentially distributed [201]. The entire number of users in cluster i is $m_i + 1$, and $(m_i + 1)\lambda_{u_i}$

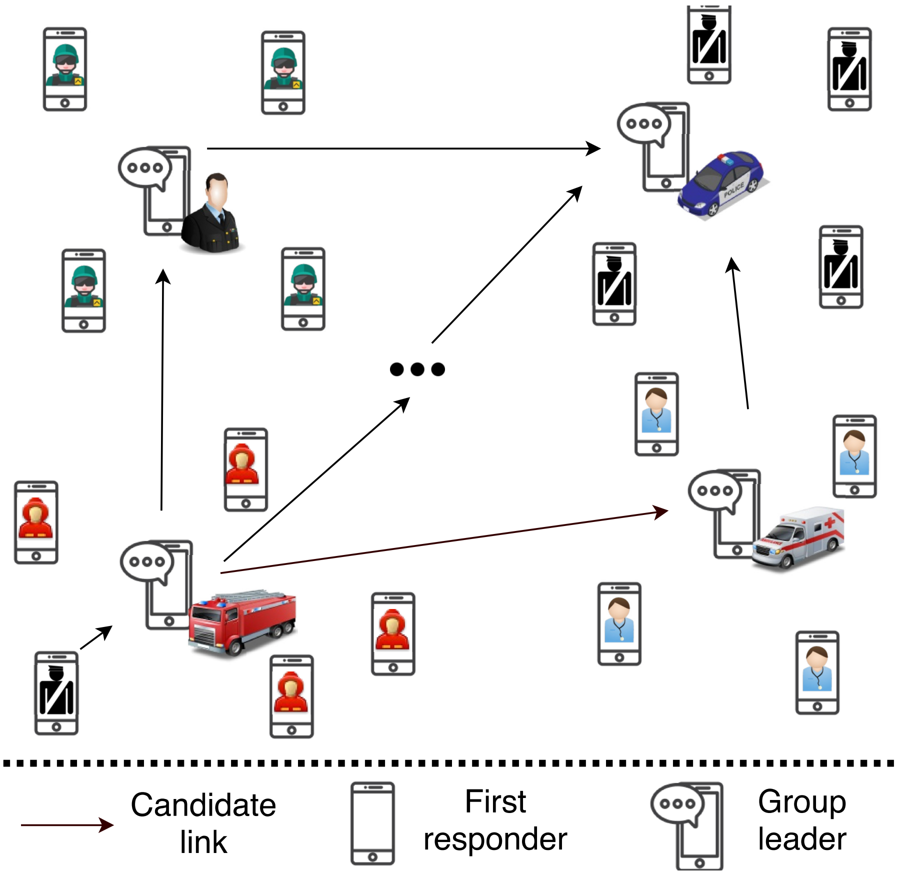

Figure 4.1: A mission-critical public safety scenario. © 2019 IEEE.

is the total mean call arrival rate.

4.2.2 Coverage Modeling

The coverage is a study of the link performance in the presence of path loss, multipath fading, interference, and noise. By taking coverage into consideration, a path with qualified link performance will be used for route selection.

4.2.2.1 Signal-to-Interference-plus-Noise Ratio (SINR)

The UE receiver captures not only the signal but also the interference from the UEs who are transmitting simultaneously [171]. The total interference power measured at a receiving UE j is given by

$$I_j = \sum_{k \in L} P_{kj} = \sum_{k \in L} G_e \ell(d_{kj}) |h_{kj}|^2 P_d \tag{4.1}$$

where L denotes the set of interferers; P_{kj} is the received interference power at UE j from the UE $k \in L$; $\ell(d_{kj}) = (\lambda/4\pi)^2 d_{kj}^{-\eta}$, where λ represents the carrier wavelength, d_{kj} is the pairwise distance between UEs k and j, and η is the path loss exponent; $|h_{kj}|^2$ is the instantaneous power of Rayleigh fading. The SINR at UE j while transmitting from UE i is given by

$$\mathrm{SINR}_{ij} = \frac{P_{ij}}{N_0 + I_j} \tag{4.2}$$

where N_0 is the additive white Gaussian noise (AWGN) power at each UE. Next, the average interference based on the spatial distributions of the simultaneous transmitting UEs within the clusters is characterized.

4.2.2.2 Interference from One Cluster

According to the floor control in the mission-critical group communications, the UEs of a cluster work in a delay-and-served manner so that at most one UE is transmitting on the shared resource blocks. For simplicity of notation, let the cluster and the cluster head inside have the same index. Given that a cluster k is active when a UE within is transmitting, let E_k denote the event that cluster head k is transmitting and $\overline{\mathrm{E}}_k$ denote the event that a cluster member of k is transmitting. The Laplace transform of the interference from cluster heads k to j given E_k is written as

$$\mathcal{L}_I^h(s \mid a_{kj}) = \frac{1}{1 + sG_e \ell(a_{kj}) P_d} \tag{4.3}$$

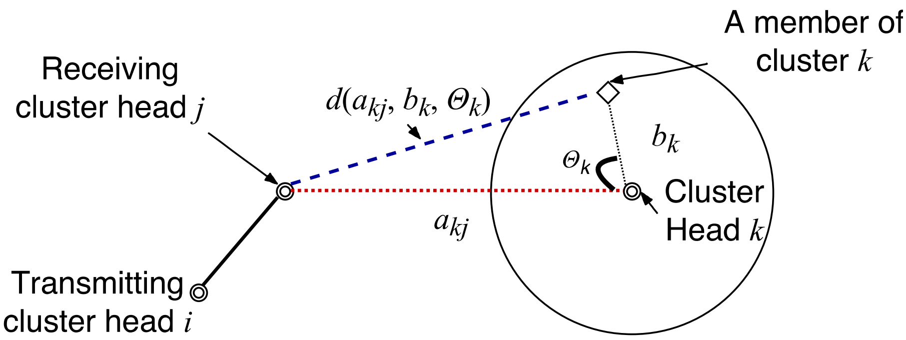

Figure 4.2: The interference is coming from the head or member of cluster k when cluster head i is transmitting a message to cluster head j. © 2019 IEEE.

where a_{kj} is the distance between cluster heads k and j as shown in Figure 4.2. When the members of cluster k need to transmit, at most one UE is active. Hence, the Laplace transform of the interference from a member, which is uniformly distributed in cluster k, to the head of cluster j given $\overline{\mathrm{E}}_k$ is written as

$$\mathcal{L}_I^m(s \mid a_{kj}) = \int_0^R \int_0^{2\pi} \frac{1}{1 + sGd(a_{kj}, b_k, \theta_k)^{-\eta}} \frac{b_k}{\pi R^2} \mathrm{d}b_k \mathrm{d}\theta_k \tag{4.4}$$

where $d(a_{kj}, b_k, \theta_k) = \sqrt{a_{kj}^2 + b_k^2 - 2a_{kj}b_k \cos\theta_k}$ is the distance between a member of cluster k and the head of cluster j by using the Law of Cosines as shown in Figure 4.2, and b_k is the distance between cluster head k and a possible location of a member of cluster k, and $G = G_e P_d(\lambda/4\pi)^2$.

A closed-form expression for (4.3) exists for $\eta = 2$, which is given by

$$\begin{aligned}\mathcal{L}_I^m(s \mid a_{kj}) =& 1 + \frac{Gs}{R^2}\Bigg(\ln(2Gs) - \ln\Bigg(Gs + R^2 - a_{kj}^2 + \\ & \sqrt{(Gs + (R - a_{kj})^2)(Gs + (R + a_{kj})^2)}\Bigg)\Bigg).\end{aligned} \tag{4.5}$$

For $\eta > 2$, instead of using (4.4), $\mathcal{L}_I^m(s \mid a_{kj})$ can also be obtained by numerically evaluating a single integral, which is written as

$$\mathcal{L}_I^m(s \mid a_{kj}) = \int_{a_{kj}-R}^{a_{kj}+R} \frac{f_{R_d}(x \mid a_{kj})}{1 + sGx^{-\eta}} \mathrm{d}x \tag{4.6}$$

where $f_{R_d}(r_d \mid R_y)$ is the conditional distance PDF of a Matérn cluster in (3.10). The Laplace transform of the interference from cluster k to head j is written as

$$\mathcal{L}_I(s \mid a_{kj}) = \mathbb{P}\{Q_k\}\left[\mathcal{L}_I^h(s \mid a_{kj})\mathbb{P}\{\mathrm{E}_k\} + \mathcal{L}_I^m(s \mid a_{kj})\mathbb{P}\{\overline{\mathrm{E}}_k\}\right] + \mathbb{P}\{\overline{Q}_k\} \tag{4.7}$$

where $\mathbb{P}\{\cdot\}$ denotes the probability of an event. Assuming that the head and members of cluster k statistically have equal opportunities to access the resource blocks, $\mathbb{P}\{\mathrm{E}_k\} = 1/(1+m_k)$. $\mathbb{P}\{Q_k\}$ is the probability of queuing since the resource blocks have already been occupied by another UE when a UE requests its transmission. A detailed discussion of the probability of queuing is given in Section 4.2.3.2. Therefore, the Laplace transform of the interference in (4.7) considers both the spatial distributions and transmission activities of UEs within clusters, and it is used to characterize the coverage probability as discussed below.

4.2.2.3 Coverage Probability

The coverage probability of a link is the likelihood that the SINR of the link is higher than a predetermined threshold $\zeta = 2^t - 1$ with link spectrum efficiency t [1]. The coverage probability from cluster heads i to j, can be written as

$$\begin{aligned} H_{ij} =& \mathbb{P}\{\mathrm{SINR}_{ij} > \zeta\} \\ =& \exp\left(-\frac{\zeta \mathrm{N}_0}{g(d_{ij})}\right) \prod_{k \in C \setminus i,j} \mathcal{L}_I\left(\frac{\zeta}{g(d_{ij})} \,\middle|\, a_{kj}\right) \end{aligned} \tag{4.8}$$

[1] Note that a coefficient 0.5 on the link capacity due to the half-duplex constraint is assumed to be implicitly absorbed in the target spectrum efficiency t.

where C denotes the indices of all clusters.

According to (4.7), the number of UEs and their transmission requests within a cluster will affect the amount of interference to other links; consequently, this will affect the coverage probability given by (4.8). Meanwhile, the request to transmit a message will be queued if the resource blocks are not immediately available. Therefore, it is of great importance to study the delay in an MCC network for route selection.

4.2.3 Delay Modeling

4.2.3.1 Lost Call Delayed (LCD) System

The flow control in mission-critical group communications can be modeled as an LCD system where the incoming transmission request is held in a queue until an in-progress transmission terminates and the resources blocks become free [191]. The probability of queuing is used to characterize the likelihood that the resources blocks are already in use when a new call request happens. If no resource blocks are immediately available after a call request to a cluster, it will be helpful to know the level of confidence that this call can be served within τ seconds.

4.2.3.2 Probability of Queuing

Let Q_i denote the event that a call request needs to queue because all servers are busy in cluster i. The probability of queuing in cluster i is given by the Erlang C formula as follows:

$$\mathbb{P}\{Q_i\} = \frac{\frac{A_i^N}{N!}\frac{N}{N-A_i}}{\sum_{n=0}^{N-1}\frac{A_i^n}{n!} + \frac{A_i^N}{N!}\frac{N}{N-A_i}} \tag{4.9}$$

where $A_i = (m_i + 1)\lambda_{u_i}/\mu$ is the traffic intensity, $\mu = 1/\tau_{hold}$ is the mean service rate, and τ_{hold} is the average duration of a call; N is the number of servers. The condition $0 < A_i < 1$ is required so that the system is stable; otherwise, it would result in a queue which grows without bound. For MCC group communications, the resource blocks are utilized by a UE per unit time. Therefore, the probability of queuing for the $M/M/1$ system can be derived from the Erlang C formula for one server, i.e., $N = 1$, which is given by $\mathbb{P}\{Q_i\} = A_i$, and (4.7) can be further expanded as

$$\mathcal{L}_I(s \mid a_{kj}) = A_i \left[\frac{\mathcal{L}_I^h(s \mid a_{kj})}{1 + m_i} + \frac{m_i \mathcal{L}_I^m(s \mid a_{kj})}{1 + m_i} \right] + 1 - A_i. \tag{4.10}$$

4.2.3.3 Timeliness Probability

Meanwhile, if no resource blocks are immediately available, the call will be delayed. In steady-state, the delay time for a call request in the queue obeys the exponential distribution [201]. Let the random variable W_i denote the delay of a user in cluster i; the probability of a call waiting for more than τ seconds in the queue is given by

$$\mathbb{P}\{W_i > \tau \mid Q_i\} = e^{-\frac{N - A_i}{\tau_{hold}}\tau} = e^{-\frac{1 - A_i}{\tau_{hold}}\tau} \tag{4.11}$$

where τ is the delay time of interest. Hence, the timeliness probability that a caller in cluster i needs to wait for at most τ seconds to be served in cluster is given by

$$\begin{aligned} D_i &= \mathbb{P}\{W_i \leq \tau\} \\ &= 1 - \mathbb{P}\{W_i > \tau \mid Q_i\}\mathbb{P}\{Q_i\} - \mathbb{P}\{W_i > \tau \mid \overline{Q}_i\}\mathbb{P}\{\overline{Q}_i\} \\ &= 1 - \mathbb{P}\{W_i > \tau \mid Q_i\}\mathbb{P}\{Q_i\} \\ &= 1 - A_i e^{-\frac{1 - A_i}{\tau_{hold}}\tau}. \end{aligned} \tag{4.12}$$

Thus, the timeliness probability from cluster heads i to j is defined as D_{ij}, which equals to D_j. Apparently, if the selected threshold τ is 0, the timeliness probability will be solely decided by $1 - A_i$, which is a linear function of m_i. Figure 4.3 gives the timeliness probabilities in cluster i under different values of the delay threshold τ and the average number of calls per unit time λ_{u_i}. It is also clear that as the number of

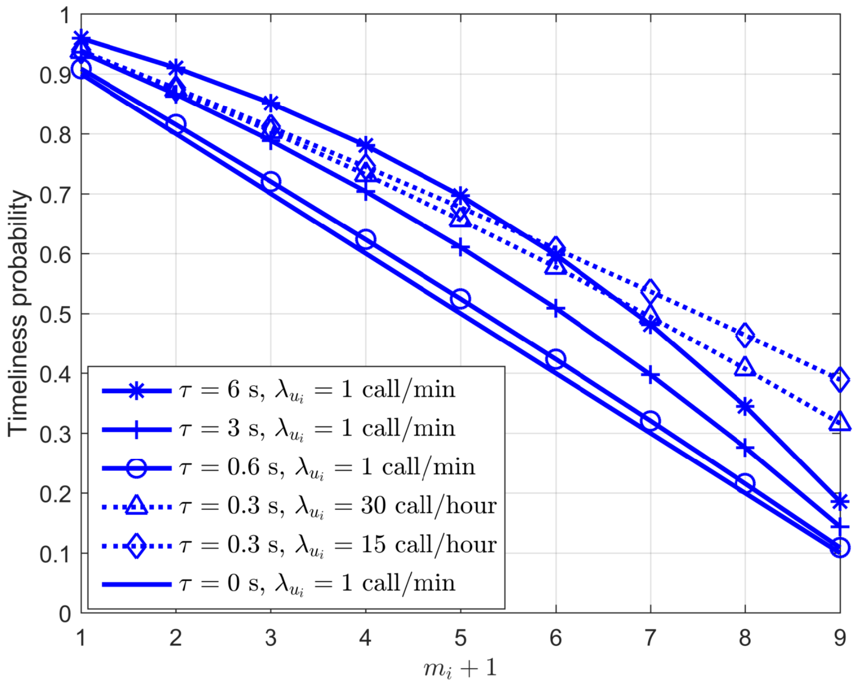

Figure 4.3: The timeliness probability of cluster i under different parameters, and $\tau_{hold} = 6$ s. © 2019 IEEE.

users increases, the timeliness probability drops heavily. The timeliness probability can be increased by either increasing τ or decreasing λ_{u_i}.

4.2.4 Trust Modeling

Due to the broadcast nature of the wireless medium, a node can collect its message forwarded by a neighbor node by snooping all received frames at the medium access control (MAC) layer and checking the integrity of the message [203]. Trust is defined as a value within $[0, 1]$, which measures the degree of belief that its neighbor node can be trusted to forward the message in the next operation based on the node's behaviors observed in the past. It describes the reliability of message forwarding carried out by nodes [203, 204], and reliability is defined as the probability that a given item will perform its intended function with no failures for a given time under a given set of conditions [205]. The reliability of message forwarding over multi-hop

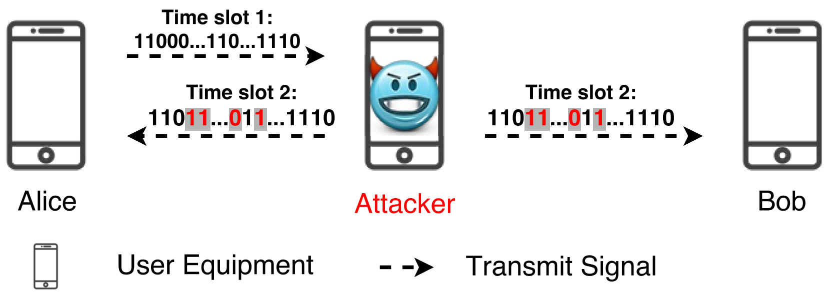

Figure 4.4: Data tampering attack by the forwarding UE. © 2019 IEEE.

routes could be affected by malicious nodes. As shown in Figure 4.4, an attacker or a misbehaving node can modify the messages while it is forwarding. Besides, a selfish node could selectively drop a message [198] due to its limited resources or malicious intention. These behaviors would create confusion and misjudgement at the receiver. As a result of the above, it would be useful to evaluate the trust of a forwarding node based on its past forwarding operations and obtain the degree of belief that a node is reliable with respect to next message forwarding[2]. To rate the trustworthiness of a link, the beta reputation system is adopted to the binary rating on whether each message forwarding operation, a.k.a. interaction, is deemed to be successful or not based on the integrity of the message.

4.2.4.1 Beta Reputation System and Mean Trust Probability

The expressions for the posterior probability estimation of binary events can be represented as beta distribution functions [195]. For completeness, the preliminary results of beta reputation are given in Appendix 4.A. Let $\alpha_{ij} - 1$ denote the number of previously successful direct forwarding operations from cluster heads i to j, while $\beta_{ij} - 1$ denotes the number of previously failed operations. The PDF of observing the

[2]An important limitation of trust is that it could not be applied to some stringent environments, where a node should be redeemed as completely unreliable as long as a malicious behavior is observed.

successful message forwarding in the next operation is given by

$$f(\theta_{ij} \mid \alpha_{ij}, \beta_{ij}) = \frac{{\theta_{ij}}^{\alpha_{ij}-1}(1-\theta_{ij})^{\beta_{ij}-1}}{\mathrm{Beta}(\alpha_{ij}, \beta_{ij})} \tag{4.13}$$

where

$$\mathrm{Beta}(\alpha_{ij}, \beta_{ij}) = \frac{\Gamma(\alpha_{ij})\Gamma(\beta_{ij})}{\Gamma(\alpha_{ij}+\beta_{ij})}. \tag{4.14}$$

The parameter $\theta_{ij} \in [0, 1]$ denotes the probability of observing successful forwarding operations in the next operation; the shape parameters satisfy $\alpha_{ij}, \beta_{ij} > 0$, and $\Gamma(n) = (n-1)!$ for $n \in \mathbb{N}$. The *mean trust probability* from cluster heads i to j is the expectation value of the reputation function, which is written as

$$T_{ij}^{\mathrm{mean}} = \mathrm{E}[\theta_{ij} \mid \mathcal{O}] = \frac{\alpha_{ij}}{\alpha_{ij}+\beta_{ij}} \tag{4.15}$$

where $\mathcal{O}$ denotes the information about the observed interactions between cluster heads i and j until now. When the number of interactions is very large, T_{ij}^{mean} is the accurate mean trust probability.

4.2.4.2 Confidence of Trust and Robust Trust Probability

In an MCC network, two cluster heads may have very few interactions due to lack of forwarding interest, early stage of a network running, and network topology changes. Thus, adequate observations are missing to calculate the accurate mean trust probability. The confidence intervals of trust can be used to infer the robustness of the trust from a limited number of observations. Intuitively, a confidence level describes an interval where the data will lie with strong confidence. This is important because consequential decisions can be made based on uncertain results. Depending on classical and Bayesian statistics, there are two definitions for the confidence interval [206]: In classical sampling theory, an estimated parameter has a somewhat true fixed value.

Then, the confident interval can be stated as that $c \times 100\%$ of samples will give a pair of confidence limits (i.e., upper and lower bounds of a confidence interval), which include the true fixed value of the estimated parameter. In particular, it is often the case in reliability forecasting that only a lower bound is of interest [207]. Meanwhile, for Bayesian models, a confidence interval c of a random variable θ makes sure that θ will lie in a probability range with $c \times 100\%$ certainty. With limited prior information, the fundamental difference between these two definitions is of little consequence.

Based on above discussion, a confidence interval c of θ_{ij} makes sure that the θ_{ij} will lie in a probability range with $c \times 100\%$ certainty. Since the Bayesian-based definition provides more satisfactory behavior even when evaluating a confidence interval for data in small to intermediate size [208], and the trust model was formulated under the Bayesian framework, the confidence intervals based on the Bayesian framework are sought. Consequently, the quantiles at a nominal confidence level of c are given by

$$\int_0^{T_{ij}^{\text{lower}}} f(p \mid \alpha_{ij}, \beta_{ij})\,\mathrm{d}p = \frac{1-c}{2}, \text{ and } \int_{T_{ij}^{\text{upper}}}^1 f(p \mid \alpha_{ij}, \beta_{ij})\,\mathrm{d}p = \frac{1-c}{2} \tag{4.16}$$

where $T_{ij}^{\text{lower}}, T_{ij}^{\text{upper}}$ are the lower and upper bounds of an equal-tailed interval for p. Thus, the Bayesian-based lower confidence bound for θ_{ij} is given by

$$T_{ij}^{\text{lower}} = \text{Beta}^{-1}\left(\frac{1-c}{2}; \alpha_{ij}, \beta_{ij}\right) \tag{4.17}$$

where $\text{Beta}^{-1}(\text{c}; \text{a}, \text{b})$ is the cth quantile function of a beta distribution, i.e., a beta inverse cumulative distribution function, with shape parameters a and b. Compared with traditional confidence interval estimators such as the normal approximation and the Clopper & Pearson approach [209], the Bayesian confidence technique is more capable of providing a mean level of coverage close to the nominal level even for a small-to-intermediate number of interactions [208][3]. Since the accurate mean trust probability is greater than or equal to T_{ij}^{lower} for a given confidence interval c, T_{ij}^{lower} is defined as the *robust trust probability* T_{ij}^{robust}. As a result of the above discussion, two trust probabilities, namely, mean and robust trust probabilities, have been formulated. The latter considers the uncertainty in the proportion of successful interactions in a small number of observations.

Figure 4.5 gives the confidence of the trust under a different number of forwarding operations. It is clear that although the mean trust probabilities are the same, the robust trust probabilities vary. Thus, the robust trust probabilities can help to differentiate the links with the same mean trust probabilities. Meanwhile, robust trust can also give different ranking results when the mean trust probabilities are not the same. For example, comparing $(\alpha_{1,5} = 13, \beta_{1,5} = 4)$ with $(\alpha_{1,6} = 21, \beta_{1,6} = 7)$, $T_{1,5}^{\text{mean}} = 0.7647 > T_{1,6}^{\text{mean}} = 0.75$. But $T_{1,5}^{\text{robust}} = 0.5435 < T_{1,6}^{\text{robust}} = 0.5774$, which implies that the link from cluster heads 1 to 6 is more robust than the link from cluster heads 1 to 5 in terms of trust even though the latter has a better mean trust probability.

4.3 Route Selection

In this section, a route selection method is considered where the selection process explicitly takes into account the coverage, delay, and trust of an MCC network. The coverage, timeliness, and trust probabilities of each link are assumed to be exchanged among the cluster heads by a table-driven routing protocol [210]. The cryptographic primitives are used to authenticate and protect the integrity of the data [196]. In many multi-criteria route selection algorithms, the criteria are normally weighted and mapped to the costs of the links. Although the measurements of the coverage,

[3]As the CPUs in UEs become powerful, the computation time of the above bounds is trivial. Meanwhile, normal approximation and the Clopper & Pearson approach will be good candidates if a comparatively small level of accuracy is acceptable for route selection.

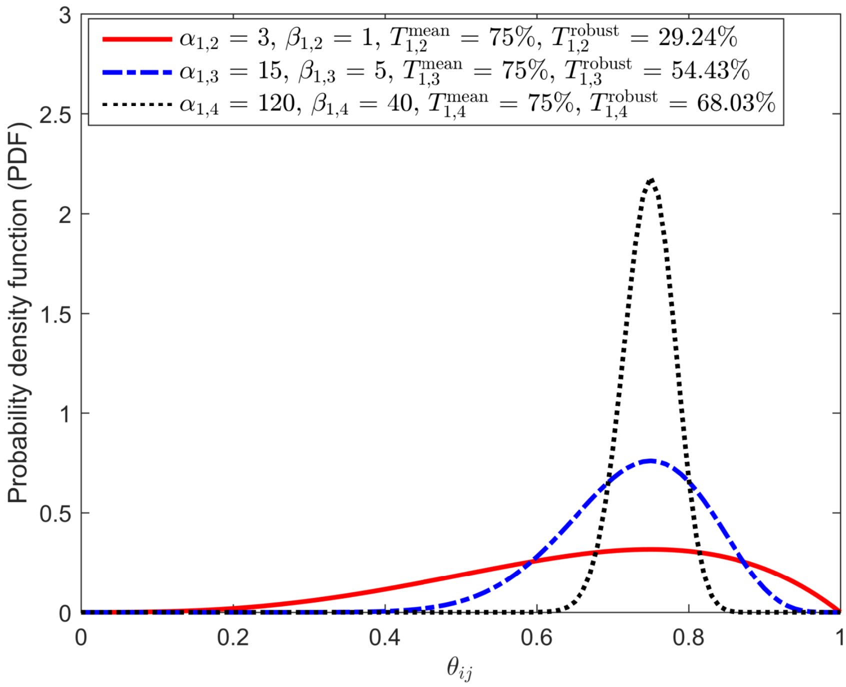

Figure 4.5: The distribution of observing successful forwarding in the next operation after the observations so far given by $(\alpha_{ij}, \beta_{ij})$. © 2019 IEEE.

delay, and trust are all probability values, the distributions of them are different. Hence, it is challenging to find proper weights to the probabilities. To make progress, the following steps are proposed to obtain the link cost for route selection.

Step 1: Based on the exchanged probability values regarding the coverage, timeliness, and trust among the cluster heads, the source cluster head forms three adjacency matrices, which are given by

$$\begin{aligned} \mathbf{H} &= (H_{ij}) \in [0,1]^{K\times K}, \\ \mathbf{D} &= (D_{ij}) \in [0,1]^{K\times K}, \\ \mathbf{T} &= (T_{ij}\ ) \in [0,1]^{K\times K} \end{aligned} \tag{4.18}$$

where each element of the matrices represents the relationships between two links regarding coverage, timeliness, and trust probabilities; the elements on the diagonal of the matrices in (4.18) are set to be one.

Step 2: Define H_t, D_t, and T_t as the thresholds of the coverage, timeliness, and trust probabilities, respectively. To define the thresholds that are appropriate to the environment, a general guideline is given as follows for reference: Firstly, the threshold H_t can be calculated based on the pairwise coverage probability in (4.8) with the exchanged information on clusters and their locations. Among the calculated coverage probabilities, the threshold is chosen such that a predefined maximum percentage $p_1 \times 100\%$ of the pairwise coverage probabilities scores above that threshold. Suppose there are N_H number of pairwise coverage probabilities available, and a maximum p_1 of them are allowed for route selection, let vector $\mathbf{a}$ denote the pairwise coverage probabilities in descending order with indices from 1 to N_H, then the threshold $H_t = \mathbf{a}(\lfloor p_1 N_H \rfloor)$, where $\lfloor \cdot \rfloor$ denotes floor function and $p_1 > 0$. Secondly, the threshold D_t can be obtained by (4.12), where the average duration of a call τ_{hold} is achieved by previous experience. Meanwhile, the method used to calculate H_t can be used to obtain D_t based on the timeliness probabilities of all forwarding nodes. Finally, the threshold T_t can be given by (4.17) with the anticipated interactive results on trust that is controlled by risk assessment. For example, the work in [211] gives four behavior levels for a node, namely malicious, suspect, abnormal, and normal, for the trust probabilities within $[0, 0.3)$, $[0.3, 0.5)$, $[0.5, 0.8)$, $[0.8, 1]$, respectively. They can be used for risk assessment so that any node with a trust probability less than a chosen lower bound of a behavior level will not be accepted as the candidate for forwarding messages. Furthermore, the method used to calculate H_t can be used to obtain T_t. A criterion from the coverage, delay, and trust is specified as the basic criterion for route selection, and the route selection is also constrained by the thresholds of the other two criteria.

Step 3: For the route selection strategy based on coverage, the following requirements must be satisfied: If $T_{ij} > T_t$ and $D_{ij} > D_t$, the cost of the directional link i, j will be H_{ij}; otherwise, the cost is zero. The resultant adjacency matrix for the cost of links is given by

$$\mathbf{R} = (R_{ij}) \in [0,1]^{K \times K} \tag{4.19}$$

where

$$R_{ij} = \begin{cases} H_{ij}, & T_{ij} > T_t \text{ and } D_{ij} > D_t \\ 0, & \text{otherwise.} \end{cases} \tag{4.20}$$

The similar method will apply to delay or trust if either of those metrics is the basic criterion for route selection.

Afterwards, the goal is to find a path with the maximum end-to-end probabilities. For a given path $J = \{l_1, l_2, ..., l_n\}$, l_1 is the index of the source forwarding UE, and l_n is the index of the final (destination) forwarding UE; n is the number of forwarding UEs involved, and $n \geq 2$. The end-to-end probability of a path is the product of every independent probability of the links consisting of the path. The end-to-end coverage, timeliness, and trust probabilities of the path J are respectively defined as

$$p_{H_J} = \prod_{i=1}^{n-1} H_{l_i l_{i+1}},\ p_{D_J} = \prod_{i=1}^{n-1} D_{l_i l_{i+1}}, \text{ and } p_{T_J} = \prod_{i=1}^{n-1} T_{l_i l_{i+1}}. \tag{4.21}$$

The probability p_{H_J} characterizes the performance for decode-and-forward based multi-hop relays, where the instantaneous data rate is the minimum rate between the $n-1$ hops [199, 212]. As a result, the hop with the lowest SINR creates a performance bottleneck.

Many route selection algorithms have been proposed to find the shortest path [201]. Among these algorithms, Dijkstra's algorithm is designed to find a path with the minimum sum of link costs. The Dijkstra's algorithm was originally designed for finding the shortest paths from the source to *all nodes*, and such search is as computationally expensive as finding the shortest path from the source to the *destination node* [213]. To find a path with the maximum multiplication of probabilities with the Dijkstra's algorithm, $-\log \mathbf{R}$ with the indices of source and destination cluster heads are the inputs to Dijkstra's algorithm. The steps of the route selection method and the Dijkstra's algorithm are summarized in Algorithms 3 and 4, respectively.

Algorithm 3: The steps of the route selection method.

```
Data: H, D, T, H_t, D_t, T_t, l_1, and l_n.
Result: Path J.
if Coverage-based then
    R = H;
    for i, j = 0 → K do
        if T_ij ≤ T_t or D_ij ≤ D_t then
            R_ij = 0;
        end
    end
else if Delay-based then
    R = D;
    for i, j = 0 → K do
        if T_ij ≤ T_t or H_ij ≤ H_t then
            R_ij = 0;
        end
    end
else
    R = T;
    for i, j = 0 → K do
        if H_ij ≤ H_t or D_ij ≤ D_t then
            R_ij = 0;
        end
    end
end
J = Dijkstra (−log R, l_1, l_n);
```

4.4 Simulations and Discussion

In this section, the simulations are provided to validate the route selection method detailed above. The parameters used in the simulation are given by Table 4.2. The

Algorithm 4: A realization of Dijkstra's algorithm.

1 function J =Dijkstra $(\mathbf{C}, l_s, l_d)$;

Input : $\mathbf{C}$: non-negative adjacency cost matrix;
l_s: index of source; l_d: index of destination.

Output: J: the path with minimum end to end costs.

2 Initialize the set P of all unvisited node indices: $P = \{..., l_s, ..., l_d, ...\}$;

3 Initialize the distance from source to node i: $D_i = -1$ for $i \in P \backslash l_s$, $D_{l_s} = 0$, where value '-1' denoted unknown distance;

4 Initialize the previous node in optimal path from source: $N_i = -1$ for $i \in P$, where value '-1' denoted unknown node.

5 Find j such that $\min_{j \in P \cap \{i | D_i > 0\}} D_j$.

6 If $j == l_d$, go to step 10.

7 $P = P \backslash \{j\}$, i.e., remove $\{j\}$ from P.

8 For any node index $k! = j$: $d = D_j + \mathbf{C}(j, k)$. If $d < D_k$ or $D_k < 0$, then $D_k = d$ and $N_k = j$.

9 Go to step 5.

10 $v = l_d$.

11 If $N_v == -1$ and $v! = l_s$, return the empty path J and stop the algorithm.

12 If $v == -1$, return the ordered path J and stop the algorithm.

13 Put v to the head of the ordered path J.

14 $v = N_v$.

15 Go to step 12.

Table 4.2: System Parameters © 2019 IEEE

Parameter	Value
Area	1 km × 1 km
Transmission bandwidth B	20 MHz
Duplex mode	Half duplex
Thermal noise power density	-174 dBm/Hz
Cluster radius R	155 m
Transmitting power level P_d	11 dBm
Coding gain	0 dB
Transmitting antenna gain	0 dBi
Receiving antenna gain	0 dBi
Transceiver noise figure	9 dB
Link spectrum efficiency	0.06 bit/s/Hz
Carrier frequency	2 GHz
Path loss exponent η	2.7
Waiting threshold per hop τ	100 ms
Number of servers	1
Average holding time	6 seconds
Mean call rate of a user λ_u	1 call/min
Route selection algorithm	Dijkstra's
Simulation iterations	10^4

given link spectrum efficiency and bandwidth offer a target rate of 1.2 megabits per second (Mbps) for group communications. There are 16 MCC clusters deployed on the plane. The cluster 1 at position $(0, 0)$ needs to send the messages to cluster 16 at position $(1000, 1000)$. The rest of the clusters are randomly deployed and could cooperate to forward the messages. For a given snapshot of the randomly deployed clusters, the route selection method is run to get a series of cluster heads for forwarding messages. The coverage, timeliness, and trust probabilities of the links are exchanged among the cluster heads by cryptographic tools [196]. The simulation results are obtained by averaging over 10^4 independent Monte Carlo trials.

Figure 4.6 shows the route selection results for a snapshot of the randomly deployed MCC clusters. The route selection is based on the link coverage probabilities and constrained by T_t and D_t. Table 4.3 gives the coordinates of the cluster heads and the number of cluster members. The selected paths and their end-to-end coverage

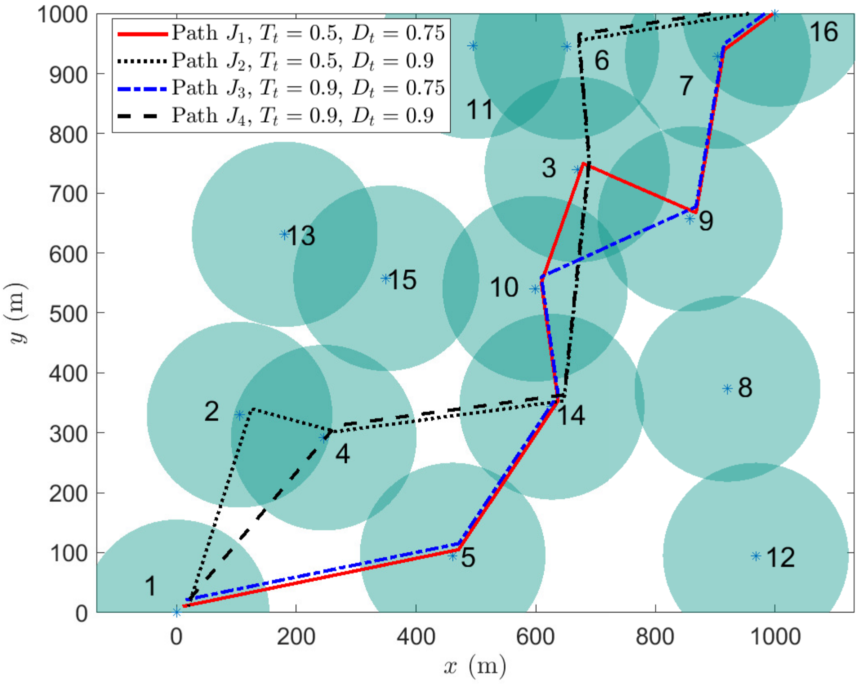

Figure 4.6: The route selection results based on coverage and constrained by T_t and D_t for a snapshot of the randomly deployed MCC clusters. The trust is calculated based on the mean trust probability. © 2019 IEEE.

probabilities are listed as follows:

1) Path $J_1 = \{1, 5, 14, 10, 3, 9, 7, 16\}$, and $p_{H_{J_1}} = 0.953$;

2) Path $J_2 = \{1, 2, 4, 14, 3, 6, 16\}$, and $p_{H_{J_2}} = 0.897$;

3) Path $J_3 = \{1, 5, 14, 10, 9, 7, 16\}$, and $p_{H_{J_3}} = 0.951$;

4) Path $J_4 = \{1, 4, 14, 3, 6, 16\}$, and $p_{H_{J_4}} = 0.892$.

Comparing J_1 with J_2, the higher the threshold D_t, the smaller the end-to-end coverage probability. This is because, as D_t increases, the cluster heads who can form paths with better end-to-end coverage probabilities may not be chosen if the consisting links by the heads could not satisfy a higher timeliness probability threshold. A similar discussion could be applied to J_3 and J_4. J_2 and J_4 which are forking from cluster 1 to clusters 2 and 4 separately imply cluster head 2 does not satisfied $T_t = 0.9$

Table 4.3: Coordinates of Cluster Heads and Number of Cluster Members © 2019 IEEE

Node i	1	2	3	4	5	6	7	8
x (m)	0	105	669	246	461	651	905	920
y (m)	0	330	739	292	95	945	929	373
m_i	1	1	1	1	3	1	3	3
Node i	9	10	11	12	13	14	15	16
x (m)	858	599	495	968	181	627	350	1000
y (m)	657	541	946	95	632	343	558	1000
m_i	3	2	1	1	3	1	2	1

by judging from the fact that $p_{H_{J_2}} > p_{H_{J_4}}$ while the other links of the two paths are established through the same nodes. The same analysis applies to the forking from cluster head 10 to cluster heads 3 and 9 for J_1 and J_3.

Figure 4.7 gives the route selection results for a snapshot of the randomly deployed MCC clusters. The route selection is based on link timeliness probabilities and constrained by T_t and H_t. H_t is set to be larger than $H_{1,16}$ so that there is no direct route from source to destination. Thus, the delay and trust among the forwarding UEs need to be considered. According to (4.12), the delay of the links to cluster i is relying on m_i. The paths and their end-to-end timeliness probabilities are listed as follows:

1) Path $J_1 = \{1, 11, 16\}$, and $p_{D_{J_1}} = 0.828$;

2) Path $J_2 = \{1, 4, 3, 16\}$, and $p_{D_{J_2}} = 0.753$;

3) Path $J_3 = \{1, 2, 15, 6, 16\}$, and $p_{D_{J_3}} = 0.641$;

4) Path $J_4 = \{1, 12, 16\}$, and $p_{D_{J_4}} = 0.828$.

From J_1 to J_3, one can easily see that the end-to-end timeliness probability is decreasing as H_t is increasing. It further implies that if there are several clusters which have the same least number of cluster members and all meet the thresholds requirements for route selection, one route formed by them with the least number of hops

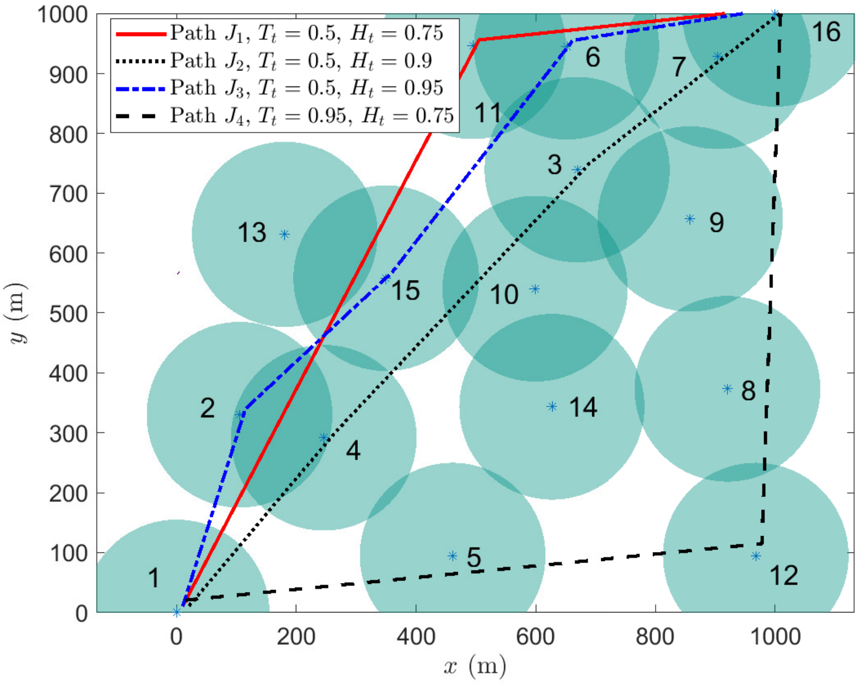

Figure 4.7: The route selection results based on link timeliness probabilities and constrained by T_t and H_t for a snapshot of the randomly deployed MCC clusters. The trust is calculated based on the mean trust probability, and $H_{1,16} < H_t$. © 2019 IEEE.

will be selected. Besides, the reason that J_1 is selected when $T_t = 0.5, H_t = 0.75$ instead of J_4, although they both have the same number of users within, is due to the implementation of Dijkstra's algorithm.

Figure 4.8 gives the route selection results based on trust probabilities and constrained by D_t and H_t. Among the given paths, J_1 and J_2 are selected based on mean trust probabilities and J_3 and J_4 are based on robust trust probabilities with $c = 0.95$. J_1 and J_3 shows that two-hop routes are available for route selection, and the route via cluster 14 gives the best end-to-end trust probabilities for both the mean and robust trust probability formulations. J_2 and J_4 also show that the selected routes given by the mean and robust trust probabilities could yield different results even though their values of D_t and H_t are the same.

Figure 4.9 gives the averaged end-to-end coverage and timeliness probabilities after

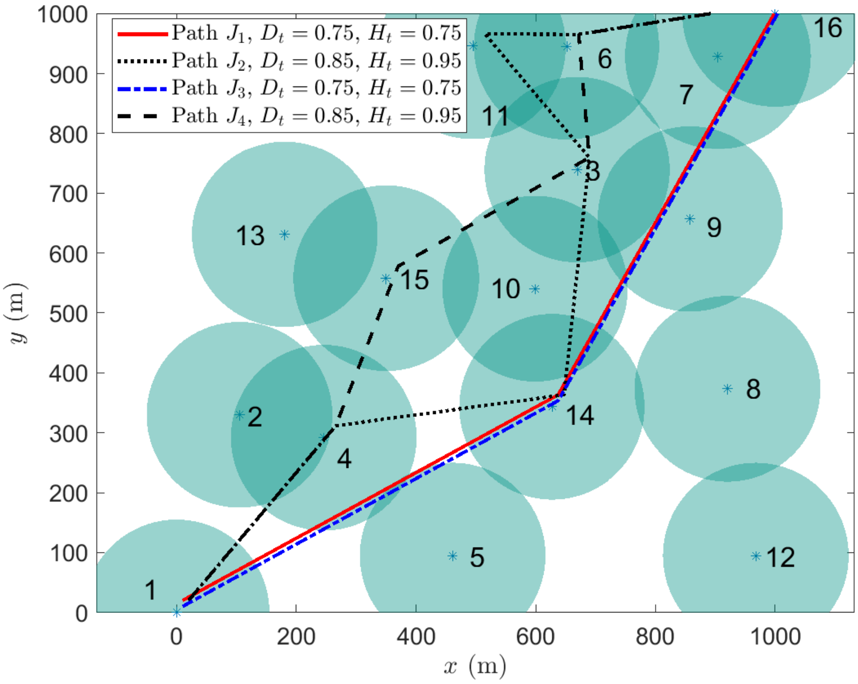

Figure 4.8: The route selection based on link trust probabilities and constrained by D_t and H_t for a snapshot of the randomly deployed MCC clusters, and $H_{1,16} < H_t$. © 2019 IEEE.

route selections over different snapshots of clusters. The proposed route selections are based on coverage probabilities and constrained by T_t only (i.e., $D_t = 0$). The average number of users within each cluster is 2. For a snapshot of the random clusters, an increasing number of cluster heads coming consecutively from clusters 2 to 15 are labeled as untrustworthy, and the route selections are performed. A head k is regarded as untrustworthy if both T_{jk} and T_{kj} are less than T_t for any $j \neq k$. To compare, a benchmark of route selection solely based on coverage [62] is given. When there is only one untrustworthy node on the plane, the end-to-end coverage probability for both the benchmark and the proposed route selection method are around 97.5%. As all cluster heads in clusters 2 to 15 become untrustworthy nodes, there is a 5% performance drop in the end-to-end coverage probability for the proposed method. Although, the benchmark achieves the best end-to-end coverage probability, it does not consider the untrustworthy node, which makes the path susceptible to attacks. Figure 4.9 also

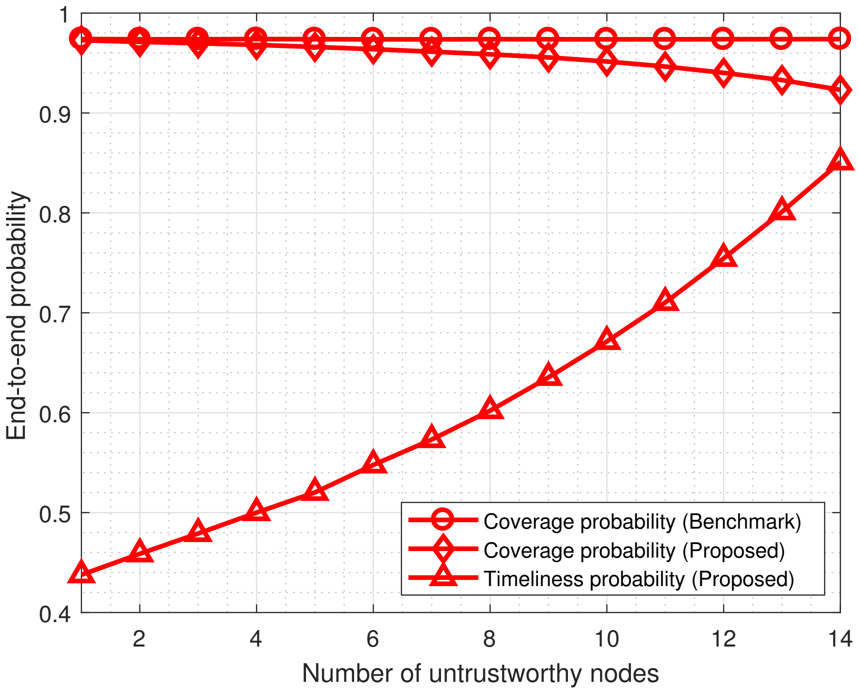

Figure 4.9: The averaged end-to-end coverage and timeliness probabilities after route selections based on coverage and constrained by T_t only. $\eta = 2$. © 2019 IEEE.

shows that the end-to-end coverage and timeliness probabilities decrease and increase respectively as the number of untrustworthy nodes increases. This is because, as the number of untrustworthy nodes increases, more nodes which can offer higher pairwise coverage probabilities are not qualified for route selection if they become untrustworthy. Meanwhile, the increasing number of untrustworthy nodes imposes the reduction of the average number of hops for a selected path. Since all clusters have the same average number of users, the delay for each cluster is the same. Therefore, as the average number of hops decreases, a higher end-to-end timeliness probability is achieved.

4.5 Summary

In this chapter, a novel route selection method based on coverage, delay, and trust has been proposed for a mission-critical public safety network. The coverage probability, where the interference analysis considers the effects of call activities within each cluster, has been characterized. The robust trust probability based on the Bayesian-based lower confidence bound has been formulated. The simulations have shown that, compared with single criterion route selection, the proposed route selection method offers versatile solutions with different basic criteria and thresholds on coverage, timeliness, and trust probabilities. The academic implications are given as follows.

Firstly, this chapter has shown that coverage, delay, and trust are all crucial to the mission-critical system since the system is susceptible to connection outages, delays, and attacks. Secondly, by incorporating the delay model into interference and coverage probability analysis, the effect of the activity of the group communications on the coverage has been captured. Thirdly, the trust probability based on the lower confidence bound could provide a more robust result than the mean trust probability especially when the number of interactions is small.

4.A Appendix: Reputation-Based Trust Model

4.A.1 Binomial Likelihood

A random variable which consists of the number of successes k in n Bernoulli trials with a probability of success p in [0,1]. Thus, the binomial likelihood is given by

$$f_{k|n,p}(k \mid n, p) = \binom{n}{k} p^k (1-p)^{n-k} \tag{4.22}$$

where $\binom{n}{k} = \frac{n!}{k!(n-k)!}$, $0 \leq k \leq n$, and $k \in \mathbb{Z}$.

4.A.2 From Uniform and Beta Priors to Beta Posterior

For a parameter p whose prior is $f_p(p)$, given k and n, the posterior is the distribution of p, which is written as

$$f_{p|k}(p \mid k) = \frac{f_{k|p}(k \mid p) f_p(p)}{\int_0^1 f_{k|p}(k \mid p) f_p(p)\,\mathrm{d}p}, \quad 0 \leq p \leq 1, \quad k = 0, 1, 2, ..., n \tag{4.23}$$

where $f_{k|p}(k \mid p) = f_{k|n,p}(k \mid n, p)$ for a given n.

For **uniform prior**, during the system initialization, the potential probability on the trust could be equally likely on $[0, 1]$. The posterior of p with the binomial likelihood and uniform prior is given by

$$f_{p|k}(p \mid k) = \frac{\binom{n}{k} p^k (1-p)^{n-k}}{\int_0^1 f_{k|p}(k \mid p) f_p(p)\,\mathrm{d}p} = (n+1)\binom{n}{k} p^k (1-p)^{n-k}. \tag{4.24}$$

The value of the normalizing integral is apparent because of the properties of the beta function with integer parameters. The posterior after the simplification has a form of beta PDF with parameters $\alpha = k + 1$ and $\beta = n - k + 1$, which is given by

$$f(p \mid \alpha, \beta) = \frac{p^{\alpha-1}(1-p)^{\beta-1}}{\mathrm{Beta}(\alpha, \beta)}. \tag{4.25}$$

For **beta prior**, suppose a system already has a_0 successes and b_0 failures, the corresponding likelihood function is given by

$$f_{a_0,b_0|p}(a_0, b_0 \mid p) = \binom{a_0 + b_0}{a_0} p^{a_0}(1-p)^{b_0}. \tag{4.26}$$

The posterior of p with the binomial likelihood and prior (4.25) is given by

$$
\begin{aligned}
f_{p|a_0,b_0}(p \mid a_0, b_0) &= \frac{f_{a_0,b_0|p}(a_0, b_0 \mid p) f_p(p)}{\int_0^1 f_{a_0,b_0|p}(a_0, b_0 \mid p) f_p(p) \, \mathrm{d}p} \\
&= \frac{\binom{a_0+b_0}{a_0} p^{a_0+\alpha-1}(1-p)^{b_0+\beta-1} / \mathrm{Beta}(\alpha, \beta)}{\int_0^1 \binom{a_0+b_0}{a_0} p^{a_0+\alpha-1}(1-p)^{b_0+\beta-1} / \mathrm{Beta}(\alpha, \beta) \, \mathrm{d}p} \\
&= \frac{p^{a_0+\alpha-1}(1-p)^{b_0+\beta-1}}{\mathrm{Beta}(a_0+\alpha, b_0+\beta)}
\end{aligned}
\tag{4.27}
$$

which is another beta PDF with parameters $(\alpha + a_0, \beta + b_0)$. As a result, the beta reputation system based on beta PDF has been used to model the trust in [195]. The corresponding mean and variance of the trust is given as follows: Let X denoted a beta distributed random variable with parameters α, β, then

$$
\mathbb{E}[X] = \frac{\int_0^1 x^{\alpha}(1-x)^{\beta-1} \, dx}{\mathrm{Beta}(\alpha, \beta)} = \frac{\mathrm{Beta}(\alpha+1, \beta)}{\mathrm{Beta}(\alpha, \beta)} = \frac{\Gamma(\alpha+1)\Gamma(\beta)}{\Gamma(\alpha+\beta+1)} \frac{\Gamma(\alpha+\beta)}{\Gamma(\alpha)\Gamma(\beta)} = \frac{\alpha}{\alpha+\beta};
\tag{4.28}
$$

$$
\mathrm{Var}(X) + (\mathbb{E}[X])^2 = \mathbb{E}[X^2] = \frac{\mathrm{Beta}(\alpha+2, \beta)}{\mathrm{Beta}(\alpha, \beta)} = \frac{\alpha(\alpha+1)}{(\alpha+\beta)(\alpha+\beta+1)}
\tag{4.29}
$$

from which

$$
\mathrm{Var}(X) = \frac{\alpha\beta}{(\alpha+\beta)^2(\alpha+\beta+1)}.
\tag{4.30}
$$

Chapter 5

Meta Distribution of the Secrecy Rate in the Presence of Randomly Located Eavesdroppers

Previous chapters have explored the reliability aspect of a wireless communication network by studying the joint performance of concurrent single-hop device-to-device (D2D) transmission links and end-to-end performance of the multi-hop D2D transmission links. This chapter starts to move on to the security aspect of a wireless communication network focusing on physical layer security (PLS). In this chapter, the meta distribution of the secrecy rate for a legitimate link in the presence of eavesdroppers (EDs) with locations modeled as a Poisson point process (PPP) has been studied, where a meta distribution is defined as the distribution of the conditional success probability [214]. Both colluding and non-colluding EDs are considered. The meta distribution of the secrecy rate can provide the fraction of spatial realizations of EDs that yield a target secrecy rate. It can either be formulated using the Gil-Pelaez theorem with the imaginary moments of the conditional secure connection probability (CSCP) given the realization of EDs or approximated by the beta distribution with the first two moments only. Hence, the bth moment of the CSCP for the colluding scenario is derived. Then, since there is no tractable form for the higher order moment of the CSCP, the first and second moments of the CSCP are formulated for the non-colluding scenario. In addition, the moments in the high signal-to-noise ratio (SNR) regime are also derived. Finally, simulations are used to validate the analytic results.

5.1 Introduction

PLS is the idea that channel coding and signal processing techniques can be used to secure data confidentiality between connected devices [43]. A common performance metric used to analyze secrecy in the presence of randomly distributed colluding and non-colluding EDs in fading channels is the secure connection probability. A detailed introduction to PLS and the secure connection probability is given by Section 2.2.

In networks with randomly distributed EDs, the secure connection probability is typically defined to capture the *average* performance of a link. This definition loses the fine-grained detail about the fraction of the realizations of EDs that allow a target secrecy rate. To overcome this issue, the meta distribution of the signal-to-interference ratio (SIR) was proposed in [214]. This distribution facilitates the study of the fraction of links fulfilling a target SIR given a realization of the point process. This basic theory was extended in [215] to study networks that exploit interference cancellation. In [216], the meta distribution of the SIR in the cellular network uplink and downlink with fractional power control was studied. The meta distribution in downlink D2D underlaid cellular networks has been analyzed in [55]. To the best of the author's knowledge, however, no progress has been made to characterize the meta distribution of the secrecy rate in networks with randomly located EDs until now. This chapter addresses exactly this task. The contributions of the work can be summarized as follows:

1. The bth moment of the CSCP is characterized in a closed-form expression for the colluding scenario so that the meta distribution can be formulated as an exact expression using the Gil-Pelaez inversion formula or as a beta approximation in the usual way.

2. For the non-colluding scenario, the exact first and second moments of the CSCP are calculated so that a suitable beta approximation to the meta distribution can be obtained.

The rest of the chapter is structured as follows. Section 5.2 begins with a description of the system model and addresses the meta distribution of the secrecy rate and its beta approximation. Section 5.3 focuses on the moments of the CSCP. Section 5.4 gives the simulation results and discussion, and Section 5.5 concludes the chapter.

5.2 System Model

5.2.1 Network Layout

The system model is depicted in Figure 5.1, where the transmitter s located at the origin sends messages to a receiver d located at a deterministic distance from the origin [42, 119, 121][1]. The EDs are assumed to be Poisson point process (PPP) distributed with density λ_e, which either collude or work independently to decode the message received on their Gaussian wire-tap links. Comparing with the Poisson bipolar model in [214], the distribution of EDs in the system model is similar to the distribution of interferers in the Poisson bipolar model. In spite of this similarity,

[1]This chapter considers the communication channels operating in a noise-limited regime where a carefully planned frequency reuse pattern is assumed, and the transmitter can occupy some resource blocks exclusively in a relatively large region [54]. The co-channel interference will be studied in the future work. Meanwhile, the interference caused by jamming will be studied in the next chapter under a different setting and performance metric.

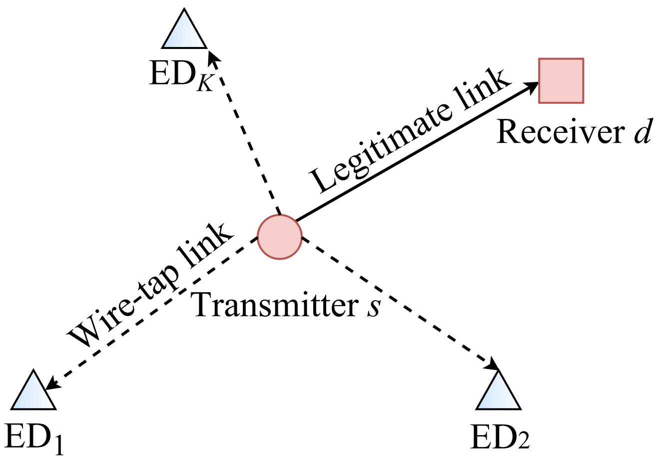

Figure 5.1: Communication in the presence of EDs, where the dashed line and solid line denote wire-tap link and legitimate link, respectively. © 2018 IEEE.

the model depicted herein studies the meta distribution of the secrecy rate under an eavesdropping assumption rather than SIR as is the case in the Poisson bipolar model. The distance between s and d is $l_{s,d}$. The path loss model is $c^2(4\pi\nu)^{-2}l_{s,y}^{-\alpha}$, where c is the speed of light and ν is the carrier frequency, $l_{s,y}$ is the distance between s and a terminal (i.e., d or EDs) y, and α is the path loss exponent. The fading of the channel is assumed to be Rayleigh, and the transmitting power is P_d. Hence, the received signal power at terminal y is denoted as $P_{s,y} = c^2(4\pi\nu)^{-2}l_{s,y}^{-\alpha}|h_{s,y}|^2 P_d$, and the receiving instantaneous SNR at terminal y is given by $\mathrm{SNR}_{s,y} = P_{s,y}/N_0$, where N_0 is the additive white Gaussian noise (AWGN) power.

5.2.2 Secrecy Capacity

The secrecy capacity of a link is the difference between the capacity of the legitimate link and the capacity achieved via a collection of wiretap links, which can be written as [119]

$$
\begin{aligned}
C_s &= \left[\log_2\left(1+\mathrm{SNR}_{s,d}\right) - \log_2\left(1+\mathscr{F}\left(\mathrm{SNR}_{s,e}\right)\right)\right]^+ \\
&= \left[\log_2\left(\frac{|h_{s,d}|^2 l_{s,d}^{-\alpha} + \hat{N}_0}{\mathscr{F}\left(|h_{s,e}|^2 l_{s,e}^{-\alpha}\right) + \hat{N}_0}\right)\right]^+ \\
&< \left[\log_2\left(\frac{|h_{s,d}|^2 l_{s,d}^{-\alpha}}{\mathscr{F}\left(|h_{s,e}|^2 l_{s,e}^{-\alpha}\right)}\right)\right]^+
\end{aligned}
\tag{5.1}
$$

where $[x]^+$ denotes $\max(0, x)$, $\hat{N}_0 = N_0/(c^2(4\pi\nu)^{-2}P_d)$, operator $\mathscr{F}(\cdot)$ is either $\sum_{e\in\Phi}(\cdot)$ for the *colluding* scenario or $\max_{e\in\Phi}(\cdot)$ for the *non-colluding* scenario, Φ denotes the PPP of the EDs, and the symbol '$<$' indicates that C_s is upper bounded by the term on the right side of the symbol as $P_d \to \infty$, i.e., in the high SNR regime. This can be explained as follows:

For $C_s > 0$, $\frac{|h_{s,d}|^2 l_{s,d}^{-\alpha}/\hat{N}_0+1}{\mathscr{F}\left(|h_{s,e}|^2 l_{s,e}^{-\alpha}\right)/\hat{N}_0+1} > 1$. Let $d_1 = |h_{s,d}|^2 l_{s,d}^{-\alpha} c^2(4\pi\nu)^{-2}/N_0$, $d_2 = \mathscr{F}\left(|h_{s,e}|^2 l_{s,e}^{-\alpha}\right) c^2(4\pi\nu)^{-2}/N_0$, then

$$
y = \frac{1+d_1P_d}{1+d_2P_d} > 1 \tag{5.2}
$$

for $P_d > 0$. Thus, only $d_1 > d_2$ is valid for $y > 1$. This is because: 1) $y = 1$ when $P_d = 0$; 2) the hyperbola y is monotonically increasing in P_d if $d_1 > d_2$, and y is monotonically decreasing in P_d if $d_1 < d_2$. Therefore, as P_d increases, y increases. As a result, C_s is upper bounded by $\left[\log_2\left(\frac{|h_{s,d}|^2 l_{s,d}^{-\alpha}}{\mathscr{F}\left(|h_{s,e}|^2 l_{s,e}^{-\alpha}\right)}\right)\right]^+$.

5.2.3 Meta Distribution of the Secrecy Rate

Conditioning on the realization of EDs in Φ, the CSCP of the legitimate link achieving a target secrecy rate R_t is given by

$$
p(R_t) = \mathbb{P}(C_s > R_t \mid \Phi). \tag{5.3}
$$

Given the link secure connection probability threshold p_t, the meta distribution is defined as

$$\overline{F}(R_t, p_t) = \mathbb{P}(p(R_t) > p_t) \tag{5.4}$$

which gives detailed information about the user experience by providing the proportion of the spatial configurations of EDs yielding R_t with a probability of p_t or above. Meanwhile, based on the above definition on meta-distribution and the inequality in (5.1), the meta distribution of the secrecy rate in the high SNR regime as $P_d \to \infty$ is the upper bound of the meta distribution of the secrecy rate. Due to the fact that the probability density function (PDF) of $p(R_t)$ is unknown, it is difficult to calculate this meta distribution directly. Since the characteristic function of any real-valued random variable completely defines its probability distribution, and the characteristic function is related to the moment-generating function, the moments $M_b = \mathbb{E}\left(p(R_t)^b\right)$ are investigated instead [214]. Specifically, let $i^2 = -1$, $M_{it} = \mathbb{E}\left(p(R_t)^{it}\right) = \mathbb{E}\left(e^{it \log p(R_t)}\right)$; the last term is denoted as the characteristic function $\varphi_X(t)$ and $X = \log p(R_t)$. The relationship between the complementary cumulative distribution function (CCDF) of a random variable X and its characteristic function is given by the Gil-Pelaez theorem [217]:

$$\overline{F}_X(x) = \frac{1}{2} + \frac{1}{\pi}\int_0^\infty \frac{\Im[e^{-itx}\varphi_X(t)]}{t}\,\mathrm{d}t \tag{5.5}$$

where $\Im[z]$ is the imaginary part of a complex number z. Thus, the meta distribution is defined by

$$\overline{F}(R_t, p_t) = \frac{1}{2} + \frac{1}{\pi}\int_0^\infty \frac{\Im(e^{-it\log p_t} M_{it})}{t}\,\mathrm{d}t. \tag{5.6}$$

5.2.4 Beta Approximations of the Meta Distribution

Since $p(R_t)$ is within $[0,1]$, the beta distribution can be used to approximate the meta distribution [214]. The PDF of a beta distributed random variable Y is given by

$$f_Y(y \mid a,b) = \frac{y^{a-1}(1-y)^{b-1}}{\mathrm{Beta}(a,b)} \tag{5.7}$$

where $\mathrm{Beta}(a,b) = \dfrac{\Gamma(a)\Gamma(b)}{\Gamma(a+b)}$, $a,b > 0$ are shape parameters, while the mean and variance of Y are respectively given by

$$\mathbb{E}[Y] = \frac{a}{a+b} \text{ and } \mathrm{Var}[Y] = \frac{ab}{(a+b)^2(a+b+1)}. \tag{5.8}$$

Let $M_1 = \mathbb{E}[Y]$ and $M_2 - M_1^2 = \mathrm{Var}[Y]$; the meta distribution of the secrecy rate can be approximated by the CCDF of Y which is written as

$$\overline{F}(R_t, p_t) \approx 1 - I_{p_t}\left(\frac{M_1M_2 - M_1^2}{M_1^2 - M_2}, \frac{(1-M_1)(M_2-M_1)}{M_1^2 - M_2}\right) \tag{5.9}$$

where $I_{p_t}(a,b)$ is the regularized incomplete beta function, which is defined as

$$I_{p_t}(a,b) = \frac{\mathrm{Beta}(p_t;\, a,b)}{\mathrm{Beta}(a,b)} \tag{5.10}$$

and

$$\mathrm{Beta}(p_t;\, a,b) = \int_0^{p_t} t^{a-1}\,(1-t)^{b-1}\,\mathrm{d}t. \tag{5.11}$$

5.3 Moments of the CSCP

5.3.1 Colluding EDs

Theorem 3. Letting $\theta = 2^{R_t}$, the bth moment of the CSCP for the colluding scenario is given by

$$M_b = \exp\left(-bl_{s,d}^{\alpha}(\theta-1)\hat{N}_0 - \lambda_e \pi l_{s,d}^2 \Gamma(1-2/\alpha)\theta^{2/\alpha}\frac{\Gamma(b+2/\alpha)}{\Gamma(b)}\right) \tag{5.12}$$

Proof.

$$\begin{aligned}
M_b &= \mathbb{E}_{\Phi}\left[\mathbb{P}(C_s > R_t \mid \Phi)^b\right] \\
&= \mathbb{E}_{\Phi}\left[\mathbb{P}\left(\frac{|h_{s,d}|^2 l_{s,d}^{-\alpha} + \hat{N}_0}{\sum_{e\in\Phi}\left(|h_{s,e}|^2 l_{s,e}^{-\alpha}\right) + \hat{N}_0} > \theta \mid \Phi\right)^b\right] \\
&\overset{(a)}{=} \exp\left(-bl_{s,d}^{\alpha}(\theta-1)\hat{N}_0\right)\mathbb{E}_{\Phi}\left[\prod_{e\in\Phi}\left(1+\theta l_{s,e}^{-\alpha}/l_{s,d}^{-\alpha}\right)^{-b}\right] \\
&\overset{(b)}{=} \exp\left(-bl_{s,d}^{\alpha}(\theta-1)\hat{N}_0\right)\exp\left(-\lambda_e\int_{\mathbb{R}^2}\left[1-\left(1+\theta\|x\|^{-\alpha}/l_{s,d}^{-\alpha}\right)^{-b}\right]\mathrm{d}x\right) \\
&= \exp\left(-bl_{s,d}^{\alpha}(\theta-1)\hat{N}_0 - \lambda_e\pi l_{s,d}^2\Gamma(1-2/\alpha)\theta^{2/\alpha}\frac{\Gamma(b+2/\alpha)}{\Gamma(b)}\right)
\end{aligned} \tag{5.13}$$

where (a) is the result of averaging over fading while conditioning on a realization of Φ, and (b) is achieved by using the probability generating functional (PGFL) of a PPP. The proof is found to be similar to the derivation of Theorem 1 in [214] with transmit probability 1 for a Poisson bipolar model. In spite of this, the model herein studies the meta distribution of the secrecy rate under an eavesdropping assumption rather than the SIR under the interference assumption in the Poisson bipolar model. □

Lemma 4. In the high SNR regime, the approximated bth moment of the CSCP for the colluding scenario is given by

$$M_b = \exp\left(-\lambda_e \pi l_{s,d}^2 \Gamma(1-2/\alpha)\theta^{2/\alpha}\frac{\Gamma(b+2/\alpha)}{\Gamma(b)}\right) \tag{5.14}$$

where M_b does not depend on the transmit power P_d.

Proof. The approximated bth moment in the high SNR regime can be obtained by letting $P_d \to \infty$. As a result, $\hat{N}_0 \approx 0$ in (5.12), and (5.14) is obtained. This concludes the proof. □

5.3.2 Non-colluding EDs

5.3.2.1 General Formula for M_b

The bth moment of the CSCP for the non-colluding scenario is given by

$$\begin{aligned} M_b &= \mathbb{E}_\Phi\left[\mathbb{P}(C_s > R_t \mid \Phi)^b\right] \\ &= \mathbb{E}_\Phi\left[\mathbb{P}\left(\max_{e\in\Phi}|h_{s,e}|^2 l_{s,e}^{-\alpha} < \left(|h_{s,d}|^2 l_{s,d}^{-\alpha} - \hat{N}_0(\theta-1)\right)/\theta \mid \Phi\right)^b\right] \\ &= \mathbb{E}_\Phi\left[\mathbb{P}\left(\max_{e\in\Phi}|h_{s,e}|^2 l_{s,e}^{-\alpha} < \left[|h_{s,d}|^2 l_{s,d}^{-\alpha} - \hat{N}_0(\theta-1)\right]^+/\theta \mid \Phi\right)^b\right] \\ &= \mathbb{E}_\Phi\left[\mathbb{E}_{h_{s,d}|\Phi}\left[\prod_{e\in\Phi}\left(1-\exp\left(-\left[|h_{s,d}|^2 l_{s,d}^{-\alpha} - \hat{N}_0(\theta-1)\right]^+ l_{s,e}^{\alpha}/\theta\right)\right)\right]^b\right] \\ &= \mathbb{E}_\Phi\left[\left(\int_0^\infty \prod_{e\in\Phi}\left(1-\exp\left(-\left[x l_{s,d}^{-\alpha} - \hat{N}_0(\theta-1)\right]^+ l_{s,e}^{\alpha}/\theta\right)\right)\exp(-x)\,\mathrm{d}x\right)^b\right]. \end{aligned} \tag{5.15}$$

This expression cannot be reduced to a simple analytic form for all the moments. To make progress, the case that can offer tractable expressions for analysis based on beta approximations is investigated as below.

5.3.2.2 Derivation of M_1 and M_2

Theorem 4. The first moment of the CSCP for the non-colluding scenario is given by

$$M_1 = \int_0^\infty \exp\left(-A_0\left(\left[xl_{s,d}^{-\alpha} - \hat{N}_0(\theta-1)\right]^+\right)^{-2/\alpha} - x\right) \mathrm{d}x \tag{5.16}$$

While the second moment is given by

$$\begin{aligned} M_2 = \int_0^\infty \int_0^\infty \exp\Bigg(&- A_0\left(\left[xl_{s,d}^{-\alpha} - \hat{N}_0(\theta-1)\right]^+\right)^{-\frac{2}{\alpha}} - A_0\left(\left[yl_{s,d}^{-\alpha} - \hat{N}_0(\theta-1)\right]^+\right)^{-\frac{2}{\alpha}} \\ &+ A_0\left(\left[xl_{s,d}^{-\alpha} - \hat{N}_0(\theta-1)\right]^+ + \left[yl_{s,d}^{-\alpha} - \hat{N}_0(\theta-1)\right]^+\right)^{-\frac{2}{\alpha}} - x - y\Bigg) \mathrm{d}x\,\mathrm{d}y \end{aligned} \tag{5.17}$$

where $A_0 = 2\pi\lambda_e\Gamma\left(\frac{2}{\alpha}\right)\frac{1}{\alpha}\theta^{2/\alpha}$.

Proof. The first moment is derived as follows:

$$\begin{aligned} M_1 =& \mathbb{E}_{h_{s,d}}\left[\mathbb{E}_{\Phi|h_{s,d}}\left[\prod_{e\in\Phi}\left(1-\exp\left(-\left[|h_{s,d}|^2 l_{s,d}^{-\alpha} - \hat{N}_0(\theta-1)\right]^+ l_{s,e}^{\alpha}/\theta\right)\right)\right]\right] \\ \overset{(a)}{=}& \int_0^\infty \exp\left(-A_0\left(\left[xl_{s,d}^{-\alpha} - \hat{N}_0(\theta-1)\right]^+\right)^{-2/\alpha}\right) \exp(-x)\,\mathrm{d}x \end{aligned} \tag{5.18}$$

where (a) is the result of the PGFL of the PPP [29].

For M_2, its derivation is given by

$$\begin{aligned} M_2 =& \mathbb{E}_{\Phi}\left[\left(\int_0^\infty \prod_{e\in\Phi}\left(1-\exp\left(-\left[xl_{s,d}^{-\alpha} - \hat{N}_0(\theta-1)\right]^+ l_{s,e}^{\alpha}/\theta\right)\right)\exp(-x)\,\mathrm{d}x\right)^2\right] \\ =& \mathbb{E}_{x,y}\left[\mathbb{E}_{\Phi|x,y}\left[\prod_{e\in\Phi}\left(1-\exp\left(-\left[xl_{s,d}^{-\alpha} - \hat{N}_0(\theta-1)\right]^+ l_{s,e}^{\alpha}/\theta\right)\right)\right.\right. \end{aligned}$$

$$
\times \left(1 - \exp\left(-\left[y l_{s,d}^{-\alpha} - \hat{N}_0(\theta-1)\right]^+ l_{s,e}^{\alpha}/\theta\right)\right)\Bigg]\Bigg]
$$

$$
\stackrel{(a)}{=} \mathbb{E}_{x,y}\Bigg[\exp\Bigg(2\pi\lambda_e \int_0^\infty \Bigg(-\exp\left(-\left[x l_{s,d}^{-\alpha} - \hat{N}_0(\theta-1)\right]^+ l_{s,e}^{\alpha}/\theta\right)
$$

$$
-\exp\left(-\left[y l_{s,d}^{-\alpha} - \hat{N}_0(\theta-1)\right]^+ l_{s,e}^{\alpha}/\theta\right)
$$

$$
+\exp\left(-\left(\left[x l_{s,d}^{-\alpha} - \hat{N}_0(\theta-1)\right]^+ + \left[y l_{s,d}^{-\alpha} - \hat{N}_0(\theta-1)\right]^+\right) l_{s,e}^{\alpha}/\theta\right)\Bigg) l_{s,e}\, \mathrm{d}l_{s,e}\Bigg)\Bigg] \tag{5.19}
$$

where (a) is the result of PGFL of a PPP. After the simplification, M_2 is given by (5.17). This concludes the proof. □

Lemma 5. In the high SNR regime, the first moment of the CSCP for the non-colluding scenario is given by

$$
M_1 = \frac{2\pi\sqrt{2pq}}{(2\pi)^{\frac{p}{2}+q}} G_{0,0}^{p+2q,0}\left(\begin{matrix} - \\ 0, \frac{1}{p}, \dots, \frac{p-1}{p}, \frac{1}{2q}, \frac{1}{q}, \dots, 1 \end{matrix}\,\middle|\, \frac{p^{-p}A_1^p}{(2q)^{2q}}\right) \tag{5.20}
$$

where $G_{0,0}^{p+2q,0}$ is the Meijer G-function, which is defined as

$$
G_{p,q}^{m,n}\left(\begin{matrix} a_1,\dots,a_p \\ b_1,\dots,b_q \end{matrix}\,\middle|\, x\right) = \frac{1}{2\pi i}\int_L \frac{\prod_{j=1}^m \Gamma(b_j - s)\prod_{j=1}^n \Gamma(1-a_j+s)}{\prod_{j=m+1}^q \Gamma(1-b_j+s)\prod_{j=n+1}^p \Gamma(a_j - s)} x^s\,\mathrm{d}s \tag{5.21}
$$

$A_1 = \lambda_e 2\pi \Gamma\left(\frac{2}{\alpha}\right)\frac{1}{\alpha}\left(\frac{l_{s,d}^2}{\theta^{-2/\alpha}}\right)$, the path loss exponent α is represented by a fraction, i.e., $\alpha = p/q$, with $p, q \in \mathbb{Z}^+$ so that α must be a rational number[2], while the second

[2] A non-rational α can be approximated by a suitable rational value.

moment is given by

$$M_2 = \int_0^\infty \int_0^\infty \exp\Bigg(- A_0 \left(x l_{s,d}^{-\alpha}\right)^{-2/\alpha} - A_0 \left(y l_{s,d}^{-\alpha}\right)^{-2/\alpha} \\ + A_0 \left(x l_{s,d}^{-\alpha} + y l_{s,d}^{-\alpha}\right)^{-2/\alpha} - x - y \Bigg) \, \mathrm{d}x \, \mathrm{d}y \tag{5.22}$$

Proof. The first moment in the high SNR regime is derived as follows:

$$\begin{aligned}
M_1 &= \mathbb{E}_{h_{s,d}} \left[\mathbb{E}_{\Phi|h_{s,d}} \left[\prod_{e\in\Phi} \left(1 - \exp\left(-\frac{|h_{s,d}|^2 l_{s,d}^{-\alpha}}{\theta l_{s,e}^{-\alpha}} \right) \right) \right] \right] \\
&\overset{(a)}{=} \int_0^\infty e^{-A_1 x^{-2/\alpha}} x e^{-x} \frac{\mathrm{d}x}{x} \\
&\overset{(b)}{=} \frac{1}{2\pi i} \int_{\delta - i\infty}^{\delta + i\infty} \frac{A_1^{-\frac{w}{2/\alpha}} \Gamma\left(\frac{w}{2/\alpha}\right)}{2/\alpha} \Gamma(w+1) \, \mathrm{d}w \\
&\overset{(c)}{=} \frac{1}{2\pi i} \int_{\frac{\delta}{2q} - i\infty}^{\frac{\delta}{2q} + i\infty} \frac{A_1^{-ps} \Gamma(ps)}{2q/p} \Gamma(2qs+1) 2q \, \mathrm{d}s \\
&\overset{(d)}{=} \frac{\sqrt{2pq}}{i(2\pi)^{\frac{p+2q}{2}}} \int_{\frac{\delta}{2q} - i\infty}^{\frac{\delta}{2q} + i\infty} \prod_{k=0}^{p-1} \Gamma\left(s + \frac{k}{p}\right) \prod_{k=0}^{2q-1} \Gamma\left(s + \frac{1+k}{2q}\right) \left(A_1^p p^{-p} (2q)^{-2q}\right)^{-s} \mathrm{d}s \\
&= \frac{2\pi\sqrt{2pq}}{(2\pi)^{\frac{p}{2}+q}} G_{0,0}^{p+2q,0}\left(\left. \begin{matrix} - \\ 0, \frac{1}{p}, \ldots, \frac{p-1}{p}, \frac{1}{2q}, \frac{1}{q}, \ldots, 1 \end{matrix} \right| \frac{p^{-p} A_1^p}{(2q)^{2q}} \right)
\end{aligned} \tag{5.23}$$

where (a) is the result of the PGFL of the PPP [29]; (b) is the Mellin convolution given by [218]

$$(f * g)(z) = \int_0^\infty f\left(\frac{z}{u}\right) g(u) \frac{\mathrm{d}u}{u} = \frac{1}{2\pi i} \int_{\delta - i\infty}^{\delta + i\infty} z^{-w} \tilde{f}(w) \tilde{g}(w) \, \mathrm{d}w, \;\; z > 0 \tag{5.24}$$

where $\tilde{f}(w)$ denotes the Mellin transform of a function $f(x)$, which is written as

$$\tilde{f}(w) = \int_0^\infty x^{w-1} f(x) \, \mathrm{d}x. \tag{5.25}$$

Step (c) is the result of a change of variables, i.e., $w = 2qs$, and δ is within the overlapped strip of analyticity of both $\tilde{f}(w)$ and $\tilde{g}(w)$; and (d) is obtained by the multiplication theorem [219, Section 5.5]

$$\Gamma(pz) = \frac{1}{(2\pi)^{\frac{p-1}{2}}\ p^{\frac{1}{2}-pz}} \prod_{k=0}^{p-1} \Gamma\left(z + \frac{k}{p}\right) . \tag{5.26}$$

Meanwhile, M_2 in the high SNR regime can be obtained by letting $P \to \infty$. As a result, $\hat{N}_0 \approx 0$ in (5.19), and (5.22) is obtained. This concludes the proof. □

5.4 Simulations and Discussion

In this section, simulations are conducted to validate the analysis detailed above. In each Monte Carlo trial, one realization of the PPP distributed EDs with density λ_e is generated in a 4×4 km^2 square. A transmitter is located in the centroid of the square, while the intended receiver d is $l_{s,d} = 80$ m away from it unless otherwise specified. $N_0 = -92$ dBm, $\alpha = 3.5$, and $\theta = 1.05$. $P_d = 0$ dBm is used to validate the analytical results in the exact formulations from Theorems 3 and 4. Afterwards, $P_d = 20$ dBm is used to validate the analytical results based on Lemma 4 and Lemma 5 in the high SNR regime. The simulation results are obtained by averaging over 10^4 independent trials.

Figure 5.2 gives the meta distribution of the secrecy rate vs. p_t for the colluding scenario with different values of λ_e, and $P_d = 0$ dBm. The simulation matches well with the numerical results based on the exact formulation in (5.12) of Theorem 3, while the beta approximation based on the exact first two moments in (5.12) shows slightly less accuracy when $\lambda_e = 50$ km^{-2}. Besides, both the numerical and beta approximation results based on (5.14) of Lemma 4 in the high SNR regime show that, when $P_d = 0$ dBm, the meta distribution of the secrecy rate $\overline{F}$ is upper bounded by the one in the high SNR regime. This is because the secrecy rate C_s

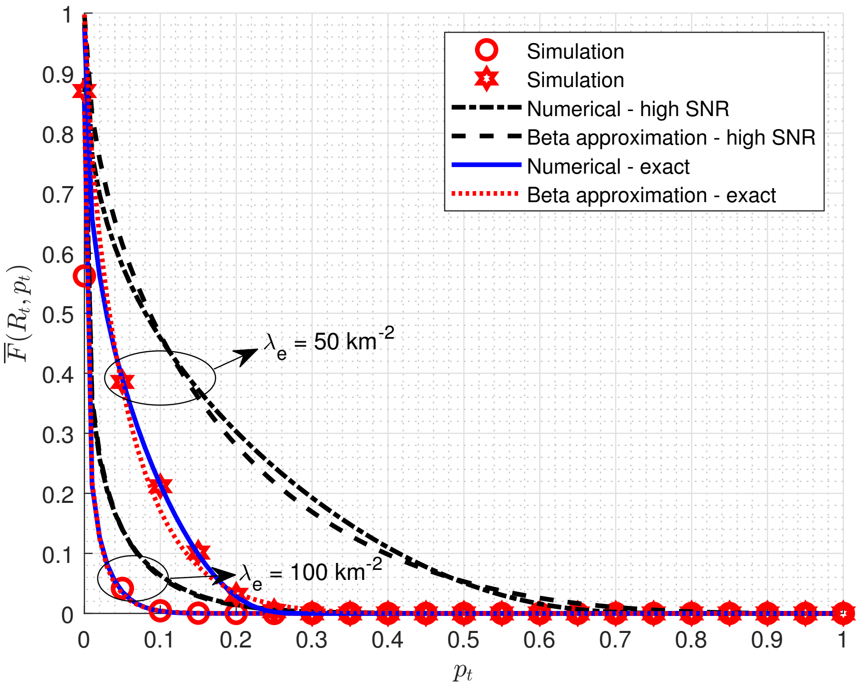

Figure 5.2: The meta distribution of the secrecy rate vs. p_t for the colluding scenario, where $P_d = 0$ dBm.

during each realization of EDs is upper bounded by the secrecy rate at $P_d \to \infty$, and the meta distribution of secrecy rate increases as the C_s in (5.3) reaches this upper bound. Therefore, one can increase the transmit power P_d to boost the link secrecy performance. In the meantime, the figure illustrates how the meta distribution varies with λ_e. The fundamental trends have been observed here, such as the benefits inherent in lowering the secrecy threshold p_t for a higher $\overline{F}$, but it is interesting to note the severe penalty that λ_e induces through the sharp decay of $\bar{F}$ in the $\lambda_e = 100$ km^{-2} curves.

Figure 5.3 presents the meta distribution of the secrecy rate vs. p_t for the non-colluding scenario with different values of λ_e, and $P_d = 0$ dBm. It shows that the beta approximations from Theorem 4 work well in characterizing the meta distribution. Compared with the results of the colluding scenario in Figure 5.2, the non-colluding scenario in Figure 5.3 shows that a higher meta distribution has been achieved as

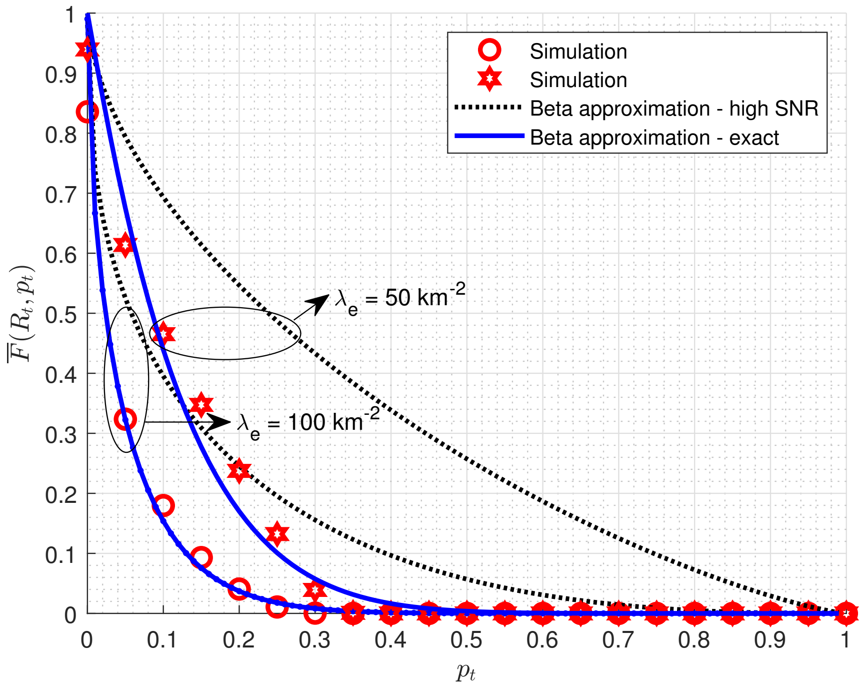

Figure 5.3: The meta distribution of the secrecy rate vs. p_t for the non-colluding scenario, where $P_d = 0$ dBm.

p_t increases. It once again [220] demonstrates that colluding among the EDs will decrease the probability of the legitimate link in achieving a target secrecy rate. In addition, $\overline{F}$ of the non-colluding scenario is lower bounded by the colluding scenario with the same parameters since the legitimate link of the non-colluding scenario will achieve a similar or even higher probability than its colluding counterpart for the same realization.

Figure 5.4 shows that the meta distribution of the secrecy rate vs. p_t where $\lambda_e = 100$ km^{-2}, and $P_d = 20$ dBm for both colluding and non-colluding scenarios. Comparing the curves for $l_{s,d} = 80$ m with the ones in the same λ_e in Figure 5.2 and Figure 5.3, they show that, after increasing the transmit power P_d from 0 dBm to 20 dBm, the simulation results match well with the results based on Lemma 4 and Lemma 5 in the high SNR regime. As a result, for a given link secure connection probability threshold $p_t = 0.6$, there are now 3% satisfied spatial configurations of EDs

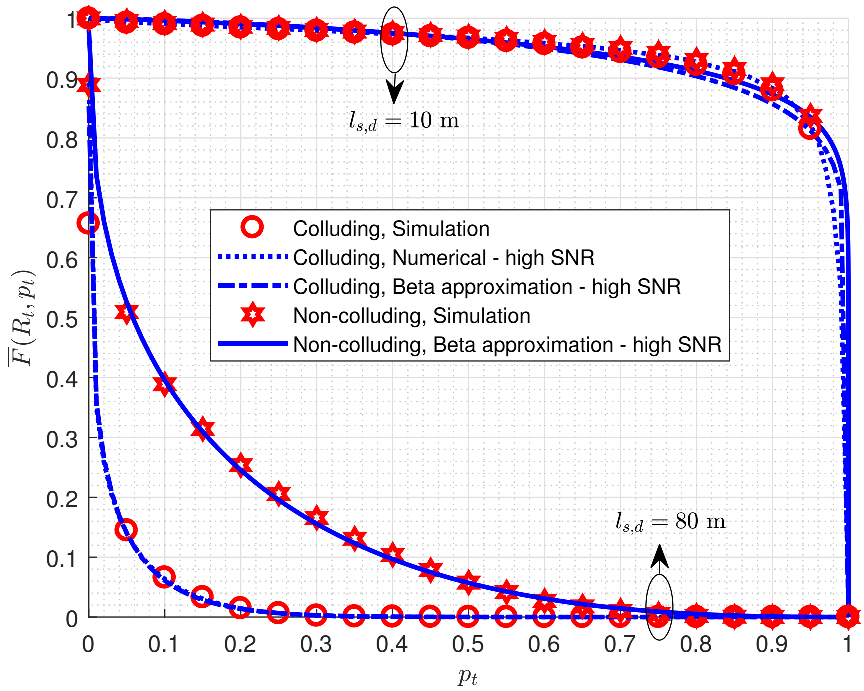

Figure 5.4: The meta distribution of the secrecy rate vs. p_t in the high SNR regime where $\lambda_e = 100$ km^{-2}, and $P_d = 20$ dBm for both colluding and non-colluding scenarios.

for $l_{s,d} = 80$ m, $\lambda_e = 100$ km^{-2} and $P_d = 20$ dBm, while, previously, there is almost no spatial configurations that can yield the same threshold for $\lambda_e = 100$ km^{-2} and $P_d = 0$ dBm. When $l_{s,d} = 10$ m, there are around 90% satisfied spatial configurations of both colluding and non-colluding EDs for a given link secure connection probability threshold $p_t = 0.8$, while $p_t = 0.9$ is achieved by the legitimate link for around 85% of the same spatial configurations of EDs.

5.5 Summary

In this chapter, the meta distribution of the secrecy rate for both colluding and non-colluding ED scenarios have been studied. For the colluding scenario, the bth moments of the CSCP have been formulated in the closed-form expressions. For the non-colluding scenario, the first two moments of the CSCP have been formulated. In addition, the same moments in the high SNR regime have also been formulated, where the formulated results are not related to the value of the transmit power, and the meta distribution in the high SNR regime is the upper bound of the meta distribution. The simulation results showed a good match with the analytic and approximate results for both EDs scenarios. The results also showed that the transmit power plays an important role in the meta distribution of the secrecy rate when the channel is noise-limited. Furthermore, the meta distribution for the non-colluding scenario is lower bounded by its colluding counterpart. The methods and analysis detailed in this chapter can offer insight and design guidelines in the PLS systems.

Chapter 6

Secrecy Performance Analysis of Ground Transmission Subject to UAV Eavesdropping and Jamming

As one result shown in the last chapter, the transmit power of the legitimate transmitter can affect the secrecy performance of a wireless link in the presence of ground eavesdroppers (EDs). Nowadays, unmanned aerial vehicles (UAVs) are being used as aerial base stations in communications networks to improve overall performance. Due to the broadcast nature of the wireless signal and the openness of the space, UAV EDs (UEDs) also pose a potential threat to ground communications. Meanwhile, the UAV-based counter drone system can be deployed to tackle the potential security threats posed by UEDs with the most popular interdiction technique, namely, jamming [221]. This final research chapter studies the communications of a legitimate ground link in the presence of friendly UAV jamming and UEDs within a finite area of space and explores the influence of jamming power, location and height to the secrecy performance. The spatial distribution of the UEDs obeying a uniform binomial point process (BPP) is used to characterize the randomness of the UEDs. The ground link is assumed to experience log-distance path loss and Rayleigh fading, while free space path loss with/without the averaged excess path loss due to the environment is used for the air-to-ground (ATG)/air-to-air links. A piecewise function is proposed to approximate the line-of-sight (LoS) probability for the ATG links, which provides a better approximation than using the existing sigmoid-based fitting. The analytical expression for the secure connection probability (SCP) of the legitimate ground link in the presence of a UAV jammer and non-colluding UEDs is derived. The analysis reveals some useful trends in the SCP as a function of the transmit signal to jamming power ratio, the location of the UAV jammer, and the height of UAVs.

6.1 Introduction

UAVs, also known as drones, constitute a promising technology that offers reliable and cost-effective wireless communication solutions in a wide range of real-world scenarios [222]. Recently, low-altitude UAVs with elevated height from hundreds of meters to several kilometers have drawn much research attention for surveillance, public safety, and secure communications [223–225]. Compared to the existing terrestrial communication systems, UAV aided wireless networks have the potential to overcome the propagation constraints due to terrain characteristics, enhance the signal coverage and reduce operating cost [225]. Due to the broadcast nature of the wireless signal and the openness of the space, ground communications are susceptible to eavesdropping. UEDs could pose a greater threat to the security of ground communications than ground EDs, since UEDs are less constrained by terrain characteristics, and there is a higher chance that a line-of-sight (LoS) link with stronger signal strength can be formed from the ground transmitter to the UEDs rather than to the ground EDs. An early proof-of-concept called 'Snoopy drone' has already been demonstrated by hackers at the Black Hat security conference during 2014 in Singapore to carry a payload containing the equipment necessary to exploit security weaknesses in mobile phones and steal data. Furthermore, many aspects of UAVs, such as low production cost, high mobility, and ease of operation, could incentivize the attackers to use UAVs as the major eavesdropping tools. According to [226], spying UAVs have already caused privacy and security concerns to the public. Consequently, it has become increasingly urgent and necessary to study the security of ground-based wireless communication in the presence of UEDs.

6.1.1 Motivation and Related Work

Stochastic geometry has been exploited for the analysis of UAV-assisted communication networks by endowing their locations with a probability distribution, such as the Poisson point process (PPP) or the BPP. For example, spectrum sharing of super dense drone small cell networks modeled by a three-dimensional (3D) PPP was studied in [227]. The authors of [126] considered the case that the number of UAVs is small and deployed to cover a given finite region with a more suitable BPP for UAV networks under Nakagami-m fading. Since it is common in deployment scenarios (especially in suburban and rural areas) to have a significantly stronger LoS component than reflected multipath components, the coverage probability in the absence of fading has been derived in [126]. Furthermore, to capture the performance of an ATG link between a ground device and a UAV, the channel propagation model incorporating blockages from buildings is required. Based on statistical model for building blockages [228], the LoS probability in the product of a sequence of terms and its approximation via a sigmoid function were formulated, and the optimal altitude for deploying a UAV with maximum coverage was studied in [229].

There have been a lot of studies on either optimizing network resources or developing techniques for realistic system-level analysis of UAV networks on coverage, but it has been pointed out by [225] that very few studies have investigated the secrecy performance of UAV networks, and only ground-based EDs were considered in those scenarios. In [230], the optimization of the secrecy rate of a UAV-enabled mobile relay system was formulated, and a performance gain over static relaying was achieved. By jointly designing the trajectory and transmit power of the UAV, an optimization algorithm designed to achieve the average worst-case secrecy rate improvement in UAV-to-ground communications was proposed in [231]. By considering the transmit power of both the ground user and the UAV in the joint design with trajectory, the average secrecy rate over a finite horizon was maximized for both the UAV-to-ground and ground-to-UAV communications in UAV assisted 5G wireless network [232]. Additionally, the authors of [225] investigated the secrecy performance of UAV networks working in the millimeter wave band, where the UAVs can be used either for information transmission or jamming, and it was revealed that the average achievable secrecy rate does not change monotonically with an increasing proportion of UAV jammers. Recently, the authors of [233] considered the application of a UAV friendly jammer to improve the PLS of a legitimate link, where the location of the ground ED is unknown. Meanwhile, the authors of [234] proposed to employ a mobile UAV-enabled jammer to improve the secrecy rate of the ground wire-tap channel by moving towards and opportunistically jamming the discovered ground ED.

UAV jamming is more appealing than ground jamming, because the air-to-air wireless channel from the UAV jammer to UEDs is in a pure LoS state with free space path loss, while the ground-to-air channel from a ground jammer to the UEDs would experience the additional excess path loss in the urban environment due to shadowing and scattering caused by man-made structures [229]. Although it is known that increasing the jamming power will pose a stronger interference to both the UEDs and the legitimate ground receiver, how the secrecy performance behaves with respect to this increase is still unknown. Furthermore, analyses of coverage and secrecy performance in the previous literature have suffered from a tractability problem when the LoS probability is considered, since the analysis always results in multi-integral expressions. This makes it difficult to extract insight from the analysis.

6.1.2 Contributions

This chapter focuses on the secrecy performance of ground-based communications in the presence of a UAV jammer and UEDs. The main contributions of the chapter are summarized as follows:

1. **LoS model:** This is the first work to propose an approximation to simplify the modeling of the probability of LoS channels, which allows us to get tractable formulations in the analysis of wireless networks concerning ATG channels. The trend of the LoS probability with respect to the height of UAVs has been captured in a simplistic manner.

2. **UAV jammer:** A UAV jammer is introduced for improving the security of the ground communication, and the cumulative distribution function (CDF) of the signal-to-interference ratio (SIR) from a ground transmitter to a UED, which is subject to interference from the UAV jammer, is derived.

3. **SCP:** The SCP of the ground link in the presence of randomly located UEDs for the non-colluding scenario is formulated. The trends of the SCP in some environments with respect to different transmit signal to jamming power ratios, and the locations of the UAV jammer have been analyzed.

The rest of the chapter is structured as follows. Section 6.2 begins with a description of the system model, then addresses the LoS probability and its approximations. Section 6.3 focuses on the derivation of the SCP. Section 6.4 focuses on the trends of the SCP for different parameters. Section 6.5 gives the simulation results and discussion, and Section 6.6 concludes the chapter.

6.2 System Model

6.2.1 Network Layout

As shown in Figure 6.1, transmitter s at $(0,0,0) \in \mathbb{R}^3$ connects to receiver d at $(x_d, y_d, 0)$ via the legitimate link, where x_d and y_d denote the locations of d on the x-axis and y-axis, respectively. There are n UEDs uniformly distributed in a disk, forming a uniform binomial point process (BPP) [126]. The disk is denoted as $O(t, R_1)$, where O denotes the disk of radius R_1 centred at t. The coordinates of the origin of the disk are $(0,0,H)$ so that the center of the circular plane t is H meters right above the transmitter s on the ground, and the disk is also parallel to the ground[1]. The UEDs work independently to decode the received signal on their links. Meanwhile, a UAV jammer j is also located within the disk $O(t, R_1)$ and continually sends a jamming signal. The ground channel is assumed to experience Rayleigh fading and path loss, while the channel model for the ATG communications is based on the probabilistic LoS and non-line-of-sight (NLoS) links given by [229,235]. The air-to-air communication channel is assumed to follow Friis free space transmission. The transmit powers of s and j are given by P_s and P_j, respectively. The proposed system model can be applied to the application scenarios such as counter-surveillance against the illegal amateur drones monitoring ground radio communications and anti-eavesdropping against compromised or untrustworthy UAV base stations in future UAV-assisted communications systems.

[1]The ground between s and d is assumed to be flat, and the effect due to the curvature of the earth is negligible.

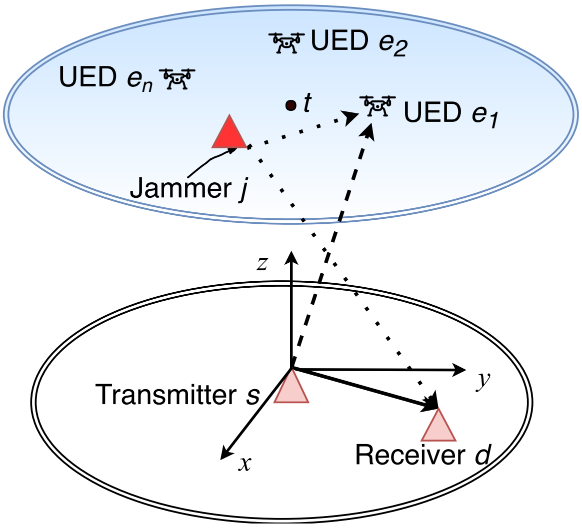

Figure 6.1: The system model for communication in the presence of UEDs and the UAV jammer. The bold solid arrow denotes the legitimate link. For UED e_1, the dashed arrow denotes the wire-tap link, and the dotted arrows denote the jamming links.

6.2.2 Channel Model

6.2.2.1 Air-to-Air Channel Model

Since no major obstacles are obstructing the communications in the sky, the air-to-air channel follows Friis free space transmission. The received jamming power from the UAV jammer j to a UED e is given by

$$P_{j,e} = P_j(\lambda/4\pi)^2 l_{j,e}^{-\alpha} \tag{6.1}$$

where $\alpha = 2$ is the free space path loss (FSPL) exponent, and $l_{x,y}$ is the distance between nodes x and y.

6.2.2.2 ATG Channel Models

The potential existence of buildings and other obstructions lying in the propagation path results in the presence of mixed LoS/NLoS distributions for channel conditions between an air terminal and a ground terminal. According to [235], the ATG channel model will be mainly based on probabilistic LoS and NLoS links instead of following a classical fading channel. Therefore, the corresponding received signal powers at e from transmitter s for LoS and NLoS links are written as

$$P_{s,e} = \begin{cases} \eta_{\mathrm{L}} P_s (\lambda/4\pi)^2 l_{s,e}^{-\alpha}, & \text{LoS link} \\ \eta_{\mathrm{N}} P_s (\lambda/4\pi)^2 l_{s,e}^{-\alpha}, & \text{NLoS link} \end{cases} \tag{6.2}$$

and $\eta_{\mathrm{L}}, \eta_{\mathrm{N}}$ refer to the mean values of excess path loss added to the FSPL, where $(\eta_{\mathrm{L}}, \eta_{\mathrm{N}})$ is measured at carrier frequency $\nu = 2$ GHz in dB for suburban, urban, dense urban, and highrise urban areas to be $(-0.1, -21), (-1.0, -20), (-1.6, -23)$, and $(-2.3, -34)$, respectively [229].

LoS probability and sigmoid fitting The probabilities for a link (s, e) to be either LoS or NLoS can be denoted as $\mathbb{P}_{\mathrm{L}}^{s,e}$ and $\mathbb{P}_{\mathrm{N}}^{s,e} = 1 - \mathbb{P}_{\mathrm{L}}^{s,e}$, respectively. According to [228, 229],

$$\begin{aligned} \mathbb{P}_{\mathrm{L}}^{s,e} &= \prod_{l=0}^{f(l_{t,e})} \left[1 - \exp\left(-\frac{\left(H - (l+1/2)H/(f(l_{t,e})+1)\right)^2}{2\sigma^2} \right) \right] \\ &\approx \frac{1}{1 + C\exp\left(-B\left(\theta_{s,e} - C\right)\right)} \end{aligned} \tag{6.3}$$

where $f(l_{t,e}) = \lfloor l_{t,e}\sqrt{\rho_1\rho_2} - 1 \rfloor$, $l_{t,e}$ is the ground distance between s and e, ρ_1 is the ratio of built-up land area to the total land area, ρ_2 is the mean number of buildings per unit area (buildings/km^2), and σ is the scale parameter of the Rayleigh probability density function (PDF), which gives the height distribution of buildings in meters. The environment parameters (ρ_1, ρ_2, σ) for typical environments are suburban $(0.1, 750, 8)$, urban $(0.3, 500, 15)$, dense urban $(0.5, 300, 20)$, and highrise urban $(0.5, 300, 50)$, respectively [229]. Note that increasing H will increase the smoothness of the plot of the product, and $\mathbb{P}_{\mathrm{L}}^{s,e}$ can be considered as a continuous function of elevation angle and the environment parameters for a large H [229]. The approximation

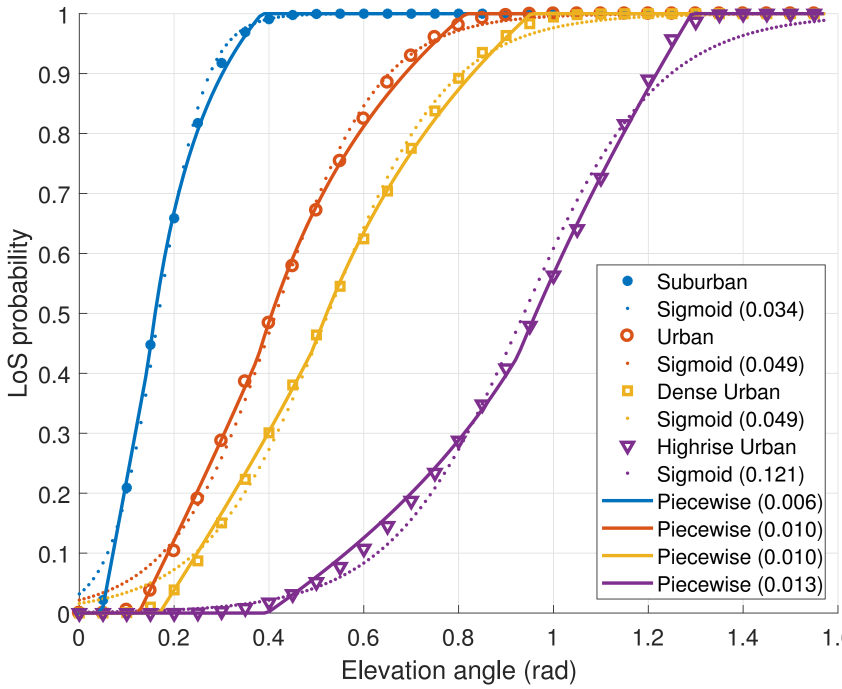

Figure 6.2: Plots of the LoS probabilities for different urban environments based on the exact product, the sigmoid fitting and the proposed piecewise fitting. The goodness of fit measured by root-mean-square error is given inside the brackets. © 2019 IEEE.

to the LoS probability of an ATG link is given by a sigmoid function, where C and B are constant values depending on the aforementioned environment, and $\theta_{s,e}$ is the elevation angle in radians, which is given by $\theta_{s,e} = \tan^{-1}\left(\frac{H}{l_{t,e}}\right)$. The ATG channel model also applies to the received jamming power $P_{j,d}$ with LoS and NLoS probability given by $\mathbb{P}_{\mathrm{L}}^{j,d}$ and $\mathbb{P}_{\mathrm{N}}^{j,d}$.

Proposed piecewise fitting Although the sigmoid fitting provides a reasonably good approximation to the actual LoS probability, it provides a non-linear relationship to $l_{t,e}$ and has been shown to only give analytical forms which are non-trivial to evaluate. Based on the value of the elevation angle, each curve of the LoS probability can be divided into three approximated regions: LoS region for the link in a pure LoS state with large elevation angles, NLoS region for the link in a pure NLoS state with small elevation angles, and a transitional region where the link is in mixed LoS/NLoS distributions. The transitional region can be further divided into two regions based on the slope of the curve. As a result, a piecewise fitting model is proposed in (6.4), which not only gives a meaningful relationship between the LoS probability and $l_{t,e}$ but also provides a tractable way to calculate the SCP. The piecewise approximation is given by

$$\mathbb{P}_{\mathrm{L}}^{s,e} = \begin{cases} 1, & \text{if } \theta_{s,e} > \tan^{-1}\frac{H}{\ell_1} \\ c_3\cot(\theta_{s,e}) + c_4, & \text{if } \tan^{-1}\frac{H}{\ell_2} < \theta_{s,e} \le \tan^{-1}\frac{H}{\ell_1} \\ 0, & \text{if } \theta_{s,e} \le \tan^{-1}\frac{H}{\ell_3} \\ c_1\tan(\theta_{s,e}) + c_2, & \text{otherwise} \end{cases} \tag{6.4}$$

where $\ell_1 = H\frac{1-c_4}{c_3}$, $\ell_2 = \frac{2Hc_1}{c_4-c_2-\sqrt{(c_4-c_2)^2+4c_1c_3}}$, $\ell_3 = -H\frac{c_1}{c_2}$, c_1, c_2, c_3 and c_4 are given in Table 6.1, and they are obtained by Algorithm 5. The corresponding results for different typical environments are plotted in Figure 6.2. In this figure, the proposed piecewise fitting outperforms the sigmoid fitting in the goodness of fit measured by root-mean-square error. The former is at least four times better than the latter in the suburban, urban, and dense urban environments and nine times better in the highrise urban environment. Since $\tan(\theta_{s,e}) = \frac{H}{l_{t,e}}$, (6.4) can be further written as

$$\mathbb{P}_{\mathrm{L}}^{s,e} = \begin{cases} 1, & \text{if } l_{t,e} < \ell_1 \\ c_3 l_{t,e}/H + c_4, & \text{if } \ell_1 \le l_{t,e} < \ell_2 \\ c_1 H/l_{t,e} + c_2, & \text{if } \ell_2 \le l_{t,e} < \ell_3 \\ 0, & \text{otherwise.} \end{cases} \tag{6.5}$$

Algorithm 5: Finding parameters c_1, c_2, c_3 and c_4 for link (s, e) given environment parameters (ρ_1, ρ_2, σ).

Given: Environment parameters (ρ_1, ρ_2, σ), thresholds: $c_l = 0.005$, $c_m = 0.5$, and $c_u = 0.995$.

1 Generate 10^4 evenly spaced samples from $[0, \pi/2]$, and obtain the corresponding samples of LoS probabilities with the first step of (6.3).

2 Create a new data set D_{t_1} from the samples of LoS probabilities whose values are bigger than c_l and smaller than c_m.

3 Find the coefficients c_1 and c_2 of the model function $c_1 \tan(\theta_{s,e}) + c_2$ by fitting the function to D_{t_1} with the trust region reflective least squares algorithm.

4 Let $c_1 \tan(\theta_{s,e}) + c_2 = 0$, the maximum elevation angle for having only the NLoS link state is $\tan^{-1}\left(-\frac{c_2}{c_1}\right)$.

5 Create a new data set D_{t_2} from the samples of LoS probabilities whose values are bigger than c_m and smaller than c_u.

6 Find the coefficients c_3 and c_4 of the model function $c_3 \cot(\theta_{s,e}) + c_4$ by fitting the function to D_{t_2} with the trust region reflective least squares algorithm.

7 Let $c_3 \cot(\theta_{s,e}) + c_4 = 1$, the minimum elevation angle for having only the LoS link state is $\tan^{-1}\left(\frac{c_3}{1-c_4}\right)$.

8 The elevation angle at the inflection point, where the LoS probability changes from $c_1 \tan(\theta_{s,e}) + c_2$ to $c_3 \cot(\theta_{s,e}) + c_4$ is $\tan^{-1}\left(\frac{c_4 - c_2 - \sqrt{(c_4-c_2)^2 + 4c_1c_3}}{2c_1}\right)$, is obtained by solving $c_1 \tan(\theta_{s,e}) + c_2 = c_3 \cot(\theta_{s,e}) + c_4$, and then selecting the root which provides a better fit to the samples of LoS probabilities.

6.2.2.3 Ground-to-Ground Channel Model

For ground communications, the log-distance path loss model is used to characterize the legitimate wireless link from the transmitter s to the receiver d. The received power at d from s is written as

$$P_{s,d} = P_s(\lambda/4\pi)^2 l_{s,d}^{-\beta} |h_{s,d}|^2 \tag{6.6}$$

where λ is the carrier wavelength, $|h_{s,d}|^2$ is the channel gain associated with the Rayleigh fading, and β is the path loss exponent for ground communications.

Table 6.1: Parameters for (6.4) and (6.5) © 2019 IEEE

	Suburban	Urban	Dense urban	Highrise urban
c_1	4.215	1.581	1.201	0.4717
c_2	-0.2007	-0.1991	-0.2051	-0.1972
c_3	-0.1341	-0.3618	-0.4864	-1.223
c_4	1.331	1.341	1.346	1.351

6.3 Derivation of the SCP

6.3.1 Secrecy Capacity

Let $\Phi = \{1, 2, ..., n\}$ denote the collection of n UEDs. The secrecy capacity of a wireless link is the difference between the capacity of this link and the capacity achieved via a collection of wire-tap links. The general form is given as [236]

$$\begin{aligned} C_s &= \left[\log_2(1+\mathrm{SINR}_{s,d}) - \log_2\left(1+\max_{e\in\Phi}(\mathrm{SINR}_{s,e})\right)\right]^+ \\ &= \left[\log_2\left(\frac{1+\frac{P_{s,d}}{P_{j,d}+N_0}}{1+\max_{e\in\Phi}\left(\frac{P_{s,e}}{P_{j,e}+N_e}\right)}\right)\right]^+ \\ &> \left[\log_2\left(\frac{\Gamma_1}{\max_{e\in\Phi}\Gamma_2}\right)\right]^+ \end{aligned} \tag{6.7}$$

where $\mathrm{SINR}_{s,y}$ denotes the signal-to-interference-plus-noise ratio from s to y, N_0 is the additive white Gaussian noise (AWGN) power at the ground receiver d, N_e is the AWGN power at a UED, and $[x]^+$ denotes $\max(0, x)$ [220]. $\Gamma_1 = 1+\frac{P_{s,d}}{P_{j,d}+N_0}$ represents $1+\mathrm{SINR}_{s,d}$, and $\Gamma_2 = 1+\frac{P_{s,e}}{P_{j,e}}$ represents $1+\mathrm{SIR}$ from s to e, where the interference is due to UAV jammer j.

6.3.2 SCP Formulation

The SCP is defined as

$$p_c = \mathbb{P}(C_s > \mathcal{R}_t) \geq \mathbb{P}\left(\frac{\Gamma_1}{\max_{e\in\Phi}\Gamma_2} > 2^{\mathcal{R}_t}\right) \tag{6.8}$$

where $\mathcal{R}_t \geq 0$ is the target secrecy rate. In addition,

$$p_c \approx \mathbb{P}\left(\frac{\Gamma_1}{\max_{e\in\Phi}\Gamma_2} > 2^{\mathcal{R}_t}\right) \tag{6.9}$$

when all the UEDs are working in an interference-limited environment as the result of a large jamming signal. To evaluate the above probability, the following calculations are required.

Since Γ_1 is a random variable related to $|h_{s,d}|^2$, the CDF of Γ_1 can be written as

$$\begin{aligned} F_{\Gamma_1}(\gamma_1) =& \mathbb{P}\left(1 + \frac{P_{s,d}}{P_{j,d}+N_0} < \gamma_1\right) \\ =& \mathbb{P}\left(\frac{|h_{s,d}|^2}{\Lambda(\eta_{\mathrm{L}})} < \gamma_1 - 1\right)\mathbb{P}_{\mathrm{L}}^{j,d} + \mathbb{P}\left(\frac{|h_{s,d}|^2}{\Lambda(\eta_{\mathrm{N}})} < \gamma_1 - 1\right)\mathbb{P}_{\mathrm{N}}^{j,d} \\ =& 1 - \exp\left((1-\gamma_1)\Lambda(\eta_{\mathrm{L}})\right)\mathbb{P}_{\mathrm{L}}^{j,d} - \exp\left((1-\gamma_1)\Lambda(\eta_{\mathrm{N}})\right)\mathbb{P}_{\mathrm{N}}^{j,d} \end{aligned} \tag{6.10}$$

where $\Lambda(\eta) = \frac{l_{s,d}^{\beta}}{P_s}\left(\eta l_{j,d}^{-\alpha}P_j + N_0(\lambda/4\pi)^{-2}\right)$, $l_{j,d}^2 = l_{t,j}^2 + l_{s,d}^2 - 2l_{t,j}l_{s,d}\cos\left(\varphi_{j'} - \varphi_d\right) + H^2$, j' denotes the projection of j onto the xy-plane; $\varphi_{j'}$ and φ_d denote the angles of $l_{s,j'}$ and $l_{s,d}$ measured counterclockwise from the x-axis. Thus, the corresponding PDF is given by $f_{\Gamma_1}(\gamma_1) = \frac{\mathrm{d}}{\mathrm{d}\gamma_1}F_{\Gamma_1}(\gamma_1)$ such that

$$f_{\Gamma_1}(\gamma_1) = \Lambda(\eta_{\mathrm{L}})\exp\left((1-\gamma_1)\Lambda(\eta_{\mathrm{L}})\right)\mathbb{P}_{\mathrm{L}}^{j,d} + \Lambda(\eta_{\mathrm{N}})\exp\left((1-\gamma_1)\Lambda(\eta_{\mathrm{N}})\right)\mathbb{P}_{\mathrm{N}}^{j,d}. \tag{6.11}$$

Let e' denote the projection of e onto the xy-plane, $\phi = \varphi_{j'} - \varphi_{e'}$, and $\varphi_{e'}$ denotes the angle of $l_{s,e'}$ measured counterclockwise from the x-axis. Γ_2 is a random variable related to the position of one UED e, which is uniformly distributed on the disk $O(t, R_1)$. Thus, the CDF of Γ_2 is given by

$$\begin{aligned} F_{\Gamma_2}(\gamma_2) &= \mathbb{E}_e\left[F_1(\gamma_2, l_{t,e}, \phi)\right] \\ &= \frac{1}{\pi R_1^2}\int_0^{2\pi}\int_0^{R_1} F_1(\gamma_2, l_{t,e}, \phi) l_{t,e}\, \mathrm{d}l_{t,e}\mathrm{d}\phi \end{aligned} \tag{6.12}$$

where

$$F_1(\gamma_2, l_{t,e}, \phi) = g(\gamma_2, \eta_{\mathrm{L}}, l_{t,e}, \phi)\mathbb{P}_{\mathrm{L}}^{s,e} + g(\gamma_2, \eta_{\mathrm{N}}, l_{t,e}, \phi)\mathbb{P}_{\mathrm{N}}^{s,e} \tag{6.13}$$

and $g(\gamma, \eta, \ell, \phi) = \mathbb{1}\left(1 + \frac{(H^2+\ell^2)^{\frac{-\alpha}{2}}\eta P_s}{\left(l_{t,j}^2+\ell^2-2l_{t,j}\ell\cos\phi\right)^{\frac{-\alpha}{2}} P_j} \le \gamma\right)$.

6.3.3 Calculation of the SCP

When $\mathbb{P}_{\mathrm{L}}^{s,e}$ is given by (6.3), it is hard to find a closed-form expression for (6.12). To make progress, (6.5) is used instead, which can yield a closed-form expression for (6.12) with any given R_1 and H. With the help of (6.5), the LoS probability can be divided into multiple regions so that their contributions to $F_{\Gamma_2}(\gamma_2)$ can be calculated independently. This decomposition technique to obtain (6.12) seems to be tedious, but necessary, because it leads to a tractable solution. Throughout the following discussion, a number of propositions are referred to, which will be presented in Section 6.3.4.

For $R_1 < \ell_1$, where l_1 is considered in (6.5), the ATG link between transmitter s and UED e is always in a pure LoS state since $l_{t,e} \le R_1$. Following Proposition 1, then

$$F_{\Gamma_2}(\gamma_2) = \int_0^{2\pi}\int_0^{R_1} g(\gamma_2, \eta_{\mathrm{L}}, l_{t,e}, \phi)\frac{l_{t,e}}{\pi R_1^2}\, \mathrm{d}l_{t,e}\mathrm{d}\phi = F_{\Gamma_3}(\gamma_2, \eta_{\mathrm{L}}, R_1). \tag{6.14}$$

For $\ell_1 \le R_1 < \ell_2$, the ATG link between transmitter s and UED e is in a pure LoS state if $l_{t,e} < \ell_1$, and the ATG link between transmitter s and UED e is in the mixed LoS/NLoS distributions with $\mathbb{P}_{\mathrm{L}}^{s,e} = c_3 l_{t,e}/H + c_4$ if $\ell_1 \le l_{t,e} \le R_1$. Following Propositions 1 and 3, then

$$\begin{aligned} F_{\Gamma_2}(\gamma_2) = & \int_0^{2\pi} \int_0^{\ell_1} g(\gamma_2, \eta_{\mathrm{L}}, l_{t,e}, \phi) \frac{l_{t,e}}{\pi R_1^2} \, \mathrm{d}l_{t,e} \mathrm{d}\phi + \int_0^{2\pi} \int_{\ell_1}^{R_1} F_1(\gamma_2, l_{t,e}, \phi) \frac{l_{t,e}}{\pi R_1^2} \, \mathrm{d}l_{t,e} \mathrm{d}\phi \\ = & F_{\Gamma_3}(\gamma_2, \eta_{\mathrm{L}}, \ell_1) + F_{\Gamma_5}(\gamma_2, \eta_{\mathrm{L}}, \eta_{\mathrm{N}}, R_1) - F_{\Gamma_5}(\gamma_2, \eta_{\mathrm{L}}, \eta_{\mathrm{N}}, \ell_1). \end{aligned} \tag{6.15}$$

For $\ell_2 \le R_1 < \ell_3$, the ATG link between transmitter s and UED e is in a pure LoS state if $l_{t,e} < \ell_1$, the ATG link between transmitter s and UED e is in the mixed LoS/NLoS distributions with $\mathbb{P}_{\mathrm{L}}^{s,e} = c_3 l_{t,e}/H + c_4$ if $\ell_1 \le l_{t,e} < \ell_2$, and the ATG link between transmitter s and UED e is in the mixed LoS/NLoS distributions with $\mathbb{P}_{\mathrm{L}}^{s,e} = c_1 H / l_{t,e} + c_2$ if $\ell_2 \le l_{t,e} \le R_1$. Following Propositions 1, 2, and 3, then

$$\begin{aligned} F_{\Gamma_2}(\gamma_2) = & \int_0^{2\pi} \int_0^{\ell_1} g(\gamma_2, \eta_{\mathrm{L}}, l_{t,e}, \phi) \frac{l_{t,e}}{\pi R_1^2} \, \mathrm{d}l_{t,e} \mathrm{d}\phi + \int_0^{2\pi} \int_{\ell_1}^{R_1} F_1(\gamma_2, l_{t,e}, \phi) \frac{l_{t,e}}{\pi R_1^2} \, \mathrm{d}l_{t,e} \mathrm{d}\phi \\ = & F_{\Gamma_3}(\gamma_2, \eta_{\mathrm{L}}, \ell_1) + F_{\Gamma_5}(\gamma_2, \eta_{\mathrm{L}}, \eta_{\mathrm{N}}, \ell_2) - F_{\Gamma_5}(\gamma_2, \eta_{\mathrm{L}}, \eta_{\mathrm{N}}, \ell_1) + \\ & F_{\Gamma_4}(\gamma_2, \eta_{\mathrm{L}}, \eta_{\mathrm{N}}, R_1) - F_{\Gamma_4}(\gamma_2, \eta_{\mathrm{L}}, \eta_{\mathrm{N}}, \ell_2). \end{aligned} \tag{6.16}$$

For $R_1 \ge \ell_3$, the ATG link between transmitter s and UED e is in a pure LoS state if $l_{t,e} < \ell_1$, the ATG link between transmitter s and UED e is in the mixed LoS/NLoS distributions with $\mathbb{P}_{\mathrm{L}}^{s,e} = c_3 l_{t,e}/H + c_4$ if $\ell_1 \le l_{t,e} < \ell_2$, the ATG link between transmitter s and UED e is in the mixed LoS/NLoS distributions with $\mathbb{P}_{\mathrm{L}}^{s,e} = c_1 H / l_{t,e} + c_2$ if $\ell_2 \le l_{t,e} < \ell_3$, and the ATG link between transmitter s and UED e is in a pure NLoS state if $\ell_3 \leq l_{t,e} \leq R_1$. Following Propositions 1, 2 and 3, then

$$
\begin{aligned}
F_{\Gamma_2}(\gamma_2) =& \int_0^{2\pi} \int_0^{\ell_1} g(\gamma_2, \eta_{\mathrm{L}}, l_{t,e}, \phi) \frac{l_{t,e}}{\pi R_1^2} \, \mathrm{d}l_{t,e} \mathrm{d}\phi + \int_0^{2\pi} \int_{\ell_1}^{\ell_3} F_1(\gamma_2, l_{t,e}, \phi) \frac{l_{t,e}}{\pi R_1^2} \, \mathrm{d}l_{t,e} \mathrm{d}\phi + \\
& \int_0^{2\pi} \int_{\ell_3}^{R_1} g(\gamma_2, \eta_{\mathrm{N}}, l_{t,e}, \phi) \frac{l_{t,e}}{\pi R_1^2} \, \mathrm{d}l_{t,e} \mathrm{d}\phi \\
=& F_{\Gamma_3}(\gamma_2, \eta_{\mathrm{L}}, \ell_1) + F_{\Gamma_5}(\gamma_2, \eta_{\mathrm{L}}, \eta_{\mathrm{N}}, \ell_2) - F_{\Gamma_5}(\gamma_2, \eta_{\mathrm{L}}, \eta_{\mathrm{N}}, \ell_1) + F_{\Gamma_4}(\gamma_2, \eta_{\mathrm{L}}, \eta_{\mathrm{N}}, \ell_3) - \\
& F_{\Gamma_4}(\gamma_2, \eta_{\mathrm{L}}, \eta_{\mathrm{N}}, \ell_2) + F_{\Gamma_3}(\gamma_2, \eta_{\mathrm{N}}, R_1) - F_{\Gamma_3}(\gamma_2, \eta_{\mathrm{N}}, \ell_3).
\end{aligned} \tag{6.17}
$$

As a result of the above decomposition, p_c is lower bounded by

$$
\mathbb{P}\left(\frac{\Gamma_1}{\max_{e \in \Phi} \Gamma_2} > 2^{\mathcal{R}_t} \right) = \int_1^{\infty} F_{\Gamma_2} \left(\frac{\gamma_1}{2^{\mathcal{R}_t}} \right)^n f_{\Gamma_1}(\gamma_1) \, \mathrm{d}\gamma_1. \tag{6.18}
$$

6.3.4 Propositions

All three propositions given below rely on Lemma 6, which is given in the Appendix at the end of the chapter.

Proposition 1. Let $r \leq R_1$, assuming that the link (s, e) is always in the same channel state (i.e, pure LoS or pure NLoS) with gain η, the CDF of Γ_2 conditioning on the UED e being active only within the disk $O(t, r)$ is given by

$$
F_{\Gamma_3}(y, \eta, r) = \int_0^{2\pi} \int_0^{r} \frac{g(\gamma_2, \eta, l_{t,e}, \phi) l_{t,e}}{\pi R_1^2} \, \mathrm{d}l_{t,e} \mathrm{d}\phi = \frac{S_1(y, \eta, r)}{\pi R_1^2 / 2} \tag{6.19}
$$

Table 6.2: Table of Conditions © 2019 IEEE

Case index	Condition
1	$A < 0, B \leq 0, r^2 A < B, \frac{-r^2A-B}{2r} \leq l_{t,j}, l_{t,j} \neq \sqrt{BA}$
2	$A < 0, B \leq 0, r^2 A = B, \frac{-r^2A-B}{2r} \leq l_{t,j}, l_{t,j} \neq \sqrt{BA}$
3	$A < 0, B \leq 0, r^2 A < B, \sqrt{BA} < l_{t,j} < \frac{-r^2A-B}{2r}$
4	$A < 0, B \leq 0, r^2 A > B, \frac{-r^2A-B}{2r} \leq l_{t,j}$
5	Other cases under $A < 0, B \leq 0$
6	$A > 0, B \geq 0, r^2 A > B, \frac{r^2A+B}{2r} \leq l_{t,j}, l_{t,j} \neq \sqrt{BA}$
7	$A > 0, B \geq 0, r^2 A = B, \frac{r^2A+B}{2r} \leq l_{t,j}, l_{t,j} \neq \sqrt{BA}$
8	$A > 0, B \geq 0, r^2 A > B, \sqrt{BA} < l_{t,j} < \frac{r^2A+B}{2r}$
9	$A > 0, B \geq 0, r^2 A < B, \frac{r^2A+B}{2r} \leq l_{t,j}$
10	$A < 0, B > 0, l_{t,j} \geq \frac{\left\|r^2A+B\right\|}{2r}$
11	$A < 0, B > 0, -r^2A > B, l_{t,j} < \frac{-r^2A-B}{2r}$
12	Other cases under $A < 0, B > 0$
13	$A > 0, B < 0, -r^2A > B, l_{t,j} < \frac{-r^2A-B}{2r}$
14	$A > 0, B < 0, l_{t,j} \geq \frac{\|r^2A+B\|}{2r}$
15	$A > 0, B < 0, -r^2A < B, l_{t,j} < \frac{r^2A+B}{2r}$
16	$A = 0, \frac{l_{t,j}^2-H^2}{2r} \leq l_{t,j}, l_{t,j} > H$
17	$A = 0, \frac{H^2-l_{t,j}^2}{2r} \leq l_{t,j}, l_{t,j} < H$
18	$A = 0, l_{t,j} = H$
19	$A = 0, l_{t,j} < \frac{H^2-l_{t,j}^2}{2r}$

where

$$S_1(y, \eta, r) = \begin{cases} D_1 + D_2 - \frac{1}{2}D_3, & \text{cases 1, 9, 10} \\ D_2 + D_4, & \text{cases 2, 7} \\ \frac{1}{2}\pi r^2 - D_3, & \text{cases 3, 11} \\ D_1 + D_2 + \frac{1}{2}D_3, & \text{cases 4, 6, 14} \\ \frac{1}{2}\pi r^2, & \text{cases 5, 12, 13, 19} \\ D_3, & \text{cases 8, 15} \\ D_5, & \text{cases 16, 17, 18} \\ 0, & \text{otherwise} \end{cases} \tag{6.20}$$

and all the cases with index numbers are given in Table 6.2,

$$A = 1 - \left((y-1)\frac{P_j}{\eta P_s}\right)^{\frac{2}{\alpha}}$$

$$B = l_{t,j}^2 - (1-A)H^2$$

$$a_1 = Ar^2 + B$$

$$D_1 = \frac{AB - l_{t,j}^2}{2A^2}\cot^{-1}\left(\frac{a_1 - 2B}{\sqrt{4l_{t,j}^2 r^2 - {a_1}^2}}\right)$$

$$D_2 = \frac{\pi r^2}{4} - \frac{A}{4A^2}\sqrt{4l_{t,j}^2 r^2 - {a_1}^2} - \frac{a_1 A - l_{t,j}^2}{2A^2}\csc^{-1}\left(\frac{2l_{t,j}r}{a_1}\right)$$

$$D_3 = \frac{l_{t,j}^2 - AB}{2A^2}\pi$$

$$D_4 = \frac{(a_1 - 2B)\sqrt{4j^2 r^2 - {a_1}^2}}{4A^2 r^2}$$

$$D_5 = \frac{1}{2}r^2\sec^{-1}\left(\frac{2l_{t,j}r}{a_1}\right) - \frac{\left(l_{t,j}^2 - H^2\right)\sqrt{4l_{t,j}^2 r^2 - \left(H^2 - l_{t,j}^2\right)^2}}{8l_{t,j}^2}.$$

Proof.

$$\begin{aligned}
&\frac{1}{\pi R_1^2}\int_0^{2\pi}\int_0^r g(y,\eta_{\mathrm{L}},l_{t,e},\phi)l_{t,e}\,\mathrm{d}l_{t,e}\mathrm{d}\phi \\
&= \frac{1}{\pi R_1^2}\int_{o_\phi(\eta)}\int_{o_{l_{t,e}}(\eta)} l_{t,e}\,\mathrm{d}l_{t,e}\mathrm{d}\phi \\
&= \frac{r^2}{R_1^2} - \frac{1}{\pi R_1^2}\int_{o'_\phi(\eta)}\int_{o'_{l_{t,e}}(\eta)} l_{t,e}\,\mathrm{d}l_{t,e}\mathrm{d}\phi
\end{aligned} \tag{6.21}$$

where $o_\phi(\eta)$ and $o_{l_{t,e}}(\eta)$ are the domains so that

$$1 + \frac{(H^2 + l_{t,e}^2)^{\frac{-\alpha}{2}}\eta P_s}{\left(l_{t,j}^2 + l_{t,e}^2 - 2l_{t,j}l_{t,e}\cos\phi\right)^{\frac{-\alpha}{2}}P_j} \le y$$

while $o'_{\phi}(\eta)$ and $o'_{l_{t,e}}(\eta)$ are the domains so that

$$1+\frac{(H^2+l_{t,e}^2)^{\frac{-\alpha}{2}}\eta P_s}{\left(l_{t,j}^2+l_{t,e}^2-2l_{t,j}l_{t,e}\cos\phi\right)^{\frac{-\alpha}{2}}P_j}>y.$$

Given Lemma 6, (6.19) is achieved. This concludes the proof. □

Proposition 2. Let $r \leq R_1$, assuming that the mixed LoS/NLoS distributions exist for link (s, e), and the (quasi-) LoS probability is $\mathbb{P}_{\mathrm{L}}^{s,e} = c_1 H/l_{t,e} + c_2$, the CDF of Γ_2 conditioning on the UED e being active only within the disk $O(t, r)$ is given by

$$\begin{aligned} F_{\Gamma_4}(y,\eta_{\mathrm{L}},\eta_{\mathrm{N}},r) =& \frac{2}{\pi R_1^2}\big(c_2 S_1(y,\eta_{\mathrm{L}},r)+c_1 H S_2(y,\eta_{\mathrm{L}},r)+ \\ & (1-c_2)S_1(y,\eta_{\mathrm{N}},r)-c_1 H S_2(y,\eta_{\mathrm{N}},r)\big) \end{aligned} \tag{6.22}$$

$$S_2(y,\eta,r)=\begin{cases} G_1-G_2+G_3-G_4, & \text{cases 1, 2} \\ \pi r+G_1-2G_2, & \text{cases 3} \\ G_3+G_4-G_2, & \text{cases 4, 14} \\ \pi r, & \text{cases 5, 12, 13, 19} \\ G_3+G_4-G_5, & \text{cases 6, 7} \\ -G_5, & \text{case 8} \\ G_3-G_4, & \text{cases 9, 10} \\ \pi r-G_2, & \text{case 11} \\ -G_2, & \text{case 15} \\ G_6, & \text{cases 16, 17} \\ \frac{1}{2}\pi r, & \text{case 18} \\ 0, & \text{otherwise} \end{cases} \tag{6.23}$$

with Table 6.2,

$$G_0 = \frac{2\sqrt{-AB + l_{t,j}^2}}{-A}$$

$$G_1 = G_0 \mathsf{E}\left(\sec^{-1}\frac{-l_{t,j}}{\sqrt{BA}} | \frac{l_{t,j}^2}{l_{t,j}^2 - AB}\right)$$

$$G_2 = G_0 \mathsf{E}\left(\frac{l_{t,j}^2}{l_{t,j}^2 - AB}\right)$$

$$G_3 = -\frac{\sqrt{4l_{t,j}^2 r^2 - {a_1}^2}}{2Ar} + r\sec^{-1}\left(\frac{2l_{t,j}r}{a_1}\right)$$

$$G_4 = G_0 \mathsf{E}\left(\sec^{-1}\left(\frac{2l_{t,j}r}{a_1}\right) | \frac{l_{t,j}^2}{l_{t,j}^2 - AB}\right)/2$$

$$G_5 = G_0 \mathsf{E}\left(\sec^{-1}\left(\frac{l_{t,j}}{\sqrt{BA}}\right) | \frac{l_{t,j}^2}{l_{t,j}^2 - AB}\right)$$

$$G_6 = r\cos^{-1}\left(\frac{l_{t,j}^2 - H^2}{2l_{t,j}r}\right) - \frac{l_{t,j}^2 - H^2}{2l_{t,j}}\ln\frac{\sqrt{4l_{t,j}^2 r^2 - \left(H^2 - l_{t,j}^2\right)^2} + 2l_{t,j}r}{\left|l_{t,j}^2 - H^2\right|}$$

$\mathsf{E}(k) = \mathsf{E}(\pi/2 \mid k)$ and $\mathsf{E}(\phi \mid k) = \int_0^\phi \sqrt{1 - k^2\sin^2\theta}\,\mathrm{d}\theta$ denote complete and incomplete elliptic integral of the 2nd kind, where $1 - \sin^2\phi \in \mathbb{C} \setminus (-\infty, 0]$ and $1 - k^2\sin^2\phi \in \mathbb{C} \setminus (-\infty, 0]$, except that one of them may be 0 [219]. $\mathbb{C}$ denotes the set of complex numbers.

Proof.

$$\begin{aligned}
&\int_0^{2\pi}\int_0^r (g(y, \eta_{\mathrm{L}}, l_{t,e}, \phi)\mathbb{P}_{\mathrm{L}}^{s,e} + g(y, \eta_{\mathrm{N}}, l_{t,e}, \phi)\mathbb{P}_{\mathrm{N}}^{s,e})l_{t,e}\ \mathrm{d}l_{t,e}\mathrm{d}\phi \\
&= \int_{o_\phi(\eta_{\mathrm{L}})}\int_{o_{l_{t,e}}(\eta_{\mathrm{L}})} (c_1 H + c_2 l_{t,e})\ \mathrm{d}l_{t,e}\mathrm{d}\phi + \int_{o_\phi(\eta_{\mathrm{N}})}\int_{o_{l_{t,e}}(\eta_{\mathrm{N}})} (-c_1 H + (1 - c_2)l_{t,e})\ \mathrm{d}l_{t,e}\mathrm{d}\phi \\
&= c_1 H \int_{o_\phi(\eta_{\mathrm{L}})}\int_{o_{l_{t,e}}(\eta_{\mathrm{L}})} \mathrm{d}l_{t,e}\mathrm{d}\phi + 2c_2 S_1(y, \eta_{\mathrm{L}}, r) - \\
&\quad c_1 H \int_{o_\phi(\eta_{\mathrm{N}})}\int_{o_{l_{t,e}}(\eta_{\mathrm{N}})} \mathrm{d}l_{t,e}\mathrm{d}\phi + 2(1 - c_2)S_1(y, \eta_{\mathrm{N}}, r)
\end{aligned} \tag{6.24}$$

where $\int_{o_\phi(\eta)}\int_{o_{l_{t,e}}(\eta)} \mathrm{d}l_{t,e}\mathrm{d}\phi = 2\pi r - \int_{o'_\phi(\eta)}\int_{o'_{l_{t,e}}(\eta)} \mathrm{d}l_{t,e}\mathrm{d}\phi$. Given the domains in Lemma 6 and dividing (6.24) by πR_1^2, (6.22) is achieved. This concludes the proof. □

Proposition 3. Let $r \leq R_1$, assuming that the mixed LoS/NLoS distributions exist for link (s,e), and the (quasi-) LoS probability is $\mathbb{P}_{\mathrm{L}}^{s,e} = c_3 l_{t,e}/H + c_4$, the CDF of Γ_2 conditioning on the UED e being active only within the disk $O(t,r)$ is given by

$$\begin{aligned} F_{\Gamma_5}(y,\eta_{\mathrm{L}},\eta_{\mathrm{N}},r) =& \frac{2}{\pi R_1^2}\Big(c_4 S_1(y,\eta_{\mathrm{L}},r) + \frac{c_3}{3H}S_3(y,\eta_{\mathrm{L}},r) + \\ & (1-c_4)S_1(y,\eta_{\mathrm{N}},r) - \frac{c_3}{3H}S_3(y,\eta_{\mathrm{N}},r)\Big) \end{aligned} \tag{6.25}$$

$$S_3(y,\eta,r) = \begin{cases} M_3 + M_4 - M_1 - M_2, & \text{cases 1, 2} \\ \pi r^3 - 2M_2 + M_3, & \text{case 3} \\ M_1 - M_2 + M_4, & \text{cases 4, 14} \\ \pi r^3, & \text{cases 5, 12, 13, 19} \\ M_1 - M_3 + M_4, & \text{cases 6, 7} \\ -M_3, & \text{case 8} \\ -M_1 + M_4, & \text{cases 9, 10} \\ -M_2 + \pi r^3, & \text{case 11} \\ -M_2, & \text{case 15} \\ \pi r^3 - M_5 - M_6, & \text{case 16} \\ M_5 + M_6, & \text{case 17} \\ \pi r^3/2, & \text{case 18} \\ 0, & \text{otherwise} \end{cases} \tag{6.26}$$

with Table 6.2,

$$M_0 = \frac{\sqrt{-AB + l_{t,j}^2}}{-3A^3/2}$$

$$\frac{2M_1}{M_0} = \left(8l_{t,j}^2 - 7BA\right) \mathsf{E}\left(\sec^{-1}\left(\frac{l_{t,j}r}{a_1/2}\right) | \frac{l_{t,j}^2}{l_{t,j}^2 - AB}\right) + 4BA\mathsf{F}\left(\sec^{-1}\frac{l_{t,j}r}{a_1/2} | \frac{l_{t,j}^2}{l_{t,j}^2 - AB}\right)$$

$$M_2 = M_0 4BA\mathsf{K}\left(\frac{l_{t,j}^2}{l_{t,j}^2 - AB}\right) + M_0\left(8l_{t,j}^2 - 7BA\right)\mathsf{E}\left(\frac{l_{t,j}^2}{l_{t,j}^2 - AB}\right)$$

$$M_3 = M_0\left(8l_{t,j}^2 - 7BA\right)\mathsf{E}\left(\sec^{-1}\left(\frac{-l_{t,j}}{\sqrt{BA}}\right) | \frac{l_{t,j}^2}{l_{t,j}^2 - AB}\right) + M_0 4BA\mathsf{F}\left(\sec^{-1}\left(\frac{-l_{t,j}}{\sqrt{BA}}\right) | \frac{l_{t,j}^2}{l_{t,j}^2 - AB}\right)$$

$$M_4 = r^3\cos^{-1}\frac{Ar^2 + B}{2l_{t,j}r} + \frac{M_0}{4r}\left(A(2a_1 - 9B) + 8l_{t,j}^2\right)\sqrt{\frac{4l_{t,j}^2 r^2 - {a_1}^2}{l_{t,j}^2 - AB}}$$

$$M_5 = r^3\cos^{-1}\frac{\left|H^2 - l_{t,j}^2\right|}{-2l_{t,j}r}$$

$$M_6 = \frac{r|H^2 - l_{t,j}^2|}{8l_{t,j}^2}\sqrt{4l_{t,j}^2 r^2 - \left(H^2 - l_{t,j}^2\right)^2} + \frac{|H^2 - l_{t,j}^2|^3}{16l_{t,j}^3}\ln\frac{\sqrt{4l_{t,j}^2 r^2 - \left(H^2 - l_{t,j}^2\right)^2} + 2l_{t,j}r}{\left|H^2 - l_{t,j}^2\right|}$$

$\mathsf{K}(k) = \mathsf{F}(\pi/2 \mid k)$ and $\mathsf{F}(\phi \mid k) = \int_0^\phi (1 - k^2\sin^2\theta)^{-\frac{1}{2}}\,\mathrm{d}\theta$ denote complete and incomplete elliptic integral of the 1st kind, where $1 - \sin^2\phi \in \mathbb{C} \setminus (-\infty, 0]$ and $1 - k^2\sin^2\phi \in \mathbb{C} \setminus (-\infty, 0]$, except that one of them may be 0 [219].

Proof.

$$\begin{aligned}
&\int_0^{2\pi}\int_0^r (g(y,\eta_\mathrm{L},l_{t,e},\phi)\mathbb{P}_\mathrm{L}^{s,e} + g(y,\eta_\mathrm{N},l_{t,e},\phi)\mathbb{P}_\mathrm{N}^{s,e})l_{t,e}\,\mathrm{d}l_{t,e}\mathrm{d}\phi \\
&= \int_{o_\phi(\eta_\mathrm{L})}\int_{o_{l_{t,e}}(\eta_\mathrm{L})}\left(c_3{l_{t,e}}^2/H + c_4 l_{t,e}\right)\mathrm{d}l_{t,e}\mathrm{d}\phi + \\
&\int_{o_\phi(\eta_\mathrm{N})}\int_{o_{l_{t,e}}(\eta_\mathrm{N})}\left(-c_3{l_{t,e}}^2/H + (1 - c_4)l_{t,e}\right)\mathrm{d}l_{t,e}\mathrm{d}\phi \\
&= \frac{c_3}{H}\int_{o_\phi(\eta_\mathrm{L})}\int_{o_{l_{t,e}}(\eta_\mathrm{L})} l_{t,e}^2\,\mathrm{d}l_{t,e}\mathrm{d}\phi + 2c_4 S_1(y,\eta_\mathrm{L},r) - \\
&\frac{c_3}{H}\int_{o_\phi(\eta_\mathrm{N})}\int_{o_{l_{t,e}}(\eta_\mathrm{N})} l_{t,e}^2\,\mathrm{d}l_{t,e}\mathrm{d}\phi + 2(1 - c_4)S_1(y,\eta_\mathrm{N},r)
\end{aligned} \tag{6.27}$$

where $\int_{o_\phi(\eta)}\int_{o_{l_{t,e}}(\eta)} l_{t,e}^2 \mathrm{d}l_{t,e}\mathrm{d}\phi + \int_{o'_\phi(\eta)}\int_{o'_{l_{t,e}}(\eta)} l_{t,e}^2 \mathrm{d}l_{t,e}\mathrm{d}\phi = \frac{2}{3}\pi r^3$. Given Lemma 6 and dividing (6.27) by πR_1^2, (6.25) is achieved. This concludes the proof. □

6.4 Analysis of the SCP

6.4.1 Trend of the SCP with respect to P_j

Although the SCP is directly related to P_j, its trend varies. This can be explained as follows: as P_j increases, both $\log_2(1+\mathrm{SINR}_{s,d})$ and $\log_2(1+\max_{e\in\Phi}(\mathrm{SINR}_{s,e}))$ in (6.7) decrease. If the former decreases faster than the latter, C_s decreases; otherwise, C_s increases. This will, in turn, affect the performance of the SCP. This is because C_s is a variable related to the instantaneous channel state, and the SCP in (6.8) is the relative average frequency with which the event $C_s > \mathcal{R}_t$ occurs throughout all instantaneous channel states (assuming the system is ergodic). If C_s increases as P_j increases for all instantaneous channel states, the SCP increases; if C_s decreases as P_j increases for all instantaneous channel states, the SCP decreases. Otherwise, the trend of the SCP depends on the trends of C_s for the majority of the instantaneous channel states.

6.4.2 Trend of the SCP with respect to $\frac{P_s}{P_j}$

This subsection investigates the trend of the SCP with respect to transmitting-to-jamming power ratio $\frac{P_s}{P_j}$ for d and UEDs working in an interference-limited regime. Let variable $x = \frac{P_s}{P_j}$, and random variables $d_1 = \frac{l_{s,d}^{-\beta}|h_{s,d}|^2}{l_{j,d}^{-\alpha}\eta_{j,d}}$, $d_2 = \max_{e\in\Phi}\left(\frac{l_{s,e}^{-\alpha}\eta_{s,e}}{l_{j,e}^{-\alpha}}\right)$, we have

$$y = \frac{1+\frac{P_{s,d}}{P_{j,d}}}{1+\max_{e\in\Phi}\left(\frac{P_{s,e}}{P_{j,e}}\right)} = \frac{1+d_1 x}{1+d_2 x} \tag{6.28}$$

for $x \geq 0$. As shown in Figure 6.3, y is a hyperbola for $d_1, d_2 > 0$. Its horizontal asymptote is $y = d_1/d_2$. A special point that the curve passes through the x-axis is $(-1/d_1, 0)$, and the vertical asymptote of the hyperbola is given by $x = -1/d_2$. Clearly, when $x = 0$, $y = 1$, and the achievable secrecy rate is zero.

For $d_1 > d_2$, the hyperbola y is monotonically increasing in x, and if $d_1 < d_2$, y is monotonically decreasing in x. Note that (6.8) defines the statistical comparison between (6.28) and $2^{\mathcal{R}_t}$ where $\mathcal{R}_t \geq 0$. For $d_1 < d_2$, y is always less than one. Hence, it is smaller than $2^{\mathcal{R}_t}$. Therefore, when $d_1 < d_2$, neither increasing nor decreasing P_s/P_j will affect the results of the comparison between (6.28) and $2^{\mathcal{R}_t}$. Consequently, the monotonicity of (6.8) is solely decided by $d_1 > d_2$. As a result, the SCP is monotonically increasing as P_s/P_j increases.

Meanwhile, when $\mathcal{R}_t = 0$, neither increasing nor decreasing P_s/P_j will affect the results of the comparison between (6.8) and $2^{\mathcal{R}_t}$ because (6.28) is always larger than one for $d_1 > d_2$, while (6.28) is always smaller than one for $d_1 < d_2$. To conclude, the analysis above shows that for a given P_s, the less P_j the better the SCP in the interference-limited environment. As it will be shown in the following section, deploying the UAV jammer to a carefully chosen position would benefit the communication networks more than the case without the UAV jammer.

6.4.3 Trend of the SCP with respect to Jammer's Position

This subsection investigates the trend of the SCP with respect to the jammer's position when all ATG links are in a pure LoS state and $H^2 >> (R_1 + l_{s,d})^2$. An important aspect of UAV networks is the high likelihood of having significantly stronger LoS components than the reflected multipath components in some deployment scenarios (especially in suburban and rural morphologies) [126]. Hence, it is very important to study the performance of the SCP for the ATG links in a pure LoS state. According to (6.5), for ATG links in a pure LoS state, as H increases, they will remain in a pure

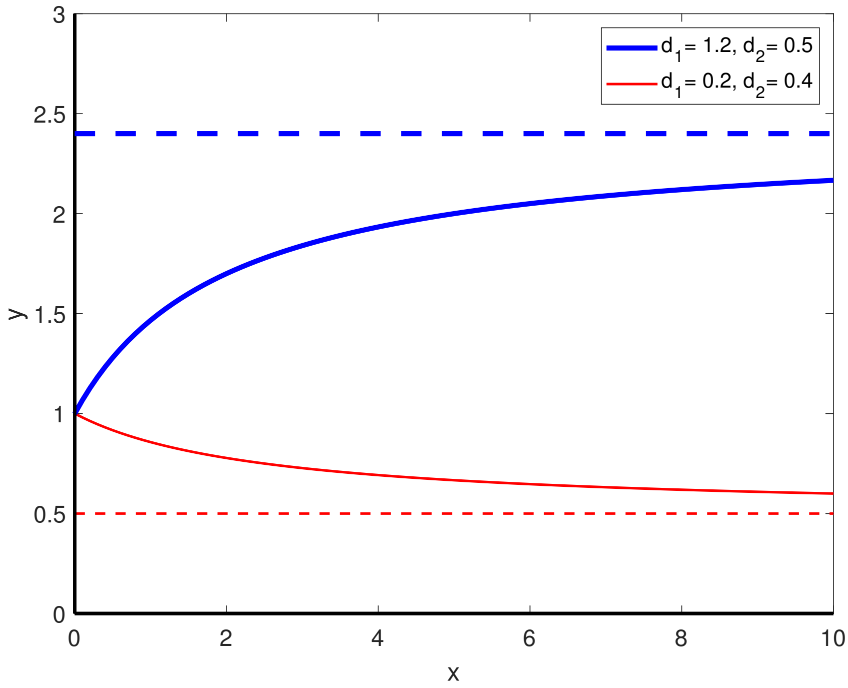

Figure 6.3: The plot of hyperbola (6.28). The solid lines are the hyperbolas in the first quadrant and the dashed lines are horizontal asymptotes. © 2019 IEEE.

LoS state.

Given $l_{j,d}^2 = l_{t,j}^2 + l_{s,d}^2 - 2l_{t,j}l_{s,d}\cos(\varphi_{j'} - \varphi_d) + H^2$ and $l_{s,e}^2 = H^2 + l_{t,e}^2$, when $H^2 >> (R_1 + l_{s,d})^2$ and $R_1 \geq l_{t,j}$, then $l_{j,d} \approx l_{s,e} \approx H$, and

$$\frac{1 + \frac{P_{s,d}}{P_{j,d}+N_0}}{1 + \max_{e\in\Phi}\left(\frac{P_{s,e}}{P_{j,e}+N_e}\right)} \approx \frac{1 + \frac{P_s(\lambda/4\pi)^2 l_{s,d}^{-\beta}|h_{s,d}|^2}{P_j(\lambda/4\pi)^2 H^{-\alpha}\eta_L + N_0}}{1 + \frac{P_s\eta_L}{H^\alpha}\max_{e\in\Phi}\left(\frac{1}{P_j l_{j,e}^{-\alpha} + N_e}\right)}. \tag{6.29}$$

According to (6.29), the performance of the SCP is related to $\max_{e\in\Phi} l_{j,e}$. Similar to Appendix 3.A.2, for a UED e uniformly distributed within a disk, the PDF of $l_{j,e}$ conditioning on $l_{t,j}$ is proportional to the arc of the circle $O(j, l_{j,e})$ that is enclosed by the disk $O(t, R_1)$. Assume that for a given $l_{t,j}$, the domain of $l_{j,e}$ with non-zero density is $[0, Z_1]$, where $Z_1 > 0$. Then, as $l_{t,j}$ increases by $\delta > 0$ and j still stays within the circle $O(t, R_1)$, the new non-zero domain of $l_{j,e}$ is $[0, Z_1 + \delta]$, and the density of $l_{j,e}$ is decreasing in $l_{t,j}$ for any $l_{j,e} \in \left[0, \sqrt{R_1^2 + l_{t,j}^2}\right]$ while it is increasing for any $l_{j,e} \in \left(\sqrt{R_1^2 + l_{t,j}^2}, Z_1\right]$. Thus, the chance to have a higher $l_{j,e}$ increases as $l_{t,j}$ increases. As a result, when the number of the UEDs is one, placing UAV jammer j to t (i.e., $l_{t,j} = 0$) will provide the optimum SCP for $H^2 >> (R_1 + l_{s,d})^2$.

Meanwhile, for multiple UEDs, let n i.i.d. random variables $X_1, ..., X_n$ denote the distances from n UEDs to j, and $Y = \max(X_1, ..., X_n)$; since the chance for X_n to have a higher value increases as $l_{t,j}$ increases for any n, the chance for Y to have a higher value increases as $l_{t,j}$ increases. Thus, placing UAV jammer j at t will obtain the optimum SCP for $H^2 >> (R_1 + l_{s,d})^2$.

6.5 Simulation Results and Discussion

To validate the derivation and the analysis of the SCP with respect to different variables, simulations based on LTE parameters were developed. The parameters used in the simulation are given in Table 6.3 unless otherwise specified. The receiver d and UEDs are assumed to have the same noise power. During each Monte Carlo trial, a sample of n locations is obtained from uniformly distributed UEDs. Along with the locations of the UAV jammer and receiver, 10^4 different instantaneous channel states are generated, which characterize the random channel statistics due to Rayleigh fading and the probabilistic LoS and NLoS channel conditions. Then, the corresponding C_s based on each instantaneous channel state is achieved, and the average results on the event $C_s > \mathcal{R}_t$ throughout all generated instantaneous channel states are saved in one trial. The simulation results are obtained by averaging over 10^5 independent Monte Carlo trials.

Figure 6.4 shows the performance of the SCP in the simulation for UEDs at different heights. The numerical results in this section are obtained by evaluating (6.18) for the same parameters as the simulations. One can easily see that the numerical results act as the lower bound to the simulation results of the SCP when P_j is

Table 6.3: System Parameters © 2019 IEEE

Parameter	Value
Environment	Suburban
Disk radius R_1	500 m
Receiver location d	$(100, 0, 0)$
Coding gain	0 dB
Tx/Rx antenna gain	0 dBi
Receiver noise figure	9 dB
Carrier frequency	2.0 GHz
Spectrum allocation	20 MHz
Duplex mode	Half duplex
Thermal noise power density	-174 dBm/Hz
Path loss exponent β	3
Transmit power P_s	0.1 W
Target secrecy rate $\mathcal{R}_t$	1 bit/s/Hz
Number of UEDs n	2

small. The simulation curves match well with the numerical results as P_j reaches the interference-limited regime. In this regime, the performance of the SCP is decreasing as P_j increases. This can be easily explained by the discussion on P_s/P_j in (6.28). Meanwhile, the same figure also shows that introducing a UAV jammer to the ground communications could change the performance of the SCP significantly. On the one hand, for $H = 500$ m and 1000 m, the SCP increases as P_j increases until around 10^{-3} W and then starts to decrease until the SCP reaches zero. Compared to the benchmark case of no jammer, introducing a UAV jammer with proper P_j would allow the ground communications to achieve a higher SCP. For $H = 500$ m and 1000 m, the ground communications with a UAV jammer allow the maximum of 8% and 60% increase in SCP, respectively, over the case without a UAV jammer as given by the dashed lines. On the other hand, for $H = 50$ m, the SCP decreases as P_j increases. By having a UAV jammer in this height, the SCP of the ground communications will be affected severely when the UAV jammer is enabled. Meanwhile, noticing the case without the UAV jammer, the achieved SCP in dashed lines show that the SCP at $H = 50$ m is higher than the one at $H = 500$ m and 1000 m. It is because increasing H will cause not only a higher LoS probability from the transmitter to a UED but also a longer receiving distance (i.e., a higher path loss). In general, the ground

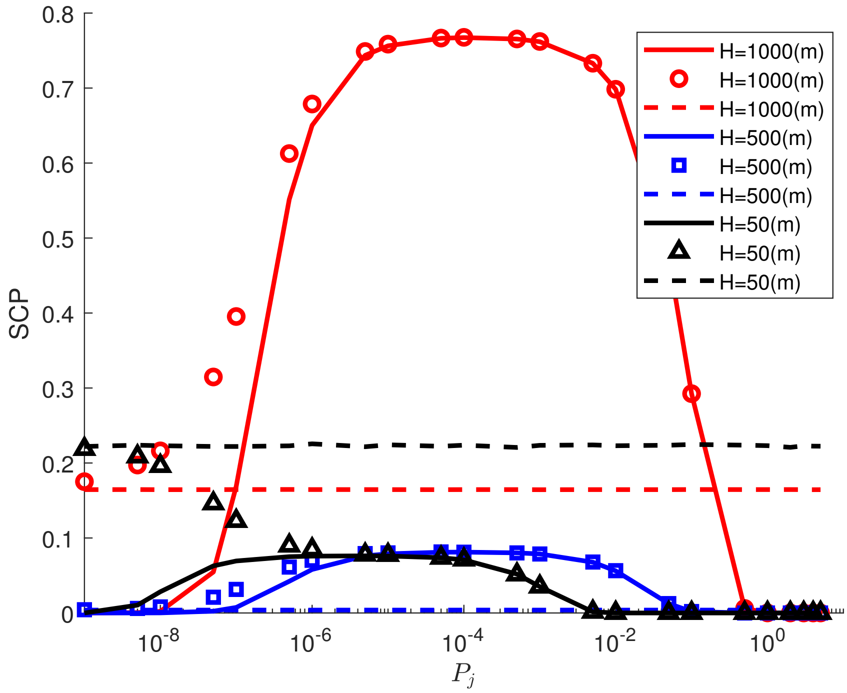

Figure 6.4: SCP *vs.* P_j in watts for H given by the figure legends. For the same color, the solid line represents the numerical results with the UAV jammer at $(0, 0, H)$, the markers represent the corresponding simulation results, and the dashed line represents the simulated benchmark case of no jammer. © 2019 IEEE.

communications prefer to have NLoS links towards the UEDs and have a maximum distance from it, however, these two objectives conflict with each other. If the LoS probability from the transmitter to a UED contributes more than the path loss does to the SCP as H increases, the SCP will decrease. Otherwise, the SCP will increase.

Figure 6.5 depicts the simulation results on the SCP when all ATG links are in a pure LoS state. When $H = 2000$ m, the performance of the SCP is optimum when placing the UAV jammer at $(0, 0, H)$. This can be explained by the discussion on (6.29). The performance curves from $H = 300$ to $H = 2000$ show that, for the UAV jammer with the same x and y coordinates, the SCP increases as H increases. This can also be explained by (6.29), where the terms increase as H increases for the ATG links in a pure LoS state. Meanwhile, Figure 6.6 gives the cases without the requirement on a pure LoS state for ATG links. In general, the trend of the

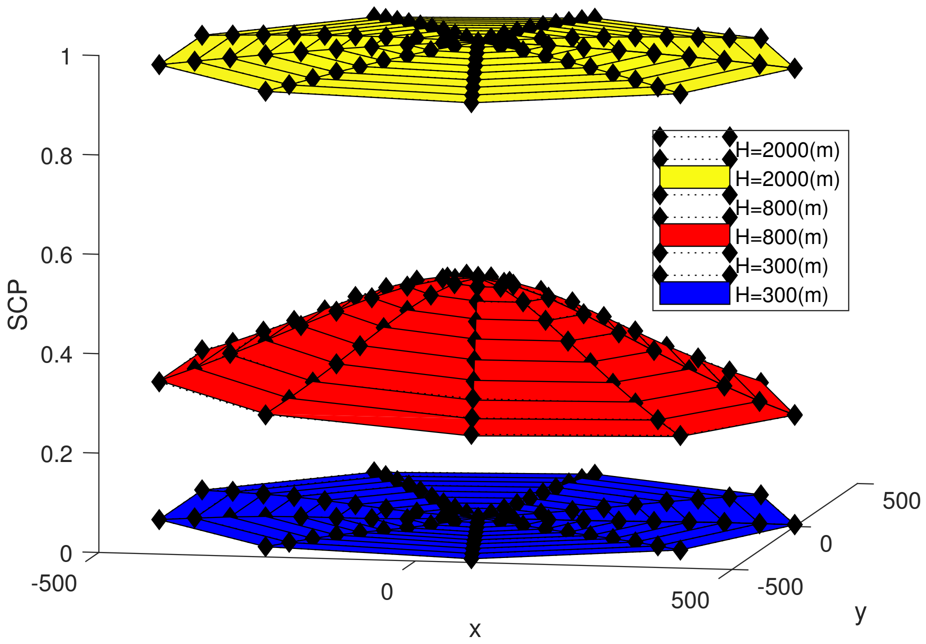

Figure 6.5: SCP *vs.* UAV jammer at (x, y, H). $P_j = 0.01$ W. The markers represent the simulation results, and the mesh grids represent the numerical results. © 2019 IEEE.

SCP with respect to the height of UAVs is hard to capture, because increasing H will not only cause a higher LoS probability but also decreases the jamming and received signal powers. A higher LoS probability from s to UED will cause the SCP to drop while a smaller jamming power will cause the SCP to increase. Meanwhile, the surface shows that the jammer should move away from the receiver d in order to achieve a higher SCP. Furthermore, by observing both Figure 6.5 and Figure 6.6, the numerical results of the SCP matching with the simulation results suggest that both receiver d and UEDs are working in the interference-limited regime for $P_j = 0.01$ W. By increasing H from 50 m to 2000 m, the SCP at the given x and y coordinates decreases first and then increases.

As shown in Figure 6.7, the UAV jammer will affect the SCP heavily as compared to the benchmark case of no jammer for different $l_{s,d}$. For a ground link distance $l_{s,d} = 100$ m, the SCP changes significantly for different H in the benchmark. This is

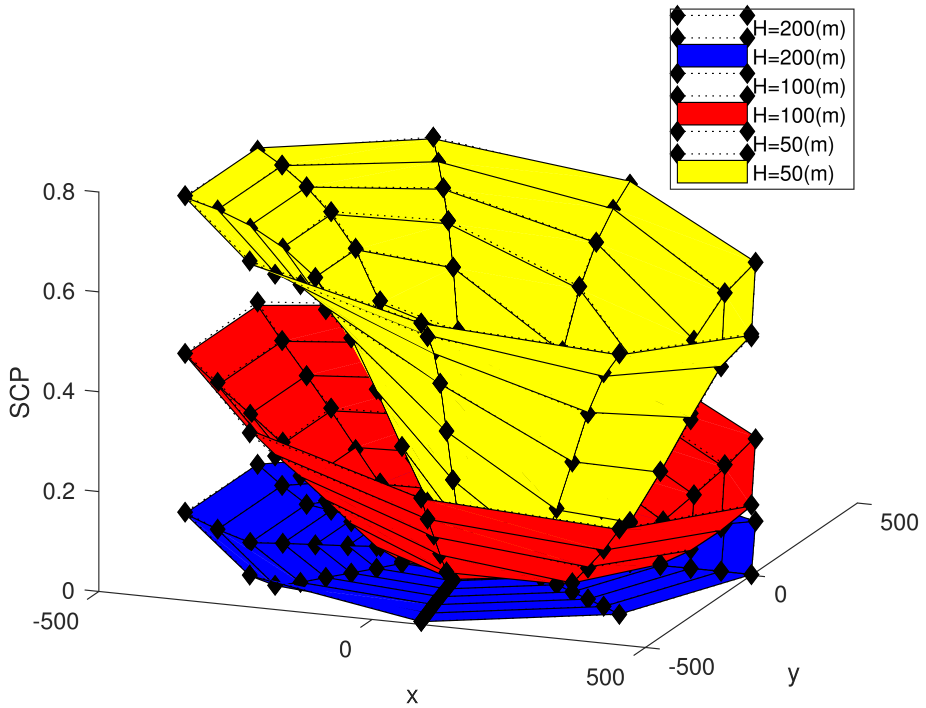

Figure 6.6: SCP *vs.* UAV jammer at (x, y, H). $P_j = 0.01$ W. The markers represent the simulation results, and the mesh grids represent the numerical results. © 2019 IEEE.

because a larger H causes not only the larger average path loss, but also the higher LoS probability from the transmitter s to the UEDs. Because the benchmarked SCP for $l_{s,d} = 100$ m is decreasing as H increases until around 400 m in Figure 6.7, the effect of the LoS probability on the SCP is stronger than that of the path loss from the transmitter s to the UEDs. This trend reverses after $H = 400$ m due to the stronger effect of the path loss than that of the LoS probability. Then, both the simulation and numerical results reveal that, when $l_{s,d} = 100$ m, the ground link can increase its SCP to at most 15% for $H = 10$ m to 30 m and for $H = 300$ m to 2000 m in the presence of UAV jammer. Meanwhile, between 30 m and 300 m, the SCP is smaller than the benchmark. This implies that the UAV jammer has a stronger influence on the receiver than to the UEDs in this range. Meanwhile, for a ground link distance $l_{s,d} = 500$ m, where the corresponding path loss from the transmitter s to the receiver d is very large, the SCP is close to zero for the benchmark and the

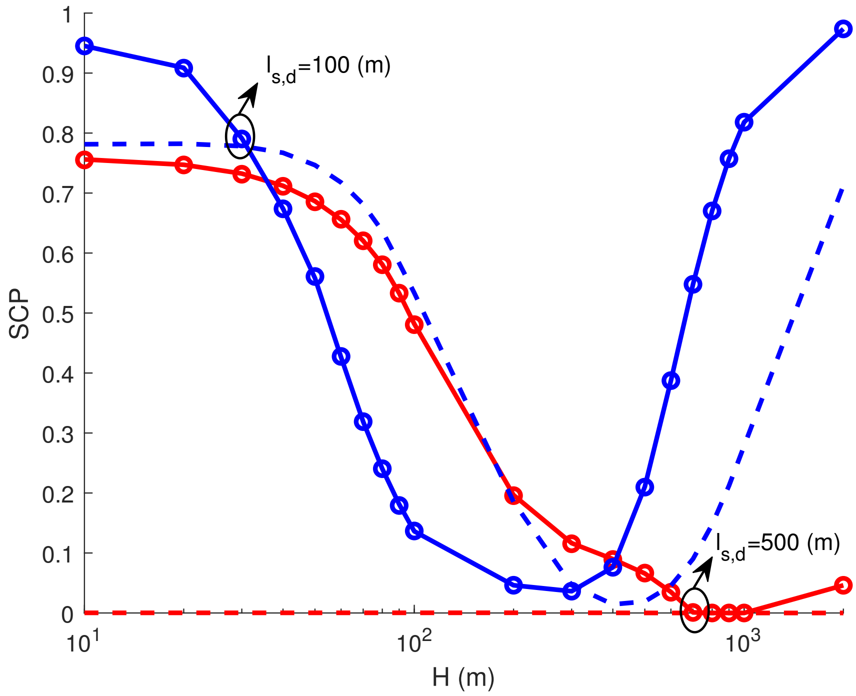

Figure 6.7: SCP *vs.* H for different $l_{s,d}$. $P_j = 0.01$ W, and the UAV jammer is located at $(0, 0, H)$. The solid line represents the numerical results, the circles represent the corresponding simulation results, and the dashed line represents the simulated benchmark case of no jammer. © 2019 IEEE.

ground link is more susceptible to eavesdropping when compared to $l_{s,d} = 100$ m. Then, by enabling the UAV jammer, a maximum of 75% increase can be achieved in the SCP for the given setting.

6.6 Summary

This chapter investigates the secrecy performance of the ground link in the presence of randomly deployed non-colluding UEDs. A piecewise fitting model has been proposed to characterize the LoS probability of an ATG link with higher accuracy than the existing sigmoid fitting. The SCP has been formulated based on the piecewise fitting model so that the formulation becomes tractable. The performance of the SCP with respect to the transmitting-to-jamming power ratio, the height of the UAVs, and the UAV jammer location has been investigated. The effective jamming power and location of the UAV jammer have been discussed. A combination of the optimum jamming position and power is expected to achieve the optimum secrecy performance, and we leave the optimization problem to find the best jamming position and/or power for both the LoS and NLoS link states to our future work. The model and analysis frameworks presented in this chapter will help to facilitate the analysis of the UAV-aided communications.

6.A Appendix: Proof of Lemma 6

Lemma 6. For a UED e which is uniformly distributed within the disk $O(t,r)$, denote $\phi = \varphi_{j'} - \varphi_{e'}$ and η as the excess path loss, the domains of ϕ and $l_{t,e}$ so that $1 + \frac{(H^2+l_{t,e}^2)^{\frac{-\alpha}{2}}\eta P_s}{\left(l_{t,j}^2+l_{t,e}^2-2l_{t,j}l_{t,e}\cos\phi\right)^{\frac{-\alpha}{2}}P_j} \leq y$ are denoted by $\{o_\phi(\eta), o_{l_{t,e}}(\eta)\}$, while the domains of ϕ and $l_{t,e}$ so that $1 + \frac{(H^2+l_{t,e}^2)^{\frac{-\alpha}{2}}\eta P_s}{\left(l_{t,j}^2+l_{t,e}^2-2l_{t,j}l_{t,e}\cos\phi\right)^{\frac{-\alpha}{2}}P_j} > y$ are denoted by $\{o'_\phi(\eta), o'_{l_{t,e}}(\eta)\}$. Let $\mathcal{F}_1 = \cos^{-1}\frac{-\sqrt{BA}}{l_{t,j}}$, $\mathcal{F}_2 = \cos^{-1}\frac{r^2A+B}{2rl_{t,j}}$, $A = 1 - \left((y-1)\frac{P_j}{\eta P_s}\right)^{\frac{2}{\alpha}}$, $B = l_{t,j}^2 - (1-A)H^2$. $x_1 = \frac{l_{t,j}\cos\phi + \sqrt{(l_{t,j}\cos\phi)^2 - BA}}{A}$, and $x_2 = \frac{l_{t,j}\cos\phi - \sqrt{(l_{t,j}\cos\phi)^2 - BA}}{A}$. Based on different A and B, these domains are given as follows.

For $A < 0, B \leq 0$, it gives $o'_{l_{t,e}}(\eta) = [x_1, x_2]$ and

$$o'_\phi(\eta) = \begin{cases} [\mathcal{F}_1, \mathcal{F}_2], & \text{if } r^2A \leq B, \frac{-r^2A-B}{2r} \leq l_{t,j} \\ [\mathcal{F}_1, \pi], & \text{if } r^2A < B, \sqrt{BA} \leq l_{t,j} < \frac{-r^2A-B}{2r} \\ \{\emptyset\}, & \text{otherwise}; \end{cases} \tag{6.30}$$

or $o'_{l_{t,e}}(\eta) = [x_1, r]$ and

$$o'_{\phi}(\eta) = \begin{cases} (\mathcal{F}_2, \pi], & \text{if } r^2 A \leq B, \frac{-r^2A-B}{2r} \leq l_{t,j} \\ [\mathcal{F}_2, \pi], & \text{if } r^2 A > B, \frac{-r^2A-B}{2r} \leq l_{t,j} \\ \{\emptyset\}, & \text{otherwise.} \end{cases} \tag{6.31}$$

For $A > 0, B \geq 0$, it gives $o_{l_{t,e}}(\eta) = [x_2, x_1]$ and

$$o_{\phi}(\eta) = \begin{cases} [\mathcal{F}_2, \pi - \mathcal{F}_1], & \text{if } r^2 A \geq B, l_{t,j} \geq \frac{r^2A+B}{2r} \\ [0, \pi - \mathcal{F}_1], & \text{if } r^2 A > B, \sqrt{BA} \leq l_{t,j} < \frac{r^2A+B}{2r} \\ \{\emptyset\}, & \text{otherwise;} \end{cases} \tag{6.32}$$

or $o_{l_{t,e}}(\eta) = [x_2, r]$ and

$$o_{\phi}(\eta) = \begin{cases} [0, \mathcal{F}_2], & \text{if } r^2 A \leq B, \frac{r^2A+B}{2r} \leq l_{t,j} \\ [0, \mathcal{F}_2), & \text{if } r^2 A > B, \frac{r^2A+B}{2r} \leq l_{t,j} \\ \{\emptyset\}, & \text{otherwise.} \end{cases} \tag{6.33}$$

For $A < 0, B > 0$, it gives $o'_{l_{t,e}}(\eta) = [0, r]$ and

$$o'_{\phi}(\eta) = \begin{cases} [0, \pi], & \text{if } -r^2 A < B, l_{t,j} < \frac{r^2A+B}{2r} \\ (\mathcal{F}_2, \pi], & \text{if } l_{t,j} \geq \frac{\left|r^2A+B\right|}{2r} \\ \{\emptyset\}, & \text{otherwise;} \end{cases} \tag{6.34}$$

or $o'_{l_{t,e}}(\eta) = [0, x_2]$ and

$$o'_{\phi}(\eta) = \begin{cases} [0, \pi], & \text{if } -r^2 A > B, l_{t,j} < \frac{-r^2A-B}{2r} \\ [0, \mathcal{F}_2], & \text{if } l_{t,j} \geq \frac{\left|r^2A+B\right|}{2r} \\ \{\emptyset\}, & \text{otherwise.} \end{cases} \tag{6.35}$$

For $A > 0, B < 0$, it gives $o_{l_{t,e}}(\eta) = [0, r]$ and

$$o_{\phi}(\eta) = \begin{cases} [0, \pi], & \text{if } -r^2 A > B, l_{t,j} < \frac{-r^2 A - B}{2r} \\ \left[0, \mathcal{F}_2\right], & \text{if } l_{t,j} \geq \frac{|r^2 A + B|}{2r} \\ \{\emptyset\}, & \text{otherwise;} \end{cases} \tag{6.36}$$

or $o_{l_{t,e}}(\eta) = [0, x_1]$ and

$$o_{\phi}(\eta) = \begin{cases} [0, \pi], & \text{if } -r^2 A < B, l_{t,j} < \frac{r^2 A + B}{2r} \\ \left[\mathcal{F}_2, \pi\right], & \text{if } l_{t,j} \geq \frac{|r^2 A + B|}{2r} \\ \{\emptyset\}, & \text{otherwise.} \end{cases} \tag{6.37}$$

For $A = 0$, it gives $o_{l_{t,e}}(\eta) = \left[\frac{\left|l_{t,j}^2 - H^2\right|}{2l_{t,j}}, r\right]$ and

$$o_{\phi}(\eta) = \begin{cases} \left[0, \cos^{-1}\left(\frac{l_{t,j}^2 - H^2}{2l_{t,j} l_{t,e}}\right)\right], & \text{if } \frac{\left|l_{t,j}^2 - H^2\right|}{2l_{t,j}} \leq r \\ \{\emptyset\}, & \text{otherwise;} \end{cases} \tag{6.38}$$

or $o_{l_{t,e}}(\eta) = \left[0, \frac{-l_{t,j}^2 + H^2}{2l_{t,j}}\right)$ and

$$o_{\phi}(\eta) = \begin{cases} [0, \pi], & \text{if } r \geq \frac{-l_{t,j}^2 + H^2}{2l_{t,j}} \\ \{\emptyset\}, & \text{otherwise;} \end{cases} \tag{6.39}$$

or $o_{l_{t,e}}(\eta) = [0, r]$ and

$$o_{\phi}(\eta) = \begin{cases} [0, \pi], & \text{if } r < \frac{-l_{t,j}^2 + H^2}{2l_{t,j}} \\ \{\emptyset\}, & \text{otherwise.} \end{cases} \tag{6.40}$$

Proof. For $A \neq 0$, the corresponding solutions of $l_{t,e}$ in $1+\frac{(H^2+l_{t,e}^2)^{\frac{-\alpha}{2}}\eta P_s}{\left(l_{t,j}^2+l_{t,e}^2-2l_{t,j}l_{t,e}\cos\phi\right)^{\frac{-\alpha}{2}}P_j} = y$ are denoted as

$$\begin{aligned} x_1 &= \frac{l_{t,j}\cos\phi + \sqrt{(l_{t,j}\cos\phi)^2 - BA}}{A} \\ x_2 &= \frac{l_{t,j}\cos\phi - \sqrt{(l_{t,j}\cos\phi)^2 - BA}}{A} \end{aligned} \tag{6.41}$$

where $x_1 \leq x_2$ for $A < 0$, while $x_2 \leq x_1$ for $A > 0$. For x_1 and x_2 to exist,

$$(l_{t,j}\cos\phi)^2 - BA \geq 0. \tag{6.42}$$

As a result, $\cos\phi \geq \frac{\sqrt{BA}}{l_{t,j}}$ or $\cos\phi \leq -\frac{\sqrt{BA}}{l_{t,j}}$ for $BA \geq 0$, and $(l_{t,j}\cos\phi)^2 \geq 0$ for $BA < 0$. Since $\phi = \varphi_{j'} - \varphi_{e'}$ and the impact from j to e for $\phi \in [0, \pi]$ is the same as the case for $\phi \in [\pi, 2\pi]$. Thus, only $\phi \in [0, \pi]$ is considered in the following analysis. The domains of ϕ in (6.42) are given by

$$\phi \leq \pi - \mathcal{F}_1, \text{ for } l_{t,j} \geq \sqrt{BA}, BA \geq 0 \tag{6.43}$$

$$\phi \geq \mathcal{F}_1, \text{ for } l_{t,j} \geq \sqrt{BA}, BA \geq 0 \tag{6.44}$$

$$\phi \in [0, \pi], \text{ for } BA < 0. \tag{6.45}$$

Meanwhile, $1 + \frac{(H^2+l_{t,e}^2)^{\frac{-\alpha}{2}}\eta P_s}{\left(l_{t,j}^2+l_{t,e}^2-2l_{t,j}l_{t,e}\cos\phi\right)^{\frac{-\alpha}{2}}P_j} \leq y$ gives

$$Al_{t,e}^2 - 2l_{t,j}\cos(\phi)l_{t,e} + l_{t,j}^2 - (1-A)H^2 \leq 0. \tag{6.46}$$

Apparently, when $A < 0$, $l_{t,e} \geq x_2$ or $l_{t,e} \leq x_1$; when $A > 0$, $x_2 \leq l_{t,e} \leq x_1$. To simplify analysis, $x_1 \leq l_{t,e} \leq x_2$ for $A < 0$ and $x_2 \leq l_{t,e} \leq x_1$ for $A > 0$ are investigated. As a result, the former is the case for $A < 0$ and

$$Al_{t,e}^2 - 2l_{t,j}\cos(\phi)l_{t,e} + l_{t,j}^2 - (1-A)H^2 \geq 0. \tag{6.47}$$

For $A < 0, B \leq 0$**:** Assuming that (6.42) holds, comparing x_1 with 0 gives

$$\phi \in \left[\frac{\pi}{2}, \pi\right], \text{ for } x_1 \geq 0; \text{ and } \phi \in \left[0, \frac{\pi}{2}\right], \text{ for } x_1 < 0. \tag{6.48}$$

Assuming that (6.42) holds, comparing x_2 with 0 and considering that $x_1 \leq x_2$ for $A < 0$, then

$$\phi \in \left[\frac{\pi}{2}, \pi\right], x_2 \geq 0. \tag{6.49}$$

Comparing x_1 with r, then

$$x_1 \leq r \Rightarrow \sqrt{(l_{t,j}\cos\phi)^2 - BA} \geq rA - l_{t,j}\cos\phi. \tag{6.50}$$

If

$$rA - l_{t,j}\cos\phi \geq 0, \tag{6.51}$$

then

$$\phi \in \begin{cases} [\mathcal{F}_3, \pi], & \text{if } l_{t,j} \geq -rA \\ \{\emptyset\}, & \text{if } l_{t,j} < -rA \end{cases} \tag{6.52}$$

where $\mathcal{F}_3 = \cos^{-1}\frac{rA}{l_{t,j}}$.

Assuming that (6.42) and (6.51) hold, solving (6.50) gives

$$\phi \in \begin{cases} [\mathcal{F}_2, \pi], & \text{if } l_{t,j} \geq \frac{-r^2A-B}{2r} \\ \{\emptyset\}, & \text{otherwise.} \end{cases} \tag{6.53}$$

Combining (6.52) and (6.53) with intersections yields

$$\phi \in \begin{cases} [\mathcal{F}_3, \pi], & \text{if } r^2A \leq B,\ l_{t,j} \geq -rA \\ [\mathcal{F}_2, \pi], & \text{if } r^2A > B,\ l_{t,j} \geq \frac{-r^2A-B}{2r} \\ \{\emptyset\}, & \text{otherwise.} \end{cases} \tag{6.54}$$

Combining (6.54) and (6.44) with intersections yields

$$\phi \in \begin{cases} [\mathcal{F}_3, \pi], & \text{if } r^2A \leq B,\ l_{t,j} \geq -rA \\ [\mathcal{F}_2, \pi], & \text{if } r^2A > B,\ l_{t,j} \geq \frac{-r^2A-B}{2r} \\ \{\emptyset\}, & \text{otherwise.} \end{cases} \tag{6.55}$$

If $rA - l_{t,j}\cos\phi < 0$, then

$$\phi \in \begin{cases} [0, \pi], & \text{if } l_{t,j} < -rA \\ [0, \mathcal{F}_3), & \text{if } l_{t,j} \geq -rA. \end{cases} \tag{6.56}$$

Combining (6.56) and (6.44) with intersections yields

$$\phi \in \begin{cases} [\mathcal{F}_1, \pi], & \text{if } r^2A < B, \sqrt{BA} \leq l_{t,j} < -rA \\ [\mathcal{F}_1, \mathcal{F}_3), & \text{if } r^2A < B, l_{t,j} \geq -rA \\ \{\emptyset\}, & \text{otherwise.} \end{cases} \tag{6.57}$$

The unions of (6.55) and (6.57) give

$$\phi \in \begin{cases} [\mathcal{F}_2, \pi], & \text{if } r^2A > B,\ l_{t,j} \geq \frac{-r^2A-B}{2r} \\ [\mathcal{F}_1, \pi], & \text{if } r^2A \leq B, \sqrt{BA} \leq l_{t,j} \\ \{\emptyset\}, & \text{otherwise.} \end{cases} \tag{6.58}$$

Comparing r with x_2,

$$x_2 > r \Rightarrow \sqrt{(l_{t,j}\cos\phi)^2 - BA} > -rA + l_{t,j}\cos\phi. \tag{6.59}$$

If

$$-rA + l_{t,j}\cos\phi \geq 0 \tag{6.60}$$

then

$$\phi \in \begin{cases} [0,\pi], & \text{if } l_{t,j} < -rA \\ [0,\mathcal{F}_3], & \text{if } l_{t,j} \geq -rA. \end{cases} \tag{6.61}$$

Assuming that (6.42) and (6.60) hold, solving (6.59) gives

$$\phi \in \begin{cases} (\mathcal{F}_2,\pi], & \text{if } l_{t,j} \geq \frac{-r^2A-B}{2r} \\ \{\emptyset\}, & \text{otherwise.} \end{cases} \tag{6.62}$$

Combining (6.61) and (6.62) with intersections yields

$$\phi \in \begin{cases} (\mathcal{F}_2,\pi], & \text{if } r^2A < B,\ \frac{-r^2A-B}{2r} \leq l_{t,j} < -rA \\ (\mathcal{F}_2,\mathcal{F}_3], & \text{if } r^2A < B,\ l_{t,j} \geq -rA \\ \{\emptyset\}, & \text{otherwise.} \end{cases} \tag{6.63}$$

Then, the intersections of (6.63) and (6.44) yield (6.63).

If $-rA + l_{t,j}\cos\phi < 0$, then

$$\phi \in \begin{cases} (\mathcal{F}_3,\pi], & \text{if } l_{t,j} \geq -rA \\ \{\emptyset\}, & \text{otherwise.} \end{cases} \tag{6.64}$$

Then, combining (6.64) and (6.44) with intersections yields

$$\phi \in \begin{cases} (\mathcal{F}_3, \pi], & \text{if } r^2 A \le B, l_{t,j} \ge -rA \\ [\mathcal{F}_1, \pi], & \text{if } r^2 A > B, l_{t,j} \ge \sqrt{BA} \\ \{\emptyset\}, & \text{otherwise.} \end{cases} \tag{6.65}$$

Therefore, the regions for $x_2 > r$ are given by the unions of (6.63) and (6.65):

$$\phi \in \begin{cases} (\mathcal{F}_2, \pi], & \text{if } r^2 A \le B, \ \frac{-r^2 A - B}{2r} \le l_{t,j} \\ [\mathcal{F}_1, \pi], & \text{if } r^2 A > B, l_{t,j} \ge \sqrt{BA} \\ \{\emptyset\}, & \text{otherwise.} \end{cases} \tag{6.66}$$

Meanwhile,

$$x_2 \le r \Rightarrow \sqrt{(l_{t,j} \cos\phi)^2 - BA} \le -rA + l_{t,j} \cos\phi. \tag{6.67}$$

If $-rA + l_{t,j} \cos\phi \ge 0$, (6.61) is obtained.

Assuming that (6.42) and (6.61) hold, solving (6.67) gives

$$\phi \in \begin{cases} [0, \mathcal{F}_2], & \text{if } l_{t,j} \ge \frac{-r^2 A - B}{2r} \\ [0, \pi], & \text{if } l_{t,j} < \frac{-r^2 A - B}{2r}. \end{cases} \tag{6.68}$$

Combining (6.61) and (6.68) with intersections yields

$$\phi \in \begin{cases} [0, \mathcal{F}_2], & \text{if } r^2 A \leq B, l_{t,j} \geq \frac{-r^2A-B}{2r} \\ [0, \mathcal{F}_3], & \text{if } r^2 A > B, l_{t,j} \geq -rA \\ [0, \pi], & \text{if } r^2 A \leq B, l_{t,j} < \frac{-r^2A-B}{2r} \\ [0, \pi], & \text{if } r^2 A > B, l_{t,j} < -rA \\ \{\emptyset\}, & \text{otherwise.} \end{cases} \tag{6.69}$$

The intersections of (6.69) and (6.44) are given by (6.30). As a result, when $0 \leq x_1 \leq r$ and $x_2 \leq r$, (6.30) is obtained. Meanwhile, when $0 \leq x_1 \leq r$ and $x_2 > r$, (6.31) is achieved.

For $A > 0, B \geq 0$: Assuming that (6.42) holds, comparing x_2 with 0 gives

$$\phi \in \left[\frac{\pi}{2}, \pi\right], \text{ for } x_2 < 0; \text{ and } \phi \in \left[0, \frac{\pi}{2}\right], \text{ for } x_2 \geq 0. \tag{6.70}$$

Assuming that (6.42) holds, comparing x_1 with 0 gives

$$\phi \in \left[\frac{\pi}{2}, \pi\right], \text{ for } x_1 < 0; \text{ and } \phi \in \left[0, \frac{\pi}{2}\right], \text{ for } x_1 \geq 0. \tag{6.71}$$

Since x_1 must be larger than 0 for a valid region to exist, $\phi \in \left[0, \frac{\pi}{2}\right]$ and (6.43) stands.

Comparing x_2 with r, then

$$x_2 \leq r \Rightarrow \sqrt{(l_{t,j}\cos\phi)^2 - BA} \geq l_{t,j}\cos\phi - rA. \tag{6.72}$$

If

$$l_{t,j}\cos\phi - rA \geq 0, \tag{6.73}$$

then

$$\phi \in \begin{cases} [0, \mathcal{F}_3], & \text{if } l_{t,j} \geq rA \\ \{\emptyset\}, & \text{if } l_{t,j} < rA. \end{cases} \tag{6.74}$$

Assuming that (6.42) and (6.73) hold, solving (6.72) gives

$$\phi \in \begin{cases} [0, \mathcal{F}_2], & \text{if } l_{t,j} \geq \frac{r^2A+B}{2r} \\ \{\emptyset\}, & \text{if } l_{t,j} < \frac{r^2A+B}{2r}. \end{cases} \tag{6.75}$$

Then, combining (6.74), (6.75) and (6.43) with intersections yields

$$\phi \in \begin{cases} [0, \mathcal{F}_3], & \text{if } r^2A > B, l_{t,j} \geq rA \\ [0, \mathcal{F}_2], & \text{if } r^2A \leq B, l_{t,j} \geq \frac{r^2A+B}{2r} \\ \{\emptyset\}, & \text{otherwise.} \end{cases} \tag{6.76}$$

If $l_{t,j} \cos\phi - rA < 0$, then

$$\phi \in \begin{cases} [0, \pi], & \text{if } l_{t,j} < rA \\ (\mathcal{F}_3, \pi], & \text{if } l_{t,j} \geq rA. \end{cases} \tag{6.77}$$

Then, combining (6.77) and (6.43) with intersections yields

$$\phi \in \begin{cases} [0, \pi - \mathcal{F}_1], & \text{if } r^2A > B, \sqrt{BA} \leq l_{t,j} < rA \\ (\mathcal{F}_3, \pi - \mathcal{F}_1], & \text{if } r^2A > B, rA \leq l_{t,j} \\ \{\emptyset\}, & \text{otherwise.} \end{cases} \tag{6.78}$$

The unions of (6.76) and (6.78) yield

$$\phi \in \begin{cases} [0, \mathcal{F}_2], & \text{if } r^2 A \leq B, l_{t,j} \geq \frac{r^2 A + B}{2r} \\ [0, \pi - \mathcal{F}_1], & \text{if } r^2 A > B, \sqrt{BA} \leq l_{t,j} \\ \{\emptyset\}, & \text{otherwise.} \end{cases} \tag{6.79}$$

Comparing r with x_1,

$$x_1 \leq r \Rightarrow \sqrt{(l_{t,j} \cos\phi)^2 - BA} \leq rA - l_{t,j}\cos\phi. \tag{6.80}$$

If

$$rA - l_{t,j}\cos\phi \geq 0, \tag{6.81}$$

then

$$\phi \in \begin{cases} [0, \pi], & \text{if } l_{t,j} < rA \\ [\mathcal{F}_3, \pi], & \text{if } l_{t,j} \geq rA. \end{cases} \tag{6.82}$$

Assuming that (6.42) and (6.81) hold, solving (6.80) gives

$$\phi \in \begin{cases} [0, \pi], & \text{if } l_{t,j} < \frac{r^2 A + B}{2r} \\ [\mathcal{F}_2, \pi], & \text{if } l_{t,j} \geq \frac{r^2 A + B}{2r}. \end{cases} \tag{6.83}$$

Combining (6.83) and (6.82) with intersections yields

$$\phi \in \begin{cases} [0, \pi], & \text{if } r^2A < B, l_{t,j} < rA \\ [0, \pi], & \text{if } r^2A \geq B, l_{t,j} < \frac{r^2A+B}{2r} \\ [\mathcal{F}_3, \pi], & \text{if } r^2A < B, rA \leq l_{t,j} \\ [\mathcal{F}_2, \pi], & \text{if } r^2A \geq B, \frac{r^2A+B}{2r} \leq l_{t,j} \\ \{\emptyset\}, & \text{otherwise.} \end{cases} \tag{6.84}$$

Then, combining (6.84) and (6.43) with intersections yields

$$\phi \in \begin{cases} [\mathcal{F}_2, \pi - \mathcal{F}_1], & \text{if } r^2A \geq B, l_{t,j} \geq \frac{r^2A+B}{2r} \\ [0, \pi - \mathcal{F}_1], & \text{if } r^2A \geq B, \sqrt{BA} \leq l_{t,j} < \frac{r^2A+B}{2r} \\ \{\emptyset\}, & \text{otherwise.} \end{cases} \tag{6.85}$$

$$x_1 > r \Rightarrow \sqrt{(l_{t,j}\cos\phi)^2 - BA} > rA - l_{t,j}\cos\phi. \tag{6.86}$$

If

$$rA - l_{t,j}\cos\phi \geq 0, \tag{6.87}$$

(6.82) is obtained.

Assuming that (6.42) and (6.87) hold, solving (6.86) gives

$$\phi \in \begin{cases} [0, \mathcal{F}_2), & \text{if } l_{t,j} \geq \frac{r^2A+B}{2r} \\ \{\emptyset\}, & \text{otherwise.} \end{cases} \tag{6.88}$$

Combining (6.82) and (6.88) with intersections yields

$$\phi \in \begin{cases} [\mathcal{F}_3, \mathcal{F}_2), & \text{if } r^2 A > B, l_{t,j} \geq rA \\ [0, \mathcal{F}_2), & \text{if } r^2 A > B, \frac{r^2 A + B}{2r} \leq l_{t,j} < rA \\ \{\emptyset\}, & \text{otherwise.} \end{cases} \tag{6.89}$$

If $rA - l_{t,j} \cos\phi < 0$, then

$$\phi \in \begin{cases} [0, \mathcal{F}_3), & \text{if } l_{t,j} \geq rA \\ \{\emptyset\}, & \text{otherwise.} \end{cases} \tag{6.90}$$

The unions of (6.89) and (6.90) yield

$$\phi \in \begin{cases} [0, \mathcal{F}_2), & \text{if } r^2 A > B, l_{t,j} \geq \frac{r^2 A + B}{2r} \\ [0, \mathcal{F}_3), & \text{if } r^2 A \leq B, l_{t,j} \geq rA \\ \{\emptyset\}, & \text{otherwise.} \end{cases} \tag{6.91}$$

Then, combining (6.91) and (6.43) with intersections yields

$$\phi \in \begin{cases} [0, \mathcal{F}_2), & \text{if } r^2 A > B, l_{t,j} \geq \frac{r^2 A + B}{2r} \\ [0, \pi - \mathcal{F}_1], & \text{if } r^2 A \leq B, l_{t,j} \geq \sqrt{BA} \\ \{\emptyset\}, & \text{otherwise.} \end{cases} \tag{6.92}$$

The feasible regions of ϕ, where $x_2 \leq r$ and $x_1 \leq r$, are the intersections of (6.79) and (6.92). As a result,

$$\phi \in \begin{cases} [\mathcal{F}_2, \pi - \mathcal{F}_1], & \text{if } r^2A \geq B, l_{t,j} \geq \frac{r^2A+B}{2r} \\ [0, \pi - \mathcal{F}_1], & \text{if } r^2A > B, \sqrt{BA} \leq l_{t,j} < \frac{r^2A+B}{2r} \\ \{\emptyset\}, & \text{otherwise.} \end{cases} \tag{6.93}$$

The feasible regions of ϕ, where $x_2 \leq r$ and $x_1 > r$, are the intersections of (6.79) and (6.85). As a result,

$$\phi \in \begin{cases} [0, \mathcal{F}_2], & \text{if } r^2A \leq B, \frac{r^2A+B}{2r} \leq l_{t,j} \\ [0, \mathcal{F}_2), & \text{if } r^2A > B, \frac{r^2A+B}{2r} \leq l_{t,j} \\ \{\emptyset\}, & \text{otherwise.} \end{cases} \tag{6.94}$$

As a result, when $x_2 \leq r$ and $x_1 \leq r$, (6.32) is obtained. Meanwhile, when $x_2 \leq r$ and $x_1 > r$, (6.33) is obtained.

For $A < 0, B > 0$**:** Comparing x_1 with 0 gives

$$\phi \in [0, \pi]\,, \text{ for } x_1 < 0; \text{ and } \phi = \emptyset, \text{ for } x_1 \geq 0. \tag{6.95}$$

Comparing x_2 with 0 gives

$$\phi = \emptyset, \text{ for } x_2 < 0; \text{ and } \phi \in [0, \pi]\,, \text{ for } x_2 \geq 0. \tag{6.96}$$

Comparing x_2 with r,

$$x_2 > r \Rightarrow \sqrt{(l_{t,j}\cos\phi)^2 - BA} > l_{t,j}\cos\phi - rA. \tag{6.97}$$

If $l_{t,j}\cos\phi - rA < 0$, then

$$\phi \in \begin{cases} (\mathcal{F}_3, \pi], & \text{if } l_{t,j} \geq -rA \\ \{\emptyset\}, & \text{if } l_{t,j} < -rA. \end{cases} \tag{6.98}$$

If

$$l_{t,j}\cos\phi - rA \geq 0 \tag{6.99}$$

then

$$\phi \in \begin{cases} [0, \mathcal{F}_3], & \text{if } l_{t,j} \geq -rA \\ [0, \pi], & \text{if } l_{t,j} < -rA. \end{cases} \tag{6.100}$$

Assuming that (6.42) and (6.99) hold, solving (6.97) gives

$$\phi \in \begin{cases} [0, \pi], & \text{if } -r^2A < B, l_{t,j} < \frac{r^2A+B}{2r} \\ (\mathcal{F}_2, \pi], & \text{if } -r^2A \geq B, l_{t,j} \geq \frac{-r^2A-B}{2r} \\ (\mathcal{F}_2, \pi], & \text{if } -r^2A < B, l_{t,j} \geq \frac{r^2A+B}{2r} \\ \{\emptyset\}, & \text{otherwise.} \end{cases} \tag{6.101}$$

Then, combining (6.100) and (6.101) with intersections yields

$$\phi \in \begin{cases} [0,\pi], & \text{if } -A < \frac{B}{r^2}, -A \geq \frac{B}{3r^2}, l_{t,j} < \frac{r^2A+B}{2r} \\ [0,\pi], & \text{if } -A < \frac{B}{r^2}, -A < \frac{B}{3r^2}, l_{t,j} < -rA \\ (\mathcal{F}_2,\pi], & \text{if } -A \geq \frac{B}{r^2}, \frac{-r^2A-B}{2r} \leq l_{t,j} < -rA \\ (\mathcal{F}_2,\pi], & \text{if } -A < \frac{B}{r^2}, -A > \frac{B}{3r^2}, \frac{r^2A+B}{2r} \leq l_{t,j} < -rA \\ [0,\mathcal{F}_3], & \text{if } -A < \frac{B}{r^2}, -A < \frac{B}{3r^2}, -rA \leq l_{t,j} < \frac{r^2A+B}{2r} \\ (\mathcal{F}_2,\mathcal{F}_3], & \text{if } -A \geq \frac{B}{r^2}, l_{t,j} \geq -rA \\ (\mathcal{F}_2,\mathcal{F}_3], & \text{if } -A < \frac{B}{r^2}, -A \geq \frac{B}{3r^2}, l_{t,j} \geq -rA \\ (\mathcal{F}_2,\mathcal{F}_3], & \text{if } -A < \frac{B}{r^2}, -A < \frac{B}{3r^2}, l_{t,j} \geq \frac{r^2A+B}{2r} \\ \{\emptyset\}, & \text{otherwise.} \end{cases} \tag{6.102}$$

The unions of (6.98) and (6.102) yield

$$\phi \in \begin{cases} [0,\pi], & \text{if } -r^2A < B, l_{t,j} < \frac{r^2A+B}{2r} \\ (\mathcal{F}_2,\pi], & \text{if } l_{t,j} \geq \frac{\left|r^2A+B\right|}{2r} \\ \{\emptyset\}, & \text{otherwise.} \end{cases} \tag{6.103}$$

Meanwhile,

$$x_2 \leq r \Rightarrow \sqrt{\left(l_{t,j}\cos\phi\right)^2 - BA} \leq l_{t,j}\cos\phi - rA. \tag{6.104}$$

If $l_{t,j}\cos\phi - rA \geq 0$, then

$$\phi \in \begin{cases} [0,\mathcal{F}_3], & \text{if } l_{t,j} \geq -rA \\ [0,\pi], & \text{if } l_{t,j} < -rA. \end{cases} \tag{6.105}$$

Assuming that (6.42) hold, solving (6.104) gives

$$\phi \in \begin{cases} [0, \pi], & \text{if } -r^2 A > B, l_{t,j} < \frac{-r^2 A - B}{2r} \\ [0, \mathcal{F}_2], & \text{if } l_{t,j} \geq \frac{\left|-r^2 A - B\right|}{2r} \\ \{\emptyset\}, & \text{otherwise.} \end{cases} \tag{6.106}$$

The intersections of (6.105) and (6.106) are given by (6.106). Hence, the feasible regions for $x_2 > r$ or $0 \leq x_2 \leq r$ are given by (6.103) and (6.106), respectively. As a result, when $x_2 > r$, (6.34) is obtained. Meanwhile, when $0 \leq x_2 \leq r$, (6.35) is obtained.

For $A > 0, B < 0$**:** Comparing x_1 with 0 gives

$$\phi \in [0, \pi], \text{ for } x_1 \geq 0; \text{ and } \phi = \emptyset, \text{ for } x_1 < 0. \tag{6.107}$$

Comparing x_2 with 0 gives

$$\phi = \emptyset, \text{ for } x_2 \geq 0; \text{ and } \phi \in [0, \pi] \text{ for } x_2 < 0. \tag{6.108}$$

Comparing x_1 with r,

$$x_1 > r \Rightarrow \sqrt{(l_{t,j} \cos\phi)^2 - BA} > rA - l_{t,j} \cos\phi. \tag{6.109}$$

If $rA - l_{t,j} \cos\phi < 0$, then

$$\phi \in \begin{cases} [0, \mathcal{F}_3), & \text{if } l_{t,j} \geq rA \\ \{\emptyset\}, & \text{if } l_{t,j} < rA. \end{cases} \tag{6.110}$$

If

$$rA - l_{t,j} \cos\phi \geq 0 \tag{6.111}$$

then

$$\phi \in \begin{cases} [\mathcal{F}_3, \pi], & \text{if } l_{t,j} \geq rA \\ [0, \pi], & \text{if } l_{t,j} < rA. \end{cases} \tag{6.112}$$

Assuming that (6.42) and (6.111) hold, solving (6.109) gives

$$\phi \in \begin{cases} [0, \pi], & \text{if } -r^2A > B, l_{t,j} < \frac{-r^2A-B}{2r} \\ [0, \mathcal{F}_2], & \text{if } -r^2A \leq B, l_{t,j} \geq \frac{r^2A+B}{2r} \\ [0, \mathcal{F}_2], & \text{if } -r^2A > B, l_{t,j} \geq \frac{-r^2A-B}{2r} \\ \{\emptyset\}, & \text{otherwise.} \end{cases} \tag{6.113}$$

Then, combining (6.112) and (6.113) with intersections yields

$$\phi \in \begin{cases} [0, \pi], & \text{if } -A > \frac{B}{r^2}, -A \geq \frac{B}{3r^2}, l_{t,j} < rA \\ [0, \pi], & \text{if } -A > \frac{B}{r^2}, -A < \frac{B}{3r^2}, l_{t,j} < \frac{-r^2A-B}{2r} \\ [0, \mathcal{F}_2], & \text{if } -A \leq \frac{B}{r^2}, \frac{r^2A+B}{2r} \leq l_{t,j} < rA \\ [0, \mathcal{F}_2], & \text{if } -A > \frac{B}{r^2}, -A < \frac{B}{3r^2}, \frac{-r^2A-B}{2r} \leq l_{t,j} < rA \\ [\mathcal{F}_3, \pi], & \text{if } -A > \frac{B}{r^2}, -A > \frac{B}{3r^2}, rA \leq l_{t,j} < \frac{-r^2A-B}{2r} \\ [\mathcal{F}_3, \mathcal{F}_2], & \text{if } -A \leq \frac{B}{r^2}, l_{t,j} \geq rA \\ [\mathcal{F}_3, \mathcal{F}_2], & \text{if } -A > \frac{B}{r^2}, -A \geq \frac{B}{3r^2}, l_{t,j} \geq \frac{-r^2A-B}{2r} \\ [\mathcal{F}_3, \mathcal{F}_2], & \text{if } -A > \frac{B}{r^2}, -A < \frac{B}{3r^2}, l_{t,j} \geq rA \\ \{\emptyset\}, & \text{otherwise.} \end{cases} \tag{6.114}$$

The unions of (6.110) and (6.114) yield

$$\phi \in \begin{cases} [0, \pi], & \text{if } -r^2A > B, l_{t,j} < \frac{-r^2A-B}{2r} \\ [0, \mathcal{F}_2], & \text{if } l_{t,j} \geq \frac{|r^2A+B|}{2r} \\ \{\emptyset\}, & \text{otherwise.} \end{cases} \tag{6.115}$$

Meanwhile,

$$x_1 \leq r \Rightarrow \sqrt{(l_{t,j}\cos\phi)^2 - BA} \leq rA - l_{t,j}\cos\phi. \tag{6.116}$$

If

$$rA - l_{t,j}\cos\phi \geq 0 \tag{6.117}$$

then

$$\phi \in \begin{cases} [\mathcal{F}_3, \pi], & \text{if } l_{t,j} \geq rA \\ [0, \pi], & \text{if } l_{t,j} < rA. \end{cases} \tag{6.118}$$

Assuming that (6.42) and (6.117) hold, solving (6.116) gives

$$\phi \in \begin{cases} [0, \pi], & \text{if } -r^2A < B, l_{t,j} < \frac{r^2A+B}{2r} \\ [\mathcal{F}_2, \pi], & \text{if } l_{t,j} \geq \frac{|r^2A+B|}{2r} \\ \{\emptyset\}, & \text{otherwise.} \end{cases} \tag{6.119}$$

The intersections of (6.118) and (6.119) is (6.119). Hence, the feasible regions for $x_1 > r$ or $0 \leq x_1 \leq r$ are given by (6.115) and (6.119), respectively. As a result of the above discussions, when $x_1 > r$, (6.36) is obtained. Meanwhile, when $0 \leq x_1 \leq r$, (6.37) is obtained.

For $A = 0$**:** The corresponding solution to $1 + \frac{(H^2+l_{t,e}^2)^{\frac{-\alpha}{2}}\eta P_s}{\left(l_{t,j}^2+l_{t,e}^2-2l_{t,j}l_{t,e}\cos(\phi)\right)^{\frac{-\alpha}{2}}P_j} \leq y$ is given by $\cos\phi \geq \frac{l_{t,j}^2 - H^2}{2l_{t,j}l_{t,e}}$. Thus,

$$\phi \in \begin{cases} \left[0, \cos^{-1}\left(\frac{l_{t,j}^2 - H^2}{2l_{t,j}l_{t,e}}\right)\right], & \text{if } \frac{\left|l_{t,j}^2 - H^2\right|}{2l_{t,j}} \leq l_{t,e} \\ [0, \pi], & \text{if } \frac{-l_{t,j}^2 + H^2}{2l_{t,j}} > l_{t,e} \\ \{\emptyset\}, & \text{otherwise.} \end{cases} \tag{6.120}$$

Comparing $l_{t,e}$ from (6.120) with r, (6.38) - (6.40) are obtained. This concludes the proof.

□

Chapter 7

Conclusions and Future Work

7.1 Conclusions

In this thesis, the fundamentals of device-to-device (D2D) technology and physical layer security have been introduced. Four research chapters cover a wide range of application scenarios in future wireless networks with demands on reliability and security. Stochastic geometry models the spatial realizations of the network nodes and reveals the coverage and secrecy performance of a typical wireless link.

In detail, Chapter 1 briefly discusses the development of reliability and security in wireless communications. Then, a comprehensive research overview is provided in Chapter 2, covering the fundamentals of D2D technology, physical layer security and stochastic geometry.

The first technical chapter focuses on the reliability enhancement of concurrent D2D communications by maximizing the joint coverage probability or minimizing the power consumption of the D2D user equipments (DUEs) under the joint coverage constraint in a clustered network, in which Poisson cluster process is employed to model the location distribution of D2D pairs. The formulations on the joint coverage probability with different amount of device location information allow the applicability of the optimization schemes to both centralized and localized networks. The simulation results show that the proposed schemes outperform the conventional open loop and fixed power schemes in joint coverage enhancement.

The second research chapter focuses on the end-to-end reliability enhancement for the clustered mission-critical public safety networks via route selection, in which the end-to-end reliability depends on coverage, delay and trust criteria. The route selection method is developed to find the maximum end-to-end probability of one criterion while the consisting links of other criteria must satisfy the given thresholds. The simulations have shown that, compared with the shortest path selection for end-to-end reliability based on coverage only in the literature, the proposed method can reduce the chance of selecting the congested and malicious forwarding user equipments (UEs).

In the third research chapter, the meta distribution of the secrecy rate is formulation to give a fraction of spatial realizations of the Poisson point process modeled colluding and non-colluding ground eavesdroppers (EDs) that yield a secrecy rate for the legitimate link. It has been shown that the formulated results are not related to the exact value of the transmit power if the legitimate and eavesdropping links are in the high signal-to-noise ratio (SNR) regime. Also, the meta distribution in the high SNR regime is an upper bound of the one in the noise-limited regime. Furthermore, the meta distribution for the non-colluding scenario is lower bounded by its colluding counterpart.

The last research chapter studies the secrecy performance of wireless communications in the presence of unmanned aerial vehicle (UAV) jammer and randomly located non-colluding UAV eavesdroppers (UEDs), where the uniform binomial point process (BPP) is used to characterize the randomness of the UEDs. A highly accurate fitting function to the line-of-sight (LoS) probability has been proposed so that a tractable expression on the secure connection probability (SCP) is obtained. The analyses on the SCP show that the effect on the SCP due to the increased jamming power varies. In general, when the jamming power is very small, the SCP could either increase or decrease. Then, the SCP starts to drop as the jamming power increases when the legitimate and eavesdropping links reach the interference-limited regime. Besides, when the UAV altitude is much higher than a value related to the radius of the UAV plane and the distance of the ground link, the optimum position on the jamming location for the pure LoS channel is proved to be the center of the UAV plane.

As observed from the above scenarios, the reliability of both centralized and distributed D2D clustered networks can be enhanced by joint optimizing the transmit power of the D2D concurrent links with the help of stochastic geometry. Meanwhile, the route selection for multi-hop D2D networks, modeled by stochastic geometry, queuing theory and trust reputation system, overcomes the interference, delay and trust issues in forwarding so that the end-to-end reliability is enhanced. Furthermore, the meta distribution of the secrecy rate modeled by stochastic geometry for physical layer security reveals that the legitimate link working in the interference-limited regime performs better than working in the noise-limited regime by increasing the transmit power substantially. Finally, stochastic geometry modeled UAV jamming and eavesdropping framework for physical layer security shows that the UAV jammer does not always contribute positively to combat the UEDs, and the UAV jammer at a given position should only be activated if the SCP improved when enabling the UAV jammer.

Thus, the analyses and methodologies presented in the thesis will help to facilitate the modeling and design of the reliability and security for the future wireless communication networks.

7.2 Future Work

Throughout the research, a number of potential research activities to extend the work have been discovered. Acting as the signpost for advanced research activities, the work in this thesis can be extended as follows:

For the first research chapter on reliable concurrent transmission, a minimum coverage performance target may be required for each D2D pair to meet the quality of service (QoS) that is similar to the traditional cellular communications. In detail, this can be achieved by adding the coverage probability thresholds for each link to the constraints of the optimization schemes. One may assign different thresholds for the links when considering their different level of QoS to the subscribers. Besides, rather than working at dedicated channel resources, D2D users could share the channel resources with cellular users aiming at the maximizing the reliability of concurrent cellular and D2D communications.

For the second research chapter on end-to-end reliability, it would be interesting to study different types of clusters such as the one with Gaussian distributed members. In the meantime, power control such as the minimization of the end-to-end power for a fixed route and the minimization of the transmit power under a reliability constraint before route selection can be applied. As a result, the lifetimes of the nodes in the selected path are prolonged. Meanwhile, the energy of the UEs on the shortest path would deplete rapidly if a UE keeps using this path for transmitting messages, and this will reduce the lifetime of the whole network. Therefore, it is of great interest to design a route selection algorithm to balance the usage of several candidate links with acceptable reliability so that a network can survive for a longer time. Furthermore, it would be useful to consider traffic with different levels of priorities. In addition, it is worthwhile to investigate how to carry out the trust rating when the observing UE is busy and cannot witness the forwarding behavior of neighboring UEs.

For the third research chapter on the meta distribution of the secrecy rate, the interference from neighboring users can be considered in future work. The analysis on the problem would be similar to the one in the final research chapter since interference and jamming are inherently the same in a mathematical sense. Meanwhile, it would be worthwhile to check the link secrecy performance under the power control such as channel inversion. In the channel inversion, the transmitter varies the power and phase of its transmitted signals from itself to the legitimate receiver in order to keep the signal power at the receiver equal to a certain constant value. One of the great advantages of channel inversion is that it does not require the receiver's channel state information when the channel is reciprocal in time division duplex (TDD) communication systems [237]. This, in turn, can help to hide the existence of the transmitter from EDs [238]. Furthermore, an investigation can be done to optimize the meta distribution directly to improve the fraction of users achieving a certain secrecy rate.

For the final research chapter on the secrecy performance with UAV jamming and eavesdropping, it is necessary to analyze the trend of the SCP and provide a clear guideline to find the optimum jamming position in future work. Besides, since there are cases where no jamming or less jamming power could provide a higher SCP, the optimization of the jamming power would be useful. In addition, a combination of the optimum jamming position and power is expected to achieve the optimum SCP. Furthermore, UAV jamming should also consider the power constraint so that it can work for a longer time. In contrast to the above method based on UAV jammers, it would also be useful to study the power allocation on the legitimate link to maximize the SCP. A combination of the power allocation on the UAV jammer and the transmitter would be useful to maximize the SCP while maintaining a longer jamming time.

References

[1] C. E. Shannon, "A mathematical theory of communication," *The Bell System Technical Journal*, vol. 27, no. 3, pp. 379–423,623–656, July, Oct. 1948.

[2] W. Mohr, "The 5G infrastructure association," ITU-R. [Online]. Available: https://www.itu.int/en/ITU-R/study-groups/rsg5/rwp5d/imt-2020/Documents/S03-1_5GPPP[Accessed: Mar. 29, 2019]

[3] G. I. P. Association *et al.*, "5G vision-the 5G infrastructure public private partnership: the next generation of communication networks and services," *White Paper, February*, Feb. 2015. [Online]. Available: https://5g-ppp.eu/wp-content/uploads/2015/02/5G-Vision-Brochure-v1.pdf [Accessed: Mar. 29, 2019]

[4] ITU, "IMT Vision – Framework and overall objectives of the future development of IMT for 2020 and beyond," ITU, Recommendation M.2083-0, Sept. 2015. [Online]. Available: http://www.itu.int/rec/R-REC-M.2083-0-201509-I [Accessed: Mar. 29, 2019]

[5] Y. Wu, A. Khisti, C. Xiao, G. Caire, K.-K. Wong, and X. Gao, "A survey of physical layer security techniques for 5G wireless networks and challenges ahead," *IEEE Journal on Selected Areas in Communications*, vol. 36, no. 4, pp. 679–695, Apr. 2018.

[6] G. Miao and G. Song, *Energy and spectrum efficient wireless network design.* Cambridge, UK: Cambridge University Press, 2014.

[7] D. Tse and P. Viswanath, *Fundamentals of wireless communication.* Cambridge, UK: Cambridge university press, 2005.

[8] R. Ghosh, *Wireless networking and mobile data management.* Gateway East, Singapore: Springer, 2017.

[9] Z. Ding, X. Lei, G. K. Karagiannidis, R. Schober, J. Yuan, and V. K. Bhargava, "A survey on non-orthogonal multiple access for 5G networks: Research challenges and future trends," *IEEE Journal on Selected Areas in Communications*, vol. 35, no. 10, pp. 2181–2195, Oct. 2017.

[10] P. Elias, "Coding for noisy channels," *IRE Convention Record, Part 4*, vol. 3, pp. 37–46, 1955.

[11] M. Chiang, P. Hande, T. Lan, C. W. Tan *et al.*, "Power control in wireless cellular networks," *Foundations and Trends® in Networking*, vol. 2, no. 4, pp. 381–533, June 2008.

[12] C. Berrou, A. Glavieux, and P. Thitimajshima, "Near Shannon limit error-correcting coding and decoding: Turbo-codes," in *Proc. IEEE Int. Conf. Commun. (ICC)*, vol. 2. Geneva, Switzerland: IEEE, May 1993, pp. 1064–1070.

[13] V. K. Garg and T. S. Rappaport, *Wireless network evolution: 2G to 3G.* Upper Saddle River, NJ: Prentice Hall PTR, 2001.

[14] 3GPP, "Soft frequency reuse scheme for UTRAN LTE," 3GPP, TSG RAN WG1 Meeting #41 R1-050507, May 2005. [Online]. Available: http://www.3gpp.org/ftp/tsg_ran/WG1_RL1/TSGR1_41/Docs/R1-050507.zip [Accessed: Mar. 29, 2019]

[15] X. Yang, "A multilevel soft frequency reuse technique for wireless communication systems," *IEEE Communications Letters*, vol. 18, no. 11, pp. 1983–1986, Nov. 2014.

[16] A. Burr, "Turbo-codes: the ultimate error control codes?" *Electronics & Communication Engineering Journal*, vol. 13, no. 4, pp. 155–165, Aug. 2001.

[17] C. Cox, *An introduction to LTE: LTE, LTE-advanced, SAE and 4G mobile communications.* Chichester, West Sussex, UK: John Wiley & Sons, 2012.

[18] Creonic, "IEEE 802.11n/ac/ax (WiFi) LDPC decoder and encoder," Creonic GmbH. [Online]. Available: https://www.creonic.com/en/ip-core/ieee-802-11n-ac-wifi-ldpc-decoder/ [Accessed: Mar. 29, 2019]

[19] Cisco, "802.11ac: The fifth generation of Wi-Fi technical white paper," Cisco, Tech. Rep., Jan. 2018. [Online]. Available: https://www.cisco.com/c/dam/en/us/products/collateral/wireless/aironet-3600-series/white-paper-c11-713103.pdf [Accessed: Mar. 29, 2019]

[20] D. Qiao, S. Choi, and K. G. Shin, "Interference analysis and transmit power control in IEEE 802.11 a/h wireless LANs," *IEEE/ACM Transactions on Networking*, vol. 15, no. 5, pp. 1007–1020, Oct. 2007.

[21] D. Câmara and N. Nikaein, *Wireless Public Safety Networks Volume 1: Overview and Challenges.* Kidlington, Oxford, UK: Elsevier, 2015.

[22] M. Höyhtyä, O. Apilo, and M. Lasanen, "Review of latest advances in 3GPP standardization: D2D communication in 5G systems and its energy consumption models," *Future Internet*, vol. 10, no. 1, p. 3, Jan. 2018.

[23] S. Verdu, "Fifty years of Shannon theory," *IEEE Transactions on Information Theory*, vol. 44, no. 6, pp. 2057–2078, Oct. 1998.

[24] R. N. Clarke, "Expanding mobile wireless capacity: The challenges presented by technology and economics," *Telecommunications Policy*, vol. 38, no. 8-9, pp. 693–708, Sept. 2014.

[25] D. Tsolkas, E. Liotou, N. Passas, and L. Merakos, "LTE-A access, core, and protocol architecture for D2D communication," in *Smart Device to Smart Device Communication*. Cham, Switzerland: Springer, 2014, pp. 23–40.

[26] A. Abdallah, M. M. Mansour, and A. Chehab, "Power control and channel allocation for D2D underlaid cellular networks," *IEEE Transactions on Communications*, vol. 66, no. 7, pp. 3217–3234, July 2018.

[27] A. Paramonov, O. Hussain, K. Samouylov, A. Koucheryavy, R. Kirichek, and Y. Koucheryavy, "Clustering optimization for out-of-band D2D communications," *Wireless Communications and Mobile Computing*, vol. 2017, Oct. 2017.

[28] F. Baccelli, B. Błaszczyszyn *et al.*, "Stochastic geometry and wireless networks: Volume II applications," *Foundations and Trends® in Networking*, vol. 4, no. 1–2, pp. 1–312, 2010.

[29] M. Haenggi, *Stochastic geometry for wireless networks*. Cambridge, UK: Cambridge University Press, 2012.

[30] A. Al-Hourani, S. Kandeepan, and A. Jamalipour, "Stochastic geometry study on device-to-device communication as a disaster relief solution," *IEEE Transactions on Vehicular Technology*, vol. 65, no. 5, pp. 3005–3017, May 2016.

[31] C. E. Shannon, "Communication theory of secrecy systems," *Bell system technical journal*, vol. 28, no. 4, pp. 656–715, Oct. 1949.

[32] W. Saad, X. Zhou, M. Debbah, and H. V. Poor, "Wireless physical layer security: Part 1 [guest editorial]," *IEEE Communications Magazine*, vol. 53, no. 6, pp. 15–15, June 2015.

[33] T. Pecorella, L. Brilli, and L. Mucchi, "The role of physical layer security in IoT: A novel perspective," *Information*, vol. 7, no. 3, p. 49, Aug. 2016.

[34] J. Zhang, T. Q. Duong, R. Woods, and A. Marshall, "Securing wireless communications of the internet of things from the physical layer, an overview," *Entropy*, vol. 19, no. 8, p. 420, Aug. 2017.

[35] L. Sun and Q. Du, "Physical layer security with its applications in 5G networks: A review," *China Communications*, vol. 14, no. 12, pp. 1–14, Dec. 2017.

[36] A. Mukherjee, S. A. A. Fakoorian, J. Huang, and A. L. Swindlehurst, "Principles of physical layer security in multiuser wireless networks: A survey," *IEEE Communications Surveys & Tutorials*, vol. 16, no. 3, pp. 1550–1573, Aug. 2010.

[37] A. D. Wyner, "The wire-tap channel," *Bell system technical journal*, vol. 54, no. 8, pp. 1355–1387, Oct. 1975.

[38] I. Csiszár and J. Korner, "Broadcast channels with confidential messages," *IEEE Transactions on Information Theory*, vol. 24, no. 3, pp. 339–348, May 1978.

[39] H. V. Poor and R. F. Schaefer, "Wireless physical layer security," *Proceedings of the National Academy of Sciences*, vol. 114, no. 1, pp. 19–26, Jan. 2017.

[40] S. Leung-Yan-Cheong and M. Hellman, "The Gaussian wire-tap channel," *IEEE Transactions on Information Theory*, vol. 24, no. 4, pp. 451–456, July 1978.

[41] U. M. Maurer, "Secret key agreement by public discussion from common information," *IEEE Transactions on Information Theory*, vol. 39, no. 3, pp. 733–742, May 1993.

[42] M. Bloch, J. Barros, M. R. Rodrigues, and S. W. McLaughlin, "Wireless information-theoretic security," *IEEE Transactions on Information Theory*, vol. 54, no. 6, pp. 2515–2534, June 2008.

[43] W. K. Harrison, J. Almeida, M. R. Bloch, S. W. McLaughlin, and J. Barros, "Coding for secrecy: An overview of error-control coding techniques for physical-layer security," *IEEE Signal Processing Magazine*, vol. 30, no. 5, pp. 41–50, Sept. 2013.

[44] Y.-S. Shiu, S. Y. Chang, H.-C. Wu, S. C.-H. Huang, and H.-H. Chen, "Physical layer security in wireless networks: A tutorial," *IEEE Wireless Communications*, vol. 18, no. 2, Apr. 2011.

[45] M. A. Kishk and H. S. Dhillon, "Stochastic geometry-based comparison of secrecy enhancement techniques in D2D networks," *IEEE Wireless Communications Letters*, vol. 6, no. 3, pp. 394–397, June 2017.

[46] A. Asadi, Q. Wang, and V. Mancuso, "A survey on device-to-device communication in cellular networks," *IEEE Communications Surveys & Tutorials*, vol. 16, no. 4, pp. 1801–1819, Apr. 2014.

[47] G. A. Safdar, M. Ur-Rehman, M. Muhammad, M. A. Imran, and R. Tafazolli, "Interference mitigation in D2D communication underlaying LTE-A network," *IEEE Access*, vol. 4, pp. 7967–7987, Oct. 2016.

[48] T. Koskela, S. Hakola, T. Chen, and J. Lehtomaki, "Clustering concept using device-to-device communication in cellular system," in *Proc. IEEE Wireless Commun. Netw. Conf. (WCNC)*. Sydney, Australia: IEEE, Apr. 2010.

[49] G. Fodor, S. Parkvall, S. Sorrentino, P. Wallentin, Q. Lu, and N. Brahmi, "Device-to-device communications for national security and public safety," *IEEE Access*, vol. 2, pp. 1510–1520, Dec. 2014.

[50] A. Asadi and V. Mancuso, "Network-assisted outband D2D-clustering in 5G cellular networks: theory and practice," *IEEE Transactions on Mobile Computing*, vol. 16, no. 8, pp. 2246–2259, Oct. 2017.

[51] W. Yi, Y. Liu, and A. Nallanathan, "Modeling and analysis of D2D millimeter-wave networks with Poisson cluster processes," *IEEE Transactions on Communications*, vol. 65, no. 12, pp. 5574–5588, Dec. 2017.

[52] T. Lynch, "Whitepaper: LTE in Public Safety," IHS Technology, Whitepaper, May 2016. [Online]. Available: https://technology.ihs.com/580532/whitepaper-lte-in-public-safety [Accessed: Mar. 29, 2019]

[53] L. Wang, *Physical Layer Security in Wireless Cooperative Networks.* Cham, Switzerland: Springer, 2018.

[54] H. Wang, X. Zhou, and M. C. Reed, "Physical layer security in cellular networks: A stochastic geometry approach," *IEEE Transactions on Wireless Communications*, vol. 12, no. 6, pp. 2776–2787, May 2013.

[55] M. Salehi, A. Mohammadi, and M. Haenggi, "Analysis of D2D underlaid cellular networks: SIR meta distribution and mean local delay," *IEEE Transactions on Communications*, vol. 65, pp. 2904–2916, Jul. 2017.

[56] M. A. Kishk and H. S. Dhillon, "Stochastic geometry-based comparison of secrecy enhancement techniques in D2D networks," *IEEE Wireless Communications Letters*, vol. 6, no. 3, pp. 394–397, June 2017.

[57] J. Tang, G. Chen, and J. P. Coon, "Joint coverage enhancement by power allocation in Poisson clustered out-of-band D2D networks," *IEEE Transactions on Vehicular Technology*, vol. 67, no. 12, pp. 11 537–11 548, Dec. 2018.

[58] J. Tang, G. Chen, J. P. Coon, and D. E. Simmons, "Distance distributions for Matérn cluster processes with application to network performance analysis," in *Proc. IEEE Int. Conf. Commun. (ICC).* Paris, France: IEEE, May 2017.

[59] J. Tang, J. P. Coon, and G. Chen, "Optimal cross-tier power allocation for D2D multi-cell networks," in *Proc. IEEE Global Commun. Conf. (GLOBECOM)*, Washington, D.C., Dec. 2016.

[60] A. E. Khandani, J. Abounadi, E. Modiano, and L. Zheng, "Reliability and route diversity in wireless networks," *IEEE Transactions on Wireless Communications*, vol. 7, no. 12, pp. 4772–4776, Dec. 2008.

[61] B. Gui, L. Dai, and L. J. Cimini, "Routing strategies in multihop cooperative networks," *IEEE Transactions on Wireless Communications*, vol. 8, no. 2, pp. 843–855, Feb. 2009.

[62] A. Fida, D. H. Pham, N. J. Tuah, and T. D. Ngo, "Communication-aware route selection in wireless sensor networks," in *Proc. 13th Int. Conf. Intell. Auton. Syst. (IAS).* Padua, Italy: Springer, July 2014, pp. 605–619.

[63] J. Tang, G. Chen, and J. P. Coon, "Route selection based on connectivity-delay-trust in public safety networks," *IEEE Systems Journal*, vol. 13, no. 2, pp. 1558–1567, June 2019.

[64] J. Tang and G. Chen and J. P. Coon, "Meta distribution of the secrecy rate in the presence of randomly located eavesdroppers," *IEEE Wireless Communications Letters*, vol. 7, no. 4, pp. 630–633, Aug. 2018.

[65] J. Tang, G. Chen, and J. P. Coon, "Secrecy performance analysis of wireless communications in the presence of UAV jammer and randomly located UAV eavesdroppers," *IEEE Transactions on Information Forensics and Security*, vol. 14, no. 11, pp. 3026–3041, Nov. 2019.

[66] X. Lin, J. Andrews, A. Ghosh, and R. Ratasuk, "An overview of 3GPP device-to-device proximity services," *IEEE Communications Magazine*, vol. 52, no. 4, pp. 40–48, Apr. 2014.

[67] Qualcomm, "Expanding your horizons with LTE direct enabling the next generation of proximal services," Signals Research Group, Qualcomm, Tech. Rep., Sept. 2015. [Online]. Available: https://www.qualcomm.com/documents/srg-whitepaper-expanding-your-horizons-lte-direct [Accessed: Mar. 29, 2019]

[68] S. Bayhan, G. Gür, and A. Zubow, "The future is unlicensed: Coexistence in the unlicensed spectrum for 5G," *CoRR*, vol. abs/1801.04964, 2018. [Online]. Available: http://arxiv.org/abs/1801.04964

[69] P. Gawlowicz, A. Zubow, and A. Wolisz, "Enabling cross-technology communication between LTE unlicensed and WiFi," in *Proc. IEEE INFOCOM 2018-IEEE Conf. Comput. Commun.* Honolulu, HI: IEEE, Apr. 2018, pp. 144–152.

[70] Y. Mekonnen, M. Haque, I. Parvez, A. Moghadasi, and A. Sarwat, "LTE and Wi-Fi coexistence in unlicensed spectrum with application to smart grid: A review," in *Proc. IEEE/PES Transmission Distrib. Conf. Exposition (T&D)*. Denver, CO: IEEE, Apr. 2018, pp. 1–5.

[71] C. X. Wang, F. Haider, X. Gao, X. H. You, Y. Yang, D. Yuan, H. M. Aggoune, H. Haas, S. Fletcher, and E. Hepsaydir, "Cellular architecture and key technologies for 5G wireless communication networks," *IEEE Communications Magazine*, vol. 52, no. 2, pp. 122–130, Feb. 2014.

[72] S. Yasukaw, H. Harada, S. Nagata, and Q. Zhao, "D2D communications in LTE-Advanced release 12," *NTT DOCOMO Technical Journal*, vol. 17, no. 2, pp. 56–64, Oct. 2015.

[73] G. Fodor, E. Dahlman, G. Mildh, S. Parkvall, N. Reider, G. Miklós, and Z. Turányi, "Design aspects of network assisted device-to-device communications," *IEEE Communications Magazine*, vol. 50, no. 3, pp. 170–177, Mar. 2012.

[74] A. Al-Hourani, S. Kandeepan, and E. Hossain, "Relay-assisted device-to-device communication: A stochastic analysis of energy saving," *IEEE Transactions on Mobile Computing*, vol. 15, no. 12, pp. 3129–3141, Dec. 2016.

[75] S. Jung and J. Kim, "A new way of extending network coverage: Relay-assisted D2D communications in 3GPP," *ICT Express*, vol. 2, no. 3, pp. 117–121, Sept. 2016.

[76] U. Uyoata and M. Dlodlo, "Relay assisted device-to-device communication: Approaches and issues," *arXiv preprint arXiv:1810.07799*, 2018.

[77] M. Iwamura, H. Takahashi, and S. Nagata, "Relay technology in LTE-advanced," *NTT DOCOMO Technical Journal*, vol. 12, no. 2, pp. 29–36, July 2010.

[78] M. N. Tehrani, M. Uysal, and H. Yanikomeroglu, "Device-to-device communication in 5G cellular networks: challenges, solutions, and future directions," *IEEE Communications Magazine*, vol. 52, no. 5, pp. 86–92, 2014.

[79] S. Sesia, M. Baker, and I. Toufik, *LTE-the UMTS long term evolution: from theory to practice.* John Wiley & Sons, 2011.

[80] A. E. Azhar, A. L. Yusof, M. Rosdi, A. Idris, and N. Ya'acob, "Interferences and solutions in long term evolution (LTE) network: A review," *Journal of Telecommunication, Electronic and Computer Engineering (JTEC)*, vol. 9, no. 1-4, pp. 139–143, Mar. 2017.

[81] T. Ozan, K. and F. Gianluigi, Eds., *Ad Hoc Wireless Networks: A Communication-Theoretic Perspective.* Chichester, West Sussex, UK: John Wiley & Sons Ltd, 2006.

[82] H. ElSawy, A. Sultan-Salem, M.-S. Alouini, and M. Z. Win, "Modeling and analysis of cellular networks using stochastic geometry: A tutorial," *IEEE Communications Surveys & Tutorials*, vol. 19, no. 1, pp. 167–203, Jan. 2017.

[83] A. J. Goldsmith and P. P. Varaiya, "Capacity of fading channels with channel side information," *IEEE Transactions on Information Theory*, vol. 43, no. 6, pp. 1986–1992, Nov. 1997.

[84] M. Haenggi, "A geometric interpretation of fading in wireless networks: Theory and applications," *IEEE Transactions on Information Theory*, vol. 54, no. 12, pp. 5500–5510, Dec. 2008.

[85] Z. Jakó and G. Jeney, "Outage probability in Poisson-cluster-based LTE two-tier femtocell networks," *Wireless Communications and Mobile Computing*, vol. 15, no. 18, pp. 2179–2190, June 2015.

[86] S. Kandukuri and S. Boyd, "Optimal power control in interference-limited fading wireless channels with outage-probability specifications," *IEEE Transactions on Wireless Communications*, vol. 1, no. 1, pp. 46–55, Jan. 2002.

[87] Y. D. Yao and A. U. H. Sheikh, "Outage probability analysis for microcell mobile radio systems with cochannel interferers in Rician/Rayleigh fading environment," *Electronics Letters*, vol. 26, no. 13, pp. 864–866, June 1990.

[88] C. Tellambura, "Cochannel interference computation for arbitrary Nakagami fading," *IEEE Transactions on Vehicular Technology*, vol. 48, no. 2, pp. 487–489, Mar. 1999.

[89] P. Fan and K. B. Letaief, "Understanding of transmission throughput and channel capacity in a systematic way," in *Proc. 20th Annu. Wireless Optical Commun. Conf. (WOCC)*. Newark, NJ: IEEE, 2011.

[90] M. Noura and R. Nordin, "A survey on interference management for device-to-device (D2D) communication and its challenges in 5G networks," *Journal of Network and Computer Applications*, vol. 71, pp. 130–150, Aug. 2016.

[91] Y. L. Lee, T. C. Chuah, J. Loo, and A. Vinel, "Recent advances in radio resource management for heterogeneous LTE/LTE-A networks," *IEEE Communications Surveys & Tutorials*, vol. 16, no. 4, pp. 2142–2180, June 2014.

[92] G. Fodor, "Performance comparison of practical resource allocation schemes for device-to-device communications," *Wireless Communications and Mobile Computing*, vol. 2018, 2018.

[93] Y. Huang, A. A. Nasir, S. Durrani, and X. Zhou, "Mode selection, resource allocation, and power control for D2D-enabled two-tier cellular network," *IEEE Transactions on Communications*, vol. 64, no. 8, pp. 3534–3547, Aug. 2016.

[94] Y. Li, T. Wu, P. Hui, D. Jin, and S. Chen, "Social-aware D2D communications: Qualitative insights and quantitative analysis," *IEEE Communications Magazine*, vol. 52, no. 6, pp. 150–158, June 2014.

[95] H. ElSawy, E. Hossain, and M.-S. Alouini, "Analytical modeling of mode selection and power control for underlay D2D communication in cellular networks," *IEEE Transactions on Communications*, vol. 62, no. 11, pp. 4147–4161, Nov. 2014.

[96] F. S. Moya, V. Venkatasubramanian, P. Marsch, and A. Yaver, "D2D mode selection and resource allocation with flexible UL/DL TDD for 5G deployments," in *Proc. IEEE Int. Conf. Commun. Workshop (ICCW)*. London, UK: IEEE, June 2015, pp. 657–663.

[97] D. Della Penda, L. Fu, and M. Johansson, "Energy efficient D2D communications in dynamic TDD systems," *IEEE Transactions on Communications*, vol. 65, no. 3, pp. 1260–1273, Mar. 2017.

[98] B. Cho, K. Koufos, and R. Jantti, "Spectrum allocation and mode selection for overlay D2D using carrier sensing threshold," in *Proc. 9th Int. Conf. Cognitive Radio Oriented Wireless Netw. Commun. (CROWNCOM)*. IEEE, 2014, pp. 26–31.

[99] X. Lin, J. G. Andrews, and A. Ghosh, "Spectrum sharing for device-to-device communication in cellular networks," *IEEE Transactions on Wireless Communications*, vol. 13, no. 12, pp. 6727–6740, Dec. 2014.

[100] N. Golrezaei, A. G. Dimakis, and A. F. Molisch, "Device-to-device collaboration through distributed storage," in *Proc. IEEE Global Commun. Conf. (GLOBECOM)*. Anaheim, CA: IEEE, Dec. 2012, pp. 2397–2402.

[101] Y. Zhang, J. Zheng, P.-S. Lu, and C. Sun, "Interference graph construction for cellular D2D communications," *IEEE Transactions on Vehicular Technology*, vol. 66, no. 4, pp. 3293–3305, Apr. 2017.

[102] F. Wang, C. Xu, L. Song, and Z. Han, "Energy-efficient resource allocation for device-to-device underlay communication," *IEEE Transactions on Wireless Communications*, vol. 14, no. 4, pp. 2082–2092, Apr. 2015.

[103] L. Wang, H. Tang, H. Wu, and G. L. Stüber, "Resource allocation for D2D communications underlay in Rayleigh fading channels," *IEEE Transactions on Vehicular Technology*, vol. 66, no. 2, pp. 1159–1170, Feb. 2017.

[104] X. Li, R. Shankaran, M. A. Orgun, G. Fang, and Y. Xu, "Resource allocation for underlay D2D communication with proportional fairness," *IEEE Transactions on Vehicular Technology*, vol. 67, no. 7, pp. 6244–6258, July 2018.

[105] A. Abrardo and D. Sennati, "On the analytical evaluation of closed-loop power-control error statistics in DS-CDMA cellular systems," *IEEE Transactions on Vehicular Technology*, vol. 49, no. 6, pp. 2071–2080, Nov. 2000.

[106] H. Holma and A. Toskala, *WCDMA for UMTS: HSPA evolution and LTE*. John Wiley & Sons, 2007.

[107] A. Knapp and L. Pap, "A novel mobile communication system using pulse position based chirp spread spectrum modulation," *Journal of Communications Software and Systems*, vol. 14, no. 3, pp. 228–238, Sept. 2018.

[108] M. Coupechoux and J.-M. Kelif, "How to set the fractional power control compensation factor in LTE?" in *Proc. 34th IEEE Sarnoff Symp.* Princeton, NJ: IEEE, May 2011.

[109] G. Fodor, D. Della Penda, M. Belleschi, M. Johansson, and A. Abrardo, "A comparative study of power control approaches for device-to-device communications," in *Proc. IEEE Int. Conf. Commun. (ICC)*. Budapest, Hungary: IEEE, June 2013, pp. 6008–6013.

[110] T.-W. Ban, "A practical resource management scheme for cellular underlaid D2D networks," *Future Internet*, vol. 9, no. 4, p. 62, Oct. 2017.

[111] N. Lee, X. Lin, J. G. Andrews, and R. W. Heath, "Power control for D2D underlaid cellular networks: Modeling, algorithms, and analysis," *IEEE Journal on Selected Areas in Communications*, vol. 33, no. 1, pp. 1–13, Jan. 2015.

[112] G. Yu, L. Xu, D. Feng, R. Yin, G. Y. Li, and Y. Jiang, "Joint mode selection and resource allocation for device-to-device communications," *IEEE Transactions on Communications*, vol. 62, no. 11, pp. 3814–3824, Nov. 2014.

[113] M. Bei, Z. Hailin, and Z. Zhaowei, "Joint power allocation and mode selection for D2D communications with imperfect CSI," *China Communications*, vol. 12, no. 7, pp. 73–81, July 2015.

[114] J. Zhao, K. K. Chai, Y. Chen, J. Schormans, and J. Alonso-Zarate, "Joint mode selection and radio resource allocation for D2D communications based on dynamic coalition formation game," in *Proc. 21th European Wireless Conf.* Budapest, Hungary: VDE, May 2015.

[115] Y. Zhang, F. Li, M. A. A. Al-Qaness, and X. Luan, "A resource allocation scheme for multi-D2D communications underlying cellular networks with multi-subcarrier reusing," *Applied Sciences*, vol. 7, no. 2, p. 148, Feb. 2017.

[116] X. Zhou, Y. Zhang, and L. Song, *Physical layer security in wireless communications.* Boca Raton, FL: CRC Press, 2016.

[117] U. Maurer and S. Wolf, "Information-theoretic key agreement: From weak to strong secrecy for free," in *Proc. 19th Int. Conf. Theory Appl. Cryptographic Tech.* Bruges, Belgium: Springer, May 2000, pp. 351–368.

[118] H. Mahdavifar and A. Vardy, "Achieving the secrecy capacity of wiretap channels using polar codes," *IEEE Transactions on Information Theory*, vol. 57, no. 10, pp. 6428–6443, Oct. 2011.

[119] G. Chen, J. P. Coon, and M. Di Renzo, "Secrecy outage analysis for downlink transmissions in the presence of randomly located eavesdroppers," *IEEE Transactions on Information Forensics and Security*, vol. 12, no. 5, pp. 1195–1206, May 2017.

[120] J. Barros and M. R. Rodrigues, "Secrecy capacity of wireless channels," in *Proc. IEEE Int. Symp. Inf. Theory (ISIT)*. Seattle, WA: IEEE, July 2006, pp. 356–360.

[121] P. C. Pinto, J. Barros, and M. Z. Win, "Secure communication in stochastic wireless networks–Part II: Maximum rate and collusion," *IEEE Transactions on Information Forensics and Security*, vol. 7, no. 1, pp. 139–147, Feb. 2012.

[122] R. Zhang, "EE 5407 part II: Spatial based wireless communications – lecture II: Receive beamforming." [Online]. Available: https://www.ece.nus.edu.sg/stfpage/elezhang/Lecture_Notes/Lecture2_2010.pdf [Accessed: Mar. 29, 2019]

[123] R. Adve, "Receive diversity," May 2017. [Online]. Available: https://www.comm.utoronto.ca/∼rsadve/Notes/DiversityReceive.pdf [Accessed: Mar. 29, 2019]

[124] M. Haenggi, J. G. Andrews, F. Baccelli, O. Dousse, and M. Franceschetti, "Stochastic geometry and random graphs for the analysis and design of wireless networks," *IEEE Journal on Selected Areas in Communications*, vol. 27, no. 7, pp. 1029–1046, Sept. 2009.

[125] M. Afshang and H. S. Dhillon, "Fundamentals of modeling finite wireless networks using binomial point process," *IEEE Transactions on Wireless Communications*, vol. 16, no. 5, pp. 3355–3370, May 2017.

[126] V. V. Chetlur and H. S. Dhillon, "Downlink coverage analysis for a finite 3-D wireless network of unmanned aerial vehicles," *IEEE Transactions on Communications*, vol. 65, no. 10, pp. 4543–4558, Oct. 2017.

[127] H. P. Keeler, "Notes on the Poisson point process," Jan. 2015. [Online]. Available: https://www.wias-berlin.de/people/keeler/TechnicalReports/PoissonPointProcess10.pdf [Accessed: Mar. 29, 2019]

[128] M. Haenggi and R. K. Ganti, "Interference in large wireless networks," *Foundations and Trends® in Networking*, vol. 3, no. 2, pp. 127–248, Feb. 2009. [Online]. Available: http://dx.doi.org/10.1561/1300000015

[129] R. L. Streit, *Poisson point processes: imaging, tracking, and sensing.* Springer Science & Business Media, 2010.

[130] A. E. Gelfand, P. Diggle, P. Guttorp, and M. Fuentes, *Handbook of spatial statistics.* CRC press, 2010.

[131] T. X. Brown, "Cellular performance bounds via shotgun cellular systems," *IEEE Journal on Selected Areas in Communications*, vol. 18, no. 11, pp. 2443–2455, Nov. 2000.

[132] T. D. Novlan, H. S. Dhillon, and J. G. Andrews, "Analytical modeling of uplink cellular networks," *IEEE Transactions on Wireless Communications*, vol. 12, no. 6, pp. 2669–2679, June 2013.

[133] P. C. Pinto, J. Barros, and M. Z. Win, "Secure communication in stochastic wireless networks–Part I: Connectivity," *IEEE Transactions on Information Forensics and Security*, vol. 7, no. 1, pp. 125–138, Feb. 2012.

[134] R. K. Ganti and M. Haenggi, "Interference and outage in clustered wireless ad hoc networks," *IEEE Transactions on Information Theory*, vol. 55, no. 9, pp. 4067–4086, Sept. 2009.

[135] C. Saha, M. Afshang, and H. S. Dhillon, "3GPP-inspired HetNet model using Poisson cluster process: Sum-product functionals and downlink coverage," *IEEE Transactions on Communications*, vol. 66, no. 5, pp. 2219–2234, May 2018.

[136] R. Hernandez-Aquino, S. A. R. Zaidi, M. Ghogho, D. McLernon, and A. Swami, "Stochastic geometric modeling and analysis of non-uniform two-tier networks: A Stienen's model-based approach," *IEEE Transactions on Wireless Communications*, vol. 16, no. 6, pp. 3476–3491, June 2017.

[137] H. C. Tuckwell, *Elementary applications of probability theory.* London, UK: Chapman & Hall, 1995, vol. 32.

[138] B. Thirey and R. Hickman, "Distribution of Euclidean distances between randomly distributed Gaussian points in n-space," in *Presented at the ASM 2015 Joint Mathematics Meetings*, San Antonio, TX, Jan. 2015.

[139] H. Kettani and G. O. Ostrouchov, "On the distribution of the distance between two multivariate normally distributed points," in *Proc. 7th Annu. Hawaii Int. Conf. Statistics, Mathematics Related Fields*, Honolulu, HI, Jan. 2008.

[140] Y. J. Chun, M. O. Hasna, and A. Ghrayeb, "Modeling heterogeneous cellular networks interference using Poisson cluster processes," *IEEE Journal on Selected Areas in Communications*, vol. 33, no. 10, pp. 2182–2195, Oct. 2015.

[141] M. Afshang, H. Dhillon, and P. Chong, "Modeling and performance analysis of clustered device-to-device networks," *IEEE Transactions on Wireless Communications*, vol. 15, no. 7, pp. 4957–4972, July 2016.

[142] A. M. Hayajneh, S. A. R. Zaidi, D. C. McLernon, M. Di Renzo, and M. Ghogho, "Performance analysis of UAV enabled disaster recovery networks: A stochastic geometric framework based on cluster processes," *IEEE Access*, vol. 6, pp. 26 215–26 230, 2018.

[143] A. Guo, Y. Zhong, W. Zhang, and M. Haenggi, "The Gauss–Poisson process for wireless networks and the benefits of cooperation," *IEEE Transactions on Communications*, vol. 64, no. 5, pp. 1916–1929, May 2016.

[144] I. Flint, H.-B. Kong, N. Privault, P. Wang, and D. Niyato, "Analysis of heterogeneous wireless networks using Poisson hard-core hole process," *IEEE Transactions on Wireless Communications*, vol. 16, no. 11, pp. 7152–7167, Nov. 2017.

[145] Y. Wu, W. Guo, H. Yuan, L. Li, S. Wang, X. Chu, and J. Zhang, "Device-to-device meets LTE-Unlicensed," *IEEE Communications Magazine*, vol. 54, no. 5, pp. 154–159, May 2016.

[146] Y. Zhang, L. Song, W. Saad, Z. Dawy, and Z. Han, "Contract-based incentive mechanisms for device-to-device communications in cellular networks," *IEEE Journal on Selected Areas in Communications*, vol. 33, no. 10, pp. 2144–2155, Oct. 2015.

[147] G. George, R. K. Mungara, and A. Lozano, "An analytical framework for device-to-device communication in cellular networks," *IEEE Transactions on Wireless Communications*, vol. 14, no. 11, pp. 6297–6310, Nov. 2015.

[148] M. Afshang and H. S. Dhillon, "Spatial modeling of Device-to-Device networks: Poisson cluster process meets Poisson hole process," in *Proc. 49th Asilomar Conf. Signals, Syst. Comput.*, Pacific Grove, CA, Nov. 2015, pp. 317–321.

[149] C. Wu, T. Yoshinaga, X. Chen, L. Zhang, and Y. Ji, "Cluster-based content distribution integrating LTE and IEEE 802.11 p with fuzzy logic and Q-learning," *IEEE Computational Intelligence Magazine*, vol. 13, no. 1, pp. 41–50, Feb. 2018.

[150] V. Suryaprakash, J. Møller, and G. Fettweis, "On the modeling and analysis of heterogeneous radio access networks using a Poisson cluster process," *IEEE Transactions on Wireless Communications*, vol. 14, no. 2, pp. 1035–1047, Feb. 2015.

[151] C.-H. Liu, B. Rong, and S. Cui, "Optimal discrete power control in Poisson-clustered ad hoc networks," *IEEE Transactions on Wireless Communications*, vol. 14, no. 1, pp. 138–151, Jan. 2015.

[152] M. Afshang and H. S. Dhillon, "Poisson cluster process based analysis of HetNets with correlated user and base station locations," *IEEE Transactions on Wireless Communications*, vol. 17, no. 4, pp. 2417–2431, Apr. 2018.

[153] S. Krishnan and H. S. Dhillon, "Exact characterization of spatio-temporal joint coverage probability in cellular networks," in *Proc. IEEE Wireless Commun. Netw. Conf. (WCNC)*, San Francisco, CA, Mar. 2017.

[154] S. Mukherjee, *Coverage analysis using the Poisson point process model.* Cambridge, UK: Cambridge University Press, 2013, pp. 44–81.

[155] Krishnan, Shankar and Dhillon, Harpreet S, "Spatio-temporal interference correlation and joint coverage in cellular networks," *IEEE Transactions on Wireless Communications*, vol. 16, no. 9, pp. 5659–5672, June 2017.

[156] M. A. Kishk and H. S. Dhillon, "Joint uplink and downlink coverage analysis of cellular-based RF-powered IoT network," *IEEE Transactions on Green Communications and Networking*, vol. 2, no. 2, pp. 446–459, June 2018.

[157] R. Cai, J.-K. Zhang, T. N. Davidson, W. Zhang, K. M. Wong, and P.-C. Ching, "A power allocation strategy for multiple Poisson spectrum-sharing networks," *IEEE Transactions on Wireless Communications*, vol. 14, no. 4, pp. 1785–1799, Apr. 2015.

[158] A. H. Sakr and E. Hossain, "Cognitive and energy harvesting-based D2D communication in cellular networks: Stochastic geometry modeling and analysis," *IEEE Transactions on Communications*, vol. 63, no. 5, pp. 1867–1880, May 2015.

[159] S. Panichpapiboon, G. Ferrari, and O. K. Tonguz, "Optimal common transmit power in ad hoc wireless networks," in *Proc. 24th IEEE Int. Performance Comput. Commun. Conf. (IPCCC).* Phoenix, AZ: IEEE, Apr. 2005, pp. 593–597.

[160] S. Panichpapiboon, G. Ferrari, and O. K. Tonguz, "Optimal transmit power in wireless sensor networks," *IEEE Transactions on Mobile Computing*, vol. 5, no. 10, pp. 1432–1447, Oct. 2006.

[161] E. Hossain, V. K. Bhargava, and G. P. Fettweis, *Green Radio Communication Networks.* Cambridge, UK: Cambridge University Press, 2012.

[162] A. Baddeley, E. Rubak, and R. Turner, *Spatial point patterns: methodology and applications with R.* Boca Raton, FL: CRC Press, 2015.

[163] Z. Wu, V. D. Park, and J. Li, "Enabling device to device broadcast for LTE cellular networks," *IEEE Journal on Selected Areas in Communications*, vol. 34, no. 1, pp. 58–70, Jan. 2016.

[164] M. Afshang, H. S. Dhillon, and P. H. J. Chong, "Fundamentals of cluster-centric content placement in cache-enabled device-to-device networks," *IEEE Transactions on Communications*, vol. 64, no. 6, pp. 2511–2526, June 2015.

[165] M. I. Ribeiro, "Gaussian probability density functions: Properties and error characterization," Instituto Superior Tecnico, Lisboa, Portugal, Tech. Rep., Feb. 2004.

[166] S. Guo, F. Wang, Y. Yang, and B. Xiao, "Energy-efficient cooperative transmission for simultaneous wireless information and power transfer in clustered wireless sensor networks," *IEEE Transactions on Communications*, vol. 63, no. 11, pp. 4405–4417, Nov. 2015.

[167] E. McCune, *Practical digital wireless signals*, ser. The Cambridge RF and Microwave Engineering Series. Cambridge, UK: Cambridge University Press, 2013.

[168] S. Weber, J. G. Andrews, and N. Jindal, "The effect of fading, channel inversion, and threshold scheduling on ad hoc networks," *IEEE Transactions on Information Theory*, vol. 53, no. 11, pp. 4127–4149, Nov. 2007.

[169] J. G. Andrews, F. Baccelli, and R. K. Ganti, "A tractable approach to coverage and rate in cellular networks," *IEEE Transactions on Communications*, vol. 59, no. 11, pp. 3122–3134, Nov. 2011.

[170] G. Chen and J. A. Chambers, "Exact outage probability analysis for cooperative AF relay network with relay selection in presence of inter-cell interference," *Electronics Letters*, vol. 48, no. 21, pp. 1346–1347, Oct. 2012.

[171] G. Chen, Y. Gong, P. Xiao, and R. Tafazolli, "Dual antenna selection in self-backhauling multiple small cell networks," *IEEE Communications Letters*, vol. 20, no. 8, pp. 1611–1614, Aug. 2016.

[172] 3GPP, "FDD UE minimum transmission power," 3GPP, Tech. Rep. 8(99737), Oct. 1999. [Online]. Available:

http://www.3gpp.org/ftp/tsg_ran/wg4_radio/TSGR4_08/Docs/PDFs/r4-99737.pdf [Accessed: Mar. 29, 2019]

[173] 3GPP, “Evolved Universal Terrestrial Radio Access (E-UTRA); User Equipment (UE) radio transmission and reception,” 3GPP, TS 36.101, Jan. 2016. [Online]. Available: http://www.3gpp.org/dynareport/36101.htm [Accessed: Mar. 29, 2019]

[174] S. Boyd and L. Vandenberghe, *Convex optimization*. Cambridge, UK: Cambridge University Press, 2004.

[175] J. Mattingley and S. Boyd, “Real-time convex optimization in signal processing,” *IEEE Signal Processing Magazine*, vol. 27, no. 3, pp. 50–61, May 2010.

[176] J.-P. Vert, “Nonlinear optimization: Algorithms 3: Interior-point methods,” May, June 2006. [Online]. Available: http://members.cbio.mines-paristech.fr/~jvert/teaching/2006insead/slides/7_algo3/algo3.pdf [Accessed: Mar. 29, 2019]

[177] R. Hauser, “Interior-point methods for inequality constrained optimization,” Oct. 2007. [Online]. Available: https://people.maths.ox.ac.uk/hauser/hauser_lecture4.pdf [Accessed: Mar. 29, 2019]

[178] R. A. Waltz, J. L. Morales, J. Nocedal, and D. Orban, “An interior algorithm for nonlinear optimization that combines line search and trust region steps,” *Mathematical programming*, vol. 107, no. 3, pp. 391–408, July 2006.

[179] F. Khan, *LTE for 4G mobile broadband: air interface technologies and performance*. Cambridge, UK: Cambridge University Press, 2009.

[180] TE Connectivity Data and Devices, "Mass connectivity in the 5G era," July 2018. [Online]. Available: https://www.te.com/usa-en/industries/data-center/insights/mass-connectivity-5g-era.html [Accessed: Mar. 29, 2019]

[181] C. T. Ng, M. Médard, and A. Ozdaglar, "Completion time minimization and robust power control in wireless packet networks," in *Proc. IEEE Int. Conf. Commun. (ICC)*, Dresden, Germany, June 2009.

[182] M. Bagnoli and T. Bergstrom, "Log-concave probability and its applications," in *Rationality and Equilibrium.* Springer, 2006, pp. 217–241.

[183] X. Zhang and J. G. Andrews, "Downlink cellular network analysis with multi-slope path loss models," *IEEE Transactions on Communications*, vol. 63, no. 5, pp. 1881–1894, May 2015.

[184] J. Ventura-Jaume, L. Franck, and L. Girardeau, "A distributed floor control protocol for next generation PMR based on hybrid LTE and satellite networks," in *Proc. IEEE Global Humanitarian Technol. Conf. (GHTC).* San Jose, CA: IEEE, Oct. 2014, pp. 62–69.

[185] 3GPP, "Technical Specification Group Services and System Aspects; Mission Critical Push To Talk (MCPTT) over LTE; Stage 1 (Release 15)," 3GPP, TS 22.179, June 2017. [Online]. Available: http://www.3gpp.org/ftp//Specs/archive/22_series/22.179/22179-f00.zip [Accessed: Mar. 29, 2019]

[186] K. Ali, H. X. Nguyen, P. Shah, Q.-T. Vien, and N. Bhuvanasundaram, "Architecture for public safety network using D2D communication," in *Proc. IEEE Wireless Commun. Netw. Conf. Wkshps. (WCNCW).* Doha, Qatar: IEEE, Apr. 2016.

[187] K. Ali, H. X. Nguyen, P. Shah, and Q.-T. Vien, "Energy efficient and scalable D2D architecture design for public safety network," in *Proc. Int. Conf. Advanced Commun. Syst. Inf. Security (ACOSIS)*. Marrakesh, Morocco: IEEE, Oct. 2016.

[188] J. Coon, C. P. Dettmann, and O. Georgiou, "Full connectivity: corners, edges and faces," *Journal of Statistical Physics*, vol. 147, no. 4, pp. 758–778, June 2012.

[189] J. Bai, Y. Sun, C. Phillips, and Y. Cao, "Toward constructive relay-based cooperative routing in MANETs," *IEEE Systems Journal*, July 2017.

[190] R. S. Oliver and G. Fohler, "Probabilistic estimation of end-to-end path latency in wireless sensor networks," in *Proc. IEEE 6th Int. Conf. Mobile Adhoc Sensor Systems (MASS)*. Macau, China: IEEE, Oct. 2009, pp. 423–431.

[191] T. S. Rappaport, *Wireless Communications: Principles and Practice*, 2nd ed. Upper Saddle River, NJ: Prentice-Hall, 2002.

[192] M. Boushaba, A. Hafid, and M. Gendreau, "Source-based routing in wireless mesh networks," *IEEE Systems Journal*, vol. 10, no. 1, pp. 262–270, Mar. 2016.

[193] H. Imai, *Wireless communications security*. Norwood, MA: Artech House, Inc., 2005.

[194] N. Marchang and R. Datta, "Light-weight trust-based routing protocol for mobile ad hoc networks," *IET Information Security*, vol. 6, no. 2, pp. 77–83, June 2012.

[195] A. Jøsang and R. Ismail, "The beta reputation system," in *Proc. 15th Bled Conf. Electron. Commerce*, Bled, Slovenia, June 2002, pp. 324–337.

[196] C. Zouridaki, B. L. Mark, M. Hejmo, and R. K. Thomas, "A quantitative trust establishment framework for reliable data packet delivery in MANETs," in *Proc. 3rd ACM Workshop Security Ad Hoc Sensor Netw.* Alexandria, VA: ACM, 2005.

[197] J. P. Coon, "Modelling trust in random wireless networks," in *Proc. 11th Wireless Commun. Syst. (ISWCS).* Barcelona, Spain: IEEE, Aug. 2014, pp. 976–981.

[198] A. B. Usman and J. Gutierrez, "A reliability-based trust model for efficient collaborative routing in wireless networks," in *Proc. 11th Int. Conf. Queueing Theory Netw. Appl. (QTNA).* Wellington, New Zealand: ACM, 2016.

[199] S. S. Ikki and S. Aissa, "Multihop wireless relaying systems in the presence of cochannel interferences: Performance analysis and design optimization," *IEEE Transactions on Vehicular Technology*, vol. 61, no. 2, pp. 566–573, Feb. 2012.

[200] 3GPP, "LTE; Mission Critical Push To Talk (MCPTT) media plane control; Protocol specifications (Release 13)," 3GPP, TS 24.380, May 2016. [Online]. Available: http://www.etsi.org/deliver/etsi_ts/124300_124399/124380/13.00.02_60/ts_124380v130002p.pdf [Accessed: Mar. 29, 2019]

[201] D. P. Bertsekas and R. G. Gallager, *Data networks*, 2nd ed. Englewood Cliffs, NJ: Prentice-Hall, Inc, 1992.

[202] W. A. Massey, "The analysis of queues with time-varying rates for telecommunication models," *Telecommunication Systems*, vol. 21, no. 2-4, pp. 173–204, Dec. 2002.

[203] C. Zouridaki, B. L. Mark, M. Hejmo, and R. K. Thomas, "Hermes: A quantitative trust establishment framework for reliable data packet delivery in MANETs," *Journal of Computer Security*, vol. 15, no. 1, pp. 3–38, Jan. 2007.

[204] G. Han, J. Jiang, L. Shu, J. Niu, and H.-C. Chao, "Management and applications of trust in wireless sensor networks: A survey," *Journal of Computer and System Sciences*, vol. 3, no. 80, pp. 602–617, May 2014.

[205] T. Adams, "Reliability: Definition & quantitative illustration," Aug. 2015. [Online]. Available: https://kscddms.ksc.nasa.gov/Reliability/Documents/150814-3bWhatIsReliability.pdf [Accessed: Mar. 29, 2019]

[206] T. D. Ross, "Accurate confidence intervals for binomial proportion and Poisson rate estimation," *Computers in Biology and Medicine*, vol. 33, no. 6, pp. 509–531, Nov. 2003.

[207] L. C. Wolstenholme, *Reliability modelling: a statistical approach.* New York: Routledge, 1999.

[208] E. Cameron, "On the estimation of confidence intervals for binomial population proportions in astronomy: the simplicity and superiority of the Bayesian approach," *Publications of the Astronomical Society of Australia*, vol. 28, no. 2, pp. 128–139, June 2011.

[209] C. J. Clopper and E. S. Pearson, "The use of confidence or fiducial limits illustrated in the case of the binomial," *Biometrika*, vol. 26, no. 4, pp. 404–413, Dec. 1934.

[210] E. M. Royer, C.-K. Toh *et al.*, "A review of current routing protocols for ad hoc mobile wireless networks." *IEEE Personal Communications*, vol. 6, no. 2, pp. 46–55, Apr. 1999.

[211] K. Benahmed, M. Merabti, and H. Haffaf, "Distributed monitoring for misbehaviour detection in wireless sensor networks," *Security and Communication Networks*, vol. 6, no. 4, pp. 388–400, Apr. 2013.

[212] J. Cao, L.-L. Yang, and Z. Zhong, "Performance analysis of multihop wireless links over generalized-k fading channels," *IEEE Transactions on Vehicular Technology*, vol. 61, no. 4, pp. 1590–1598, May 2012.

[213] M. Yan, "Dijkstra's algorithm." [Online]. Available: http://www-math.mit.edu/~rothvoss/18.304.3PM/Presentations/1-Melissa.pdf [Accessed: Mar. 29, 2019]

[214] M. Haenggi, "The meta distribution of the SIR in Poisson bipolar and cellular networks," *IEEE Transactions on Wireless Communications*, vol. 15, no. 4, pp. 2577–2589, Apr. 2016.

[215] Y. Wang, Q. Cui, M. Haenggi, and Z. Tan, "On the SIR meta distribution for Poisson networks with interference cancellation," *IEEE Wireless Communications Letters*, vol. 7, no. 1, pp. 26–29, Feb. 2018.

[216] Y. Wang, M. Haenggi, and Z. Tan, "The meta distribution of the SIR for cellular networks with power control," *IEEE Transactions on Communications*, vol. 66, no. 4, pp. 1745–1757, Apr. 2018.

[217] J. Gil-Pelaez, "Note on the inversion theorem," *Biometrika*, vol. 38, no. 3-4, pp. 481–482, Dec. 1951.

[218] S. Yakubovich, "New inversion, convolution and Titchmarsh's theorems for the half-Hilbert transform," *Integral Transforms and Special Functions*, vol. 25, no. 12, pp. 955–968, Aug. 2014.

[219] *NIST Digital Library of Mathematical Functions.* https://dlmf.nist.gov/19.1, Release 1.0.19 of 2018-06-22. F. W. J. Olver, A. B. Olde Daalhuis, D. W. Lozier, B. I. Schneider, R. F. Boisvert, C. W. Clark, B. R. Miller and B. V. Saunders, eds. [Online]. Available: http://dlmf.nist.gov/

[220] G. Chen, Y. Gong, P. Xiao, and J. A. Chambers, "Dual antenna selection in secure cognitive radio networks," *IEEE Transactions on Vehicular Technology*, vol. 65, no. 10, pp. 7993–8002, Oct. 2016.

[221] Holland Michel, Arthur, "Counter-drone systems," Center for the Study of the Drone at Bard College, Tech. Rep., Feb. 2018. [Online]. Available: http://dronecenter.bard.edu/counter-drone-systems/ [Accessed: Mar. 29, 2019]

[222] M. Mozaffari, W. Saad, M. Bennis, Y.-H. Nam, and M. Debbah, "A tutorial on UAVs for wireless networks: Applications, challenges, and open problems," *IEEE Communications Surveys Tutorials*, to be published.

[223] H. Kim, L. Mokdad, and J. Ben-Othman, "Designing UAV surveillance frameworks for smart city and extensive ocean with differential perspectives," *IEEE Communications Magazine*, vol. 56, no. 4, pp. 98–104, April 2018.

[224] S. A. R. Naqvi, S. A. Hassan, H. Pervaiz, and Q. Ni, "Drone-aided communication as a key enabler for 5G and resilient public safety networks," *IEEE Communications Magazine*, vol. 56, no. 1, pp. 36–42, Jan. 2018.

[225] Y. Zhu, G. Zheng, and M. Fitch, "Secrecy rate analysis of UAV-enabled mmwave networks using Matérn hardcore point processes," *IEEE Journal on Selected Areas in Communications*, vol. 36, no. 7, pp. 1397–1409, July 2018.

[226] V. Chang, P. Chundury, and M. Chetty, "Spiders in the sky: User perceptions of drones, privacy, and security," in *Proc. ACM CHI Conf. Human Factors Comput. Syst.* Denver, CO: ACM, May 2017, pp. 6765–6776.

[227] C. Zhang and W. Zhang, "Spectrum sharing for drone networks," *IEEE Journal on Selected Areas in Communications*, vol. 35, no. 1, pp. 136–144, Jan. 2017.

[228] ITU-R, "Propagation data and prediction methods required for the design of terrestrial broadband radio access systems operating in a frequency range from 3 to 60 GHz," ITU-R, Recommendation P.1410-5, Feb. 2012. [Online]. Available: https://www.itu.int/dms_pubrec/itu-r/rec/p/R-REC-P.1410-5-201202-I!!PDF-E.pdf [Accessed: Mar. 29, 2019]

[229] A. Al-Hourani, S. Kandeepan, and S. Lardner, "Optimal LAP altitude for maximum coverage," *IEEE Wireless Communications Letters*, vol. 3, no. 6, pp. 569–572, Dec. 2014.

[230] Q. Wang, Z. Chen, W. Mei, and J. Fang, "Improving physical layer security using UAV-enabled mobile relaying," *IEEE Wireless Communications Letters*, vol. 6, no. 3, pp. 310–313, June 2017.

[231] M. Cui, G. Zhang, Q. Wu, and D. W. K. Ng, "Robust trajectory and transmit power design for secure UAV communications," *IEEE Transactions on Vehicular Technology*, vol. 67, no. 9, pp. 9042–9046, Sept. 2018.

[232] G. Zhang, Q. Wu, M. Cui, and R. Zhang, "Securing UAV communications via joint trajectory and power control," *IEEE Transactions on Wireless Communications*, vol. 18, no. 2, pp. 1376–1389, Feb. 2019.

[233] Y. Zhou, P. L. Yeoh, H. Chen, Y. Li, R. Schober, L. Zhuo, and B. Vucetic, "Improving physical layer security via a UAV friendly jammer for unknown eavesdropper location," *IEEE Transactions on Vehicular Technology*, vol. 67, no. 11, pp. 11 280–11 284, Nov. 2018.

[234] A. Li, Q. Wu, and R. Zhang, "UAV-enabled cooperative jamming for improving secrecy of ground wiretap channel," *IEEE Wireless Communications Letters*, vol. 8, no. 1, pp. 181–184, Feb. 2019.

[235] M. Mozaffari, W. Saad, M. Bennis, and M. Debbah, "Unmanned aerial vehicle with underlaid device-to-device communications: Performance and tradeoffs," *IEEE Transactions on Wireless Communications*, vol. 15, no. 6, pp. 3949–3963, June 2016.

[236] G. Chen, Y. Gong, P. Xiao, and J. A. Chambers, "Physical layer network security in the full-duplex relay system," *IEEE Transactions on Information Forensics and Security*, vol. 10, no. 3, pp. 574–583, Mar. 2015.

[237] G. Thiagarajan and C. R. Murthy, "Novel transmit precoding methods for Rayleigh fading multiuser TDD-MIMO systems with CSIT and no CSIR," *IEEE Transactions on Vehicular Technology*, vol. 64, no. 3, pp. 973–984, Mar. 2015.

[238] J. Hu, S. Yan, X. Zhou, F. Shu, and J. Li, "Covert wireless communications with channel inversion power control in Rayleigh fading," *arXiv preprint arXiv:1803.07812*, 2018.